UNIVERSITY OF BIRMINGHAM

DESIGN AND DEVELOPMENT OF COMBUSTOR FOR MICRO GAS TURBINE ENGINE

by

CHU YAN WONG

A thesis submitted to the University of Birmingham for the degree of

DOCTOR OF PHILOSOPHY

Department of Mechanical Engineering

School of Engineering

College of Engineering and Physical Science

The University of Birmingham

April 2024

Abstract

This thesis describes the early-stage design and development of a combustor for a turbogenerator with a radial configuration as a future range extender for electric vehicles. A novel curved-shape combustor is proposed, and a computational fluid dynamics (CFD) model was constructed to study the combustor performance.

The modelling strategy in this work was developed by studying iso-thermal flow followed by reacting flow simulations. To confirm the applicability of the strategy to modelling the proposed micro gas turbine combustor, it was applied to a swirling spray flame in a lab-scaled kerosene burner for which experimental data was available.

Flamelet generation manifold (FGM) with a prescribed joint probability density function (PDF) was employed for modelling the spray flame in designing and developing a micro gas turbine combustion chamber. The two-way coupling between droplets and the gaseous field was modelled by a Eulerian–Lagrangian approach. The enthalpy loss due to spray evaporation was considered in the FGM flamelet tabulation.

The work then continued by using design of experiment (DoE) to investigate the effect of the geometric and operational effects on the major chemical species and key operational parameters.

The optimisation of the combustor using the results of DoE and CFD models was presented and showed that the optimised combustor can potentially reduce the CO emissions by 88%, NOx by 31%, and soot by 83%. In addition, the optimised combustor showed that the combustor average outlet temperature met the requirements, and the pattern factor decreased by 41%, while the total pressure drop across the combustor increased by only 0.1%.

In summary, this thesis demonstrates the capability of the present modelling strategy to simulate a novel combustor with complex geometry as a design tool and DoE to identify the significant parameters and to determine the optimal parameter settings that give minimum pollutant emissions and maximum thermal performance.

Acknowledgements

First, I would like to express my appreciation to my supervisors Professor Kyle Jiang, Dr Carl Anthony, and Dr Mehdi Jangi for their guidance, and for sharing their knowledge and expertise throughout this PhD course. Throughout our progress meetings and discussions, their insights and intuitions have enhanced my understanding of many topics, such as combustion CFD modelling and micro gas turbine technology. The PhD work would not have happened without their support.

Technical knowledge and input were also kindly provided by Dr Pu Guang of Birmingham High Performance Turbomachinery and Professor Yuzhen Lin of Beihang University.

I would like to thank my colleagues Dr Tianchu Jiang, Dr Han Liu, and my friends at the University of Birmingham for their support and company.

I would also like to express my gratitude to London Proofreaders for the excellent proofreading.

Finally, I would like to thank my entire family, particularly my wife, Yuk Shan Leung, for their encouragement and motivation throughout the period I was studying for the PhD.

Contents

List of Figures

List of Tables

List of Abbreviations

CFD	Computational Fluid Dynamics
CFL	Courant–Friedrichs–Lewy
DNS	Direct Numerical Simulation
DRW	Discrete Random Walk
FGM	Flamelet-Generated Manifold
FTT	Flow-Through Time
FVM	Finite Volume Method
IRZ	Inner Recirculation Zone
LBO	Lean Blowout
LES	Large Eddy Simulation
LOL	Lift-Off-Length
LTC	Low-Temperature Chemistry
LPP	Lean Premixed Per-vaporised
MGT	Micro Gas Turbine
N-S	Navier–Stokes
ORZ	Outer Recirculation Zone
PDF	Probability Density Function
PIV	Particle Image Velocimetry
PVC	Processing Vortex Core
RANS	Reynolds-Averaged Navier–Stokes
RNG	Renormalized Group
RSM	Reynolds Stress Model
RQL	Rich Quench Lean
SDFM	Steady Diffusion Flamelet Model
SRS	Scale Resolving Simulation
SST	Shear Stress Transport
TCI	Turbulence–Chemistry Interaction
URANS	Unsteady Reynolds-Averaged Navier–Stokes

Chapter 1 Introduction

1.1. Introduction

This thesis describes the early-stage design and development of a micro gas turbine combustor by basic design calculations and three-dimensional computational fluid dynamics (CFD) of a reacting flow modelling approach for simulating a lab-scaled burner and novel combustor for micro gas turbine application. The modelling strategy was developed and validated by investigation of the swirling flow dynamics and spray combustion in a lab-scaled swirl-stabilised burner. Following that, the basic design calculation of a novel design of a micro gas turbine combustor is presented, and the reacting CFD modelling results are discussed to understand the combustor performance and emissions prediction. The parametric study of the novel combustor is numerically simulated and compared with the baseline design to understand the effect of geometric and operational changes on combustor performance and emissions. An experimental investigation was conducted to prove the operability of the baseline combustor design concept.

In this chapter, Section 1.2 presents the background of micro gas turbine engine market, which supports the need for combustor design. Section 1.3 lists the aims and objectives of the research. Section 1.4 gives a brief introduction to each chapter in this thesis.

1.2. Background

Micro gas turbines, also known as microturbines, are gaining interest in power generation market due to the current demand for cleaner and more efficient power generation resources. Microturbines have the advantages of proven low emissions, high power-to-weight ratio, fuel flexibility, and reliability that make research interested in developing the technology [1]. Various types of micro gas turbine (MGT) engines have been developed in many energy generation systems, such as distributed energy systems, range extenders, telecommunication, and solar power generation [2].

MGTs are a type of gas turbine with a power range of up to 500 kW [3]. The configuration is similar to large-scale gas turbines consisting of a compressor, a combustor, and a turbine. MGTs use the Brayton cycle and therefore have great potential for using various properties of fuels. In [4], [5], the development of combustion technology demonstrates that the emission of MGTs can reach a low value.

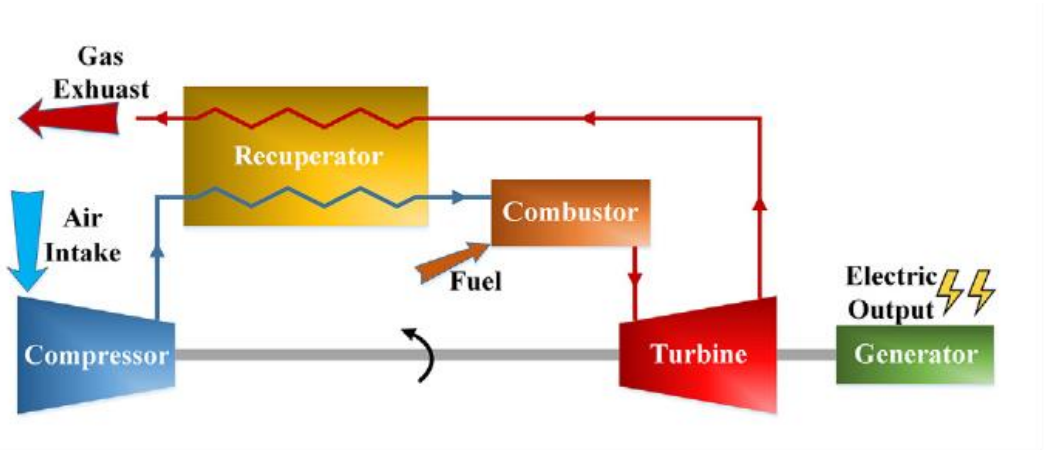

Figure 1.1 Brayton cycle of the MTGs

In recent years, some commercial MGTs have received great interest in the market. A table below shows the different MGT designed from different companies and the power range with the associated combustor technology.

Table 1.1 MTGs available in the market

Company	Power [kW]	Combustor type
Capstone [6]	30	Compact annular combustor
Bladon [7]	12	Can combustor
AlliedSignal [8]	70	Single cylinder combustor
ET group [9]	45	Can combustor

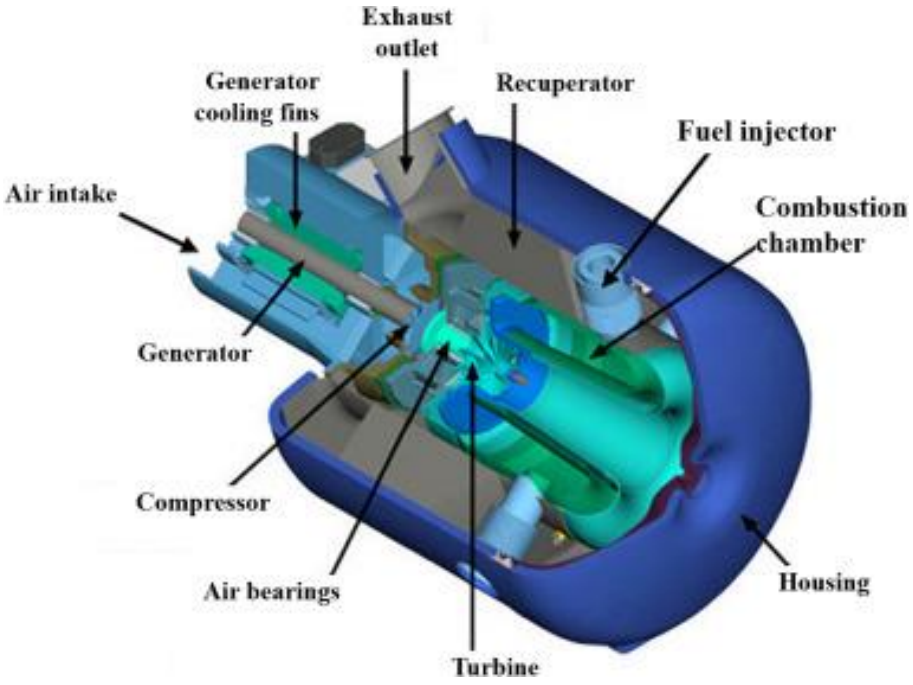

Figure 1.2 Combustor developed by Capstone Company [6]

Figure 1.2 shows the combustor developed by Capstone Company. The engine arranges the heat recovery system in a ring on the periphery of the compressor, turbine, and other components. The combustor is one example of an annual type combustor, and the combusted gas needs to turn 90 degrees from left to right to reach the exhaust outlet. The thermal efficiency of the engine can reach up to 26% with the recuperator.

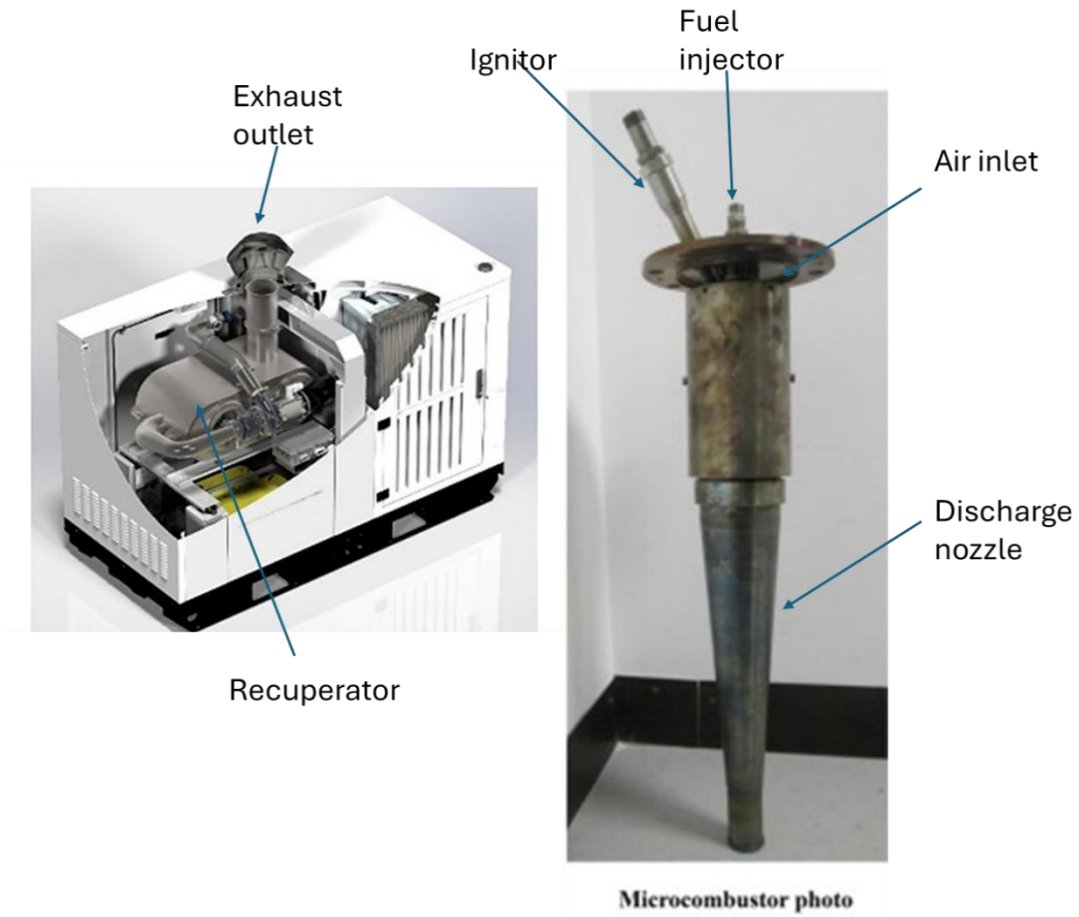

Figure 1.3 Combustor developed by Bladon [7]

Figure 1.3 shows the micro gas turbine generator and the combustor developed by Bladon. The combustor is a can combustor type. The inlet air flows tangentially through the air swirlers into the combustor. After the combustion process, the hot combusted gases flow through the discharge nozzle towards the exhaust outlet. The thermal efficiency can reach up to 25% with the use of a recuperator.

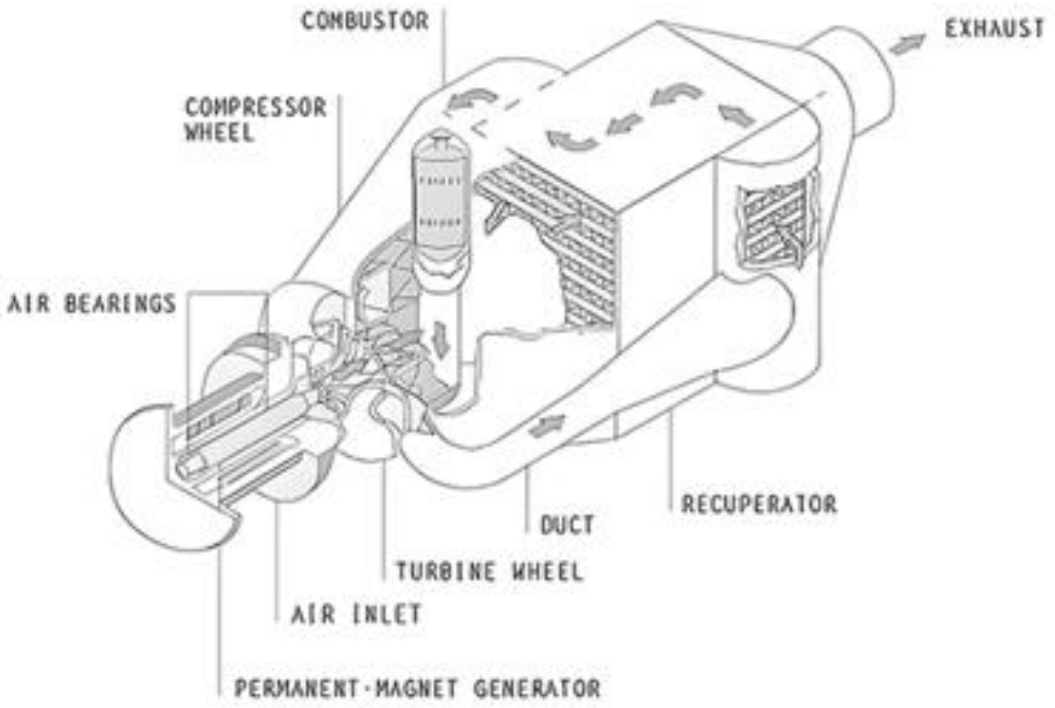

Figure 1.4 Engine developed by AlliedSignal [8]

Figure 1.4 shows the product from AlliedSignal; the engine uses a single cylinder can combustor layout with the use of recuperator to increase the thermal efficiency. The engine can reach thermal efficiency up to 28.5% with a recuperator.

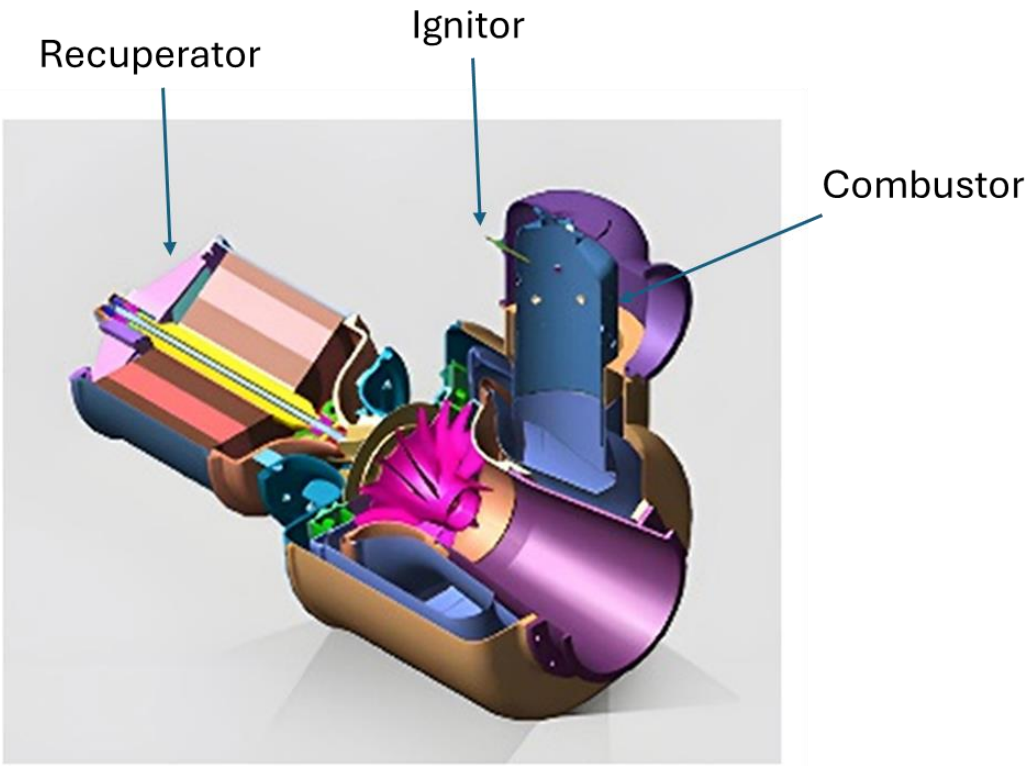

Figure 1.5 Micro gas turbine developed by the ET group [9]

Figure 1.5 shows the micro gas turbine developed by ET group, which has a single cylinder combustor and an independent recuperator. The thermal efficiency peaks at 28% with the recuperator.

From Table 1.1 above, the combustor used in these MGTs relies on the can combustor type due to its simple design and compactness. In addition, the use of a recuperator can increase the thermal efficiency to improve the low thermal efficiency characteristics of the micro gas turbines. Therefore, this motivates the design and the development work of a combustor for MGTs. A

CFD approach can be considered an effective design tool to design and develop the combustor in line with the fast transition of the market.

1.2.1 Ground-based gas turbine regulation

Table 1.2 is a summary of the European countries and Japan standard in gas turbine emissions in CO and NOx. The emission requirements in the United Kingdom are below 87 PPM for CO and 74 PPM for NOx, respectively. The emission standards in United Kingdom have been chosen to follow in the combustor design in this thesis.

Table 1.2 Gas turbine air pollution emission standard in different countries [10]

Country	Size range	CO [PPM]	NOx [PPM]
Austria	<50MWth	87	106
Belgium	<100MWth	87	186
Germany	<100MWth	87	106
Italy	<8MWth	87	-
Spain	All size	594	328
Sweden	<500MWth	87	-
United Kingdom	<50MWth	87	74
Japan	-	-	42

1.2.2. Combustor design considerations

Combustor is one of the key components in gas turbine engines, especially in micro turbines. Combustors are used to convert the chemical energy stored in fuels into mechanical energy. The higher the combustion efficiency, the lower the emission level as well as the specific fuel consumption of MGTs. A more uniform temperature distribution denoted by the pattern factor at the combustor outlet contributes to longer turbine material life. Combustor development remains by trial-and-error testing and empirical correlations in experimental rigs and in prototype and in-service engines and power plants [11]; therefore, numerical modelling plays an important role in reducing the necessity for experimental investigations and faster design cycles.

Some design parameters were set out to meet the design of a micro gas turbine engine developed in the Birmingham High Performance Turbomachinery. The micro gas turbine focuses on the application of a range extender used in electric vehicles [12].

The design specification is listed in Table 1.3 below.

Table 1.3 UoB Combustor design parameters

Design parameters	Importance
Air mass flow rate of 150 g/s	Medium
Pressure ratio of 3.7	Medium
Fuel capability of diesel	High
Inlet temperature of 442K	Medium
Expected outlet temperature of 1273K	High
Combustor diameter of the bend is about 0.5m	High
Pressure drop less than 5% of inlet	High
Pattern factor as low as possible	High

The turbine inlet temperature is set to 1273K in order to maintain the turbine material life. A thermal barrier coating and the use of ceramic materials have been considered to allow further increases in the turbine inlet temperature to increase the overall system efficiency.

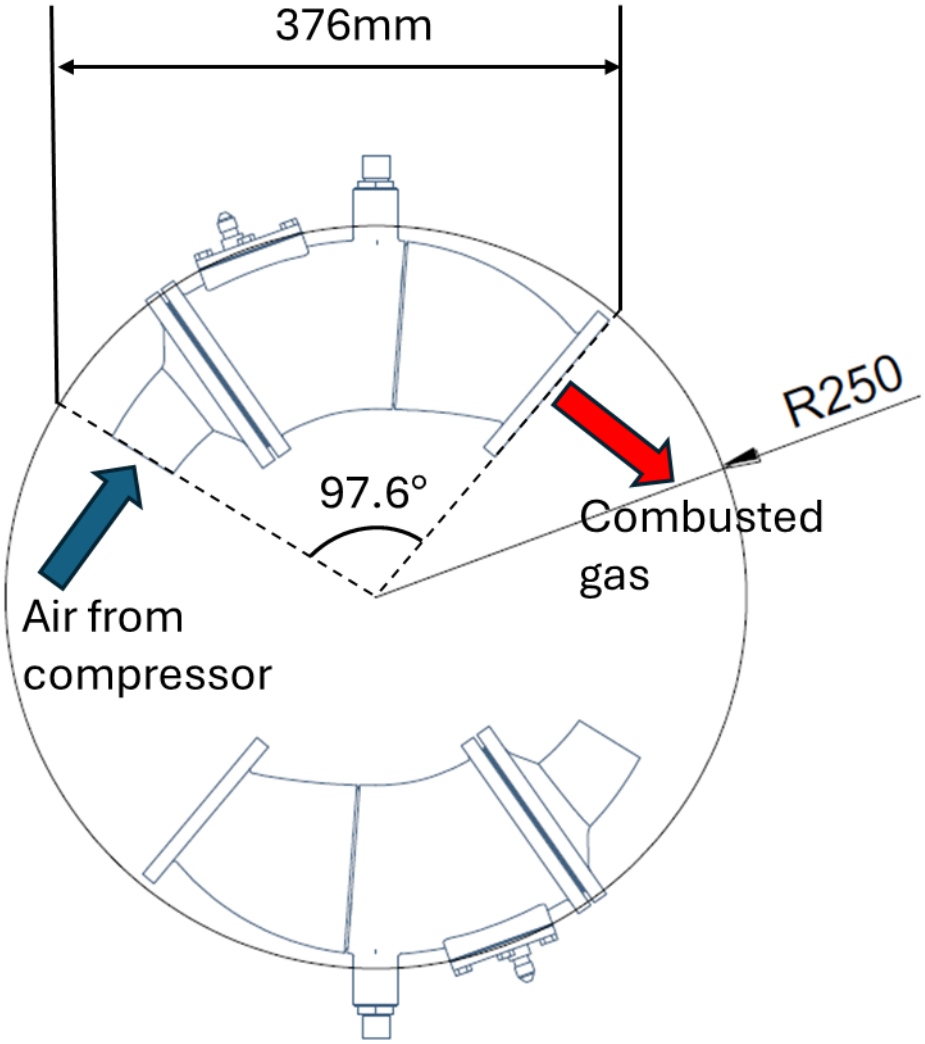

Figure 1.6 The layout of UoB combustor [12]

From Figure 1.6, the combustor geometric constraint is set to a can combustor design with a little bend around 0.5 m in diameter to fit the compressor and the turbine design [12].

Figure 1.7 Two possible shape of the UoB combustor

The diameter and the length of the combustor are secondary constraints and can be adjusted for performance consideration. Two possible shapes have been illustrated in Figure 1.7. Figure 1.7 (b) is shorter than Figure 1.7 (a) in length; therefore, the residence time is shorter. The design in Figure 1.7(b) is more suitable in annular combustor design. Hence, the shape in Figure 1.7 (a) is chosen for the can combustor design and the length of the UoB combustor is 376 mm, as shown in Figure 1.6. The capability of burning diesel liquid is highly prioritised.

1.3. Aims of the thesis

The combustion process in a combustor is extremely complex; it has a strong coupling effect of turbulent mixing, liquid fuel atomisation and evaporation, chemical reaction, mass transfer and heat transfer between solids and gases. The design of a micro gas turbine relies on experience and empirical correlations of large-scale aeroengine combustors, and the literature lacks basic design guidelines, simulation, and experimental data that cover the micro gas turbine combustor design. As a result, this research aims to generate preliminary design considerations and turbulent combustion modelling strategies via computational investigations using the commercial software Ansys Fluent. The numerical results give insight into the optimisation of the combustor in terms of aerodynamics, turbulent mixing, combustion efficiency, and emissions prediction.

The research objectives are structured as follows:

1. Simulate and analyse the popular turbulence models' performance and limitations in swirling flow dynamics in a swirl-stabilised burner.
2. Simulate and analyse the performance and limitations of the state-of-the-art turbulent combustion model in spray combustion in a swirl-stabilised burner.
3. Investigate the state-of-the-art low emissions combustor design configurations and the design calculation to design a novel combustor in a micro gas turbine application.

4. Develop a modelling strategy for spray combustion in a swirl-stabilised combustor and assess the trade-off between combustor performance and emissions through different design parameters.

1.4. Thesis structure

This thesis has a total of seven chapters. In Chapter 1, an introduction chapter presents the research problem and the design requirements and needed of combustor for micro gas turbine engines.

Chapter 2 presents a state-of-the-art low emissions combustor design and the fundamental combustion physics that discuss the underlying physics to construct the CFD turbulent combustion modelling methodology. Multiphase flow physics is also discussed, as liquid fuels are the main fuel used in this novel combustor design.

Chapter 3 discusses the underlying theory of turbulent combustion modelling. The theory of turbulence modelling, as well as combustion modelling, is discussed.

Chapter 4 presents and discusses the performance of popular turbulence models on swirling flow dynamics and validates against the experimental results of a swirl-stabilised burner. The model is used in subsequent chapters to simulate and assess the combustor aerothermal performance.

Chapter 5 presents and discusses the spray combustion model on top of the turbulence model from Chapter 4 to simulate a spray flame in a swirl-stabilised burner and validate with experimental results. The modelling strategy of spray combustion is developed and used in Chapter 6 to assess the novel combustor aerothermal performance.

Chapter 6 applies the modelling strategy developed in previous chapters and assesses the aerothermal performance based on CFD results. In addition, an optimisation of the combustor is proposed based on the simulation results.

Chapter 7 provides the conclusion and contribution of this thesis, and some future research suggestions are proposed.

1.5. Contribution to knowledge

The novelty of the present thesis is outlined as follows:

- This thesis demonstrates the potential combustor design for micro gas turbine engines using the RQL configuration for low emissions and high combustion efficiency.

- This thesis examines the steady and unsteady CFD simulations performance on complex turbulent swirling flow fields to develop a

computationally efficient methodology for designing a micro gas turbine combustor in the early design stage.

- This thesis provides detailed simulation strategies of the turbulent swirling spray flames in a lab-scaled burner to develop a design tool for micro gas turbine engine combustor design in the early stage.

- This thesis introduced a swirl number calculation for a radial blade swirler, which can be used to aid the aerodynamics of the swirler design to achieve flame stabilisation.

- This thesis investigates the operational and geometric effect on novel combustor emissions and performance using a parametric study of reacting CFD simulations.

- Unlike most other studies [13]-[17], the CFD methodology in the present thesis was conducted using the state-of-the-art turbulent combustion model flamelet-generated manifold (FGM) with a multi-step chemistry mechanism rather than a chemical equilibrium model using one-step chemistry calculations.

Chapter 2 Physics of Micro Gas Turbine Combustor

2.1. Introduction

This chapter reviews the existing knowledge related to the physics inside the combustor and the state-of-the-art low emission combustor configurations. Section 2.2 provides an overview of the typical combustion mode and combustor configurations in a gas turbine combustor. Section 2.3 reviews two design concepts on low emission combustion technology in modern aeroengines. Section 2.4 discusses the importance of the flame stabilisation mechanism inside a combustor and reviews the typical flow structures in swirling flows used as a flame holder. Section 2.5 details the different combustion classifications in laminar and turbulent combustion that contain the fundamental theory of turbulent combustion modelling. Section 2.6 reviews the physics of multiphase flows, liquid atomisation, and spray combustion. Finally, Section 2.7 gives a summary of this chapter.

2.2. Combustion fundamentals in combustors

Combustion in traditional gas turbines is divided into three modes: non-premixed combustion, premixed combustion, and partially premixed combustion. Non-premixed combustion happens when fuel and oxidiser are injected into the combustor separately before mixing with each other, whereas premixed combustion, fuel and oxidiser are mixed before injecting into the combustor. These are two extreme cases in combustion mode: partially premixed combustion is between non-premixed combustion and premixed combustion, which always occurs in practical combustion systems.

Figure 2.1 shows a typical can combustor configuration that is widely used in aeroengines [18]. This type of combustor can operate in non-premixed or partially premixed combustion due to its stable characteristics and good ignition performance. In addition, a wide range of air fuel ratios contribute to excellent operability where stable combustion can occur inside the combustor. However, due to the non-premixed flame with high adiabatic flame temperature characteristics, the NOx emission is generally higher than premixed combustion.

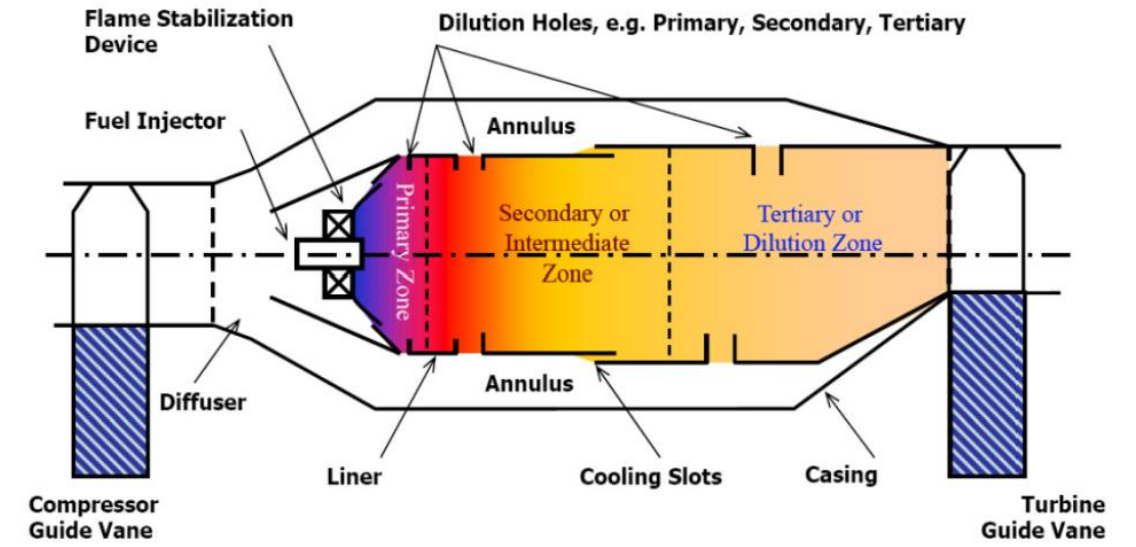

Figure 2.1 Conventional can combustor layout [18]

A diffuser is used to slow down the velocity of the flow entering the combustor. A flame tube (liner) is placed inside the combustor casing, and the combustion and hot burnt gases are kept inside the flame tube. Therefore, some cooling holes are introduced to allow the air to penetrate into the annulus to quench the combustion quickly as well as adjust the exit temperature distribution. Other types of combustors are used in aeroengines, such as annular combustors and can-annular combustors, which are multiple can combustors connected by a common ring [19]. Due to the design complexity of annular and can-annular combustors, this thesis focuses on a can combustor type.

2.3. Low emission combustion technology

The design of combustors for low emission micro gas turbines is not highly developed, and this is a new field compared to well-developed large industrial engines and aeroengines. Some of the low emission combustion technology from aeroengines can be used in micro gas turbine combustor design. In the following section, two promising low emission combustion technologies for liquid fuels are reviewed.

2.3.1. Rich-burn, quick-quench, lean-burn (RQL) combustor

The rich-burn, quick-quench, lean-burn (RQL) combustor represents state-of-the-art low emission design in aeroengines. Figure 2.2 shows the working principle of the RQL combustor. Applying this concept to the combustor shown in Figure 2.1, a primary zone is designed to be a rich-burn region to ensure flame stability. The typical equivalent ratio is between 1.2 and 1.8. A rapid mixing region in the secondary and dilution zones is used to create a quick quenching effect to dissipate smoke with large amounts of diluting air. The NOx emission level is also controlled by rapid mixing. The careful selection of equivalence ratios of different zones is a critical design consideration to compromise CO, UHC, and soot levels. A promising benefit of RQL combustion is the combustion stability due to the nature of non-premixed flames, which allows for easier re-ignition in aviation engines.

This feature also benefits micro gas turbine engines if the engine needs to be turned on and off frequently.

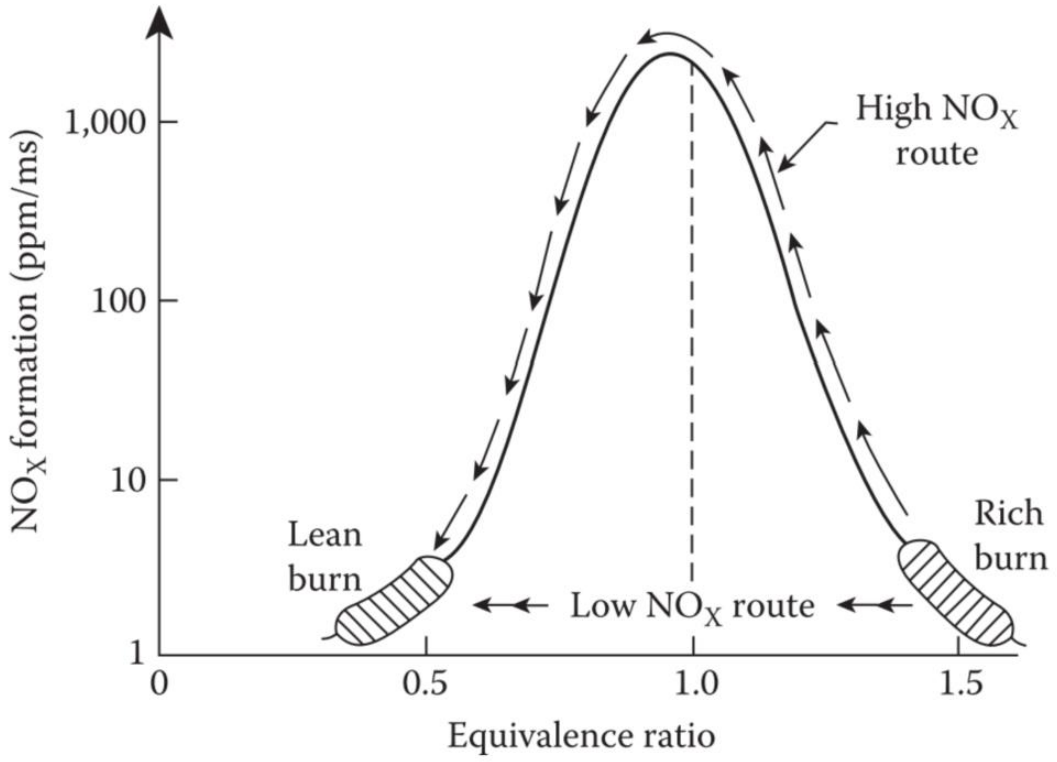

Figure 2.2 RQL combustor working principle [20]

2.3.2. Lean premixed pre-vaporised (LPP) combustor

Lean premixed pre-vaporised combustor is an alternative ultra-low NOx technology developed for liquid fuels. Figure 2.3 shows the concept of the LPP combustor. The fuel is first vaporised and then mixed with the oxidiser to create a local homogenous mixture in the fuel preparation duct to control the equivalence ratio in the combustion zone. Low NOx emissions can be achieved because the mixture burns at a low equivalence ratio that is near

the lean blowout (LBO) limit. The degree of premixing can be achieved by introducing a swirler to prompt the turbulent mixing between fuel and oxidiser. The special concern of this design is the time required for fuel to completely evaporate, and the possibility of flashback in the fuel preparation duct at higher inlet air temperatures and pressures.

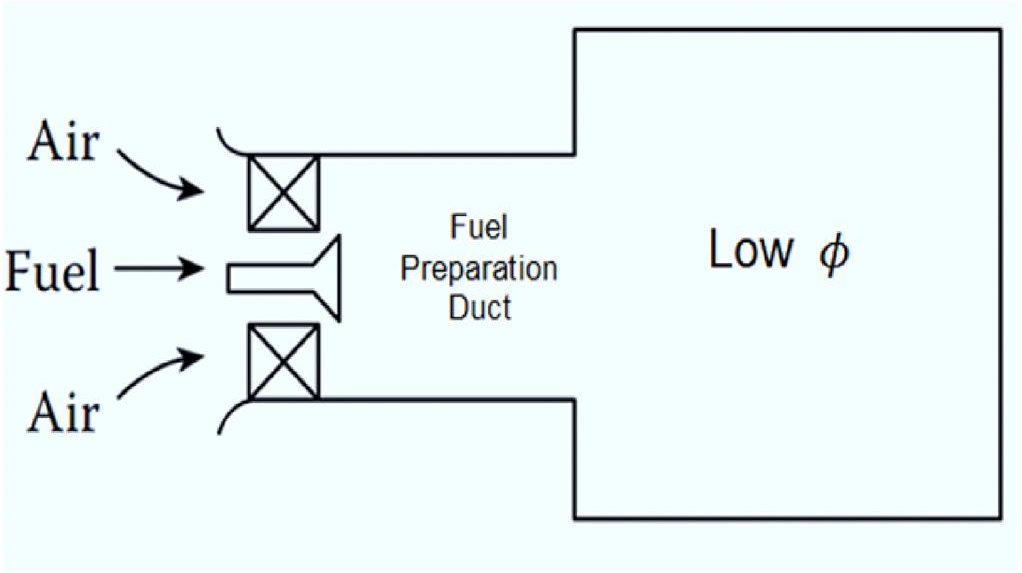

Figure 2.3 LPP combustor [20]

2.4. Flame stabilisation mechanism

Most hydrocarbons have laminar flame speed values in air around 30–45 cm/s [21]. Turbulence can enhance flame propagation, thereby increasing the flame speed to at most a few 100 cm/s [21]. However, in a practical combustion system, the air velocity is greater than the turbulent flame speed; therefore, a stabilisation mechanism is necessary. The stabilisation of flames that relies on the wake of a bluff body or swirl-induced recirculation is widely used and studied for non-premixed and premixed flames in combustion research.

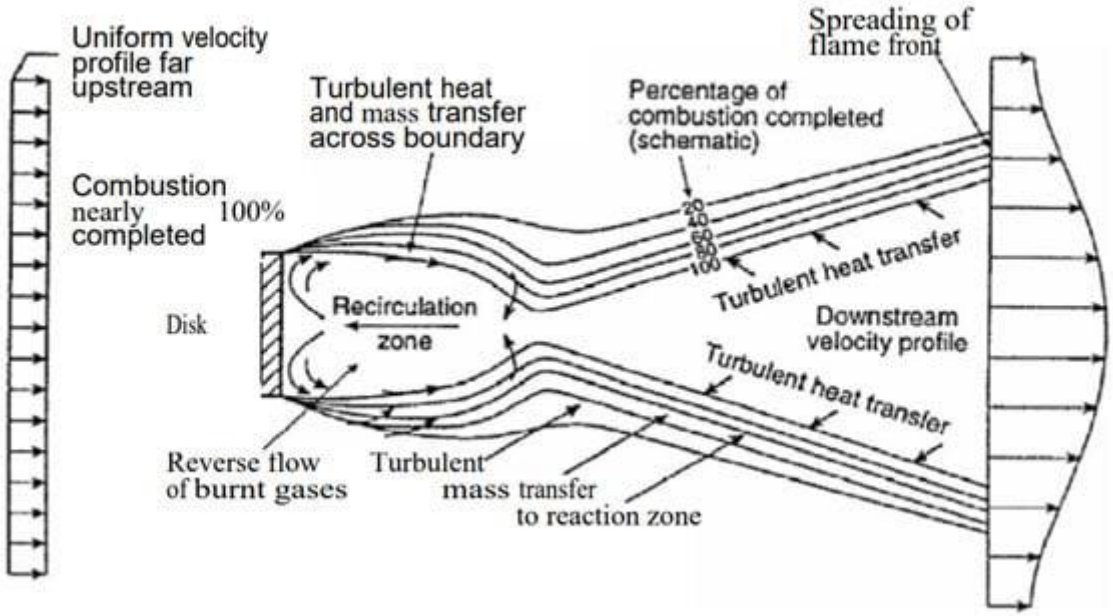

Figure 2.4 Flame stabilisation mechanism behind a bluff body [21]

Figure 2.4 shows a recirculation created by the wake of the bluff body or swirl-induced mechanism. The low velocity region, which is lower than the

laminar flame speed, is required in order not to blow off the flame. Bluff bodies are typically used in high-speed ramjet engines, and the discussion focuses on swirl-stabilised mechanisms, as this is widely used in industrial gas turbines.

The swirl-stabilised mechanism is shown in Figure 2.5, which can also represent a typical flow feature in a lab-scale swirl-stabilised burner. The vortex breakdown region is in the inner recirculation region, whereas two outer recirculation regions are near the burner wall. In such cases, flames often stabilise in the shear layer of an asymmetric bluff body. The reverse flow of burnt gases inside the inner recirculation zone can also help to continuously ignite fresh ready-to-burn mixtures.

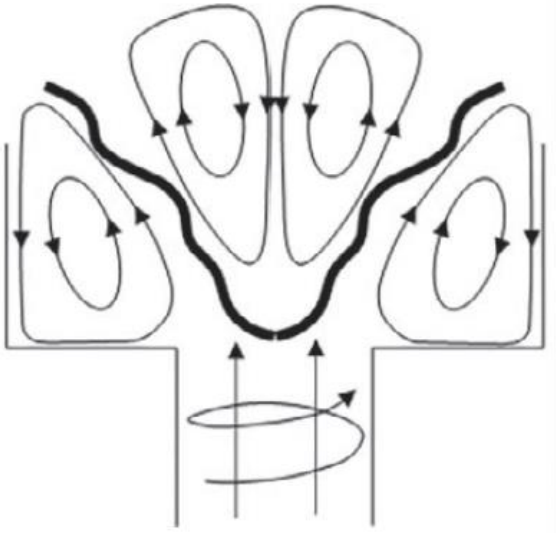

Figure 2.5 Swirl-stabilised mechanism [22]

2.5. Combustion classification

2.5.1. Non-premixed combustion

A diffusion flame (non-premixed flame) occurs when the fuel and oxidiser (usually air) enter the combustion chamber separately [23]. The Burke–Schumann flame was first in 1928 defined by Burke and Schumann [24] and used infinitely fast chemistry assumptions to predict the flame height and flame shape in diffusion flames. The one-dimensional structure of the diffusion flame is outlined in Figure 2.6. The reaction zone is located between the fuel and the oxidiser, the state of fuel and oxidiser must be gaseous, and the mixing must be sufficiently rapid to mix at the molecular level and penetrate towards the reaction zone to ensure a flame can be ignited/sustained. The fuel and oxidiser are transported towards the reaction zone through diffusion as well as convection. The diffusion process of the species is the dominating mechanism that affects the burning rate and influences the rate of heat release out of the reaction zone. The combustion products and heat of combustion are then transported away from the reaction zone. Furthermore, there is no flame propagating effect; hence, the thickness of the reaction zone and the mixing zones are controlled by the mixing of chemical species only [25].

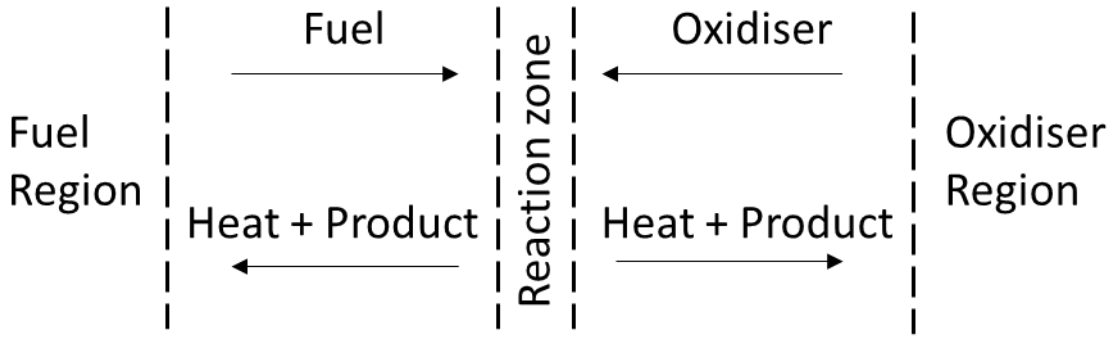

Figure 2.6 Structure of non-premixed flame [25]

Therefore, a conserved scalar called the mixture fraction (Z), which represents the mixedness between the fuel and oxidiser, was introduced by Bilger [23]. The flame shape can be represented by the value of the mixture fraction at the stoichiometric value (Z_{st}), since the flame remains located in the position of the stoichiometric surface between the fuel and the oxidiser. The mixture fraction is expressed in terms of the atomic mass as follows [26]:

$$f = \frac{Z_i - Z_{i,ox}}{Z_{i,fuel} - Z_{i,ox}} \tag{2.1}$$

where Z_i is the elemental mass fraction for element i, the subscript ox denotes the value at the oxidiser stream, and subscript $fuel$ denotes the value at the fuel stream. The mixture fraction for all elements is identical if the diffusion coefficients for all species are equal, which is valid for turbulent flows where turbulent convection dominates. The mixture fraction is one of the key parameters in turbulent combustion modelling.

2.5.2. Premixed combustion

The premixed flames refer to the reactants mixed at the molecular level to achieve a compositionally homogenous mixture at a low temperature prior to ignition [27]. Once ignition is achieved in a premixed flame, the resulting flame tends to propagate upstream and consume the unburnt mixture. A complete mixing is defined by a characteristic mixing timescale that is smaller than the rate of chemical reaction time. The convection and molecular diffusion in premixed flames are the same as in diffusion flames. The structure of a premixed flame in one-dimensional space is shown in Figure 2.7. The flame consists of three regions: the preheat zone, reaction zone (flame sheet region), and equilibrium zone [25]. The preheat zone is a region left by the flame sheet where the unburn reactant mixture is heated up through conduction. At the preheat zone, since the temperature is generally below the autoignition temperature, no chemical reaction takes place, which results in the convection and diffusion processes being the dominant mechanism. When the unburnt reactant mixture is heated to the ignition temperature, the energy is above activation energy, allowing the chemical reactions to initiate. The unburnt reactant mixture turns into burnt products. The flame sheet contains all the processes above and has a very thin thickness compared to the preheat zone. The region containing all the burnt mixtures is called the equilibrium zone, and the zone is chemically inert.

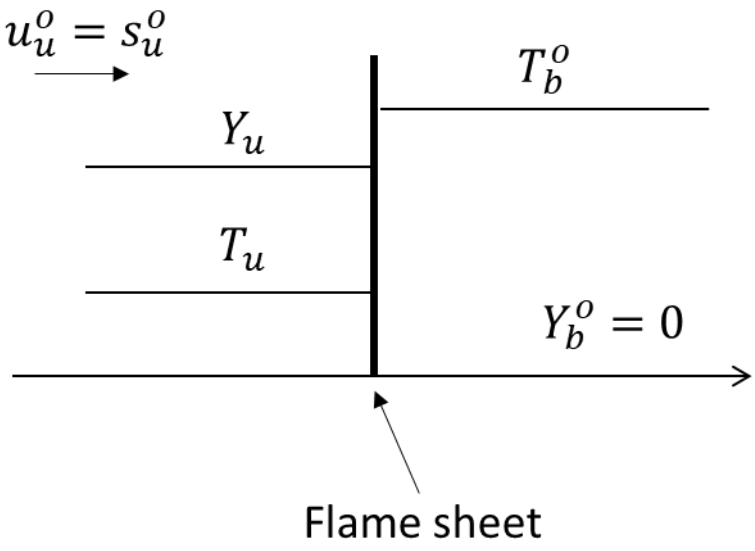

Figure 2.7 Structure of premixed flame [25]

The main difference between diffusion flame and premixed flame is the propagation effect of the flame. The laminar flame speed (s_L^0) can be introduced to describe the rate of propagating of a flame through the combustible mixture under laminar conditions. Flame speed is the property that dictates the flame shape and important flame stability characteristics, for example blowoff and flashback phenomena in numerical turbulent combustion modelling [28]. It is also a fundamental concept in numerical turbulent combustion modelling for non-premixed combustion, premixed combustion, and partially premixed combustion.

2.5.3. Partially premixed combustion

Theoretical and numerical combustion has been reviewed in [29]. A partially premixed combustion is defined as some partial premixing of the reactants that may exist before the reaction zone region develops [29]. Diffusion flame and premixed flame theory are useful for academic purposes because they can provide a fundamental understanding of how flames evolve under aerodynamic flows and flame structures. In practical combustion systems such as internal combustion engines and gas turbine engines, turbulence is present to enhance the degree of mixedness between the fuel and the oxidiser before ignition. Perfectly mixed flame is restricted in practical combustion systems because of the use of liquid fuels.

A partially premixed flame refers to a flame that is compositionally inhomogeneous [30]. Lifted flames are an example of partially premixed flames and are widely used in modern gas turbine engines with the use of swirling flows to extend the flammability limits [31]. In a lifted flame, the flames detach from the nozzle and can be characterised by lift-off length (LOL), the flame front stabilised on a position further downstream of the nozzle exit, and the degree of premixing increased before the reaction zone [32]. The premixing process takes place directly in the combustion chamber, mitigating the risk of flashback as well as the fuel coking effect. The numerical prediction of lifted flames is a very challenging task for turbulent combustion CFD modelling because of the coupling between finite rate chemistry and turbulent mixing.

The theory of turbulence presented in Chapter 3 can be used to understand the problem when turbulence and combustion can interact. The next section presents the turbulent combustion regime that describes the turbulent eddies and flame interactions, and spray combustion typically applied in modern combustion systems, such as internal combustion engines (ICEs) and gas turbines in both aviation and industry.

2.5.4. Turbulent combustion regimes

The relevant turbulent length scales ranging from the largest eddies to the smallest eddies (Kolmogorov scale) are important for studying and modelling turbulent flames. The interactions between turbulent eddy length scales and laminar flame properties, such as laminar flame speed, can be related to understanding how a flame behaves in turbulent flow. The non-dimensional parameter is defined as the ratio between the integral timescale (τ_I) and chemical time scale (τ_c) called the Damköhler number (Da).

$$Da = \frac{\tau_I}{\tau_c} \tag{2.2}$$

where the chemical timescale is defined as the time taken for the flame to propagate over a distance of its flame thickness, as shown in Figure 2.7

above. Another non-dimensional parameter used to describe the transition is the Karlovitz number (Ka), which can be related to the reciprocal of the Damköhler number as follows:

$$Ka = \frac{\tau_c}{\tau_\eta} \tag{2.3}$$

where τ_η denotes the smallest scales of turbulent eddy timescale.

The diffusion flame combustion regime is different from the premixed flames combustion regime, and the Damköhler number is a non-dimensional parameter that is widely used to show the flame operability condition and limit.

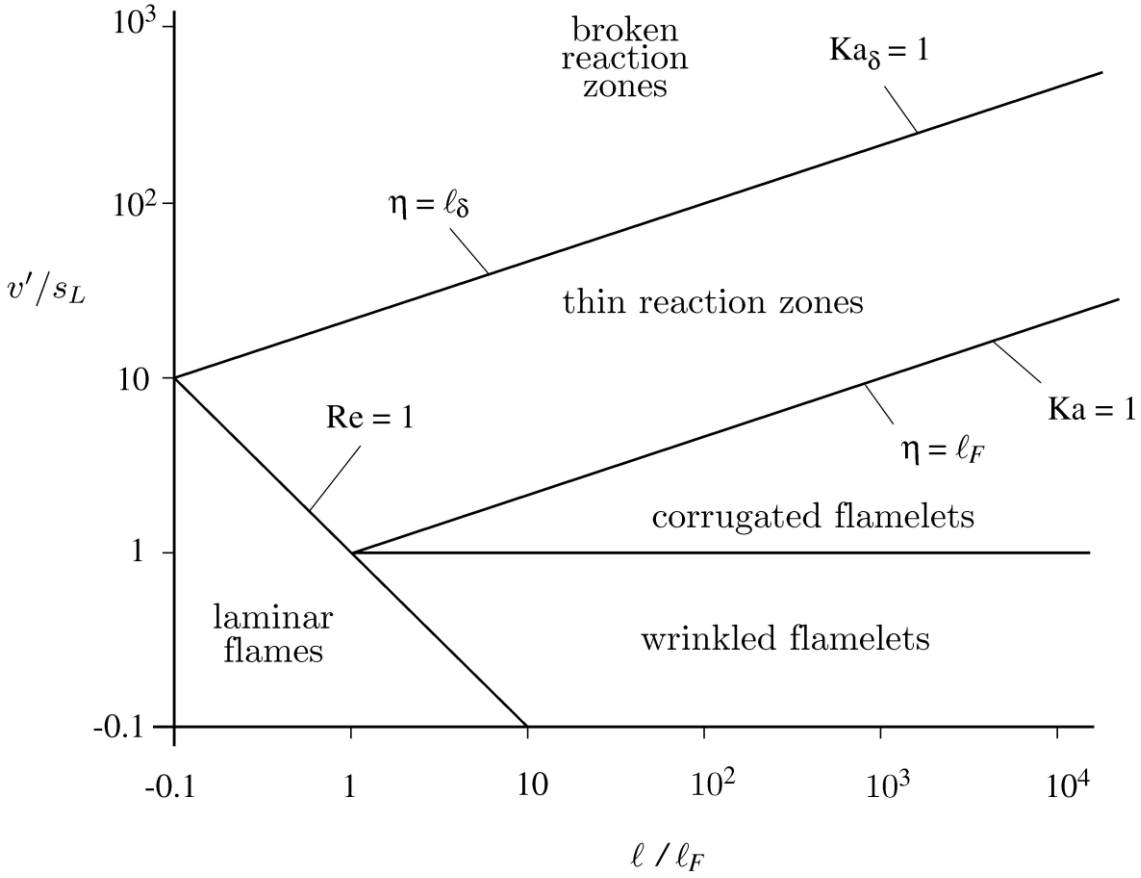

Figure 2.8 Turbulent premixed flame regime diagram [27]

For premixed combustion, if the turbulent eddy length scale is larger than the thickness of the flame sheet, the eddies cannot penetrate the inner layer zone; therefore, this can change the flame structure and distort the flame front, causing the flame to wrinkle and increasing the surface area [25]. The turbulent flame speed is related to the laminar flame speed with the area ratio of the turbulent flame and laminar flame and its wrinkling factor. Turbulence does not affect the inner layer zone structure of the flame in the Damköhler number of $Da \ll 1$. In such cases, the chemistry can be assumed to be infinitely fast, and the eddies can therefore wrinkle the flame.

Figure 2.8 illustrates the combustion regime for premixed flames in the flamelet regime, where the flame thickness is smaller than any turbulent scale ($Ka < 1$) and the chemistry is infinitely fast ($Da > 1$). Within the corrugated flamelet regime, the smallest eddies can penetrate, thereby altering the flame structure by entering the preheat zone, whereas the turbulence intensity is not strong enough to alter the flame structure within the wrinkled flamelet regime.

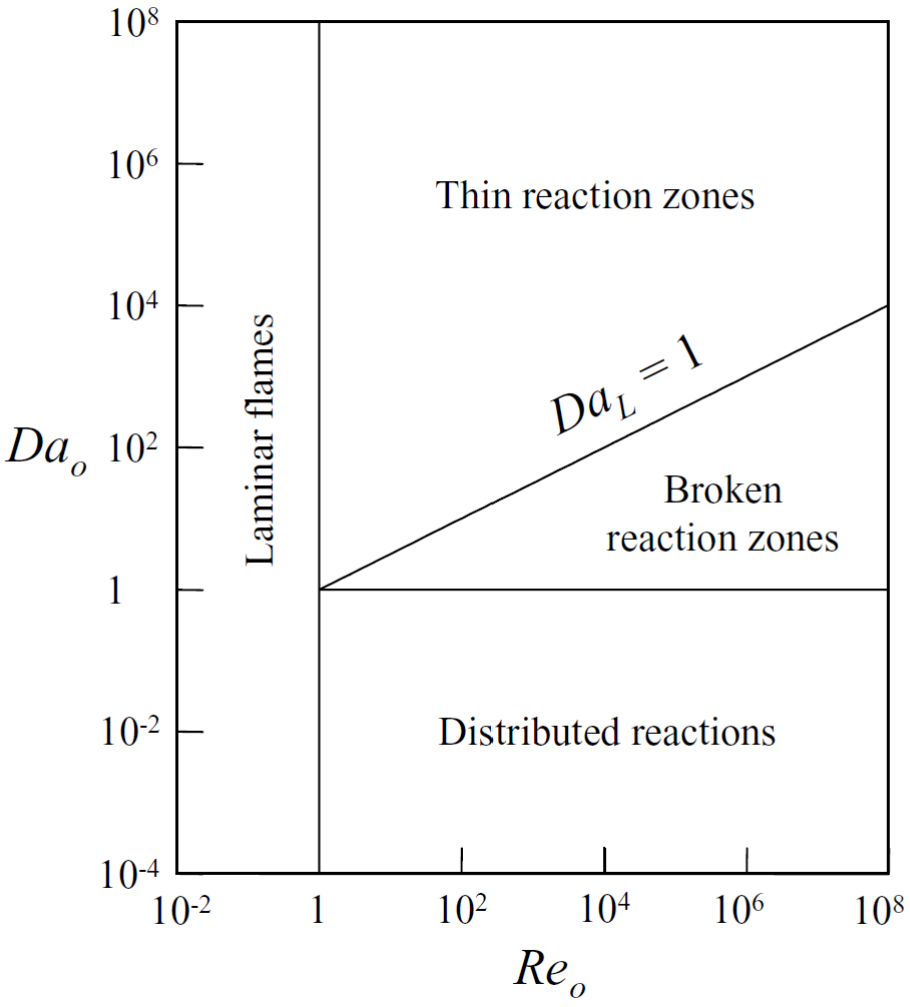

Figure 2.9 The turbulent diffusion combustion regime diagram [25]

The turbulent diffusion combustion regime is very different from the turbulent premixed combustion regime, as laminar diffusion is fundamentally different from laminar premixed flame. The diffusion flame does not have a characteristic velocity; hence, a relevant characteristic timescale is difficult to define. As shown in Figure 2.6, the preheat zone is determined by the balance between convection and diffusion transport of the mixture fraction [25]. The eddy size decreases with an increase in the Reynolds number in turbulent flow, and turbulent diffusion dominates molecular diffusion. As a result, the fast chemistry assumption cannot apply; a diffusion length scale can be expressed in terms of the mixing length thickness,

$$l_L \approx \sqrt{\frac{D_{st}}{\chi_{st}}} \tag{2.4}$$

where D_{st} is stoichiometric mass diffusion coefficient and χ_{st} is stoichiometric scalar dissipation $\chi_{st} = 2D|\nabla f|_{st}^{\ 2}$. The characteristic diffusion timescale is therefore defined as

$$\tau_L = \frac{l_L^2}{D_{st}} = \frac{1}{\chi_{st}} \tag{2.5}$$

In this case, the flame Damköhler number is written as [25]:

$$Da = \frac{\tau_L}{\tau_c} \approx \frac{\tau_I}{\tau_\eta}\frac{\tau_L}{\tau_c} = \sqrt{Re_t}Da_L \tag{2.6}$$

In Equation 2.6, for $Da_L \approx 1$, this implies that the flame is not able to sustain and extinguish, and the flamelet assumption is invalid, as the residence time within the reaction zone is not long enough for a flame to sustain [33]. For $Da_L < 1$, the Kolmogorov scale turbulent eddies are affected by a large scalar dissipation rate, in which case the extinction of some reaction zones may occur. For $Da < 1$, the eddies at all scales induced enough scalar dissipation to cause flame quenching [25].

There is no turbulent combustion regime for partially premixed flames since the flames may be either non-premixed or premixed before ignition, and the fuel and oxidiser mixture is inhomogeneous. The partially premixed flames have diffusion characteristics, and propagating flame fronts coexist. The turbulent diffusion and premixed combustion regime can still be used to approximate the flame which is operating in gas turbines environment.

2.6. Multiphase flows

Multiphase flow has become one of the core disciplines in fluid dynamics and combustion research. Multiphase flows can be defined as any fluid flow system consisting of two or more phases flowing simultaneously in a mixture [34]. Many industrial applications, such as inkjet printing, spraying, and processes within liquid-fuelled combustors, include internal combustion engines, gas turbine engines, and rocket engines [25], [35]. Gas-liquid flows are typical configurations that can be found in gas turbines. The gas (usually air) is considered the continuous phase, and the droplets are considered the dispersed phase. The understanding and modelling of multiphase flows is complex, and therefore the physics of droplet combustion, single-component liquid fuels and atomisation processes under turbulent flow fields that are typical in the application of gas turbine combustor are discussed.

2.6.1. Liquid atomisation

In many aeroengine and ground-based combustion engines, the fuel is originally present as a liquid form. Consequently, these combustion devices operate in a two-phase medium, consisting of dispersed fuel droplets in a continuous oxidising gas. Figure 2.10 shows the various flow regimes and atomisation processes involved in spray formation. Three different regimes were observed after the jet came out of the fuel injector: dense regime, dilute regime, and very dilute regime. In a dense regime, where primary

atomisation and secondary atomisation take place. Primary atomisation refers to disintegration of ligaments into relatively large droplets due to the jet instabilities effect (when Kelvin–Helmholtz instability develops at the gas-liquid interface, then Rayleigh–Taylor instability takes place). Secondary atomisation is caused by aerodynamic forces due to the relative inter-phase velocity causing instabilities. This results in the further disintegration of liquid ligaments and droplets into smaller fragments and droplets. Dilute regime and very dilute regime refer to the case of a spray consisting of very small droplets. A dispersed phase volume fraction can be used to categorise three different regimes. The dense regime has a dispersed phase volume fraction above 10^{-3} where droplet collision and coalescence dominate the dispersed phase dynamics. In the dilute regime, droplet collisions can be neglected. The dispersed phase volume fraction is in a range between 10^{-6} and 10^{-3}; a very dilute regime means the dispersed phase volume fraction is less than 10^{-6}. The influence of the dispersed phase on the continuous phase turbulence can be assumed to be insignificant, and this assumption is used in this thesis to facilitate computational cost reduction.

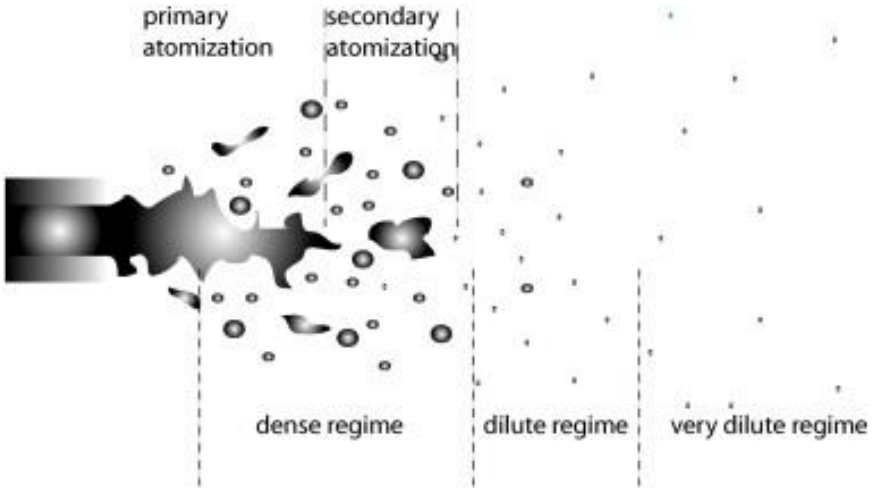

Figure 2.10 Liquid atomisation processes and spray formation [36]

2.6.2. Spray combustion

In gas turbine engines, liquid fuel is often injected into the combustor in the form of a spray. Combustion efficiency is therefore related to fuel evaporation rate, turbulent mixing rate, and the chemical reaction rate. The liquid droplets are usually very large (in an order of mm) and are disintegrated into a spray of smaller droplets (in an order of microns) to increase the rates of heat and mass transfer [37], [38].

Combustion of fossil fuels, primary coal, oil, and natural gas has been the dominant energy source for over a century. Fossil fuels account for over 80% of the world's energy consumption [39]. The use of combustion of liquid fuel is converting chemical energy into useful mechanical energy remains critical due to the high energy density content and lower costs [39].

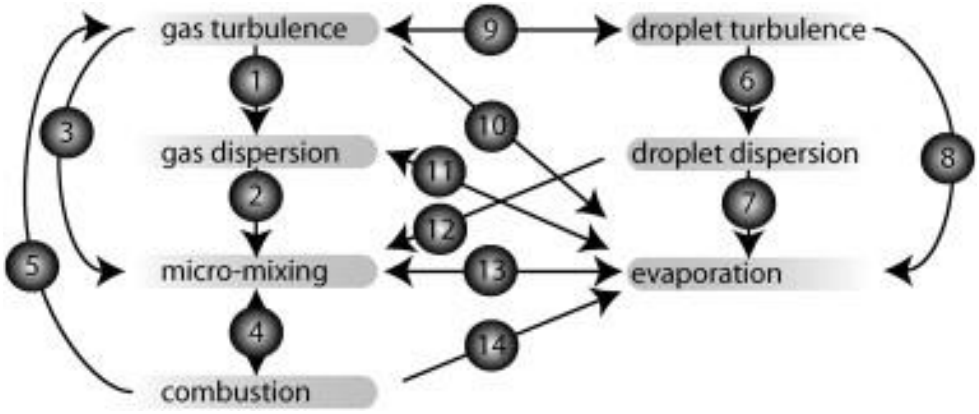

Figure 2.11 Spray combustion interactions [36]

A review of the literature presents the understanding of the structure of turbulent spray flames and categorises it into dense and dilute regimes [40]. In a dense regime, the details of the primary and secondary atomisation patterns are taken into consideration; therefore, modelling of this regime is more challenging, whereas in a dilute regime, the atomisation processes are neglected.

As discussed, in section 2.6.1, the physics of atomisation is extremely complex and poses a great challenge in modelling and experimental investigation. Therefore, the work in this thesis lies in the modelling of spray in dilute spray combustion where droplet collisions and breakup are insignificant.

2.7. Micro gas turbine combustor design and modelling approaches

In this section, the micro gas turbine combustor design and the modelling approaches from the literature [13–17] have been reviewed and summarised in Table 2.1 below.

Table 2.1 Micro gas turbine combustor design by other researchers [13–17]

Researchers	Thermal power [kW]	Combustor shape	Combustor technology	Fuel type	Air inlet pressure [bar]	Air inlet temperature [K]	Overall air-to-fuel ratio
[13]	337	Single Slio	Lean premixed	Gaseous methane	3.8	903	6.6
[14]	Not stated	Can	Not stated	Liquid	1.0	304	90.0
[15]	Not stated	Annular	Not stated	Liquid	Not stated	Not stated	Not stated
[16]	Not stated	Can	Not stated	Liquid JP-4	4.6	787	35.0
[17]	110	Can	Lean-premixed	Natural gas	4.0	905	7.0
UoB combustor	30	Can	RQL	Diesel	3.7	442	38.0

Table 2.1 shows that the combustor design analysed by the researchers is mainly from industrial partners such as Ansaldo and General Electric (GE); therefore, the detailed combustor parameters are not provided in the literature. Lean premixed combustion technology was used in [13] and [17]

for methane and natural gas, respectively. The pressure ratio is similar to the UoB combustor, but the air inlet temperature and thermal power are higher. The combustor in [14]-[16] is designed for liquid fuel; however, the details of the fuel type are not given in [14] and [15].

The UoB combustor is designed for burning liquid diesel to give a thermal power of 30 kW. The air inlet temperature is generally lower than most of the combustor designs in Table 2.1.

The CFD modelling approaches from [13–17] are summarised in Table 2.2.

Table 2.2 CFD approaches by other researchers

Researchers	Turbulence model selection	Combustion model selection	Chemical kinetic mechanism	Software
[13]	Standard k-epsilon and Reynolds Stress Model (RSM)	Eddy-dissipation model	Methane-air-2-step	Fluent
[14]	RNG k-epsilon model	Chemical equilibrium model	Not stated	Fluent
[15]	Standard k-epsilon	Chemical equilibrium model	Not stated	Fluent
[16]	Standard k-epsilon	Chemical equilibrium model	One-step reaction kinetics model	CFD-ACE
[17]	Standard k-epsilon and Reynolds Stress Model	Eddy-dissipation model	Methane-air-2-step	Fluent and KIVA3V

Table 2.2 shows that the researchers mainly use the standard k-epsilon and Reynolds stress model provided in Fluent to solve the complex swirling flows. Chemical equilibrium and eddy dissipation models are used for combustion models in the literature to simulate micro gas turbine combustors. They are both under the assumption of fast chemistry closures where the eddy dissipation model can be employed from premixed combustion to non-premixed combustion, and the chemical equilibrium model can be used in non-premixed combustion [29]. The 1-step or 2-step are used in the literature to account for chemistry in [13], [16], and [17]. These mechanisms generally cannot model slow chemistry effects, such as the oxidation of CO and NO [29]. In addition, the chemical equilibrium model tends to overpredict the temperature because there are no chemical non-equilibrium effects due to local turbulent strain [29].

2.8. Knowledge gap

In this chapter, the combustor design review has highlighted that although substantial research has been conducted on various low emission combustion technologies, there remains a clear knowledge gap regarding the potential of RQL combustors to further improve combustion efficiency and emissions. These studies provide demonstrations of the high technology readiness level combustor designs that are experimentally tested in a full-scale system. So far, studies have focused on lean premixed technology, as

this produces naturally low emissions, in particular NOx. Nevertheless, given that RQL is used in aeroengines due to its stability and is less prone to flashback, it becomes relevant to explore the RQL technology in micro gas turbine combustors. In addition, the information of the combustors has not been given in sufficient detail to be useful in designing a micro gas turbine combustor from scratch.

From the modelling perspective, chemical equilibrium and eddy dissipation rate models have been used to model the combustion process, and single-step or 2-step kinetic mechanisms have been used to describe the combustion chemistry. These methodologies are not sufficient to describe the slow chemistry process, such as the oxidation of CO and NO and over-prediction of flame temperature.

In this regard, the modelling approach in this thesis investigates the state-of-the-art flamelet-generated manifold for modelling combustion and the use of n-dodecane as a diesel fuel surrogate with a skeletal mechanism reduced from detailed chemistry to study the combustor performance.

2.9. Summary

In this chapter, the low emissions technology for gas turbine combustors and the fundamentals of combustion theory are discussed. Section 2.2 provides the general combustion fundamentals of a combustor. Two low emission combustion technologies are reviewed in Section 2.3, and one of the configurations is used to design a novel combustor for micro gas turbine engine application. Section 2.4 discusses the flame stabilisation mechanism in swirling flows. Section 2.5 discusses the combustion mode classification on non-premixed, premixed, and partially premixed combustion and reviews the turbulent combustion regimes, which is important for selecting the appropriate model for designing a combustor in this thesis. Section 2.6 discusses the challenges in multiphase flows coupled with turbulent combustion, which further complicates the problem by modelling liquid atomisation and spray combustion. Section 2.7 summarises the combustor design and modelling approaches by other researchers. Section 2.8 discusses the knowledge gap addressed in this thesis.

As demonstrated in this chapter, the RQL configuration is a promising solution for designing a novel and compact combustor for micro gas turbine engines. In addition, the existing turbulent combustion models, with particular attention to the spray combustion model, can be used to provide design guidelines and suggestions for this application.

Chapter 3 Turbulence Combustion Modelling

3.1 Introduction

This chapter introduces turbulence combustion modelling methodology and the governing equations of non-reacting and reacting flows. The model focuses on numerical analysis of turbulent spray flames and the application of simulating the practical combustor.

Section 3.2 discusses turbulence cascade theory and its wide application in engineering. Section 3.3 reviews the Navier–Stokes (N-S) equations, and the finite volume (FV) method is used to solve the N-S equations in CFD software used in this thesis. Section 3.4 reviews the Reynolds averaging method in Reynolds-averaged Navier–Stokes (RANS) modelling. Section 3.5 reviews eight different turbulent modelling methodologies that are used to simulate the turbulent swirling spray flame in a lab-scaled burner. Section 3.6 reviews the turbulent model described in Section 3.5 in simulating turbulent swirling flow. Section 3.7 discusses the treatment in variable density flows. Section 3.8 reviews governing equations in reacting flows. Section 3.9 reviews the methodology in turbulent combustion models and focuses on the reduced-order method – flamelet model. Section 3.10 discusses the turbulence–chemistry interaction (TCI), and the probability density function (PDF) is used as the TCI closure. Finally, Section 3.11

discusses the liquid atomisation phenomena and spray combustion modelling techniques.

3.2 Turbulence

Turbulence is an unsolved problem in fluid dynamics and is extremely complex but plays a critical role in various engineering applications. Turbulence can be described as chaotic and irregular fluid motions and can be characterised by the swirling motion of vortices. Majority flows in engineering practice are turbulent [41] and therefore require different techniques to solve compared to laminar flows.

Turbulent flows contain eddies of various sizes, from large-scale motions to small-scale structures; therefore, these eddies exist across a wide spectrum of length scales. Kolmogorov was the first to view the energy cascade, describing turbulence as the energy dissipation from large-scale turbulent eddies to small-scale turbulent eddies by viscosity [41], [42]. Figure 3.1 illustrates the typical energy cascade theory. The turbulence cascade theory describes the process by which the energy in the large-scale eddies is extracted from mean flow motion and the energy is transferred to small-scale eddies by viscosity. The energy finally dissipates into heat at the dissipation range until it reaches the smallest scale – the Kolmogorov microscale.

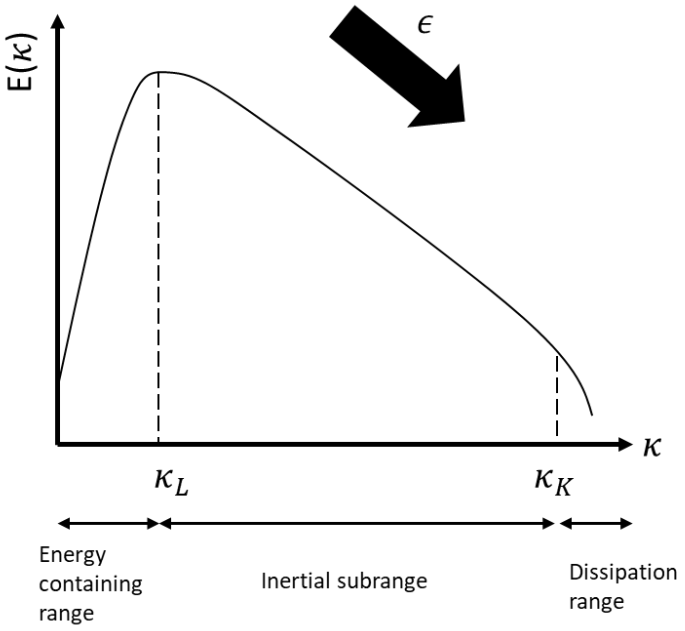

Figure 3.1 Turbulence cascade [41]

3.3 The Navier–Stokes equations

The Navier–Stokes equations are partial differential equations that describe the motion of fluids, first proposed by Navier and Stokes [41]. The Navier–Stokes equations can be written as follows, in a three-dimensional Cartesian coordinate system neglecting gravitational forces, as there are no external forces:

$$\rho\left(\frac{\partial u}{\partial t}+u\frac{\partial u}{\partial x}+v\frac{\partial u}{\partial y}+w\frac{\partial u}{\partial z}\right)=-\frac{\partial p}{\partial x}+\mu\left[\frac{\partial^2 u}{\partial x^2}+\frac{\partial^2 u}{\partial y^2}+\frac{\partial^2 u}{\partial z^2}\right]+\frac{\mu}{3}\left(\frac{\partial u}{\partial x}\right) \tag{3.1a}$$

$$\rho\left(\frac{\partial v}{\partial t}+u\frac{\partial v}{\partial x}+v\frac{\partial v}{\partial y}+w\frac{\partial v}{\partial z}\right)=-\frac{\partial p}{\partial y}+\mu\left[\frac{\partial^2 v}{\partial x^2}+\frac{\partial^2 v}{\partial y^2}+\frac{\partial^2 v}{\partial z^2}\right]+\frac{\mu}{3}\left(\frac{\partial v}{\partial x}\right)$$

(3.1b)

$$\rho\left(\frac{\partial w}{\partial t}+u\frac{\partial w}{\partial x}+v\frac{\partial w}{\partial y}+w\frac{\partial w}{\partial z}\right)$$

$$=-\frac{\partial p}{\partial z}+\mu\left[\frac{\partial^2 w}{\partial x^2}+\frac{\partial^2 w}{\partial y^2}+\frac{\partial^2 w}{\partial z^2}\right]+\frac{\mu}{3}\left(\frac{\partial w}{\partial x}\right) \quad (3.1c)$$

The momentum equations in Equation 3.1a, 3.1b and 3.1c outline the rate of change in momentum with respect to space and time.

The continuity equation is necessary to consider conserving mass, and the equation can be written as:

$$\frac{\partial \rho}{\partial t}+\frac{\partial}{\partial x}(\rho u)+\frac{\partial}{\partial y}(\rho v)+\frac{\partial}{\partial z}(\rho w)=0 \quad (3.1d)$$

There is no known general analytical solution to the Navier–Stokes equations due to their great complexity. Often, making assumptions about the flow to simplify the equations is necessary to obtain analytical solutions. Usually, simplifications assume that the flow is laminar, steady, two-dimensional, incompressible with constant properties, and that the flow is between parallel plates. Therefore, solving the equation using the numerical method is a best practice for obtaining the numerical solution for industrial applications. Computational fluid dynamics (CFD) is a numerical method used in the fluid dynamics and engineering field to simulate and analyse the flow behaviour of fluids. There have been attempts to solve the Navier–Stokes equations through discretisation and iterative numerical methods to

describe the motion of fluids. The Navier–Stokes equations have been numerically approximated in isothermal non-reacting flow, reacting flow conditions using the well-developed commercial CFD software Ansys Fluent [43].

Ansys Fluent adopts a finite volume method (FVM) to solve the Navier–Stokes equations. The computational domain is first simplified by removing unnecessary features that cause an increase in cell counts. This is followed by discretising the computational domain into a series of finite volumes or cells called grid/ mesh to represent the geometry to be solved. The Navier–Stokes equations are then integrated over these grid/mesh using the Green–Gauss divergence theorem, which results in a set of discrete equations that can be solved iteratively to obtain the approximated numerical solution to the Navier–Stokes equations. The pressure-based solver was used throughout this work as the Mach number of the flow is less than 0.3, which can be considered low-speed flows.

3.4 Reynolds averaging

Due to the complexity of directly solving the Navier–Stokes equations in Equation (3.1), direct numerical simulation (DNS) is often required to fully resolve the entire turbulent spectrum. However, DNS is a computationally expensive method in engineering applications because it scales with the flow Reynolds number. The Reynolds numbers in most industrial applications

tend to be very high, and the computational cost required would exceed the capacity of the most powerful supercomputers nowadays.

Reynolds averaging is a technique to decompose the turbulent flow variables, for example pressure and velocity, into the sum of their mean value and a fluctuating component.

$$u = \overline{u} + u' \tag{3.2}$$

All variables in Equation (3.1) of Reynolds averaging lead to the following:

$$\rho\left(\frac{\partial\overline{u}}{\partial t} + \overline{u}\frac{\partial\overline{u}}{\partial x} + \overline{v}\frac{\partial\overline{u}}{\partial y} + \overline{w}\frac{\partial\overline{u}}{\partial z}\right)$$

$$= -\frac{\partial p}{\partial x} + \mu\left[\frac{\partial^2\overline{u}}{\partial x^2} + \frac{\partial^2\overline{u}}{\partial y^2} + \frac{\partial^2\overline{u}}{\partial z^2}\right] + \frac{\mu}{3}\left(\frac{\partial\overline{u}}{\partial x}\right) - \rho\frac{\partial}{\partial x}\left(\overline{u'u'}\right) \tag{3.3a}$$

$$- \rho\frac{\partial}{\partial y}\left(\overline{u'v'}\right) - \rho\frac{\partial}{\partial z}\left(\overline{u'w'}\right) + \frac{\mu}{3}\left(\frac{\partial u'}{\partial x}\right)$$

$$\rho\left(\frac{\partial\overline{v}}{\partial t} + \overline{u}\frac{\partial\overline{v}}{\partial x} + \overline{v}\frac{\partial\overline{v}}{\partial y} + \overline{w}\frac{\partial\overline{v}}{\partial z}\right)$$

$$= -\frac{\partial p}{\partial y} + \mu\left[\frac{\partial^2\overline{v}}{\partial x^2} + \frac{\partial^2\overline{v}}{\partial y^2} + \frac{\partial^2\overline{v}}{\partial z^2}\right] + \frac{\mu}{3}\left(\frac{\partial\overline{v}}{\partial y}\right) - \rho\frac{\partial}{\partial x}\left(\overline{v'u'}\right) \tag{3.3b}$$

$$- \rho\frac{\partial}{\partial y}\left(\overline{v'v'}\right) - \rho\frac{\partial}{\partial z}\left(\overline{v'w'}\right) + \frac{\mu}{3}\left(\frac{\partial v'}{\partial y}\right)$$

$$\rho\left(\frac{\partial\overline{w}}{\partial t}+\overline{u}\frac{\partial\overline{w}}{\partial x}+\overline{v}\frac{\partial\overline{w}}{\partial y}+\overline{w}\frac{\partial\overline{w}}{\partial z}\right)$$

$$=-\frac{\partial p}{\partial z}+\mu\left[\frac{\partial^2\overline{w}}{\partial x^2}+\frac{\partial^2\overline{w}}{\partial y^2}+\frac{\partial^2\overline{w}}{\partial z^2}\right]+\frac{\mu}{3}\left(\frac{\partial\overline{w}}{\partial z}\right) \tag{3.3c}$$

$$-\rho\frac{\partial}{\partial x}\left(\overline{w'u'}\right)-\rho\frac{\partial}{\partial y}\left(\overline{w'v'}\right)-\rho\frac{\partial}{\partial z}\left(\overline{w'w'}\right)+\frac{\mu}{3}\left(\frac{\partial w'}{\partial z}\right)$$

3.5 Turbulence modelling

After the Reynolds averaging decomposition, Equation (3.3) has additional terms that appear on the right-hand side of the equation. These terms are known as Reynolds stresses. The general form of Reynolds stresses can be written as follows:

$$-\rho\frac{\partial}{\partial x_j}\left(\overline{u_i'u_j'}\right) \tag{3.4}$$

The Reynolds stresses raise challenges in modelling turbulence. Direct numerical simulation (DNS) can be used without modelling the Reynolds stresses. DNS has not been popular in solving practical problems, since the computational cost is high and usually in studying low Reynolds number lab-scale flows. In any other numerical approaches such as large eddy simulation (LES) and Reynolds-averaged Navier–Stokes Simulation (RANS), the Reynolds stresses need to be modelled – this is the closure problem of the Navier–Stokes equations.

In the RANS context, two popular models of turbulence modelling are the family of two-equation models and second-moment closures. Turbulence modelling in RANS was used throughout this thesis; a detailed comparison between the performance of different turbulence models was performed and validated against the experimental results. The popular turbulence models, including two-equation models and more advanced unsteady scale resolving models, which are widely used in solving engineering problems, will be discussed in next section. For the two-equation models family [44], these are the renormalised group (RNG) k-epsilon turbulence model, the realizable k-epsilon turbulence model, the shear stress transport (SST) k-omega turbulence model [45], and the Reynolds stress model with epsilon and omega.

3.5.1. k-epsilon turbulence models

As discussed in Section 3.4, the Reynolds stresses in Equation (3.4) need to be appropriately modelled in two-equation models. The Boussinesq hypothesis [44] was used to relate the Reynolds stresses to the mean velocity gradients in Equation (3.5):

$$-\rho\overline{u_i'u_j'} = \mu_t\left(\frac{\partial u_i}{\partial x_j}+\frac{\partial u_j}{\partial x_i}\right)-\frac{2}{3}\left(\rho k+\mu_t\frac{\partial u_k}{\partial x_k}\right)\delta_{ij} \tag{3.5}$$

where

$$\mu_t = \rho \frac{C_\mu k^2}{\epsilon} \tag{3.6}$$

$$k = \frac{1}{2}(\overline{u_x'^2} + \overline{u_y'^2} + \overline{u_z'^2}) \tag{3.7}$$

$$\epsilon = 2\nu \overline{e_{ij}' e_{ij}'} \tag{3.8}$$

δ_{ij} is the Kronecker delta function and e' is the fluctuating component of the rate of deformation of a fluid element. The development of k-epsilon turbulence models consists of many forms of transport equations that have been proposed for turbulent kinetic energy k and turbulent dissipating rate ϵ.

The standard k-epsilon turbulence model was first introduced by Launder and Spalding [44]. The transport equations are written below for completeness.

$$\frac{\partial}{\partial t}(\rho k) + \frac{\partial}{\partial x_j}(\rho k u_j) = \frac{\partial}{\partial x_j}\left[\left(\mu + \frac{\mu_t}{\sigma_k}\right)\frac{\partial k}{\partial x_j}\right] + G_k + G_b - \rho\epsilon - Y_M + S_k \tag{3.9a}$$

$$\frac{\partial}{\partial t}(\rho \epsilon) + \frac{\partial}{\partial x_j}(\rho \epsilon u_j) = \frac{\partial}{\partial x_j}\left[\left(\mu + \frac{\mu_t}{\sigma_\epsilon}\right)\frac{\partial \epsilon}{\partial x_j}\right] + C_{1\epsilon}\frac{\epsilon}{k}G_k - C_{2\epsilon}\rho\frac{\epsilon^2}{k} + S_\epsilon \tag{3.9b}$$

where G_k is the generation of turbulent kinetic energy due to the mean velocity gradients. With the Boussinesq hypothesis, the G_k can be defined as follows:

$$G_k = \mu_t S^2 \tag{3.10}$$

where the mean strain rate S can be defined as follows:

$$S \equiv \sqrt{2S_{ij}S_{ij}} \tag{3.11}$$

where

$$S_{ij} = \frac{1}{2}\left(\frac{\partial u_j}{\partial x_i} + \frac{\partial u_i}{\partial x_j}\right)$$

Several assumptions have been made during this thesis to simplify the problem. First, the gravitational effects, the buoyancy term G_b and the dilatation dissipation term Y_M were not considered because the Mach number is less than about 0.3.

The modelling constant in Equation (3.9) are $C_{1\epsilon} = 1.44$ and $C_{2\epsilon} = 1.92$, $\sigma_k = 1.0$ and $\sigma_\epsilon = 1.3$ are turbulent Prandtl numbers for k and ϵ respectively. C_μ is assumed to be a constant of 0.09 in the standard turbulence model.

3.5.2. Realizable k-epsilon turbulent model

The realizable k-epsilon model [46] has modified the standard turbulence model parameters to improve performance in predicting turbulent flows. The model used an alternative formulation for turbulent viscosity. The set of transport equations is written as follows:

$$\frac{\partial}{\partial t}(\rho k) + \frac{\partial}{\partial x_j}(\rho k u_j) = \frac{\partial}{\partial x_j}\left[\left(\mu + \frac{\mu_t}{\sigma_k}\right)\frac{\partial k}{\partial x_j}\right] + G_k - \rho\epsilon - Y_M + S_k \tag{3.11a}$$

$$\frac{\partial}{\partial t}(\rho\epsilon) + \frac{\partial}{\partial x_j}(\rho\epsilon u_j) = \frac{\partial}{\partial x_j}\left[\left(\mu + \frac{\mu_t}{\sigma_\epsilon}\right)\frac{\partial \epsilon}{\partial x_j}\right] + \rho C_1 S\epsilon - \rho C_2 \frac{\epsilon^2}{k + \sqrt{\nu\epsilon}} + S_\epsilon \tag{3.11b}$$

where modelling constant $C_1 = \max\left[0.43, \frac{\eta}{\eta+5}\right]$, $\eta = S\frac{k}{\epsilon}$, $C_2 = 1.9$, $\sigma_k = 1.0$ and $\sigma_\epsilon = 1.2$. C_μ is not a constant value in the model,

$$C_\mu = \frac{1}{A_0 + A_s k\frac{U^*}{\epsilon}} \tag{3.12}$$

where

$$U^* \equiv \sqrt{S_{ij}S_{ij} + \tilde{\Gamma}_{ij}\tilde{\Gamma}_{ij}}$$

and

$$\tilde{\Gamma}_{ij} = \Gamma_{ij} - 2\epsilon_{ijk}\omega_k$$

$$\omega_{ij} = \overline{\Gamma_{ij}} - \epsilon_{ijk}\omega_k$$

where $\overline{\Gamma_{ij}}$ is the mean rate of the rotation tensor viewed in a moving reference frame with the angular velocity ω_k.

The modelling constants $A_0 = 4.04$ and $A_s = \sqrt{6}cos\varphi$

where

$$\varphi = \frac{1}{3}\cos^{-1}(\sqrt{6}W)$$

$$W = \frac{S_{ij}S_{jk}S_{ki}}{\tilde{S}^3}$$

$$\tilde{S} = \sqrt{S_{ij}S_{ij}}$$

$$S_{ij} = \frac{1}{2}(\frac{\partial u_j}{\partial x_i} + \frac{\partial u_i}{\partial x_j})$$

Realizable k-epsilon turbulence model performs better than the standard model nevertheless, in this work, it was shown that the realizable k-epsilon model is not able to capture the swirling flow accurately compared to k-epsilon RNG turbulence model.

3.5.3. Renormalization group theory (RNG) turbulence model

The RNG-based k-epsilon turbulence model is derived from instantaneous Navier–Stokes equations using a mathematical technique renormalization group theory (RNG) method [47]. It is claimed that the effect of swirl on turbulence is included in the RNG model, improving the performance of capturing swirling turbulent flow. The RNG k-epsilon turbulence model transport equations are similar to the standard k-epsilon turbulence model, with an additional term in the transport of ϵ equation.

The transport equations for k and epsilon are written as follows:

$$\frac{\partial}{\partial t}(\rho k) + \frac{\partial}{\partial x_j}(\rho k u_j) = \frac{\partial}{\partial x_j}\left(\alpha_k \mu_{\text{eff}} \frac{\partial k}{\partial x_j}\right) + G_k - \rho\epsilon - Y_M + S_k \tag{3.13a}$$

$$\frac{\partial}{\partial t}(\rho\epsilon) + \frac{\partial}{\partial x_j}(\rho\epsilon u_j) = \frac{\partial}{\partial x_j}\left(\alpha_\epsilon \mu_{\text{eff}} \frac{\partial \epsilon}{\partial x_j}\right) + C_{1\epsilon}\frac{\epsilon}{k}G_k - C_{2\epsilon}\rho\frac{\epsilon^2}{k} - R_\epsilon + S_\epsilon \tag{3.13b}$$

The additional terms arising from Equation (2.13) are R_ϵ, α_k, α_ϵ and μ_{eff}. The effective viscosity μ_{eff} is computed using the high-Reynolds number form in Equation (2.6), and the results of $C_\mu = 0.0845$. The inverse effective Prandtl numbers σ_k and σ_ϵ are derived by the RNG theory:

$$\left|\frac{\alpha - 1.3929}{\alpha_0 - 1.3929}\right|^{0.6321} \left|\frac{\alpha + 2.3929}{\alpha_0 + 2.3929}\right|^{0.3679} = \frac{\mu_{\text{mol}}}{\mu_{\text{eff}}} \tag{3.14}$$

The final addition term R_ϵ is:

$$R_\epsilon = \frac{C_\mu \rho \eta^3 (1 - \frac{\eta}{\eta_0})}{1 + \beta \eta^3} \frac{\epsilon^2}{k} \tag{3.15}$$

where $\eta \equiv Sk/\epsilon$, $\eta_0 = 4.38$, $\beta = 0.012$, $C_{1\epsilon} = 1.42$, $C_{2\epsilon} = 1.68$ and $\alpha_k = \alpha_\epsilon \approx 1.393$ given that $\alpha_0 = 1.0$ in the high-Reynolds number limit.

3.5.4. Shear stress transport (SST) k-omega turbulence model

One of the drawbacks of k-omega family turbulence models is that they are found to be less sensitive to the assumed free stream values, and the near-wall performance is unsatisfactory for boundary layers with adverse pressure gradient [48]. The SST k-omega turbulence model was developed by Menter to a hybrid model that uses the standard k-epsilon model in the fully turbulent region far from the wall and transforms the epsilon into omega in the near-wall region [49].

The shear stress transport (SST) k-omega turbulence model is as follows:

$$\frac{\partial}{\partial t}(\rho k) + \frac{\partial}{\partial x_i}(\rho k u_i) = \frac{\partial}{\partial x_j}\left(\gamma_k \frac{\partial k}{\partial x_j}\right) + \tilde{G}_k - Y_k + S_k \tag{3.16a}$$

$$\frac{\partial}{\partial t}(\rho\omega) + \frac{\partial}{\partial x_i}(\rho\omega u_i) = \frac{\partial}{\partial x_j}\left(\gamma_\omega \frac{\partial \epsilon}{\partial x_j}\right) + G_\omega - Y_\omega + D_\omega + S_\omega \quad (3.16b)$$

where the term α^* is a low Reynolds number damping coefficient. It is unity when in the high-Reynolds number form.

The turbulent viscosity in k-omega family is computed from the following equation:

$$\mu_t = \frac{\rho k}{\omega} \frac{1}{\max\left[\frac{1}{\alpha^*}, \frac{SF_2}{a_1 \omega}\right]} \quad (3.17)$$

where S is the strain rate magnitude, $\alpha^* = 1$, and $\frac{SF_2}{a_1\omega}$ is calculated from Equation (2.6). $\tilde{G}_k$ is the generation of turbulent kinetic energy due to mean velocity gradients, and is given by:

$$\tilde{G}_k = \min(G_k, 10\rho\beta^* k\omega) \quad (3.18)$$

where G_k is defined as Equation (2.10). G_ω represents the production of the eddy dissipation rate calculated as:

$$G_\omega = \frac{\alpha}{\nu_t} G_k \quad (3.19)$$

The effective diffusivity of k and ω respectively, which are defined as:

$$\Gamma_k = \mu + \frac{\mu_t}{\sigma_k} \quad (3.20)$$

$$\Gamma_\omega = \mu + \frac{\mu_t}{\sigma_\omega} \quad (3.21)$$

where σ_k and σ_ω are the turbulent Prandtl numbers, respectively:

$$\sigma_k = \frac{1}{\frac{F_1}{\sigma_{k,1}} + (1 - F_1)/\sigma_{k,2}} \tag{3.22}$$

$$\sigma_\omega = \frac{1}{\frac{F_1}{\sigma_{\omega,1}} + (1 - F_1)/\sigma_{\omega,2}} \tag{3.23}$$

The blending functions F_1 and F_2 are used to switch on the $k - \omega$ into $k - \epsilon$ and vice versa, and are given by:

$$F_1 = \tanh(\Phi_1^4) \tag{3.24}$$

$$\Phi_1 = \min\left[\max\left(\frac{\sqrt{k}}{0.09\omega y}, \frac{500\mu}{\rho y^2 \omega}\right), \frac{4\rho k}{\sigma_{\omega,2} D_\omega^+ y^2}\right] \tag{3.25}$$

$$D_\omega^+ = \max\left[2\rho \frac{1}{\sigma_{\omega,2}} \frac{1}{\omega} \frac{\partial k}{\partial x_j} \frac{\partial \omega}{\partial x_j}, 10^{-10}\right] \tag{3.26}$$

$$F_2 = \tanh(\Phi_2^2) \tag{3.27}$$

$$\Phi_2 = \max\left[2\frac{\sqrt{k}}{0.09\omega y}, \frac{500\mu}{\rho y^2 \omega}\right] \tag{3.28}$$

where y is the distance to the next surface, D_ω^+ is the positive portion of the cross-diffusion term.

In the SST k-omega model, α_∞ is given by:

$$\alpha_\infty = F_1 \alpha_{\infty,1} + (1 - F_1)\alpha_{\infty,2} \tag{3.29}$$

where

$$\alpha_{\infty,1} = \frac{\beta_{i,1}}{\beta_{\infty}^{*}} - \frac{\kappa^2}{\sigma_{\omega,1}\sqrt{\beta_{\infty}^{*}}} \tag{3.30}$$

$$\alpha_{\infty,2} = \frac{\beta_{i,2}}{\beta_{\infty}^{*}} - \frac{\kappa^2}{\sigma_{\omega,2}\sqrt{\beta_{\infty}^{*}}} \tag{3.31}$$

where $\kappa = 0.41$.

The Y_k and Y_ω are the dissipation of turbulent kinetic energy and the dissipation of ω, which is defined as:

$$Y_k = \rho\beta^{*}k\omega \tag{3.32}$$

$$Y_\omega = \rho\beta\omega^2 \tag{3.33}$$

where β is defined as:

$$\beta = F_1\beta_{i,1} + (1 - F_1)\beta_{i,2} \tag{3.34}$$

The cross-diffusion term D_ω appears when the standard k-epsilon is transformed into a k-omega form, which is given by the following expression:

$$D_\omega = 2(1 - F_1)\rho\sigma_{\omega,2}\frac{1}{\omega}\frac{\partial k}{\partial x_j}\frac{\partial \omega}{\partial x_j} \tag{3.35}$$

The other modelling constants are $\sigma_{k,1} = 1.176$, $\sigma_{\omega,1} = 2.0$, $\sigma_{k,2} = 1.0$, $\sigma_{\omega,2} = 1.168$, $a_1 = 0.31$, $\beta_{i,1} = 0.075$ and $\beta_{i,2} = 0.0828$.

3.5.5. Second-moment closure models (Reynolds stress models)

Second-moment closure models aim to solve the Reynolds stresses in Equation (3.4) directly without the Boussinesq hypothesis [50–52]. The available models in Ansys Fluent include the linear pressure strain model with epsilon-based and omega-based models. The models can produce more accurate results in the case of flows involving strong streamline curvature, swirl, or rapid changes in the strain rate. The anisotropic behaviour of turbulence occurs in the flows mentioned above.

The transport equation of Reynolds stresses without the effects of body forces and rotation is given by:

$$\begin{aligned}\frac{\partial}{\partial t}\left(\rho\overline{u_i'u_j'}\right) + \frac{\partial}{\partial x_k}\left(\rho u_k\overline{u_i'u_j'}\right) \\ = -\frac{\partial}{\partial x_k}\left[\rho\overline{u_i'u_j'u_k'} + \overline{p\left(\delta_{kj}u_i' + \delta_{ik}u_j'\right)}\right] \\ + \frac{\partial}{\partial x_k}\left[\mu\frac{\partial}{\partial x_k}\left(\overline{u_i'u_j'}\right)\right] - \rho\left(\overline{u_i'u_j'}\frac{\partial u_j}{\partial x_k} + \overline{u_j'u_k'}\frac{\partial u_i}{\partial x_k}\right) \\ + \overline{p\left(\frac{\partial u_i'}{\partial x_j} + \frac{\partial u_j'}{\partial x_i}\right)} - 2\mu\overline{\frac{\partial u_i'}{\partial x_j}\frac{\partial u_j'}{\partial x_i}}\end{aligned} \tag{3.36}$$

where Equation (3.36) can be described as a local time derivative term and convection term on the left-hand side, and turbulent diffusion term, molecular diffusion term, stress production term, pressure strain term and dissipation term on the right-hand side.

For the epsilon-based and omega-based models, the turbulent diffusion term is modelled by:

$$-\frac{\partial}{\partial x_k}\left[\rho\overline{u_i' u_j' u_k'} + \overline{p\left(\delta_{kj}u_i' + \delta_{ik}u_j'\right)}\right] = \frac{\partial}{\partial x_k}\left(\frac{\mu_t}{\sigma_k}\frac{\partial \overline{u_i' u_j'}}{\partial x_k}\right) \tag{3.37}$$

where the epsilon-based model effective viscosity is modelled in the same way as the standard k-epsilon turbulence model with the same modelling constant. σ_k is a model constant of 0.82. The ω-based uses Equation (3.17) for effective viscosity and $\sigma_k = 2.0$. A similar blending function F_1 is used to blend the value between the inner region ($\sigma_{k,1} = 2.0$) and the outer region ($\sigma_{k,2} = 1.0$), and is written as:

$$\sigma_k = F_1\sigma_{k,1} + (1 - F_1)\sigma_{k,2} \tag{3.38}$$

The pressure strain term is modelled by the following decomposition:

$$\overline{p\left(\frac{\partial u_i'}{\partial x_j} + \frac{\partial u_j'}{\partial x_i}\right)} = \varphi_{ij,1} + \varphi_{ij,2} + \varphi_{ij,w} \tag{3.39}$$

where $\varphi_{ij,1}$ is the return-to-isotropy term (slow pressure strain term), $\varphi_{ij,2}$ is the rapid pressure strain term and $\varphi_{ij,w}$ is the wall reflection term.

The return-to-isotropy term is modelled as:

$$\varphi_{ij,1} = -C_1 \rho \frac{\epsilon}{k}\left[\overline{u_i' u_j'} - \frac{2}{3}\delta_{ij}k\right] \tag{3.40}$$

where C_1 is 1.8. The rapid pressure strain term is modelled as:

$$\varphi_{ij,2} = -C_2\left[\left(P_{ij} + \frac{5}{6G_{ij}} - C_{ij}\right) - \frac{2}{3}\delta_{ij}(P + \frac{5}{6G} - C)\right] \tag{3.41}$$

where C_2 is 0.60, $P = \frac{1}{2}P_{kk}$, $G = \frac{1}{2}G_{kk}$ and $C = C_{kk}$.

$$P_{ij} = -\rho\left(\overline{u_i' u_j'}\frac{\partial u_j}{\partial x_k} + \overline{u_j' u_k'}\frac{\partial u_i}{\partial x_k}\right)$$

$$C_{ij} = \frac{\partial}{\partial x_k}\left(\rho u_k \overline{u_i' u_j'}\right)$$

The wall reflection term is used to redistribute normal stress near the wall to damp the normal stress perpendicular to the wall while enhancing the stresses parallel to the wall, and is given by:

$$\varphi_{ij,w} = C_1' \frac{\epsilon}{k}\left(\overline{u_k' u_m'} n_k n_m \delta_{ij} - \frac{3}{2}\overline{u_i' u_k'} n_j n_k - \frac{3}{2}\overline{u_j' u_k'} n_i n_k\right)\frac{C_l k^{3/2}}{\epsilon d} + C_2' \frac{\epsilon}{k}\left(\varphi_{km,2} n_k n_m \delta_{ij} - \frac{3}{2}\varphi_{ik,2} n_j n_k - \frac{3}{2}\varphi_{jk,2} n_i n_k\right)\frac{C_l k^{3/2}}{\epsilon d} \tag{3.42}$$

where $C_1' = 0.5$, $C_2' = 0.3$, n_k is the x_k component of the unit normal to the wall, d is the normal distance to the wall, $C_l = C_\mu^{\frac{3}{4}}/\kappa$, $C_\mu = 0.09$, and $\kappa = 0.4187$.

For the omega-based model, Equation (3.39) can be re-written to exclude the wall reflection term:

$$\overline{p\left(\frac{\partial u_i'}{\partial x_j} + \frac{\partial u_j'}{\partial x_i}\right)} = \varphi_{ij,1} + \varphi_{ij,2} \tag{3.43}$$

where leads to:

$$\overline{p\left(\frac{\partial u_i'}{\partial x_j} + \frac{\partial u_j'}{\partial x_i}\right)} = -C_1 \rho \beta_{RSM}^* \omega\left[\overline{u_i' u_j'} - \frac{2}{3}\delta_{ij} k\right] - \hat{\alpha}_0\left[P_{ij} - \frac{1}{3}P_{kk}\delta_{ij}\right] - \hat{\beta}_0\left[D_{ij} - \frac{1}{3}P_{kk}\delta_{ij}\right] - k\hat{\gamma}_0\left[S_{ij} - \frac{1}{3}S_{kk}\delta_{ij}\right] \tag{3.44}$$

where

$$D_{ij} = -\rho\left[\overline{u_i'u_m'}\frac{\partial u_m}{\partial x_j} + \overline{u_j'u_m'}\frac{\partial u_m}{\partial x_i}\right] \tag{3.45}$$

The mean strain rate S_{ij} is defined in Equation (3.11) and β_{RSM}^* is written as:

$$\beta_{RSM}^* = \beta^* f_\beta^* \tag{3.46}$$

where β^* and f_β^* are defined as:

$$f_{\beta^*} = \begin{cases} 1, & \chi_k \le 0 \\ \dfrac{1+640\chi_k^2}{1+400\chi_k^2}, & \chi_k > 0 \end{cases} \tag{3.47}$$

where

$$\chi_k \equiv \frac{1}{\omega^3}\frac{\partial k}{\partial x_j}\frac{\partial \omega}{\partial x_j} \tag{3.48}$$

$$\beta^* = \beta_i^*[1+\zeta^* F(M_t)] \tag{3.49}$$

$$\beta_i^* = \beta_\infty^*\left(\frac{\frac{4}{15}+\left(\frac{Re_t}{R_\beta}\right)^4}{1+\left(\frac{Re_t}{R_\beta}\right)^4}\right) \tag{3.50}$$

where $\zeta^* = 1.5$, $R_\beta = 8$, $\beta_\infty^* = 0.09$ and $Re_t = \frac{\rho k}{\mu\omega}$.

The other modelling constants are $\hat{\alpha}_0 = \frac{8+C_2}{11}$, $\hat{\beta}_0 = \frac{8C_2-2}{11}$, $\hat{\gamma}_0 = \frac{60C_2-4}{55}$, $C_1 = 1.8$ and $C_2 = 0.52$.

3.5.6. Scale resolving simulation models

RANS remains widely used in industrial applications for modelling turbulence due to low computational requirements. However, the limitations of RANS models have become very clear in terms of accuracy in certain flows. For instance, in free shear flows, the largest turbulent scales are of the order of the shear layer thickness. For wall-bounded flows, RANS models have their strength in calibration according to the law-of-the-wall for further refinement.

Scale resolving simulation (SRS) offers the advantage of the ability to resolve a part of the turbulence spectrum in at least a portion of the computational domain. Another motivation for using SRS models is accuracy. For simple self-similar flows such as jets, mixing layers, and flows with strong swirl, the performance of RANS models is much less uniform, and even the most advanced Reynolds stress models (RSM) will not be able to provide a reliable foundation for all such flows [53].

Unsteady Reynolds-averaged Navier–Stokes (URANS) and the second-generation URANS are called scale-adaptive simulation (SAS). The latter is an improved URANS formulation modified by Menter and Egorov [54]. URANs produce only large-scale unsteadiness by including the additional

unsteady term and are successfully applied to flows for vortex shedding behind bluff bodies [55] and around cars [56].

3.5.7. The SST-SAS model

The SAS is based on introducing the von Karman length scale into the turbulence scale equation to dynamically adjust to resolve the turbulent spectrum in unstable flow conditions that URANS cannot resolve. The model is large eddy simulation (LES)-like behaviour in unsteady regions of the flow field and RANS-like behaviour in stable flow regions, which allows the model to preserve efficiency and accuracy with a faster computational time compared to LES.

The transport equations for the SST-SAS are defined as follows:

$$\frac{\partial \rho k}{\partial t} + \frac{\partial}{\partial x_i}(\rho u_i k) = G_k - \rho c_\mu k\omega + \frac{\partial}{\partial x_j}\left[\left(\mu + \frac{\mu_t}{\sigma_k}\right)\frac{\partial k}{\partial x_j}\right] \tag{3.51}$$

$$\begin{aligned}\frac{\partial \rho \omega}{\partial t} + \frac{\partial}{\partial x_i}(\rho u_i \omega) \\ = \alpha \frac{\omega}{k} G_k - \rho \beta \omega^2 + Q_{SAS} + \frac{\partial}{\partial x_j}\left[\left(\mu + \frac{\mu_t}{\sigma_\omega}\right)\frac{\partial \omega}{\partial x_j}\right] \\ + (1 - F_1)\frac{2\rho}{\sigma_{\omega,2}}\frac{1}{\omega}\frac{\partial k}{\partial x_j}\frac{\partial \omega}{\partial x_j}\end{aligned} \tag{3.52}$$

where Q_{SAS} is modelled by:

$$Q_{SAS} = \max\left[\rho\eta_2\kappa S^2\left(\frac{L}{L_{\nu\kappa}}\right)^2 - C \cdot \frac{2\rho k}{\sigma_\phi} max\left(\frac{1}{\omega^2}\frac{\partial\omega}{\partial x_j}\frac{\partial\omega}{\partial x_j}, \frac{1}{k^2}\frac{\partial k}{\partial x_j}\frac{\partial k}{\partial x_j}\right), 0\right] \tag{3.53}$$

where L is the length scale of the modelled turbulence and $L_{\nu\kappa}$ is the von Karman length scale:

$$L = \sqrt{k}/(c_\mu^{\frac{1}{4}} \cdot \omega)$$

$$L_{\nu\kappa} = \kappa\left|\frac{U'}{U''}\right|$$

where

$$U' = S = \sqrt{2 \cdot S_{ij}S_{ij}}$$

$$S_{ij} = \frac{1}{2}\left(\frac{\partial U_i}{\partial x_j} + \frac{\partial U_j}{\partial x_i}\right)$$

The model constants are $\eta_2 = 3.51$, $\sigma_\phi = \frac{2}{3}$, $C = 2$, $\kappa = 0.41$.

3.5.8. Detached eddy simulation (DES)

The DES approach is called hybrid LES/RANS models that the unsteady RANS models are employed in resolving the boundary layer, while LES treatment is applied to the core regions [57], [58], [59]. The DES model is promising because the cost of a near-wall resolving LES would be prohibitive. Many varieties of DES models have been developed, such as the realizable $k-\epsilon$-DES model and the BSL $k-\omega$-DES model. The SST-DES was used in this thesis to compare with the SST-SAS to assess the performance of the two models.

The transport equation of SST-DES is written as follows:

$$\frac{\partial \rho k}{\partial t}+\frac{\partial \rho \overline{U_j} k}{\partial x_j}=P_k-\rho\frac{k^{\frac{3}{2}}}{\min(L_t, C_{DES}\Delta_{\max})}+\frac{\partial}{\partial x_j}\left(\left(\mu+\frac{\mu_t}{\sigma_k}\right)\frac{\partial k}{\partial x_j}\right) \tag{3.54}$$

where

$$L_t=\frac{\sqrt{k}}{\beta^*\omega}$$

The model constant is C_{DES} called a calibration value of 0.61, $\Delta_{\max}$ is the maximum grid spacing.

3.6 Review of turbulence model in modelling of turbulent swirling flows

In Section 3.5, the equations and related modelling parameters of Reynolds-average Navier–Stokes (RANS), including two-equations family and Reynolds stress models, were presented. In addition, the more advanced scale-resolved simulations (SRS) and detached eddy simulation (DES) were presented. Although RANS is not as accurate as scale-resolved simulations, it is widely used to model turbulent flows as it is computationally inexpensive and can be used for modelling highly complex flow geometries [60].

Turbulent swirling flows are useful in combustion systems; in particular, swirl is added to the flow to enhance the fuel–air mixing rate and to reduce the emission of nitrogen oxides by means of a recirculation zone [61]. There have been many studies related to RANS, SRS, and DES models in simulating turbulent swirling flows, both in steady and unsteady cases [62], [63], [64], [65], and [66]. Standard k-epsilon was used by Guo et al. [61] to simulate the turbulent swirling flows in axisymmetric sudden expansions, and the results showed that the calculated mean flow field was in close agreement with the reported data. Another study showed that the k-epsilon and SSG Reynolds stress models were applied to simulate a realistic gas turbine combustor by Jochmann et al [62]. The results showed that both models were capable of reproducing the spatial and temporal dynamics of

the flow by comparing the results with particle image velocimetry and laser Doppler anemometry. Sarq et al. [63] used a realizable k-epsilon model to investigate the effect of swirl level on non-isothermal turbulent pipe flow in terms of heat transfer and entropy generation. Reasonable agreement with the experimental data was found. The studies by Brown et al. [64] and [65] showed that scale resolving simulation performs better in predicting dynamic phenomena compared to URANS.

Despite the fact that RANS and SRS can predict turbulent swirling flows, there is no unified model that can be used in predicting swirling flow dynamics. Unsteady RANS, SRS, and DES are significantly higher in computational effort compared to steady RANS; therefore, in the early design phase of combustors, many design parameters usually need to be considered and changed for the optimal design and operational conditions, and the computational time might be too expensive.

3.7 Variable density treatment – Favre averaging

In the turbulent flows where temperature variation is large, for instance, in those flows involving chemical reaction, combustion, or heat transfer problems, it is necessary to account for the fluid density variation.

Especially in gases, the density change is large compared to liquids and cannot be neglected in modelling. The conventional Reynolds decomposition is used for the turbulent density, the fluctuating components involving ρ' appear in the decomposition equation, and these terms are difficult to model [66]. Therefore, Favre [67] introduced density-weighted averaging called Favre averaging to provide equations with a simpler physical interpretation, and these are widely used in turbulent reacting flow problems.

Favre averaging is used for variable density flows to provide a simpler set of equations to solve. Farve decomposition and averaging are defined as follows:

$$
\begin{aligned}
u_i &= \tilde{u}_i + u_i'' \\
T &= \tilde{T} + T'' \\
\overline{\rho u_i''} &= 0 \\
\overline{\rho T''} &= 0 \\
\overline{u_i''} &\neq 0 \\
\overline{T''} &\neq 0 \\
\tilde{u}_i &= \frac{\overline{\rho u_i}}{\overline{\rho}}
\end{aligned}
\tag{3.55}
$$

where T is temperature, and subscript tildes represent Favre averaging.

Equation 3.55 expresses the motion for variable density flows, which is given as follows:

For the steady-state continuity equation:

$$\frac{\partial}{\partial x_j}\left(\overline{\rho}\tilde{u}_j\right) = 0 \tag{3.56}$$

For the steady-state momentum equation:

$$\frac{\partial}{\partial x_j}\left(\overline{\rho}\tilde{u}_j\tilde{u}_i\right) = -\frac{\partial \overline{p}}{\partial x_i} + \frac{\partial}{\partial x_j}\left(\overline{\sigma}_{ij} - \overline{\rho}\widetilde{u_j''u_i''}\right) \tag{3.57}$$

where $\overline{\sigma}_{ij}$ is the mean viscous stress tensor and a new term $\overline{\rho}\widetilde{u_j''u_i''}$ appears to lead to a closure problem that exists as with conventional Reynolds averaging.

3.8 Reacting flows governing equations

Turbulent combustion is a complex multi-phenomenon (for example, chemistry, heat transfer, fluid mechanics) due to the interaction between the presence of turbulence in combustion. Large temperature and density gradients and high heat release rates are the result of the two-way interactions between turbulence and combustion. The set of governing

equations in chemically reacting flows is very different from constant density non-reacting flows [68]. Additional transport data and detailed thermodynamic data must be included to describe the chemistry. The production and consumption of the species requires modelling using the mixing law of multi-component gas mixtures.

The reacting governing equations can be written as [21], [69], and [70]:

Continuity equation:

$$\frac{\partial \rho}{\partial t} + \nabla \cdot (\rho \vec{v}) = 0 \tag{3.58}$$

where ρ and $\vec{v}$ are the mixture density and the velocity vector, respectively.

Momentum equation:

$$\frac{\partial}{\partial t}(\rho \vec{v}) + \nabla \cdot (\rho \vec{v}\vec{v}) = -\nabla p + \nabla \cdot \tau \tag{3.59}$$

where p is the pressure and viscous stress tensor τ is described in expanded form in Equations 3.3a, 3.3b, and 3.3c.

Species transport equation:

$$\frac{\partial}{\partial t}(\rho Y_\alpha) + \nabla \cdot (\rho \vec{v} Y_\alpha) = \dot{\omega}_\alpha + \nabla \cdot (\rho D_\alpha \nabla Y_\alpha) \tag{3.60}$$

where Y_α is the mass fraction for a chemical species, α, D_α is the species mass diffusivity, and $\dot{\omega}_\alpha$ is the mass-based species production or consumption rate.

Energy equation in terms of total enthalpy:

$$\frac{\partial}{\partial t}(\rho H) + \nabla \cdot (\rho \vec{v} H) = \nabla \cdot \left(\frac{k_{eff}}{c_p} \nabla H \right) + S_h \tag{3.61}$$

where H is the total enthalpy that can be defined as the sum of the sensible enthalpy and chemical enthalpies, and this is expressed as:

$$H = \int_{T_0}^{T} \left(\sum_{\alpha=1}^{N} Y_\alpha \, c_{p,\alpha} \right) dT + \sum_{\alpha=1}^{N} Y_\alpha \, \Delta h_{f,\alpha}^0 = \int_{T_0}^{T} c_p dT + \Delta h_f^0 \tag{3.62}$$

where Δh_f^0 is the formation of the enthalpy of the gaseous mixture. S_h is the energy source term due to chemical reaction; this term is neglected in this thesis because the computational work was done using a reduced-order combustion model in which the heat of formation is included in the definition of enthalpy.

As mentioned in [21], three dimensionless parameters were introduced to characterise molecular transport phenomena. The Prandtl (Pr), Schmidt (Sc_α), and Lewis numbers (Le_α) are defined as:

$$\mathrm{Pr} = \frac{\mu c_p}{\lambda} = \frac{\nu}{\alpha}$$

$$\mathrm{Sc}_\alpha = \frac{\mu}{\rho D_\alpha} = \frac{\nu}{D_\alpha} \tag{3.63}$$

$$\mathrm{Le}_\alpha = \frac{\lambda}{\rho c_p D_\alpha} = \frac{\mathrm{Sc}_\alpha}{\mathrm{Pr}}$$

where c_p is the specific heat capacity at constant pressure, λ is the thermal conductivity, α is the thermal diffusivity, and ν is the kinematic viscosity of the gaseous mixture. The mass diffusivity is simplified using Fick's law [69], and therefore $\mathrm{Sc} = \mathrm{Sc}_\alpha$ and $\mathrm{Le} = \mathrm{Le}_\alpha$ for all species. In addition, the unity Lewis number assumption is commonly applied in turbulent combustion modelling [70], and this results in $\mathrm{Sc} = \mathrm{Pr}$ in all species.

Equation of state:

$$p = \rho R T \sum_{\alpha=1}^{N} \frac{Y_\alpha}{M_\alpha} \tag{3.64}$$

where R is the universal gas constant of 8.3145 kJ/kg K and M_α is the molecular mass for a chemical species.

The governing equations illustrated below are commonly adopted to provide a numerical solution for a chemically reacting flow system. Turbulence always occurs in practical systems; hence, a solid fundamental understanding of laminar flame theory is required to modify these equations for turbulent combustion modelling. The general assumption is the mixing

of the reactants by turbulence prior to ignition can be described as the properties of the laminar flame. The flames are separated into three categories: diffusion flame (non-premixed flame), premixed flame, and partially premixed flame. Laminar diffusion flame is presented in the next section.

3.9 Flamelet models

3.9.1. Steady diffusion flamelet model

The steady diffusion flamelet model (SDFM) is an approach to simulate chemical non-equilibrium due to diffusion flame stretching by turbulence [71], [72]. The model used in diffusion flame modelling involves the solution of transport equations for a conserved scalars-mixture fraction (f). Equations for individual species are not solved; instead, species concentrations are derived from the calculated mixture fraction field. The mixture fraction is assumed to follow the β-function probability density function (PDF), and scalar dissipation fluctuations are neglected. The concept of PDF is discussed in Section 3.9 below. The Favre-averaged species mass fractions and temperature in the turbulent flame can be determined from the PDF of mixture fraction and stoichiometric scalar dissipation:

$$\widetilde{\chi_{st}} = \frac{C_\chi \epsilon \widetilde{f''^2}}{k} \tag{3.70}$$

where C_χ is a model constant with a value of 2.

3.9.2. Flamelet-generated manifold model

Since the steady diffusion flamelet model relied heavily on modelling of scalar dissipation rate in turbulent flow, this methodology is limited to moderate non-equilibrium due to the aerodynamic strain effect [72]. Efficient and reliable numerical methods have become important tools in the design and optimisation process of combustor systems. Hence, in this thesis, all the reacting flow simulation used an advanced flamelet model, the flamelet-generated manifold (FGM) [73], which is a chemical reduction method that lowers the computational cost rather than resolving the detailed chemistry model but retains most of the accuracy of the flame structure. The partially premixed model solves a transport equation for the mean reaction progress variable ($\overline{c}$) as well as the mean mixture fraction ($\overline{f}$) and the mixture fraction variance ($\overline{f'^2}$) described in Section 2.5.3. The FGM models have been applied successfully in many combustion studies, such as Bao et al. [74], who used FGM to model n-dodecane spray flames, Kong et al. [75], who studied a gas turbine combustor using FGM combined with LES, Li et al. [76], who proposed a machine learning method in a simulation of a diffusion flame, and Füzesi et al. [77], who conducted FGM in modelling

ammonia-methane flames in a swirl burner and validated this against experimental data.

3.10 Turbulence–chemistry interaction

The probability density function (PDF) is a statistical approach to calculating mean quantities in the theory of turbulent combustion [78]. This approach solves the evolution of the one-point, one-time PDF for a set of scalar variables that can be used to determine local thermochemical properties [79].

Turbulence–chemistry interactions are modelled through the mixture fraction fluctuations using the presumed probability density function (presumed-PDF). The β-function is the most popular choice for the presumed-PDF for the single-mixture fraction, which depends on two parameters: the mean mixture fraction and its variance. The PDF of β-function is written as:

$$P(f) = \frac{f^{a-1}(1-f)^{b-1}}{\int f^{a-1}(1-f)^{b-1}\,df} \tag{3.71}$$

where a and b are defined by the Favre mean mixture fraction $\tilde{f}$, and the Favre mixture fraction variance $\widetilde{f''^2}$ is written as:

$$a = \tilde{f}\left[\frac{\tilde{f}\,(1-\tilde{f})}{\widetilde{f''^2}} - 1\right] \tag{3.72}$$

and

$$b = (1-\tilde{f})\left[\frac{\tilde{f}\,(1-\tilde{f})}{\widetilde{f''^2}} - 1\right] \tag{3.73}$$

Since the reacting systems in this thesis involve heat and mass transfer through droplet particles generated from breaking up the liquid fuels, the local thermochemical state is related to the Favre mean mixture fraction ($\tilde{f}$) as well as the Favre mean enthalpy ($\widetilde{H}$). The Favre mean scalars are calculated by:

$$\widetilde{\phi_i} = \int_0^1 \phi_i(f, \widetilde{H}) P(f) df \tag{3.74}$$

where an additional transport equation for mean enthalpy is required,

$$\frac{\partial}{\partial t}(\rho\widetilde{H}) + \nabla\cdot(\rho\vec{v}\widetilde{H}) = \nabla\cdot\left(\frac{k_t}{c_p}\nabla\widetilde{H}\right) + S_h \tag{3.75}$$

where S_h is the source term due to heat exchange between dispersed and continuous phases.

The distribution of the thermochemical variables can be determined by Equations 3.71, 3.72, and 3.73 for the Favre mean mixture fraction, the Favre mixture fraction variance, and the Favre mean enthalpy.

3.11 Turbulent spray flame modelling

3.11.1. Spray combustion modelling

Turbulent spray flames are difficult to accurately simulate due to their complicated configurations, including various combustion modes. The flamelet models are promising in simulating turbulent spray flames with affordable computational costs [80]. Studies in flamelet modelling for spray combustion based on the gaseous flamelet tabulation library have been computed in [81–83]. Serval spray flame has been studied using the FGM model; for instance, Wehrfritz et al. [84] used flamelet-generated manifold (FGM) with LES to simulate the spray flames under engine Combustion network (ECN) spray A conditions and with n-dodecane used as a diesel fuel surrogate. The LES-CMC of two-phase flames and n-heptane spray flames with swirl-stabilised burners has been successfully computed by Tyliszczak et al. [85].

3.11.2. Modelling techniques

Accurate prediction for turbulent spray flame is extremely difficult; hence, serval assumptions are applied in this thesis to simplify the model. Assuming the dispersed phase occupies a low-volume fraction that is less than 10^{-6}, particle-particle interactions such as droplet collision and coalescence can be neglected. The Euler–Lagrangian approach is used in this thesis to model the turbulent spray flame. The continuous phase, which is the fluid phase, is treated as solving the Navier–Stokes equations in an Eulerian frame of reference, while the dispersed phase is solved by tracking a large number of droplets in a Lagrangian frame of reference through the computed flow field. The momentum, mass, and energy can be exchanged between the fluid phase and the dispersed phase.

The trajectory of a discrete phase droplet can be predicted by integrating the force balance equation and written as:

$$m_p \frac{d\vec{u}_p}{dt} = m_p \frac{\vec{u} - \vec{u}_p}{\tau_r} \tag{3.76}$$

where m_p is the droplet mass, $\vec{u}$ is the fluid phase velocity, $\vec{u}_p$ is the droplet velocity, $m_p \frac{\vec{u}-\vec{u_p}}{\tau_r}$ is the droplet drag force, and τ_r is the droplet relaxation time [43] defined by:

$$\tau_r = \frac{\rho_p d_p^2}{18\mu} \frac{24}{C_d \mathrm{Re_d}}$$

where μ is the molecular viscosity of the fluid phase, d_p is the droplet diameter and Re is the relative Reynolds number, which is calculated by,

$$Re_d \equiv \frac{\rho d_p \left|\vec{u}_p - \vec{u}\right|}{\mu}$$

A stochastic approach called the discrete random walk (DRW) model is used to account for the turbulent dispersion effect due to the droplets interacting with fluid turbulent structures and affecting the droplet trajectory [86]. The fluctuation of velocity in three directions is assumed to obey a Gaussian probability distribution and correlate with the turbulent kinetic energy, which gives:

$$\vec{u}' = \zeta\sqrt{\overline{\vec{u}'^2}} = \sqrt{\frac{2k}{3}} \tag{3.77}$$

where ζ is a normally distributed random number and k is the turbulent kinetic energy calculated in the flow field. The characteristic eddy lifetime is defined as a constant value:

$$\tau_e = 2T_L \tag{3.78}$$

where T_L is the droplet timescale, which can be approximated in two-equation turbulent models by

$$T_L \approx 0.15\frac{k}{\epsilon}$$

The droplet is assumed to interact with the fluid phase when the droplet relaxation time is smaller than the eddy lifetime and the eddy crossing time. The droplet eddy crossing time is calculated as:

$$t_{cross} = -\tau \ln\left[1 - \left(\frac{L_e}{\tau|u - u_p|}\right)\right] \tag{3.79}$$

where L_e is the eddy length scale and $|u - u_p|$ is the magnitude of the relative velocity.

The drag coefficient (C_D) for spray droplets can be calculated by assuming that the shape of droplets is smooth and spherical [86]:

$$C_D = a_1 + \frac{a_2}{Re_d} + \frac{a_3}{Re_d{}^2} \tag{3.80}$$

where a_1, a_2 and a_3 are the model constants related to the droplet Reynolds number (Re_d).

A simple heat balance equation is used to calculate the droplet temperature (T_p):

$$m_p c_p \frac{dT_p}{dt} = hA_p(T_\infty - T_p) \tag{3.81}$$

where m_p is the droplet mass, c_p is the specific heat capacity of the droplet, A_p is the surface area of the droplet, T_∞ is the local temperature of the fluid phase, and h is the convective heat transfer coefficient, which is evaluated using the Ranz and Marshall correlation [87],[88]:

$$Nu = \frac{hd_p}{k_\infty} = 2.0 + 0.6Re_d^{0.5}\mathrm{Pr}^{\frac{1}{3}}$$

where k_∞ is the thermal conductivity of the fluid phase and Pr is the Prandtl number of the fluid phase ($c_p\mu/k_\infty$).

For droplets exposed to high-temperature environments, the vaporisation rate is considered to be high, and the effect of convective flow of the evaporating species from the droplet surface to the bulk gas phase, which is known as the Stefan flow, becomes important. The mass transfer of the droplet is described as follows:

$$\frac{dm_p}{dt} = k_c A_p \rho \ln(1 + B_m) \tag{3.82}$$

where k_c is the mass transfer coefficient calculated using the Sherwood number correlation [89],

$$Sh_{AB} = \frac{k_c d_p}{D_{i,m}} = 2.0 + 0.6Re_d^{0.5}Sc^{1/3}$$

where $D_{i,m}$ is the diffusion coefficient of vapour in the bulk, Sc is the Schmidt number ($\mu/\rho D_{i,m}$), and B_m is the Spalding mass number defined as

$$B_m = \frac{Y_{i,S} - Y_{i,\infty}}{1 - Y_{i,S}}$$

where $Y_{i,S}$ is the vapour mass fraction at the droplet surface and $Y_{i,\infty}$ is the vapour mass fraction in the bulk gas.

When unity Lewis number assumption and $c_{pv} = c_{pg}$ are used, the Spalding mass number (B_m) is equivalent to the Spalding heat number (B_T):

$$B_T = \frac{c_{pv}(T_\infty - T_p)}{h_{fg} - \dot{q}_p/\dot{m}_p} = (1 + B_m)^{\frac{1}{Le}\frac{Sh}{Nu}\frac{c_{pv}}{c_{pg}}} - 1 \tag{3.83}$$

where c_{pv} is the specific heat of droplet vapour, h_{fg} is the latent heat, $\dot{q}_p$ is the heat transfer to droplet, and $\dot{m}_p$ is the droplet evaporation rate.

The Nusselt number has a modified form as follows [81]:

$$Nu = \frac{hd_p}{k} = \frac{\ln(1 + B_T)}{B_T}(2.0 + 0.6Re_d^{0.5}\mathrm{Pr}^{\frac{1}{3}}) \tag{3.84}$$

where k is the thermal conductivity of the fluid phase.

The final form of calculating the droplet temperature correlated with convective and latent heat transfer between the droplet and the fluid phase is written as:

$$m_p c_p \frac{dT_p}{dt} = hA_p\left(T_\infty - T_p\right) - \frac{dm_p}{dt} h_{fg} \tag{3.85}$$

The heat transfer between two phases is added through the source/sink term (S_h) in Equation (3.85).

3.11.3 Modelling assumptions

The mathematical model presented in this thesis for modelling the combustor is based on the following assumptions [70]:

- Radiative heat transfer is neglected.
- Mach number is small and subsonic.
- Pressure inside the combustion chamber is assumed to be constant.
- The Lewis number is assumed to be unity.
- Effect of buoyancy is neglected.
- The gases are assumed to be ideal gas.
- The thermodynamic properties of species, density, and kinematic viscosity of fluid are functions of temperature.
- The flamelet concept is assumed to be valid.

3.12 Summary

In this chapter, the detailed description of turbulence models was reviewed in Sections 3.2 to 3.5. The chemical closure term was proposed to be modelled by the tabulated chemistry method – flamelet models, and the detailed methodology is reviewed in Sections 3.6 to 3.9. As the combustor utilises liquid fuels, the modelling techniques and the modelling assumptions for studying the combustor were discussed in Section 3.10.

In the previous and current chapters, the modelling methodology has the potential to be used in this optimisation work. In the following chapters, the methodology will be used to simulate a lab-scale burner under non-reacting as well as reacting conditions for the validation process.

Chapter 4 Computational Investigation of Swirling Flow Dynamics in a Swirl-stabilised Burner

4.1 Introduction

The previous chapter discussed the various turbulence models and numerical approaches that can be used to model turbulent swirling flows. Swirling flows are widely used in gas turbine engines to stabilise the flame; hence, the prediction of a swirling flow field is of great importance for the design of efficient and low emission combustion devices. Scale resolving simulation (SRS) is more promising than unsteady Renyolds-averaged Navier–Stokes (URANS) and RANS to describe the corresponding velocity field and the turbulent mixing accurately.

This chapter discusses the different steady-state turbulence models as well as unsteady simulations to investigate a non-reacting annular swirling jet flow. The configuration was studied experimentally by Sheen [90]. The flow is characterised by highly swirling, serval recirculation zones and coherent structures, for example precessing vortex core (PVC) [91], which make the modelling very challenging. The work in this chapter provides a detailed investigation of the capability of different turbulence models to model non-reacting turbulent annular jets and a thorough comparison against the experimental data. The model that gives the most satisfactory prediction of

the flow is used to investigate the reacting turbulent annular jet in the next chapter.

This chapter is structured as follows. Section 4.2 summarises the experimental and numerical investigations of annular swirling flows. Section 4.3 illustrates the experimental setup of the lab-scale burner. This configuration is also studied for the reacting case in Chapter 6. Sections 4.4, 4.5 and 4.6 discuss the computational parameters and approaches, such as grid generation and boundary conditions. Section 4.7 presents a thorough comparison of the steady-state RANS, URANS, and SRS models against the experimental measurements of mean velocity profiles at axial, radial, and tangential directions. Finally, the conclusions are summarised in Section 4.8.

4.2 Background

Swirl flows are important and can be found in nature as well as in a wide range of engineering applications. Swirling flow applications in non-reacting cases can be found in cyclone separators, tornadoes, and agricultural spraying machines. For practical combustion systems, swirl is extensively used in flame stabilisation and prompts better fuel and air mixing to mitigate pollutants in internal combustion engines as well as gas turbine engines.

A confined annular jet is one of the free jet configurations of interest when studying the combustor flow field. An annular flow in a sudden-expansion circular channel was studied experimentally [92]. Laser Doppler anemometry (LDA) was used to carry out the velocity measurements, with a Reynolds number ranging from 150 to 5800. Four different flow regimes were observed and reported: (I) open channel flow, (II) closed annular flow, (III) vortex shredding, and (IV) stable central flow. The increasing Renyolds number results in the flow pattern transition from (I) to (IV), and in reverse from (IV) to (I), with a decreasing Reynolds number. The flow pattern of four different regimes is illustrated in Figure 4.1.

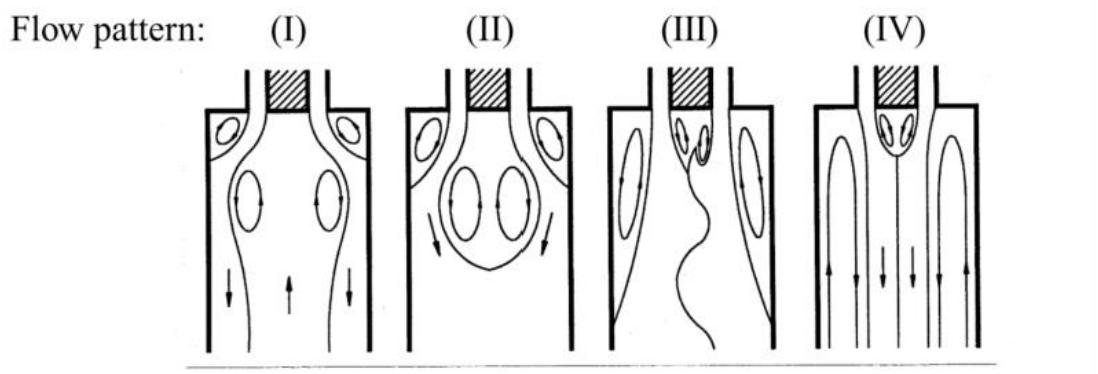

Figure 4.1 Flow pattern with different Reynolds number [92]

The presence of swirl in the flow changes the unsteady character. The ratio of angular velocity to axial velocity is a key parameter for differentiating different types of flow behaviour. A swirl number (S_n) is defined as the ratio of axial flux of angular momentum to axial flux of axial momentum [93]:

$$S_n = \frac{\int_{R_i}^{R_o} \rho u_x u_\theta r^2 dr}{(R_o - R_i) \int_{R_i}^{R_o} \rho u_x^2 r dr} \tag{4.1}$$

where R_i and R_o are the inner and outer radius of annular channel respectively, u_x and u_θ are velocity of axial and tangential component. Different swirling numbers result in different modes of recirculation zones and alter the mixing layers. Syred [94] conducted a review of the role of the precessing vortex core (PVC) in swirl combustion systems. In the presence of a high swirl, the flow structure in an annular combustor leads to serval recirculation zones. The inner recirculation zone (IRZ) and outer recirculation zone (ORZ) present an inner shear layer and outer shear layer that prompt the mixing between fuel and oxidiser. Vortex breakdown phenomena occur when the degree of swirl in the flow exceeds a critical value (swirl number greater than 0.6) and coherent structure PVCs are formed [94].

A numerical study of the simulation of turbulent swirling flow in an annular bluff body combustor was carried out using unsteady Reynolds-averaged Navier–Stokes (URANS), and URANS can capture the corresponding PVC in a swirling jet [95]. The swirl intensity was considered to be mild, as the swirl number presented in the study was 0.39. Both experimental and numerical studies on bluff body swirl-stabilised flames in a confined combustor were reported [95]. Particle image velocimetry (PIV) was used to measure the instantaneous flow fields, and large eddy simulation (LES) was

performed to validate the experimental results. The structure of PVCs is captured by LES and obtained good agreement between numerical and experimental results [96].

4.3 Experimental configuration

The experimental measurements were obtained using laser Doppler anemometry (LDA) by Sheen [92]. The burner used in the experiment is outlined in Figure 4.2. The burner is a long cylindrical tube with a diameter of 200 mm and length of 500 mm. The swirl generation device is a swirler that has 20 equally spaced guide vanes with a discharge angle of 30° to the axis, and it is placed 50 mm upstream of the front plate of the burner to obtain a circumferential uniform flow [90]. The experimental data reported the measurements of three velocity components – axial, radial, and tangential – at selected axial locations downstream from the burner exit. The flow upstream of the burner of the jet exit and swirler dimensions were not provided in the experimental investigation; therefore, the computational investigation simplified the swirler geometry into axial velocity component and tangential velocity component to represent the swirling intensity provided by the swirler geometry.

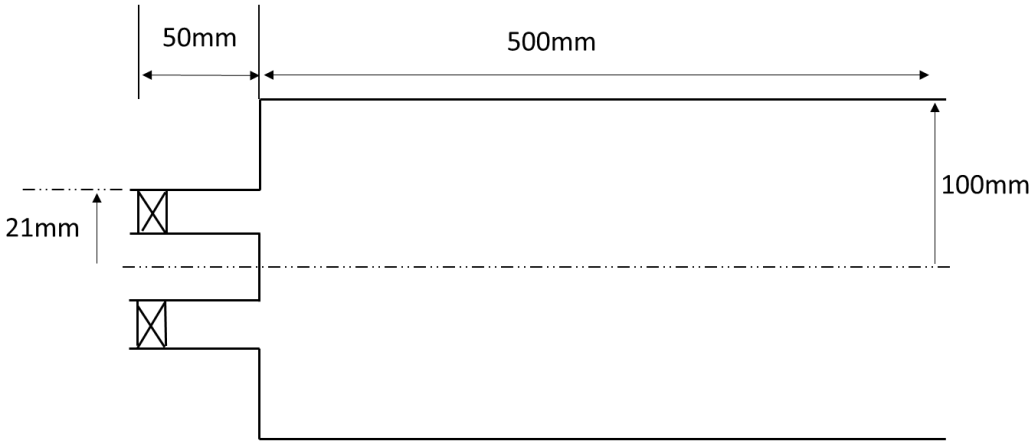

Figure 4.2 Experimental burner configuration.

4.4 Computational parameters

The computational parameters used in the RANS studies of turbulent swirling annular jet are summarised in this section. The annular channel outer radius is 21 mm and is defined as the hydraulic diameter. The axial velocity computed from the experimental air mass flow rate and the inlet is defined as the surface of the annulus. A flow-through time (FTT) is defined as the ratio of the length of the computational domain and axial velocity. One FFT is calculated as 25.3 ms. The tangential velocity was determined by a trial-and-error approach in the URANS simulation to match the experimental velocity profiles since the swirler geometry was not provided in the experimental report and the swirler number of the swirler is not clear. The uniform top-hat profile was imposed at the annular channel inlet

and a uniform static pressure outlet of the burner. The boundary condition of all walls was imposed as a smooth, non-slip, and adiabatic wall.

In the steady-state context, a coupled algorithm was used with second-order upwind schemes for momentum and turbulent quantities. In the URANS context, a time step of 1×10^{-5}s was used to properly control the Courant number that satisfied Courant–Friedrichs–Lewy (CFL) number condition $CFL \leq 1$. The PISO algorithm with second-order upwind schemes for momentum and turbulent quantities and a second-order implicit transient formulation was used for time discretisation. For the SAS/DES context, the PISO algorithm was used with bounded central differencing schemes for momentum discretisation, second-order upwind for other spatial discretisation and second-order implicit for time discretisation. A time step size was reduced to 8×10^{-6}s to satisfy $CFL \leq 1$. The detailed numeric settings are shown in Table 4.1.

Table 4.1 Numerical settings for SRS

Convection terms	Bounded central differencing
Pressure discretisation	Second order
Velocity gradients	Least square cell based
Iterative method	PISO
Time discretisation	Second-order implicit

To reach statistical convergence, three flow-through times were used to initialise and allow the unsteady flow features to evolve. After that, another three flow-through times were used to collect the statistical representative solution.

4.5 Computational grid

Figure 4.3 shows the computational grid used in Chapters 4 and 6. ICEM CFD meshing software was used to generate the grid. Block-structure grids with O-grids were used to generate high-quality hexahedral grids to provide accuracy in the prediction of the important recirculation region of high-velocity fluctuation. Two different grid densities – coarse and fine – were used for the grid independent study. In the axial direction, 430 grid points and 512 grid points were used in the coarse grid and the fine grid, respectively. In the radial direction, 110 grid points and 144 grid points were used in the coarse and fine grids. In the azimuthal direction, 68 grid points and 132 grid points were used in the coarse and fine grids. The grid expansion ratio of both grids was less than 5% in all three directions. The minimum grid size is 500μm at the exit of the jet for the coarse grid, and 250μm for the fine grid. The total number of grid elements is 2.6 million for the coarse grid, and 8 million for the fine grid.

The grid sensitivity study performed in steady-state RANS simulation showed that the results are grid insensitive. After that, the optimal grid was

used to lower the computational cost of simulating URANS and SRS due to the smaller time step size and large amount of time steps required to resolve the flow structure and achieve a statistically converged state. Figure 4.3 shows the different views of the computational grids used.

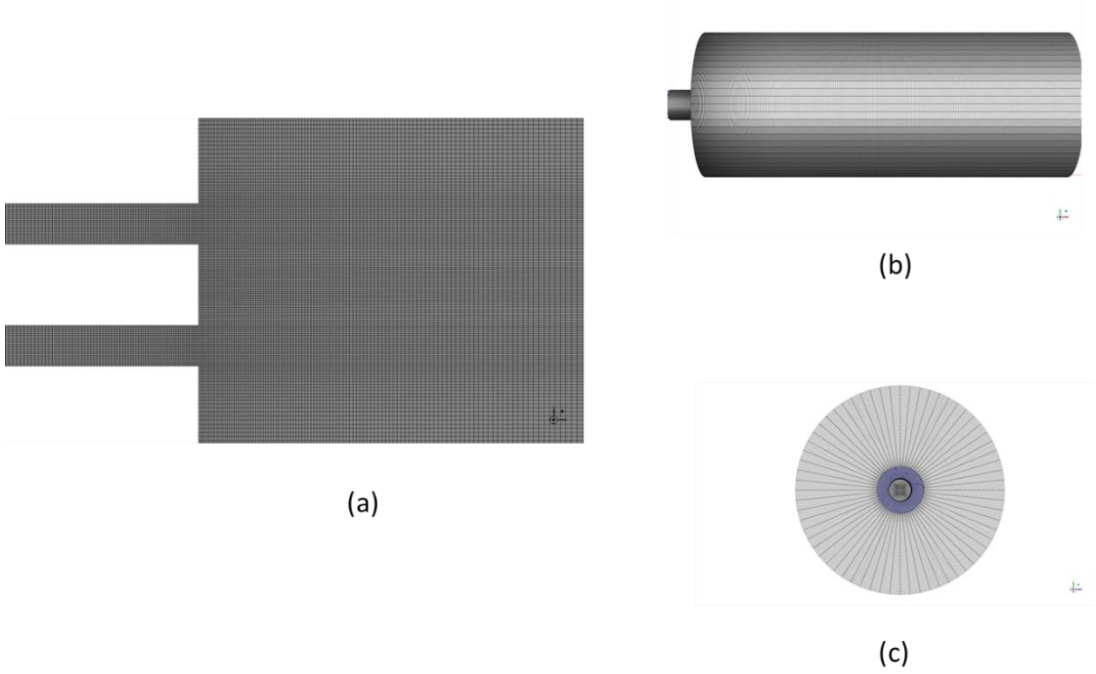

Figure 4.3 Computational grid (a) Axial plane. (b) Side plane. (c) Top plane.

4.6 Boundary conditions

At the beginning of the study, the flow was assumed to be steady-state and isothermal. The incompressible flow assumption was used, as the bulk velocity is 0.0783 Mach. A mass flow inlet with a tangential velocity

component was specified at the annular channel surface to mimic the swirling flow entering the combustor. The turbulent intensity was computed as 5% using Equation (4.2) of the correlation for a fully developed pipe flow at the core as:

$$I = 0.16\left(Re_{D_H}\right)^{-1/8} \tag{4.2}$$

where Re_{D_H} is the Reynolds number based on the hydraulic diameter D_H. A pressure outlet with a reverse flow prevention option was specified at the burner outlet to avoid backward pressure flow. The boundary conditions for different turbulence models are summarised in Table 1.

All the simulations were computed on the Birmingham Environment for Academic Research (BEAR) High Performance Cluster at the University of Birmingham, running Ansys Fluent in parallel on up to 40 cores CPU on the Linux operating system. Each core is an Intel Xeon Platinum 8360Y processor with 2.4 GHz.

Table 4.2 Boundary conditions for URANS

Axial velocity (m/s)	Tangential velocity (m/s)	Flow Reynolds number (at the annular channel)	Air viscosity (kg/(m · s)	Air density (kg/m^3)

21.73	40.0	58559	1.846×10^{-5}	1.176

Table 4.2 shows the boundary conditions used for all turbulence modelling in a URANS context. In a URANS context, a time step size of 1×10^{-5}s was used and 8×10^{-6}s was used in URANS Reynolds stress models and SAS to keep the CFL number below 1. Convergence criteria at each time step were assessed by a reduction of three orders of magnitude for residuals for continuity and each momentum equation.

4.7 Results

The results of steady-state RANS, unsteady RANS, and SRS simulation are presented in this section. All the computational results are compared with the experimental results in terms of axial, radial, and tangential velocity profiles at serval axial locations across the burner.

4.7.1 Steady-State RANS

A steady-state RANS of standard k-epsilon. The results of steady-state RANS are not able to capture the inner recirculation zone (IRZ) due to the dissipative nature of the turbulence models. The grid sensitivity study was

first computed using coarse grids and fine grids of the SST k-omega turbulence model. The results are shown in Figures 4.4 – 4.13 and the main findings are that there is grid insensitivity, and neither grid can resolve the inner recirculation zone (IRZ) that contributes to flame stabilisation; hence, all the calculations done in this thesis use coarse grids to effectively save computational cost.

In the RANS context, the Reynolds stress model (RSM) has been considered the most elaborate model to account for anisotropic turbulence; however, the computational cost is the highest due to the RSM needs to solve other transport equations for the Reynolds stresses as well as the transport equation of the dissipation equation. The difference between SST k-omega and RSM-omega was studied by comparing the velocity component profiles and the Reynolds stress matrix. Figure 4.11 shows that the RSM model performs better than SST k-omega in capturing the axial velocity profiles, especially at X = 30mm and X = 60mm. Nevertheless, the two models failed to capture the IRZ shown in X = 10 mm. Overall, both SST k-omega and RSM-omega are not able to reproduce the velocity profiles in a steady-state context. In Table 4.3, the value of the six Reynolds stress matrices is tabulated, where UU, VV and WW are the isotropic components and UV, VW and UW are anisotropic components. The results highlighted that turbulence anisotropy was negligible; therefore, the RSM-type model has no advantages in resolving this flow, although the RSM model can attempt to account for anisotropy.

The next section introduces the two-equation models and RSM models in URANS context and compares them with experimental results to determine the modelling strategy.

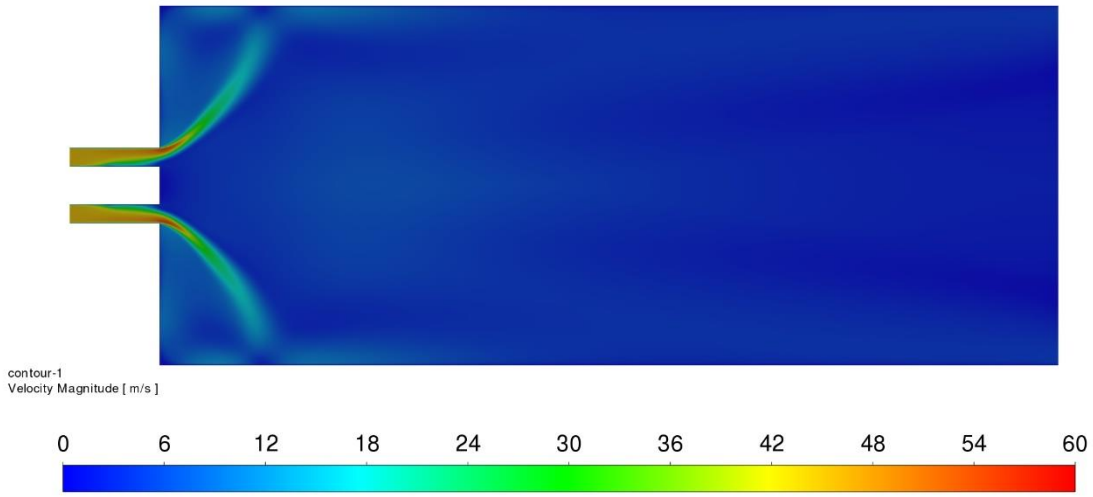

Figure 4.4 Velocity magnitude of SST-k-omega (coarse grid)

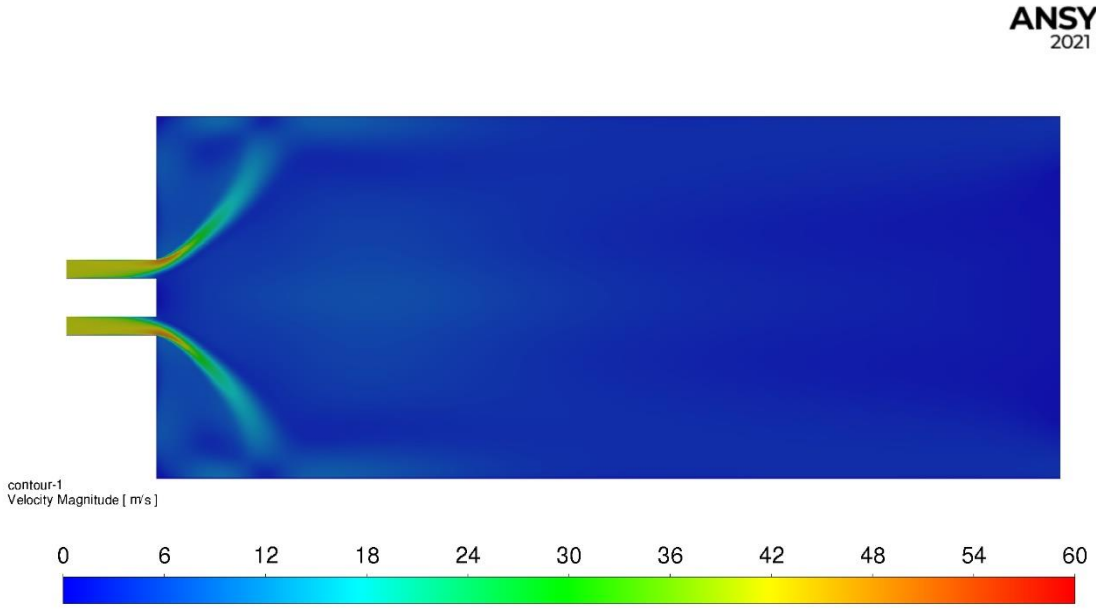

Figure 4.5 Velocity magnitude of SST-k-omega (fine grid)

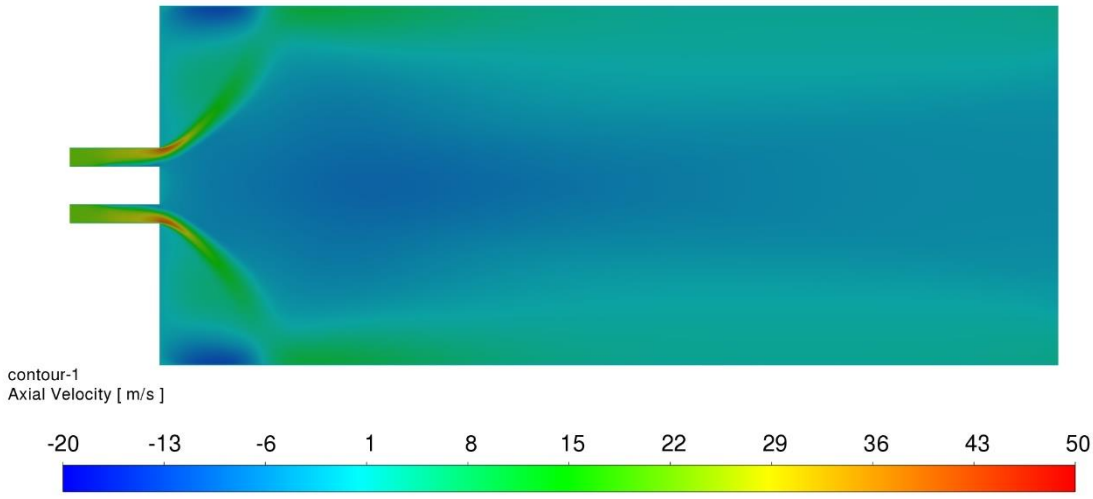

Figure 4.6 Axial velocity of SST-k-omega (coarse grid)

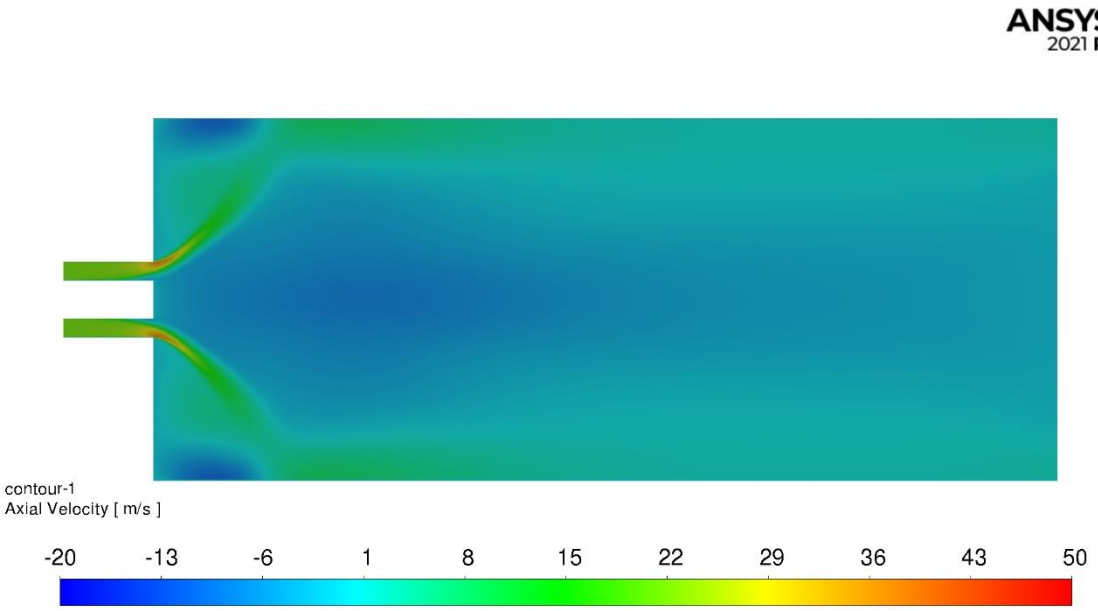

Figure 4.7 Axial velocity of SST-k-omega (fine grid)

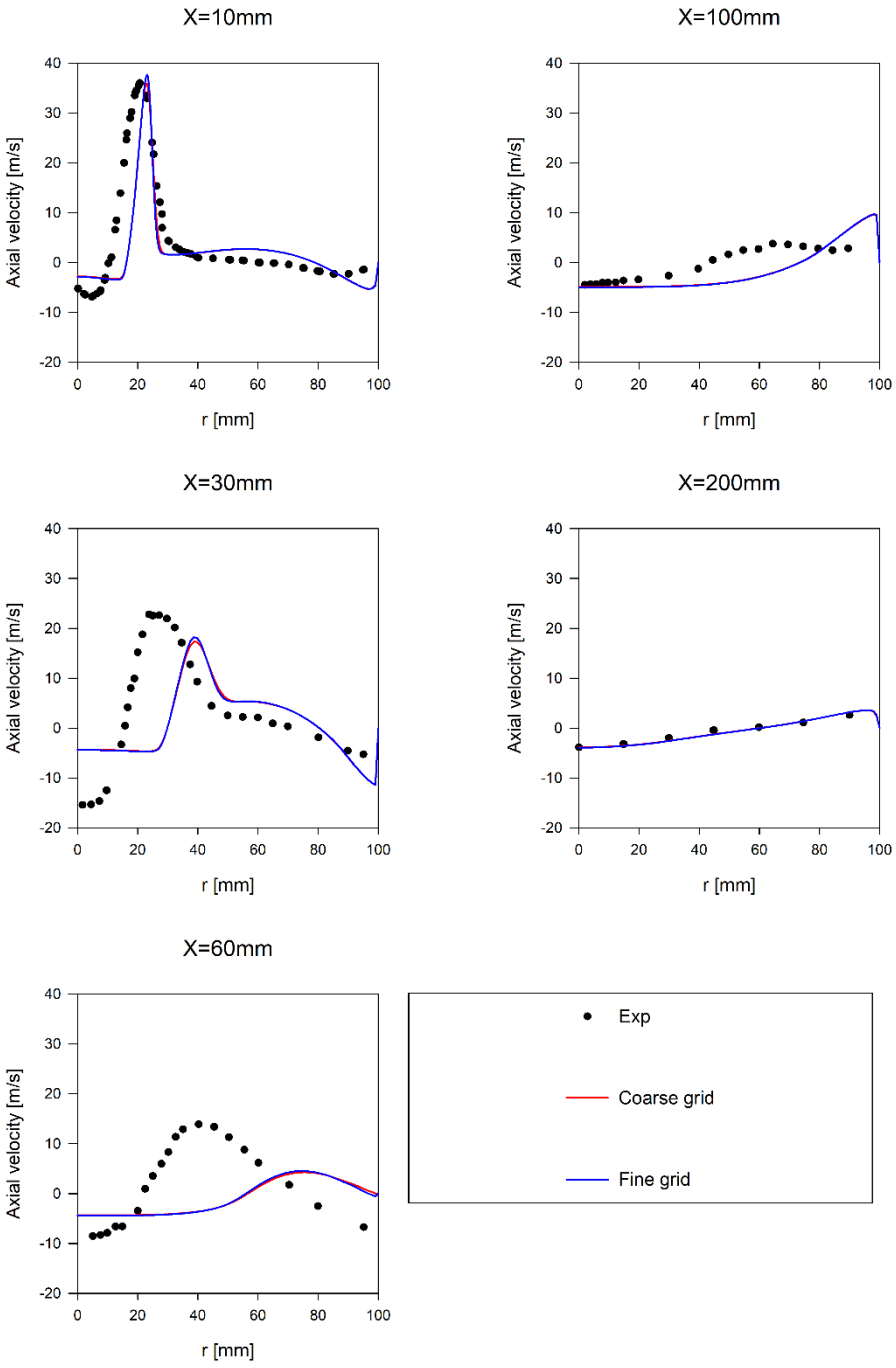

Figure 4.8 Grid sensitivity study – axial velocity profiles

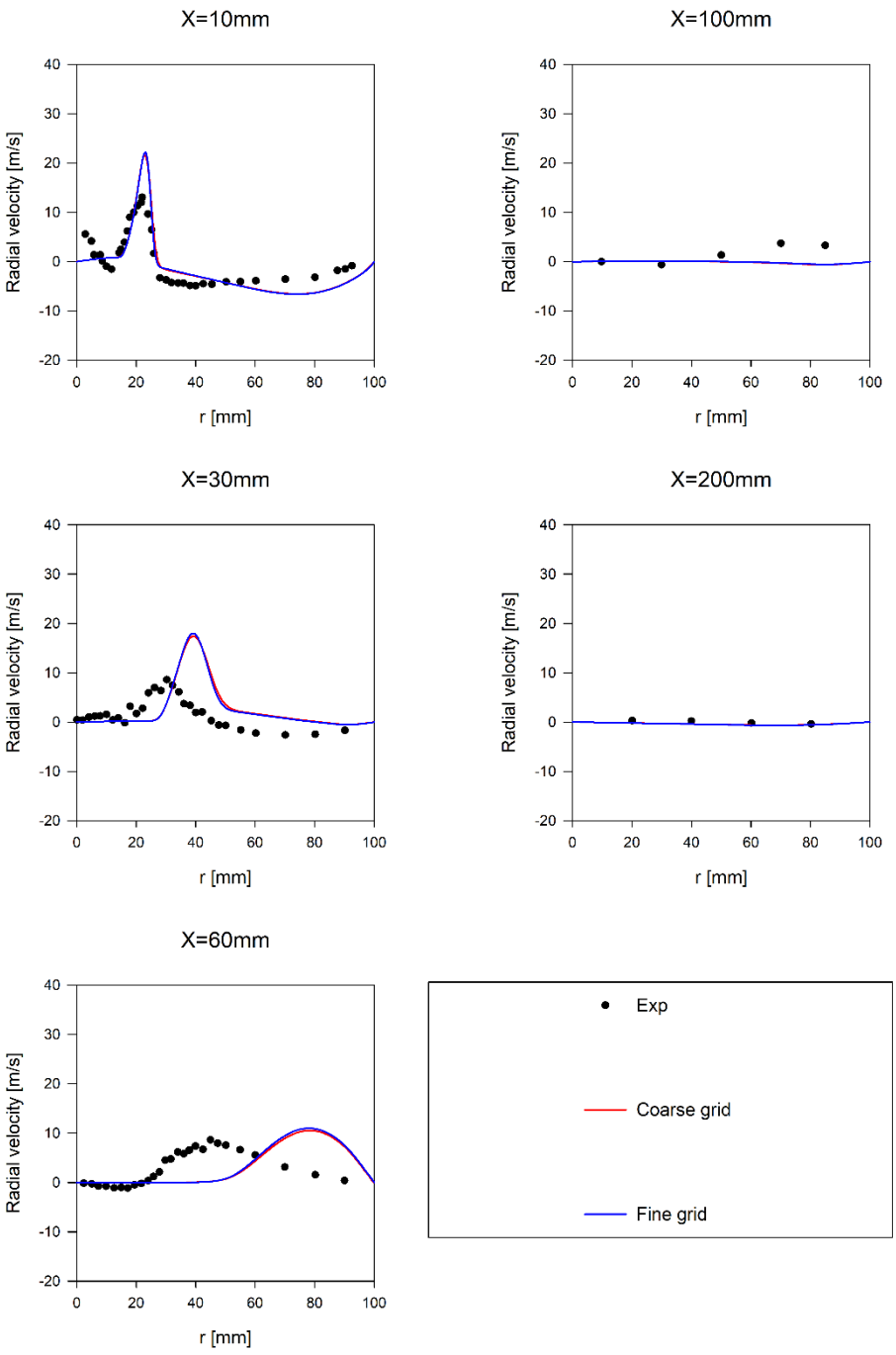

Figure 4.9 Grid sensitivity study – radial velocity profiles

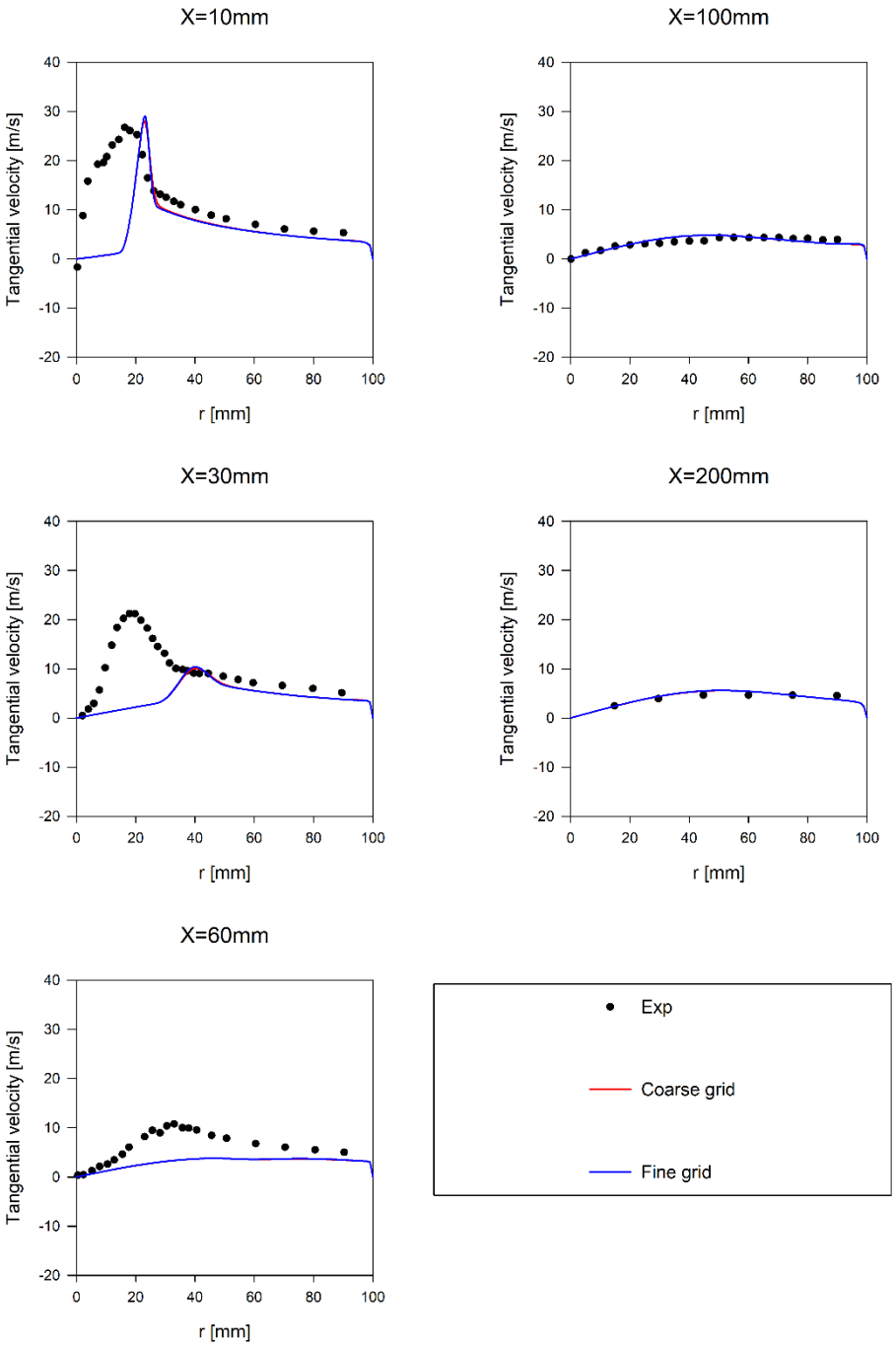

Figure 4.10 Grid sensitivity study – tangential velocity profiles

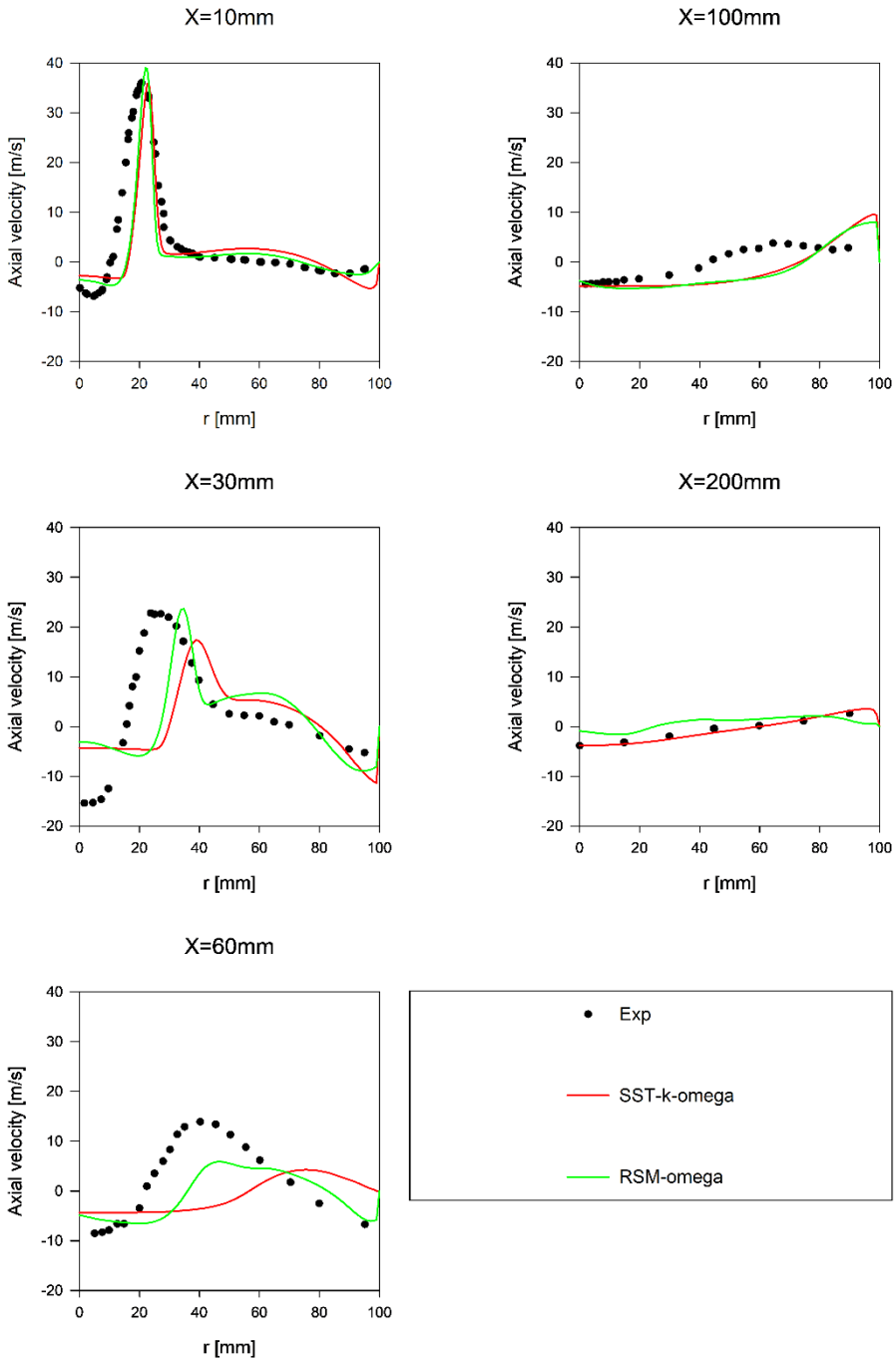

Figure 4.11 Turbulence models comparison – axial velocity profiles

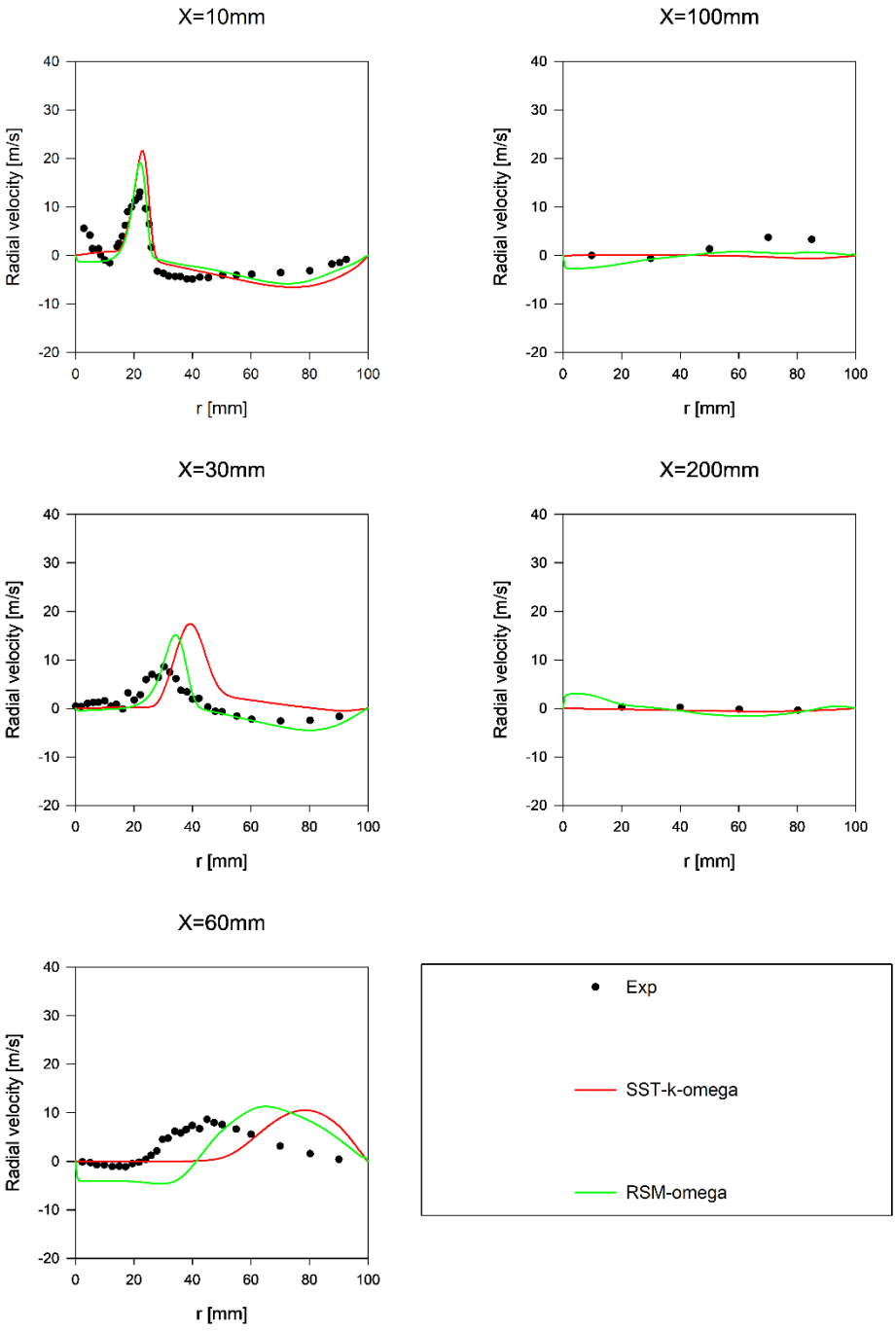

Figure 4.12 Turbulence models comparison – radial velocity profiles

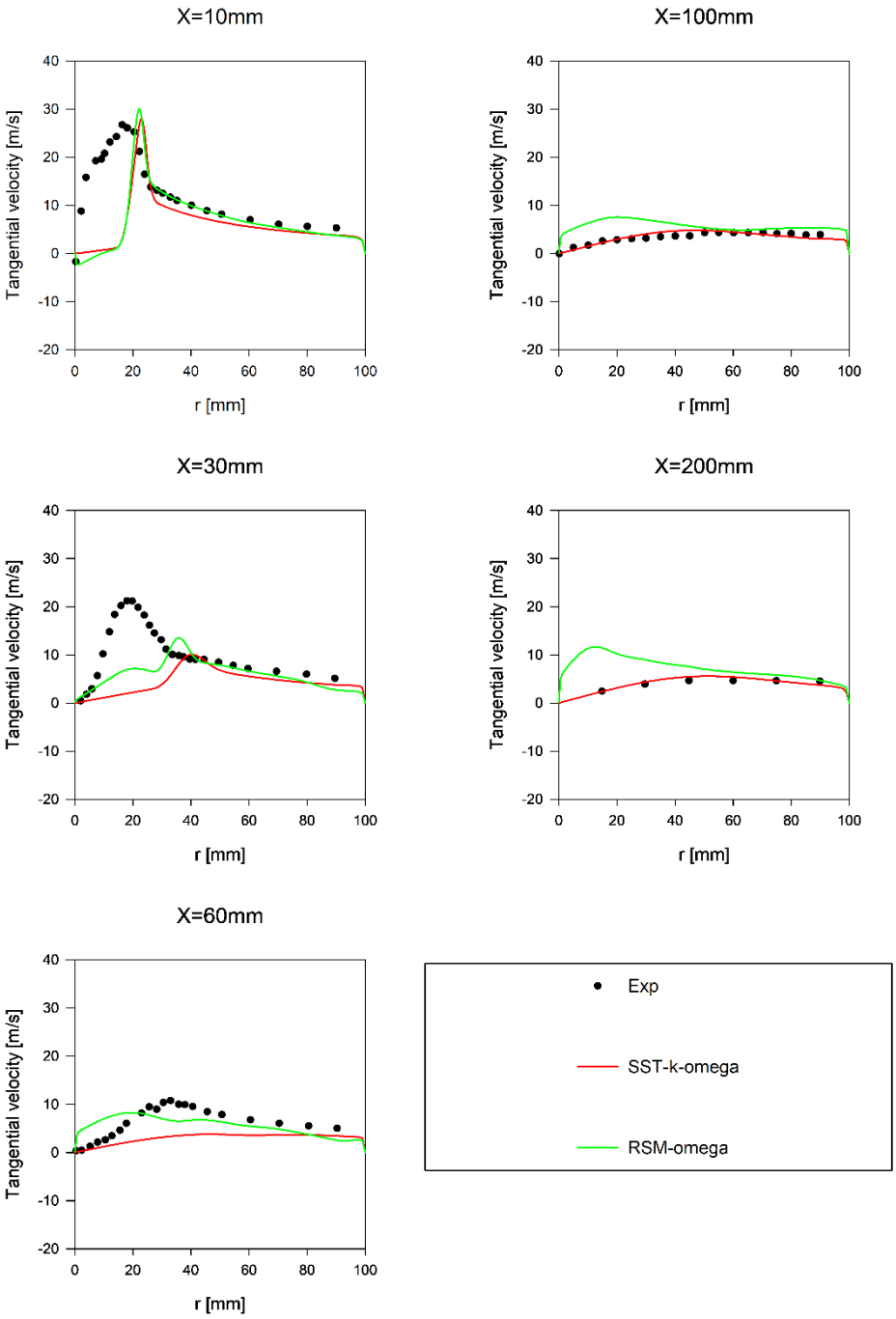

Figure 4.13 Turbulence models comparison – tangential velocity profiles

Table 4.3 Mass-weighted average Reynolds stresses

Reynolds stress	Mass-weighted average $[m^2/s^2]$
UU	2.62
VV	2.19
WW	2.18
UV	-0.015
VW	0.050
UW	-0.040

4.7.2 Unsteady RANS

Unsteady RANS is mathematically similar to RANS governing equations, except that unsteady RANS has an additional time derivative term to account for unsteadiness. Unsteady RANS simulations were performed using five different turbulence models, and the performance of these models was assessed by comparison with the experimental results. Zhang and Vanierschot reported that URANS can capture the precessing vortex core (PVC) consisting of a single and double helical structure in a swirling jet [95]. From Figure 4.14 to Figure 4.17, the results of SST k-omega turbulence models are presented. The results show that the 2-equation turbulence model cannot capture the flow unsteadiness as the instantaneous velocity magnitude and axial velocity contour are similar to the time-averaged velocity magnitude and axial velocity contour. In addition, the structure of PVC cannot be captured due to the isotropic turbulence assumption. Figures

4.18 to 4.21 illustrate the results of using the RSM-omega model. The RSM-omega result in Figure 4.21 captures three different recirculation zones– two outer recirculation zones at the top and bottom and one inner recirculation zone after the exit of the jet. The inner recirculation zone is favourable for burnt gas recirculation, flame stabilisation, and increased air and fuel mixing, which are especially important for combustion system design. Another recirculation that occurs is the precessing vortex breakdown, which is shown in Figure 4.22. An iso-contour of static pressure of -150 Pa was used to capture the helix structure. The helix structure was formed along the central axis of the geometry, starting from the exit of the jet. The other three turbulence models showed very similar results, and all the results are presented in Appendix A.

Figures 4.23 to 4.25 show the velocity profiles for axial, radial, and tangential of all five turbulence models. In the axial velocity profiles, SST k-omega overpredicted the peak value at an axial direction of 30 mm and predicted the inner recirculation profiles better than the other four models. All turbulence models failed to capture the velocity profiles at the 60 mm axial direction downstream. In the radial velocity profiles, all five turbulence models performed similarly in reproducing the flow field. However, the SST k-omega again performs better performance as the radial velocity at axial directions of 60 mm and 100 mm downstream are closer to the experimental results. Finally, in tangential velocity profiles, all turbulence models showed discrepancies at axial directions of 10 mm and 30

mm due to the flow complexity. It can also be observed that SST k-omega predictions were closer to the experimental results.

The velocity contour and profiles showed that SST k-omega has the best agreement with the experimental results, but flow unsteadiness cannot be captured due to the isotropy turbulence assumption. The Reynolds stress model abandoned the isotropy turbulence assumption and therefore is superior in resolving the flow field in detail, such as flow unsteadiness and precessing vortex core (PVC); however, the RSM model prediction of mean value is performed like any two-equation model.

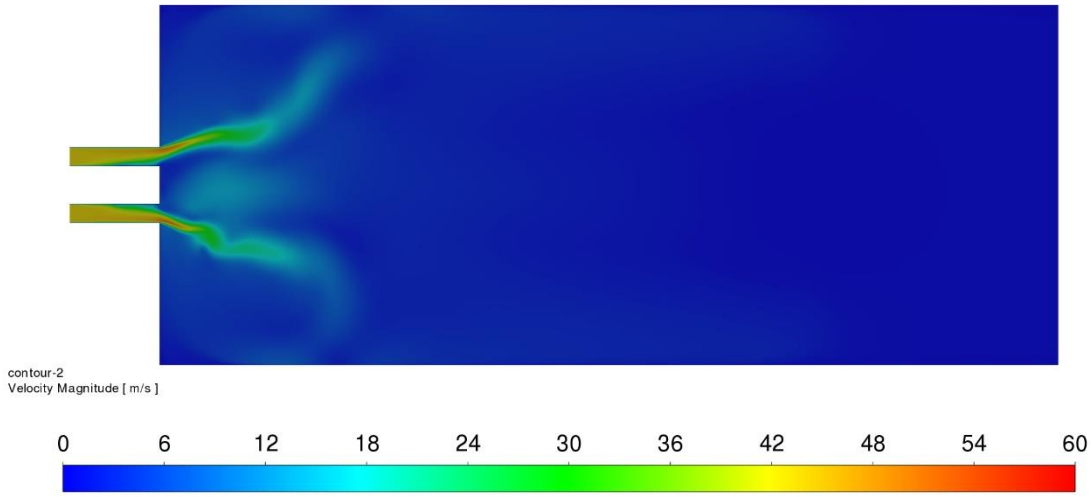

Figure 4.14 Instantaneous velocity magnitude at t = 0.2s (SST k-omega)

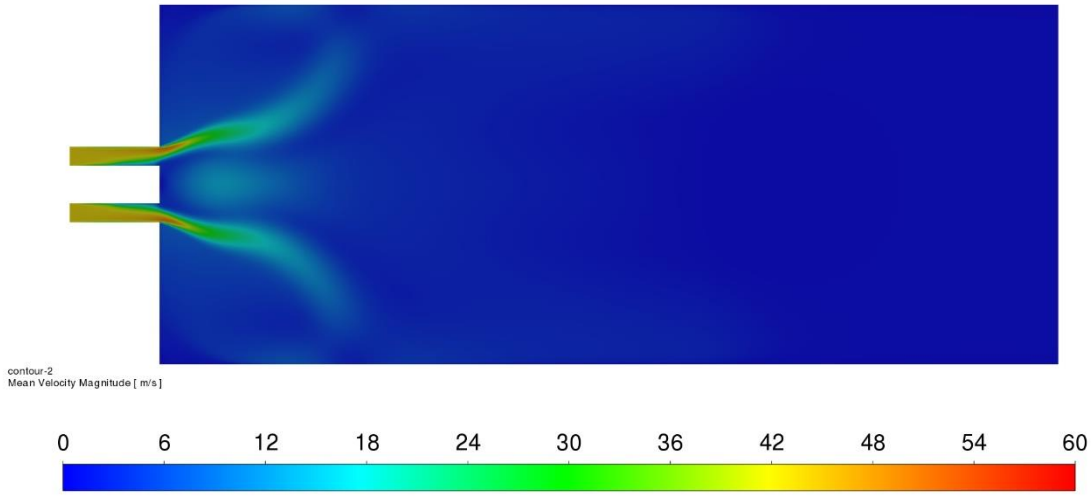

Figure 4.15 Time-averaged velocity magnitude (SST k-omega)

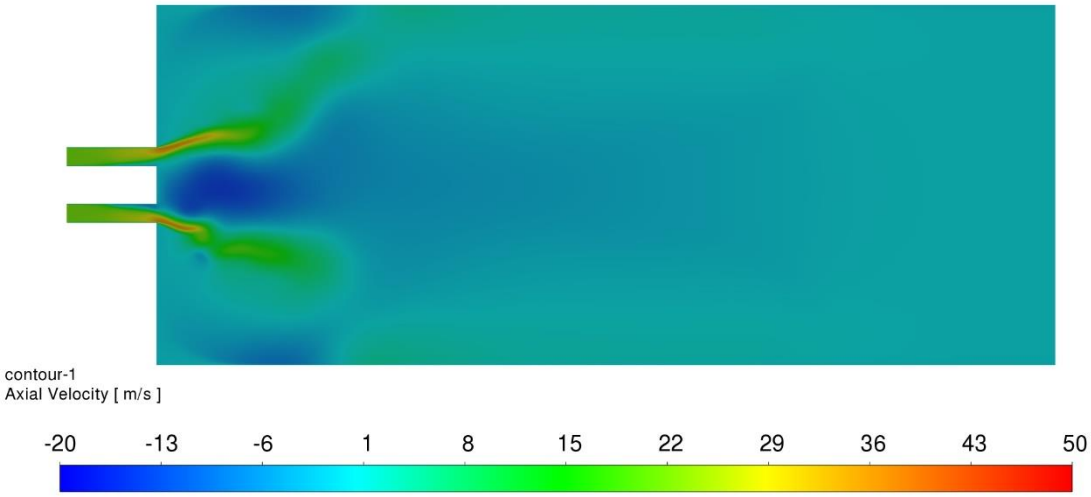

Figure 4.16 Instantaneous axial velocity at t = 0.2s (SST k-omega)

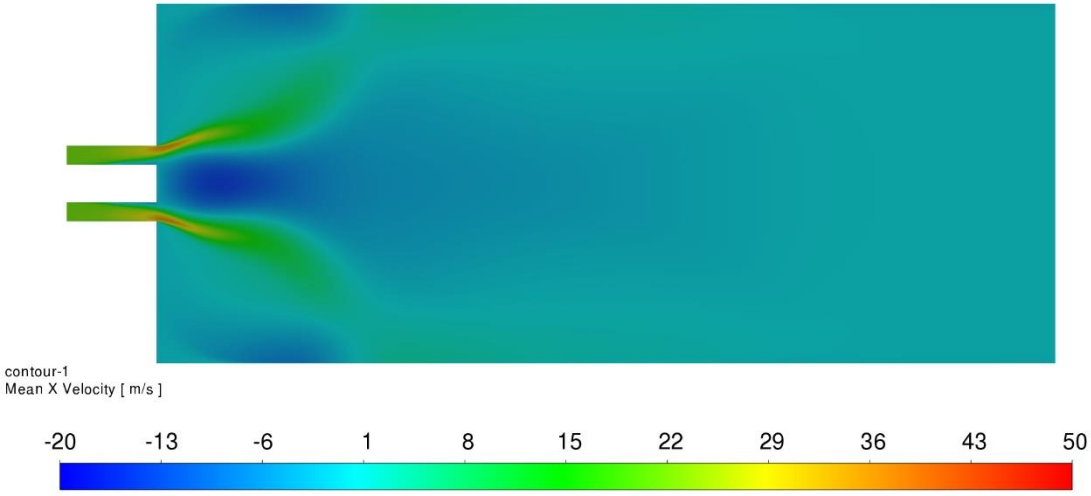

Figure 4.17 Time-averaged axial velocity (SST k-omega)

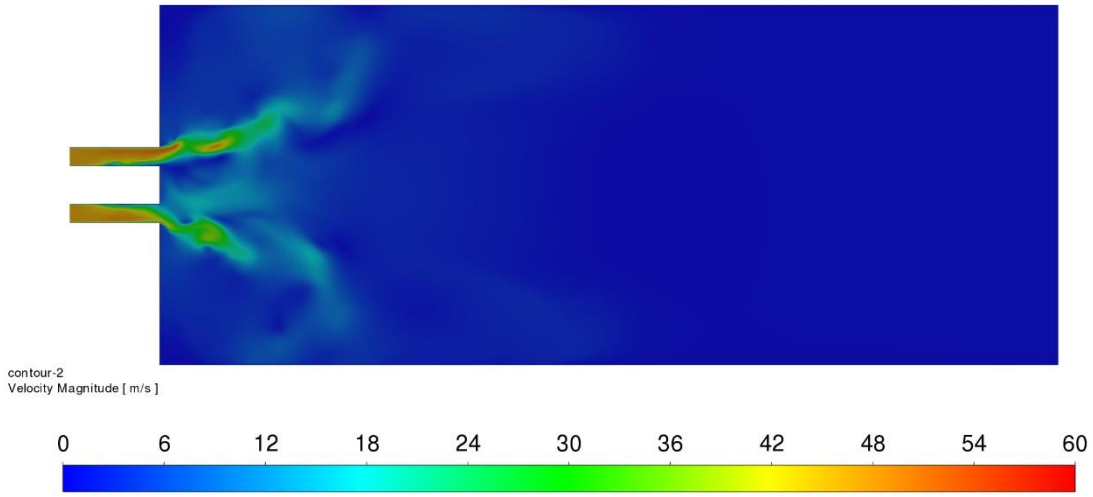

Figure 4.18 Instantaneous velocity magnitude at t = 0.2s (RSM-omega)

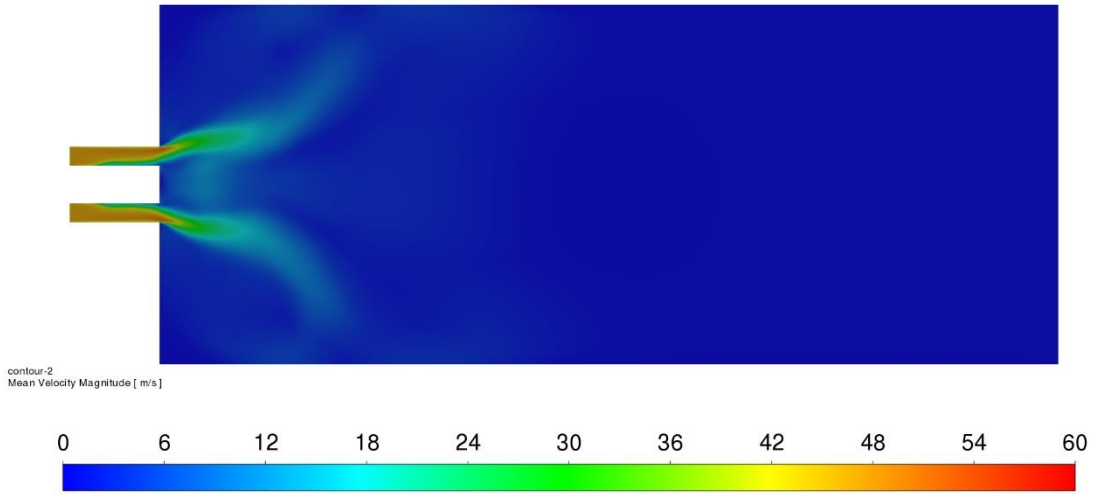

Figure 4.19 Time-averaged velocity magnitude (RSM-omega)

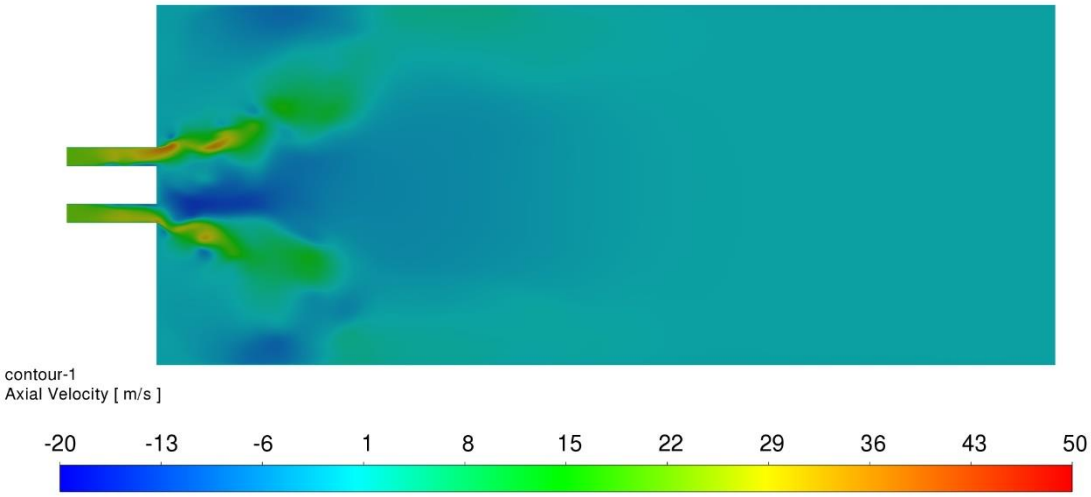

Figure 4.20 Instantaneous axial velocity at t = 0.2s (RSM-omega)

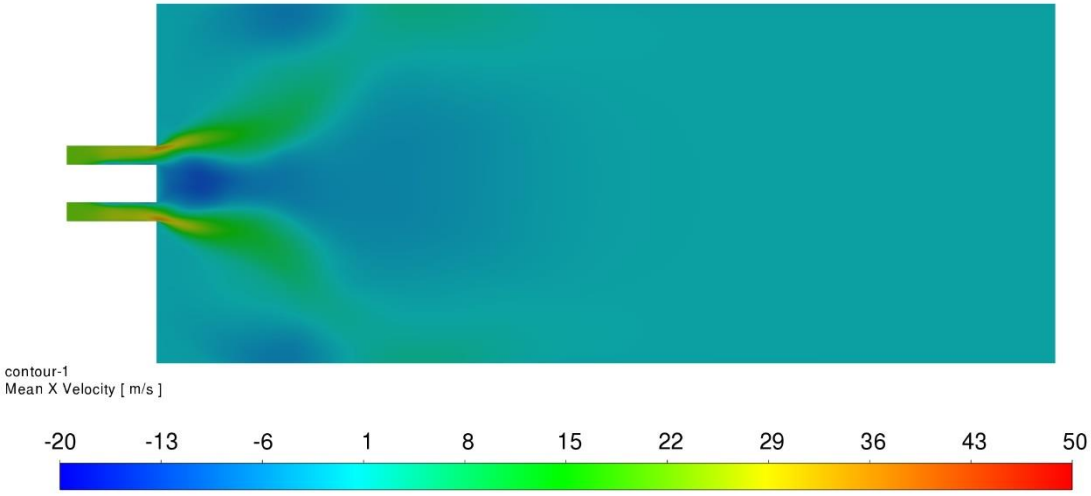

Figure 4.21 Time-averaged axial velocity (RSM-omega)

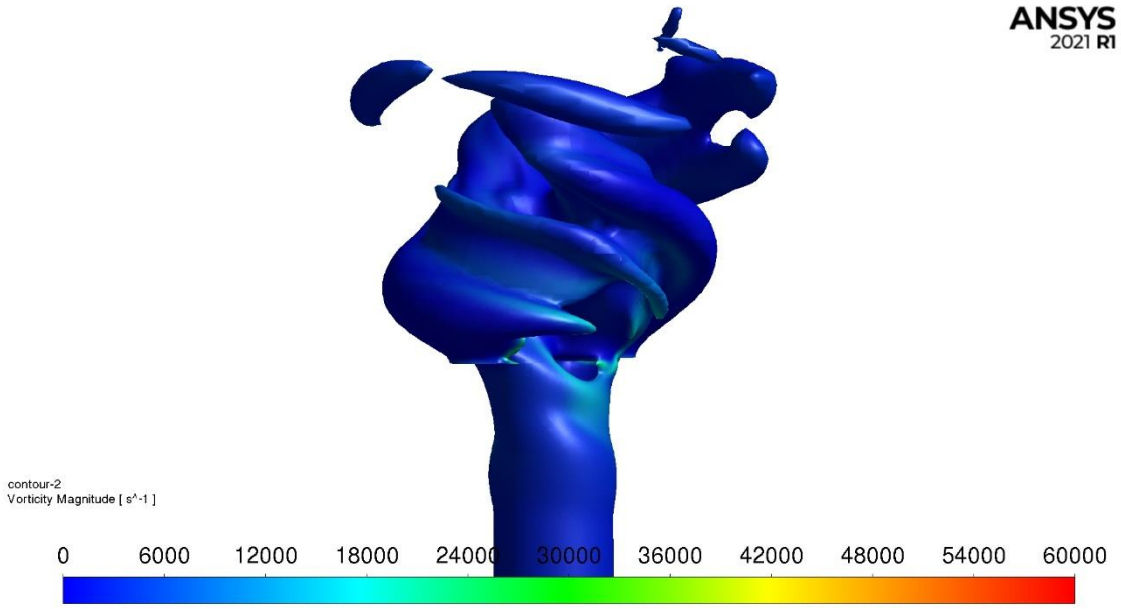

Figure 4.22 PVC visualisation (RSM-omega)

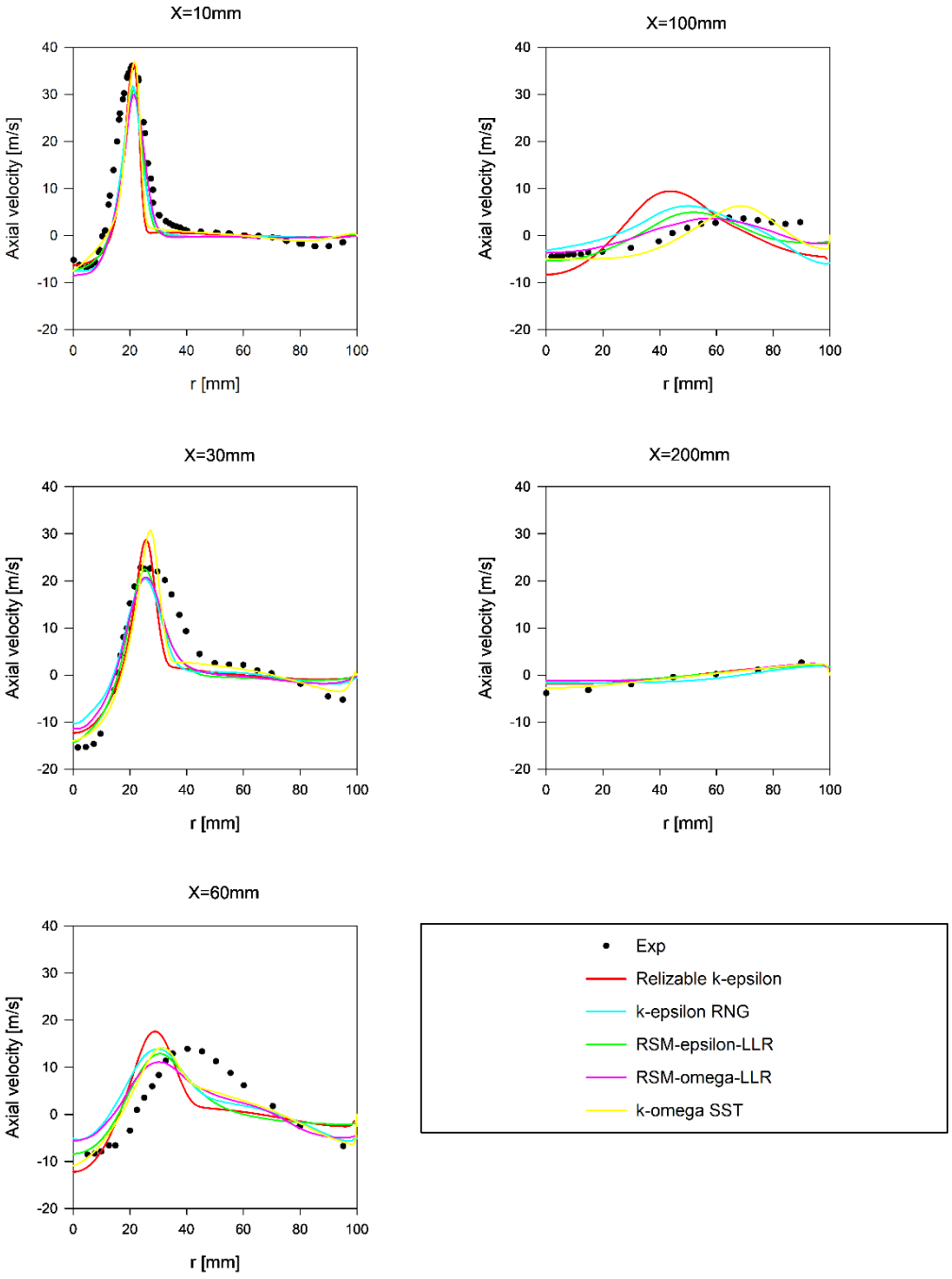

Figure 4.23 Axial velocity profiles in URANS

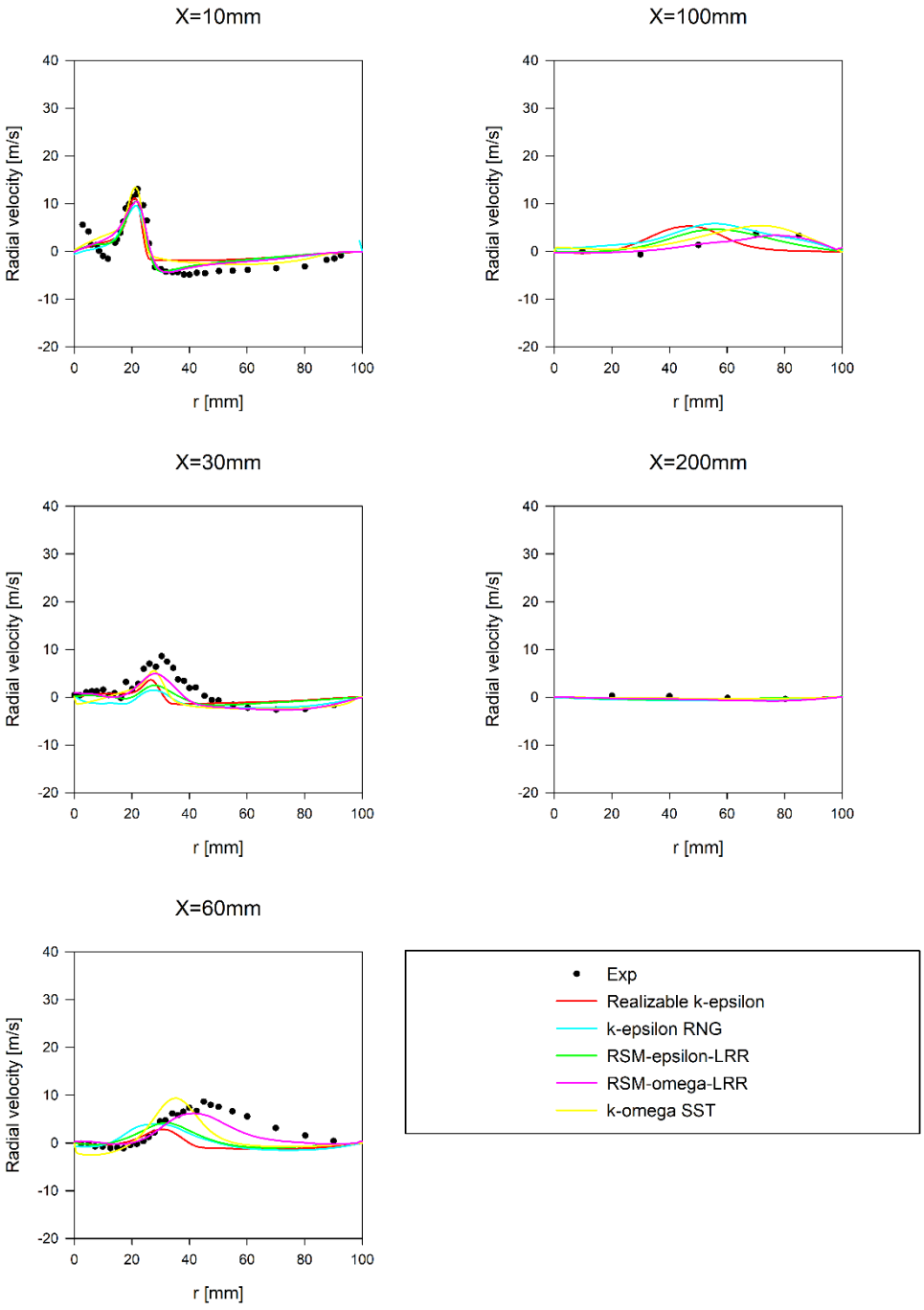

Figure 4.24 Radial velocity profiles in URANS

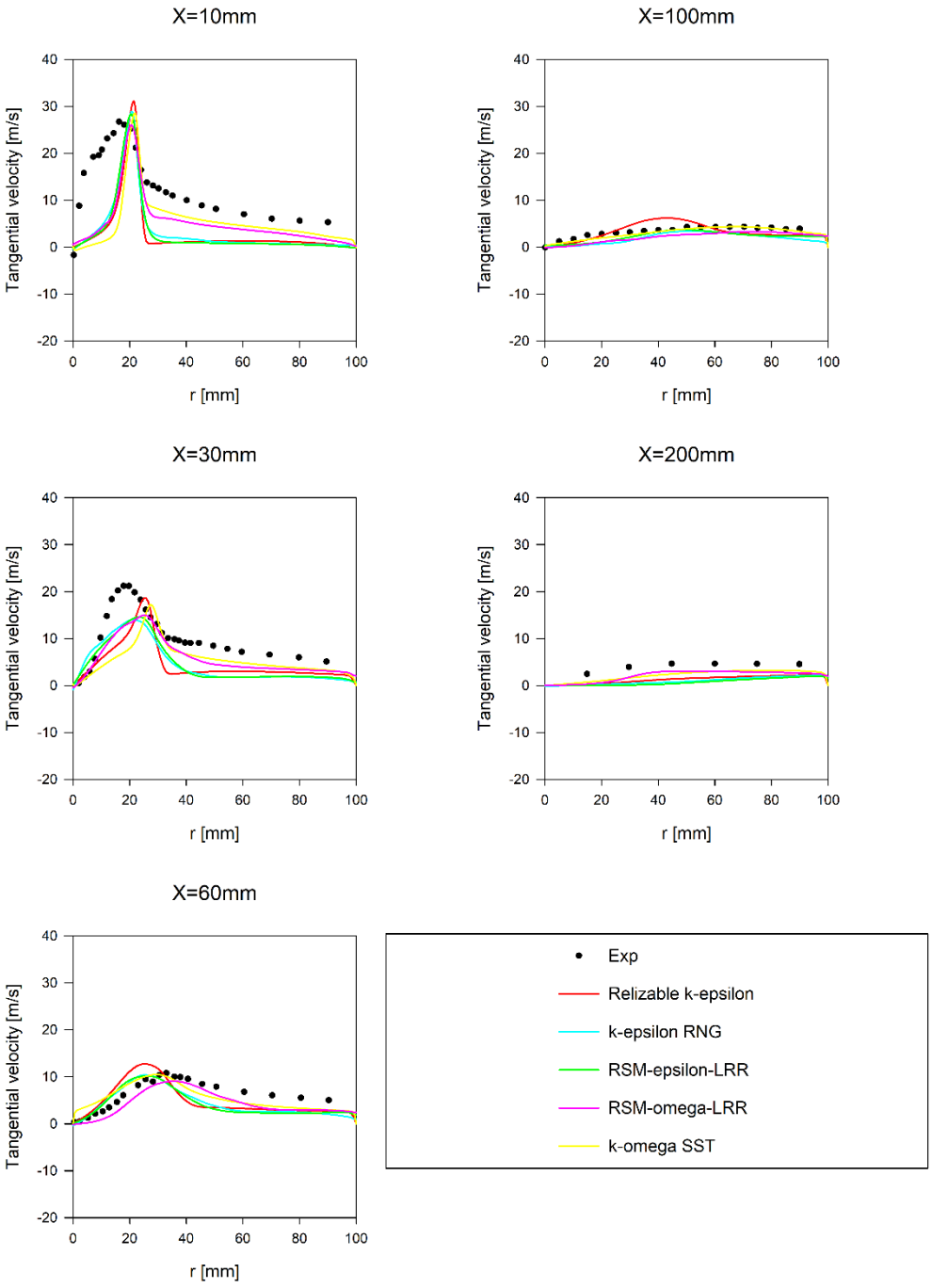

Figure 4.25 Tangential velocity profiles in URANS

4.7.3 Scale resolving simulation

Although all RANS models can be solved in an unsteady model (URANS), the first-generation URANS models do not provide any spectral content, even if the grid and time step size were sufficient for resolving the spectrum. This leads to the conclusion that this behaviour is a natural outcome of the RANS averaging procedure, typically time averaging, which eliminates all turbulence content from the velocity field. Therefore, a second-generation URANS model called scale-adaptive simulation and detached eddy simulation was used to perform the simulation and resolve the swirling flow fields in more detail.

Table 4.4 Boundary conditions for SRS

Axial velocity [m/s]	Tangential velocity [m/s]	Flow Reynolds number (at the annular channel)	Air viscosity [kg/(m · s)]	Air density [kg/m^3]
21.73	40.0	58559	1.846×10^{-5}	1.176

The results of SRS of SAS and DES family are presented in Figures 4.26 to 4.40. The instantaneous and time-averaged velocity magnitude and axial velocity are shown for all turbulence models. Three recirculation zones are

observed, namely the inner recirculation zone (IRZ) and two outer recirculation zones (ORZ), which are located at the top and bottom of the corners near the jet exit. Another typical flow feature in high swirl turbulent flows is vortex breakdown and precessing vortex core (PVC). The visualisation of a three-dimensional vortex can be obtained by setting a local minimum of the pressure [97]. An iso-surface of static pressure equal to -150 Pa was used for the visualisation of the PVC structure for all computed turbulence models. Figures 4.41, 4.42, and 4.43 show the comparison with the experimental results of axial, radial, and tangential velocity profiles, respectively. All three turbulence models outperformed RANS and URANS in capturing three velocity component profiles due to the capability of these three models to resolve at least part of the turbulent spectrum. In an axial direction of 100 mm downstream, SAS overpredicted the velocity profiles, whereas DES family models obtained good agreement against the experimental results. In radial direction, all three turbulence models underpredicted the profiles at 30 mm downstream. In the near field, none of the three models were able to reproduce the velocity decreases due to recirculation, and DDES-SST underpredicted the peak value. In tangential direction, at the near field, all three models failed to capture the velocity rises. At 30 mm downstream, the DDES-SST gave the closest peak value to the experimental results, and the other two models underpredicted the peak value.

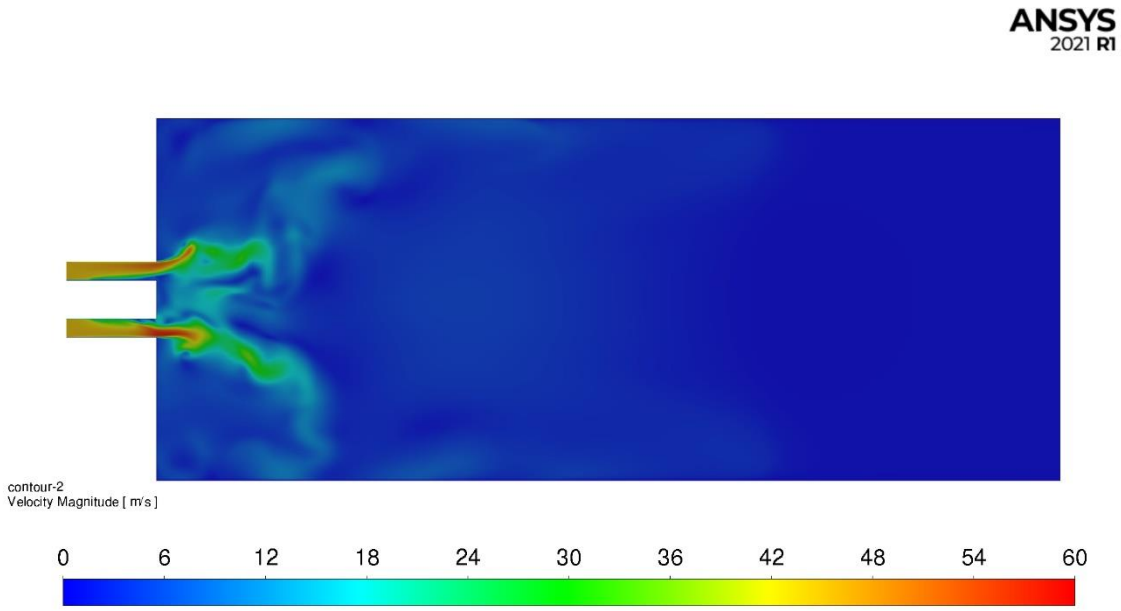

Figure 4.26 Instantaneous velocity magnitude at t = 0.2s (SAS-SST)

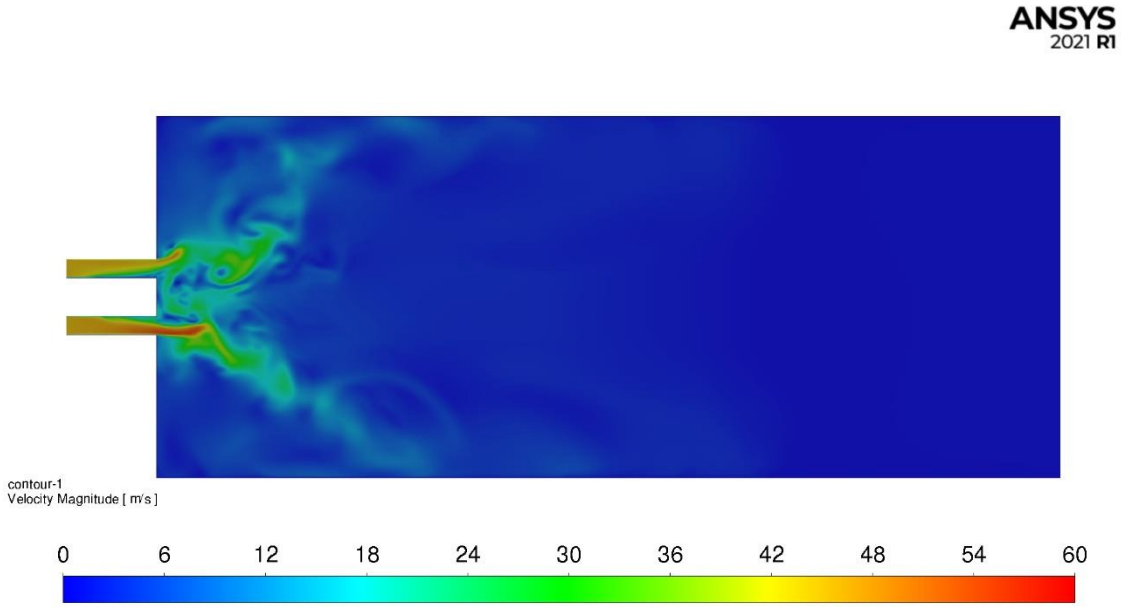

Figure 4.27 Instantaneous velocity magnitude at t = 0.2s (DDES-SST)

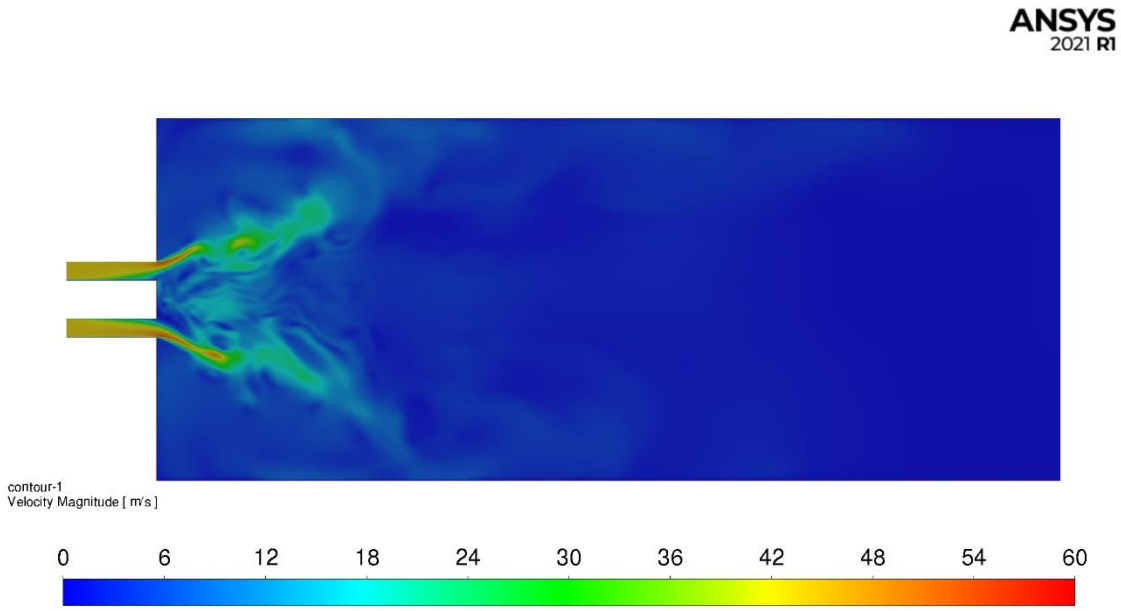

Figure 4.28 Instantaneous velocity magnitude at t = 0.25s (DDES-realizable k-epsilon)

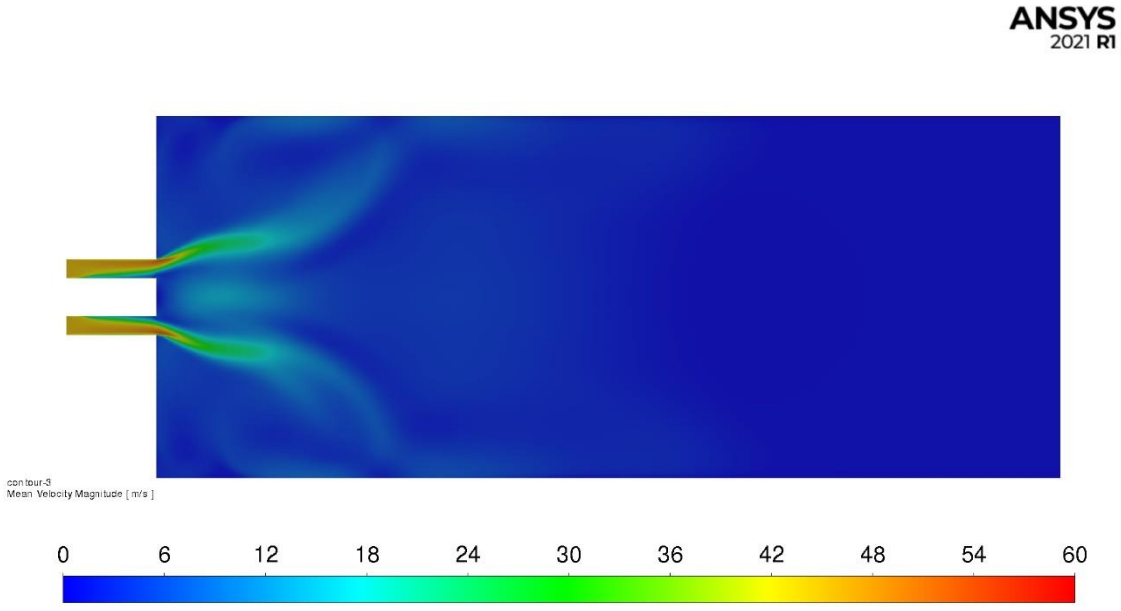

Figure 4.29 Time-averaged velocity magnitude (SAS-SST)

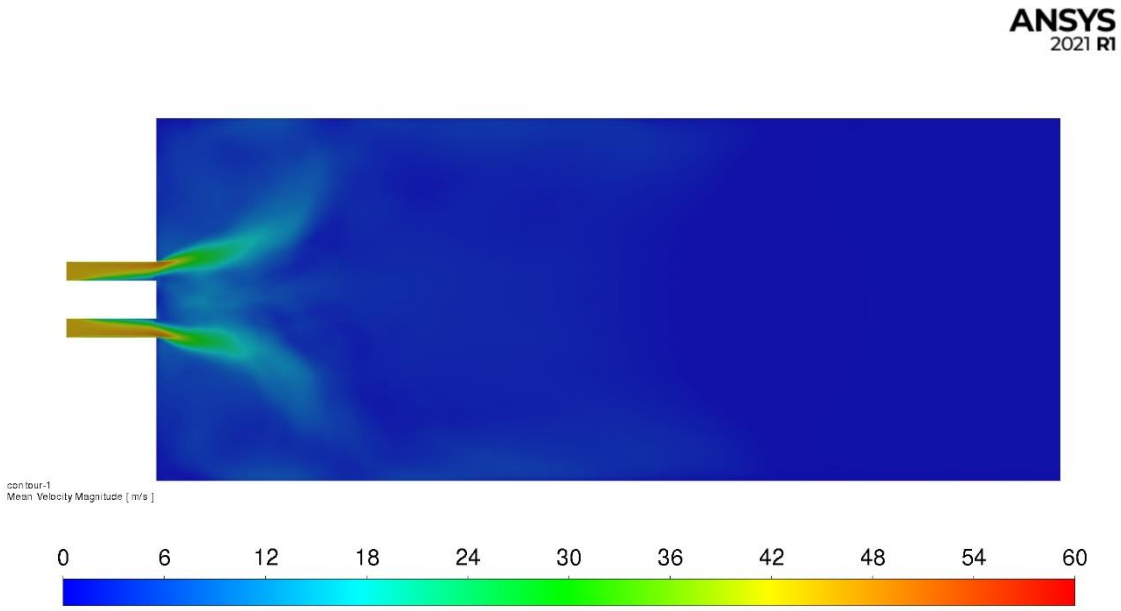

Figure 4.30 Time-averaged velocity magnitude (DDES-SST)

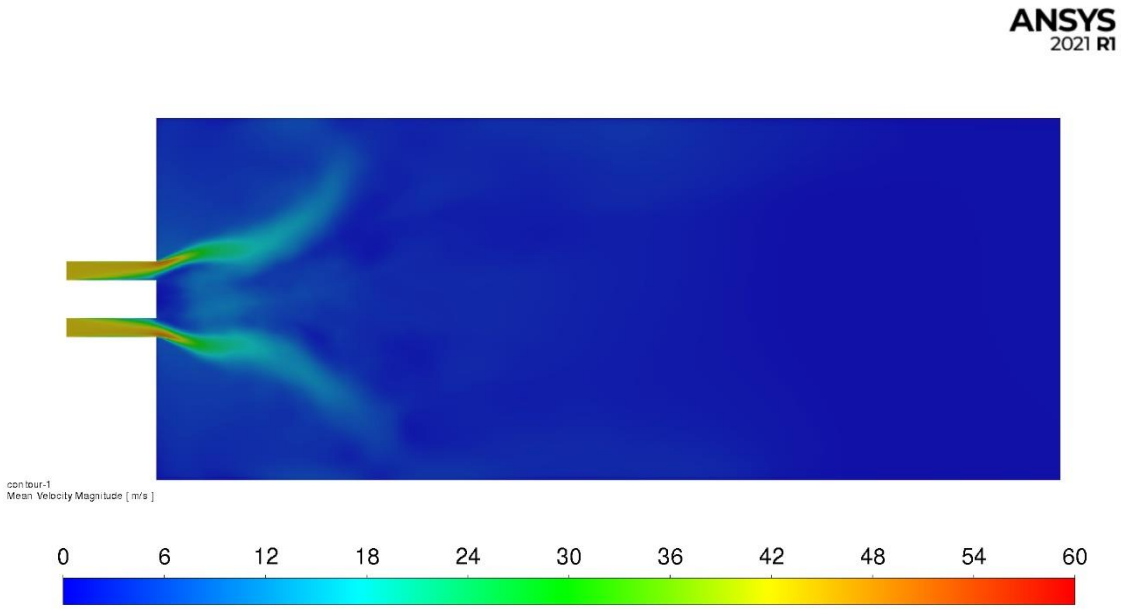

Figure 4.31 Time-averaged velocity magnitude (DDES-realizable k-epsilon)

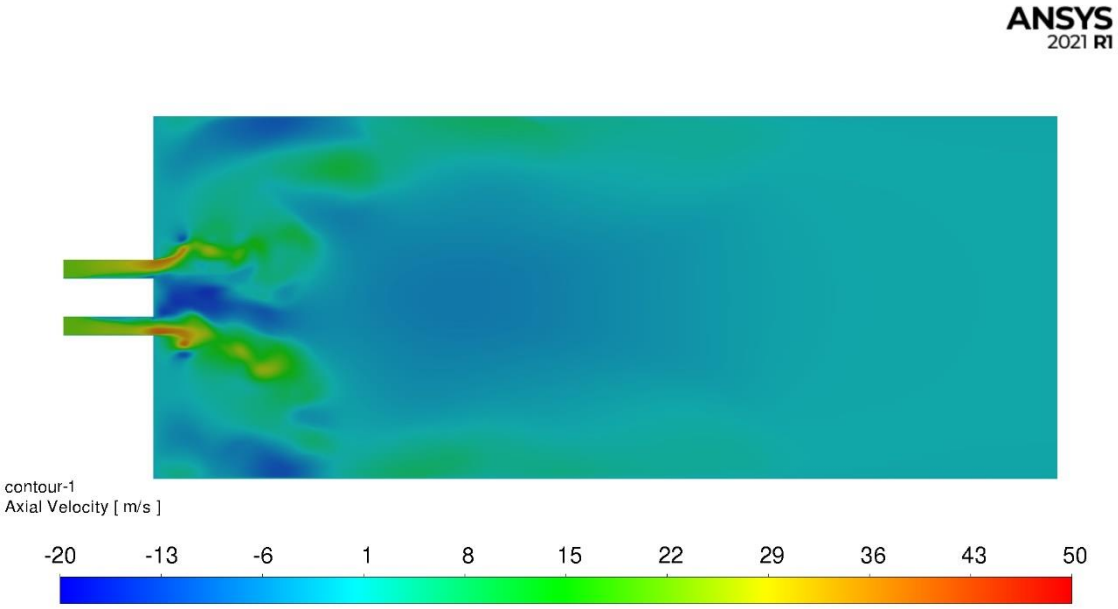

Figure 4.32 Instantaneous axial velocity at t = 0.2s (SAS-SST)

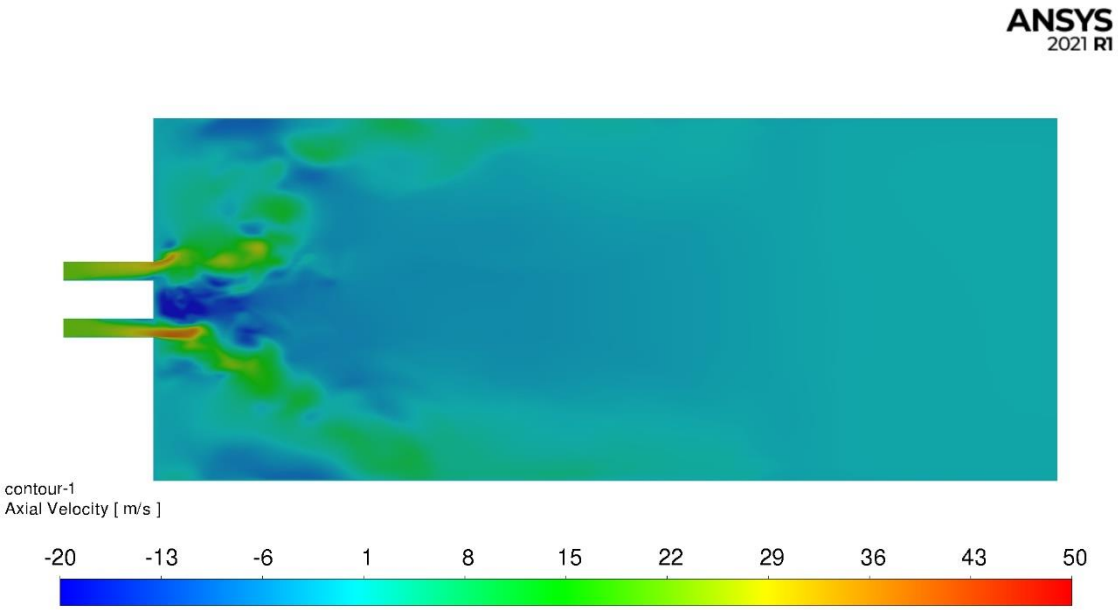

Figure 4.33 Instantaneous axial velocity at t = 0.2s (DDES-SST)

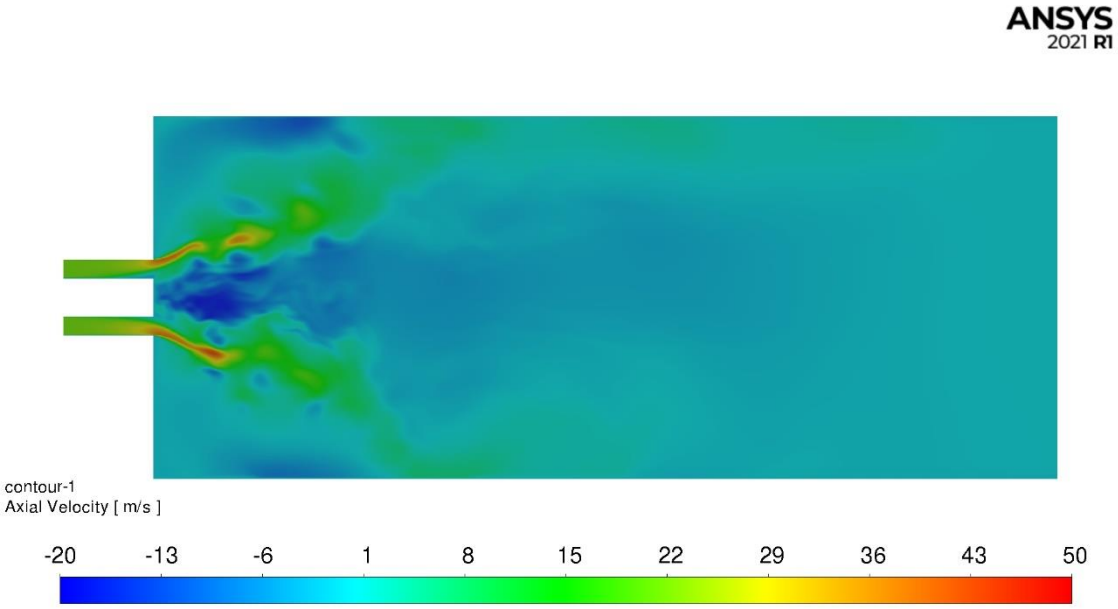

Figure 4.34 Instantaneous axial velocity at t = 0.25s (DDES-realizable k-epsilon)

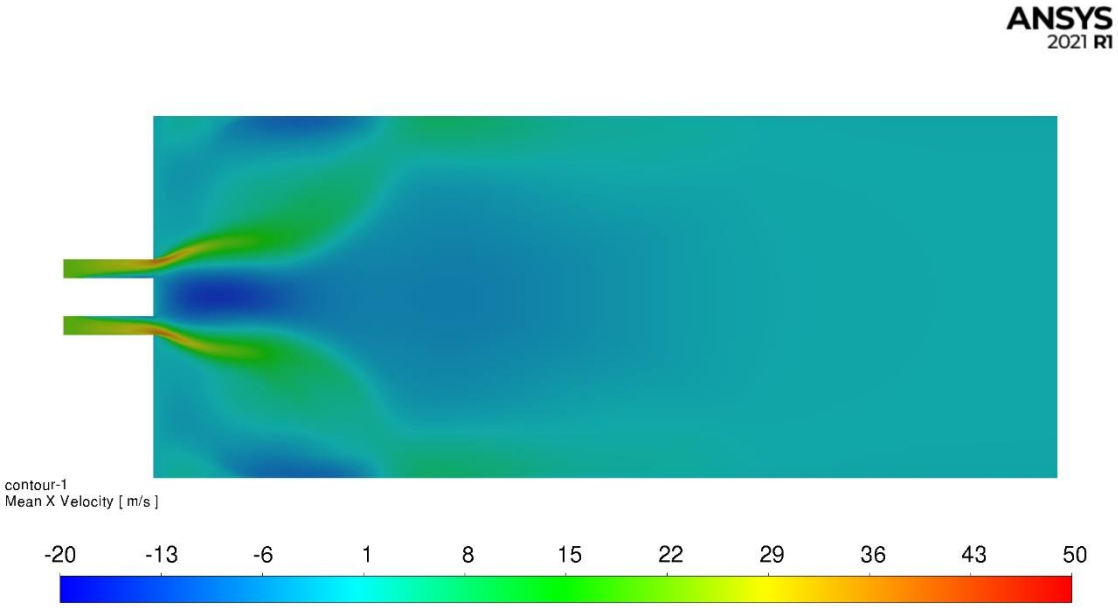

Figure 4.35 Time-averaged axial velocity (SAS-SST)

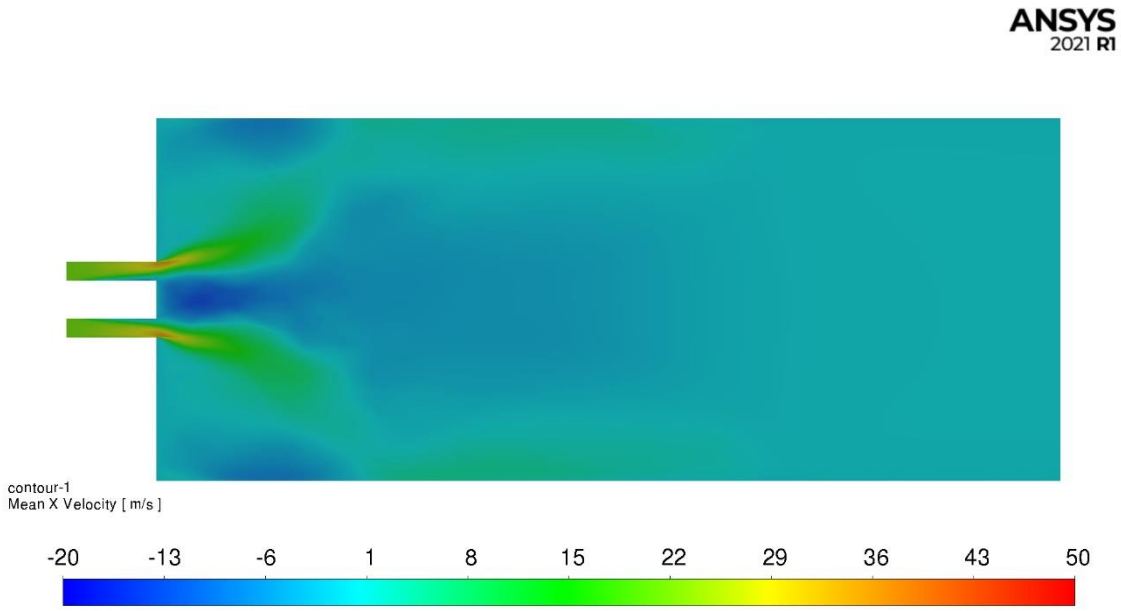

Figure 4.36 Time-averaged axial velocity (DDES-SST)

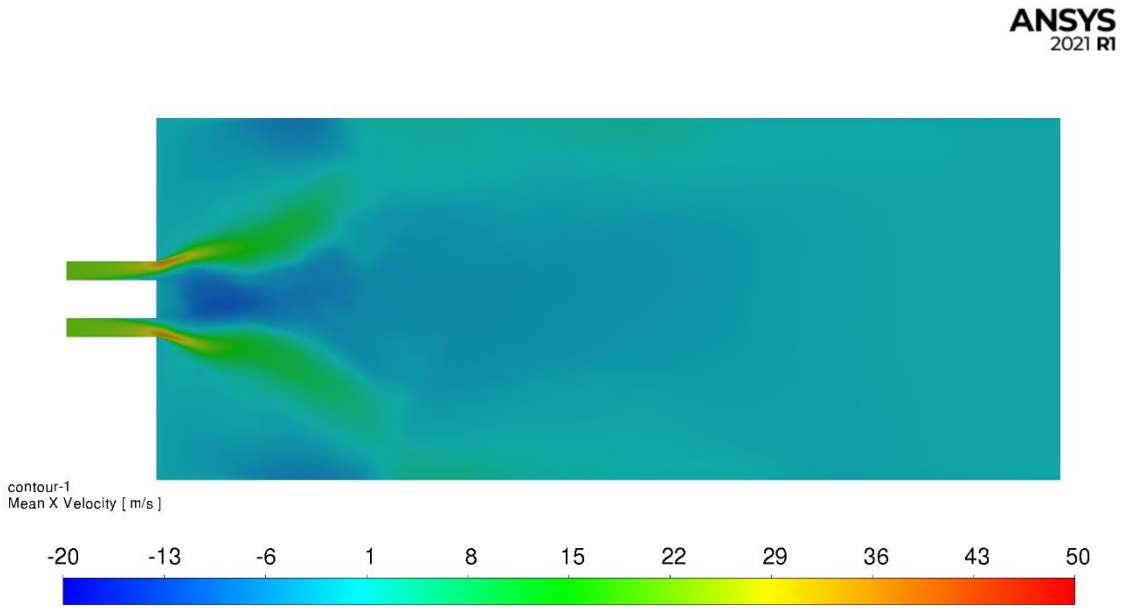

Figure 4.37 Time-averaged axial velocity (DDES-realizable k-epsilon)

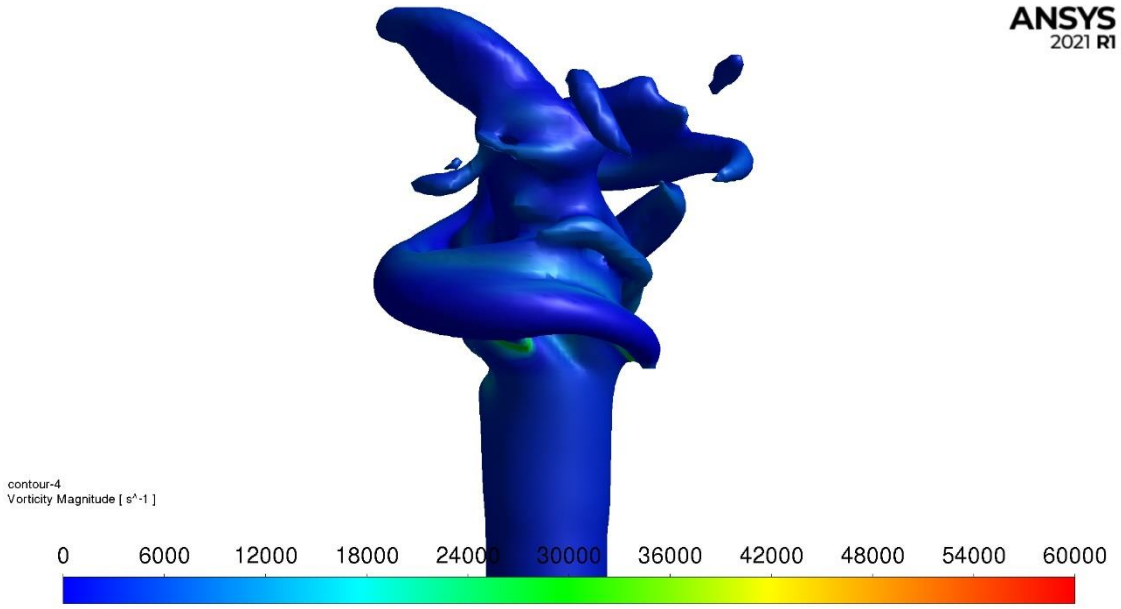

Figure 4.38 PVC visualisation coloured by vorticity magnitude (SAS-SST)

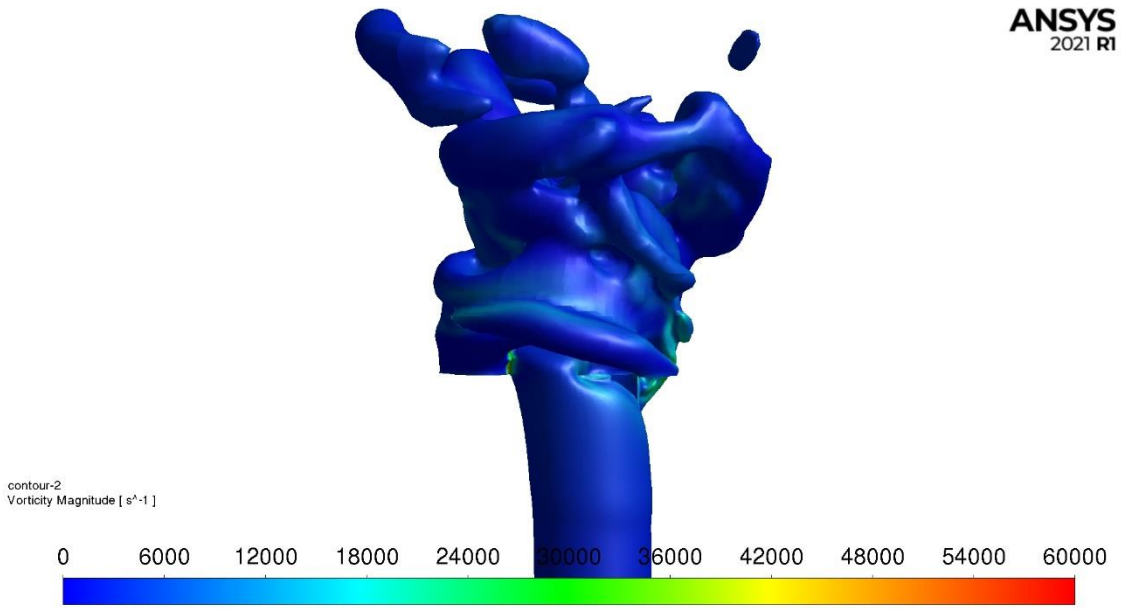

Figure 4.39 PVC visualisation coloured by vorticity magnitude (DDES-SST)

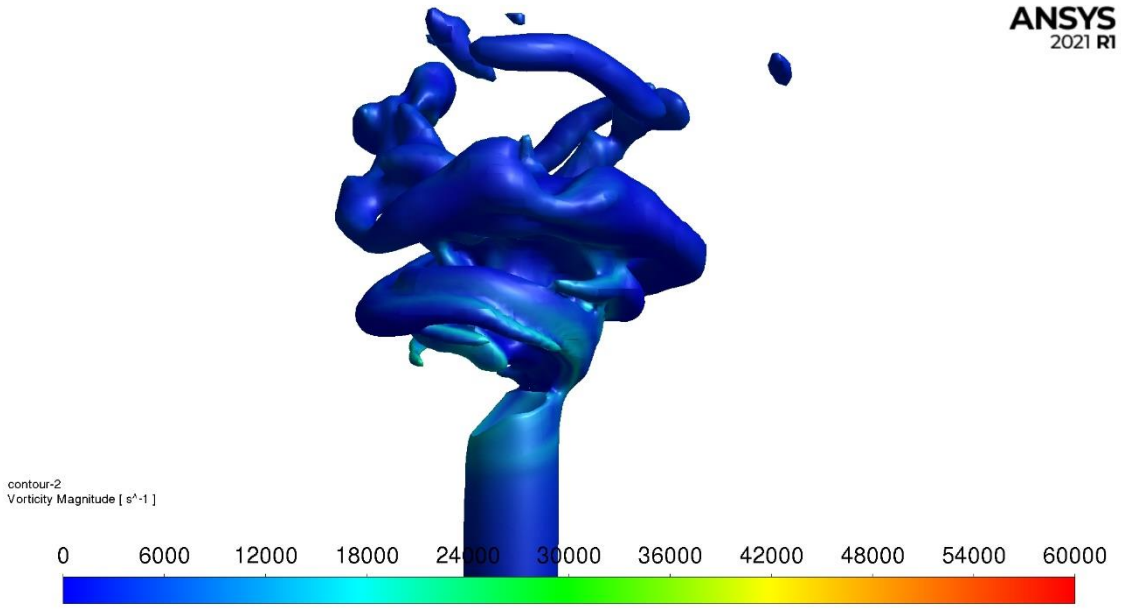

Figure 4.40 PVC visualisation coloured by vorticity magnitude (DDES-realizable k-epsilon)

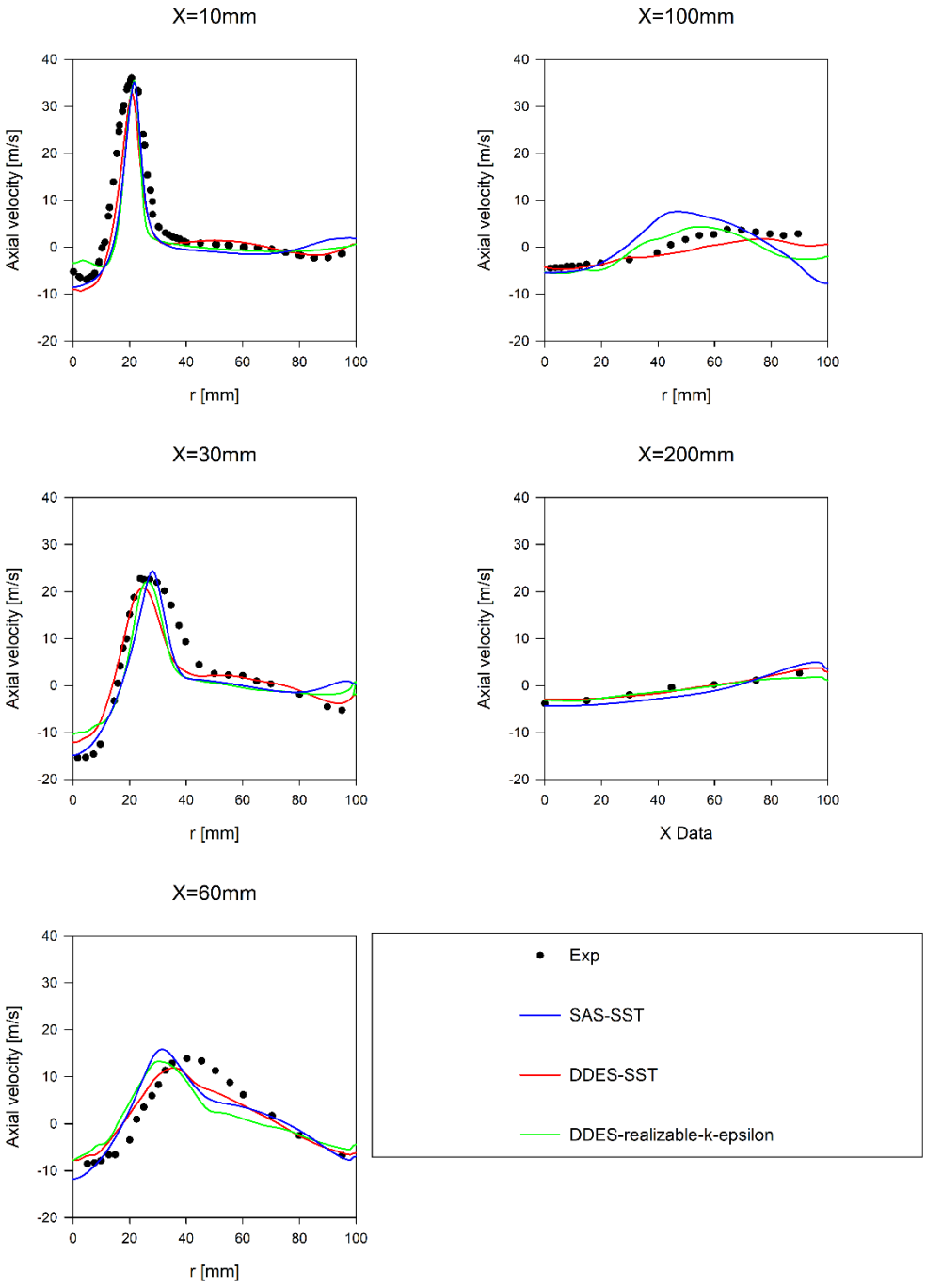

Figure 4.41 Axial velocity profiles (SRS)

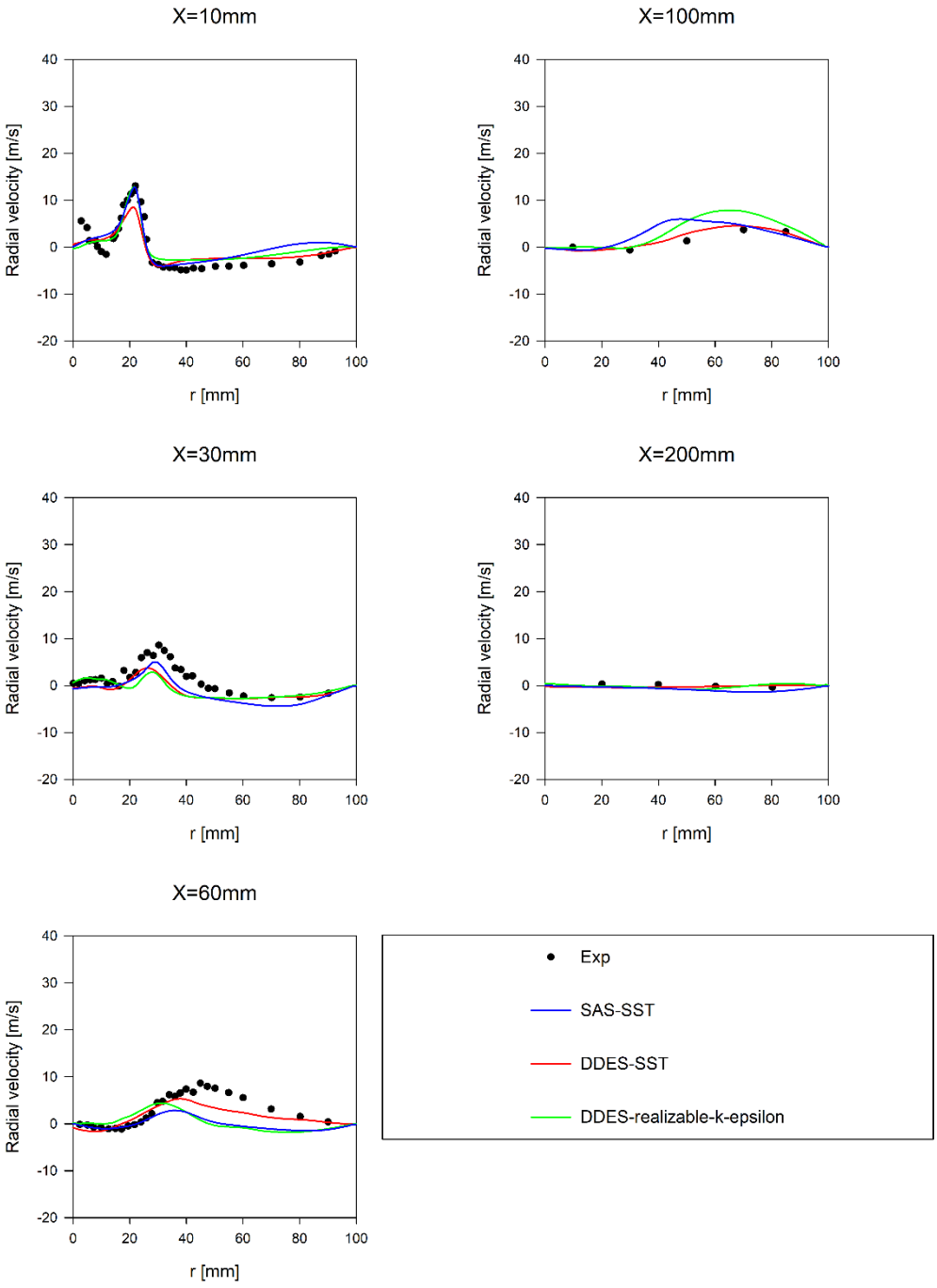

Figure 4.42 Radial velocity profiles (SRS)

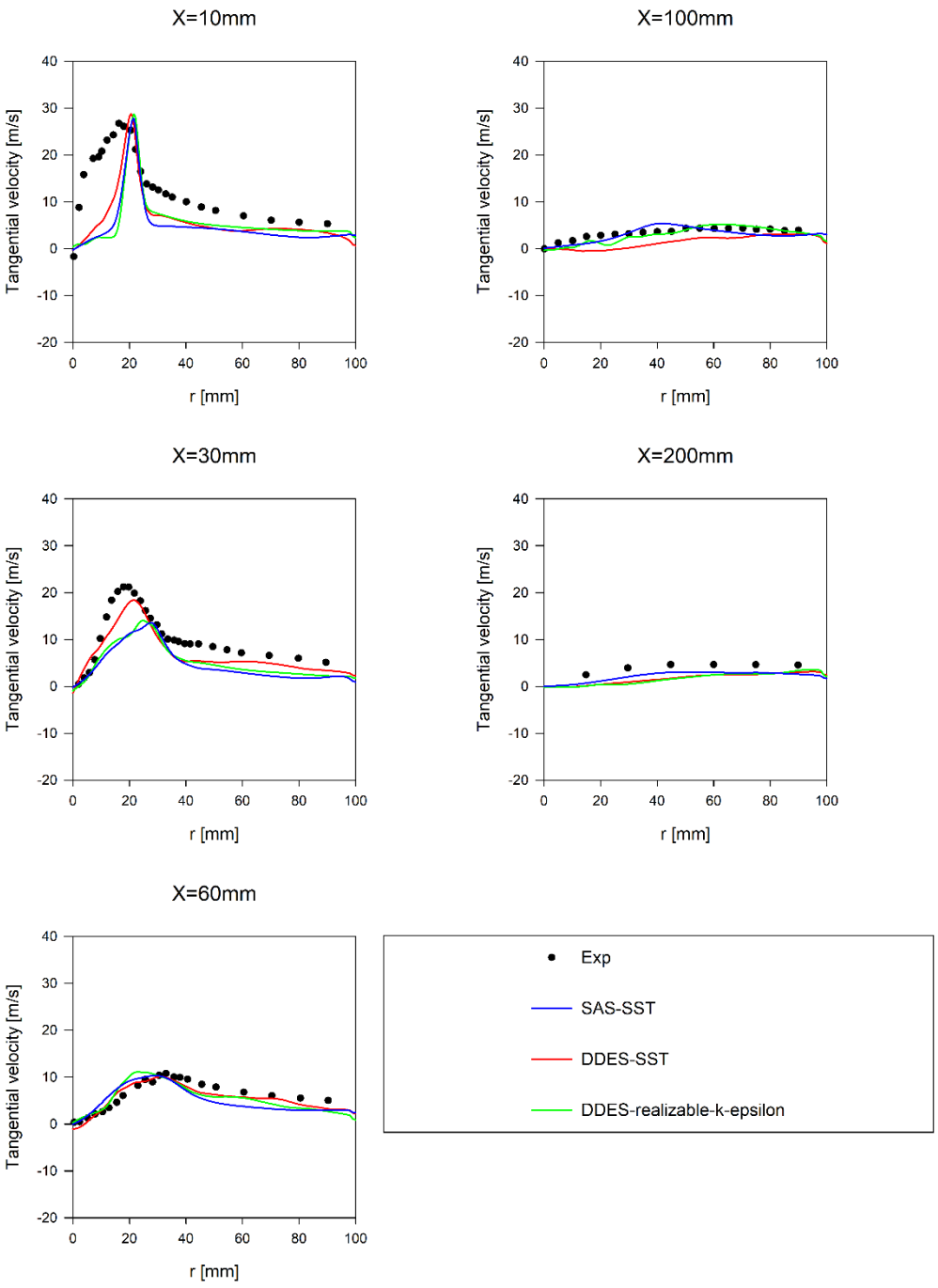

Figure 4.43 Tangential velocity profiles (SRS)

4.8 Summary

Five different turbulence models for simulating isothermal flow studies were simulated. In this chapter, the CFD results for each turbulence model were compared with time-averaged experimental measurements in terms of three components' velocity profiles and temperature profiles. The experimental configuration is relatively simple, but swirling flow physics is complicated. Comparing the experimental results in Figure 4.11, from the plot in the axial distance of 10 mm, the axial velocity profiles flattened out from radius 0 to 20 mm and failed to capture the profiles with a curvature in axial velocity. The steady-state RANS models were not able to capture the inherently unsteady features of the complex swirling flows that are typically used in gas turbine combustors for flame stabilisation mechanisms. Hence, unsteady RANS and scale resolving simulations were used to investigate the performance in capturing swirling flow dynamics. URANS and SRS showed better accuracy in capturing the flow physics, but the computational cost increased significantly. Both the URANS and SRS models showed reasonable agreement in mean velocity profiles in axial, radial, and tangential directions. The precessing vortex core (PVC) structure can only be observed by employing unsteady simulations. Chapter 5 will show the reacting flow results for the same burner configuration. Chapter 6 will present the combustor design and reacting flow simulation results to aid the design using the modelling approaches in both Chapters 4 and 5.

Chapter 5 Computational Investigation of Turbulent Spray Flame in a Swirl-stabilised Burner

5.1 Introduction

In this chapter, the three-dimensional (3D) reacting turbulent two-phase flow field of a scaled swirl-stabilised burner is investigated. The isothermal case with the same burner for the code validation study was done in Chapter 4. Reynolds-averaged Navier–Stokes (RANS) was used to perform the simulation as it is a reasonable trade-off between accuracy of results and computational cost, especially when applied to the initial design phase when many design iterations are required to obtain a reasonable flow field and temperature field. Two different single-component fuel surrogates were used for diesel fuel (n-dodecane) and jet-A1 (POSF1035). In addition, local chemical non-equilibrium effects were modelled by turbulent strain to cause flame stretching.

5.2 Background

Turbulent spray flames are widely used in devices that convert energy and combustion systems. Liquid fuel is first injected from a fuel injection process; atomisation occurs to form a fine spray directly into a turbulent environment where fuel liquid evaporates into fuel vapour. Swirling flows with strong recirculation zones are used to anchor the flame as well as to improve the evaporation rate and mixing effects between fuel and oxidiser. The flame thickness is a scale of millimetres and is often larger than the droplet diameter, which is a scale of microns. The description of the complex interactions of the gas phase turbulence, the atomisation, the spray interactions, and the chemical reaction has motivated the investigation of numerical studies of turbulent combustion.

The computational study of turbulent spray flames using a flamelet-generated manifold (FGM) with the Eulerian–Lagrangian (E–L) approach has been widely used in the literature to simulate lab-scale burners as well as realistic gas turbine combustors [98–100].

The ECN Spray A flame was simulated using LES and the n-dodecane skeletal mechanism developed by Yao et al. [101] as a diesel surrogate by Ong et al. [102]. The Largrangian particle tracking method was applied with the primary atomisation approximated by the Rosin–Rammler size distribution. The Ranz–Marshall correlation was employed to account for the droplet evaporation and heat transfer between the droplet phase and

the surrounding gas phase. The grid sensitivity suggests that the minimum grid size is a 0.1875 mm uniform grid as the coarse grid in simulating ECN spray A. Two Jet A turbulent spray flames at equivalence ratios of 0.55 and 0.47 were investigated experimentally, and a V-shape hollow cone spray was found in the lower air flow rate case [103]. A steady flamelet model and a flamelet-progress variable approach for spray combustion were investigated by a 2-D DNS [104]. The diffusion flame was dominant in the gaseous jet flame, whereas diffusion and premixed flames coexisted in the spray jet flame; therefore, a partially premixed combustion model was necessary for simulating the spray flame.

An accurate simulation of chemically reacting spray flames under reasonable computational time and resources is necessary for combustor designers. The present chapter discusses the steady-state RANS simulation of kerosene spray combustion in a swirl-stabilised combustor, which was validated by the experimental results. The experiment used kerosene and Jet A fuel, which is commonly used in aviation practical applications. As diesel fuel is very similar to kerosene fuel in the form of a molecular structure and lower heating value, the hychem (hybrid chemistry) scheme, which is designed for modelling kerosene, and the n-dodecane scheme, which is widely used in modelling diesel fuel, were tested to assess the capability of n-dodecane scheme as a unified scheme in using CFD to assist the design of the combustor, which has a fuel flexibility feature.

5.3 Computational methodology

The computational methodology applied in this section can reproduce the reasonable velocity components and temperature distribution across five different axial directions of the burner. Flame A from the experiment was studied. The operation conditions of the burner are listed in Table 1 below.

Table 5.1 Flame A operation conditions

Operating pressure [bar]	1
Inlet temperature [K]	300
Air mass flow rate [g/s]	26.51
Fuel flow rate [g/s]	0.951
Air-to-fuel ratio (AFR)	27.88

The fuel injector placed in the middle of the front plate with an orifice diameter of 0.25mm injected liquid kerosene into the central recirculation zone. The air and liquid were not preheated, and the temperature was set to 300 K. The injector spray pattern has been reported in the literature to produce a fine hollow cone spray shape and injection velocity of 30 m/s [90]. The discrete phase was modelled as discrete parcels, and the motion of the parcels was described using the Lagrangian particle tracking method. Each parcel was considered representative of a group of spherical droplets with similar position, size, and physical properties. The primary breakup was

modelled by injecting the parcels using the Rosin–Rammler size distribution function of size ranging from 1 micron to 100 microns. This wide injection angle enhances the rates of heat and mass transfer, as most of the droplets are injected in a hollow cone shape with 80°. The spray is assumed to be dilute (the volume fraction is less than 10^{-6}), spherical shape droplets and single-component droplets. The droplet interactions, such as breakup and coalescence, are not taken into consideration to reduce the computational time.

The flamelet-generated manifold approach was used to model the turbulence–chemistry interaction. A non-adiabatic version of the diffusion flamelet was generated in CHEMKIN software. A five-dimensional table of parameters – mean mixture fraction ($\tilde{f}$), mixture fraction variance ($\widetilde{f''}$) , mean progress variable ($\tilde{c}$), progress variable variance ($\widetilde{c''}$), and mean enthalpy ($\tilde{h}$) – considered the effect of the heat loss caused by the latent heat of spray vaporisation. The unity Lewis number assumption was used in solving the flamelet equations in the mixture fraction space. The ignition procedure is simplified to patch the progress variable of 1 in the flame region. The progress variable is defined as follows [105]:

$$c = \frac{Y_{CO} + Y_{CO_2}}{Y_{CO}^{eq} + Y_{CO_2}^{eq}} \tag{5.1}$$

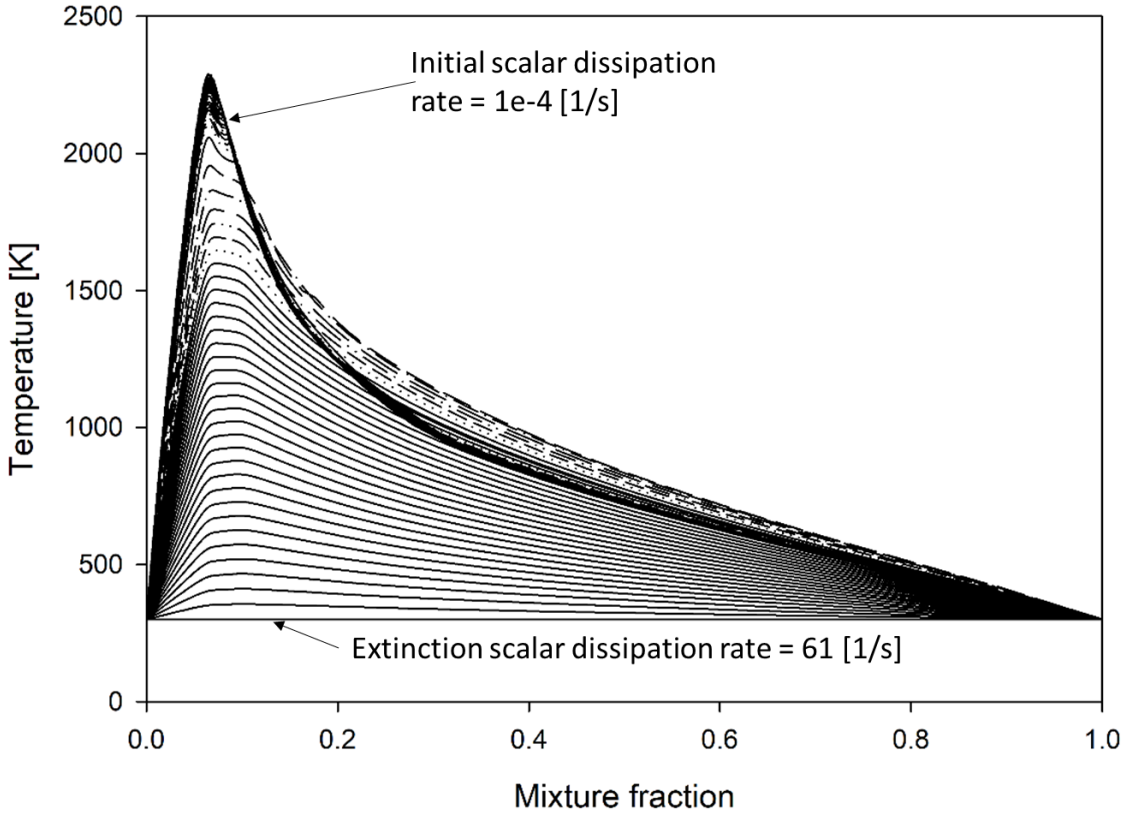

Figure 5.1 Temperature distribution in mixture fraction space

The level of scalar dissipation rate at which the flame extinguished due to the aerodynamic strain was computed as 61 1/s. The initial scalar dissipation rate was set at 1E-4 1/s, then the scalar dissipation rate was increased progressively until the extinction scalar dissipation rate. A total of 64 flamelets were calculated to capture the ignition-extinction S-curve limit.

5.4 Chemical kinetics

A 54-species skeletal mechanism with 269 reactions was developed to predict pyrolysis and oxidation of n-dodecane as a diesel fuel surrogate involving both high and low temperature conditions [101]. The mechanism was validated against Spray A from the engine combustion network (ECN) in simulating a three-dimensional turbulent spray flame at compression ignition engine conditions [101]. An LES investigation of turbulent swirling spray flames using n-dodecane showed that the results with low-temperature chemistry (LTC) were more representative where spray flame interactions were most significant, and heat release was shown to be significant in the spray flame [106].

A 48-species skeletal mechanism with negative temperature chemistry (NTC) behaviour called the HyChem approach [107] was developed to model real Jet A fuel. The approach assumes that the mono-component fuel surrogate first decomposes into small molecules via a reduced set of pyrolysis reactions, and then the products undergo an oxidation process. Both n-dodecane and HyChem applied the skeletal reduction technique to remove unimportant species, thereby eliminating stiffness. The comparison between detailed chemistry and the skeletal mechanism are shown in Figures 5.2 and 5.3. The results show that the skeletal scheme provides reasonable unstrained laminar flame speed over a wide range of mixture fractions.

The n-dodecane skeletal mechanism and the HyChem skeletal scheme for kerosene were developed covering a pressure of 1-80 bar, equivalence ratio of 0.5-2.0, and initial temperature of 800-1600K [101], [107].

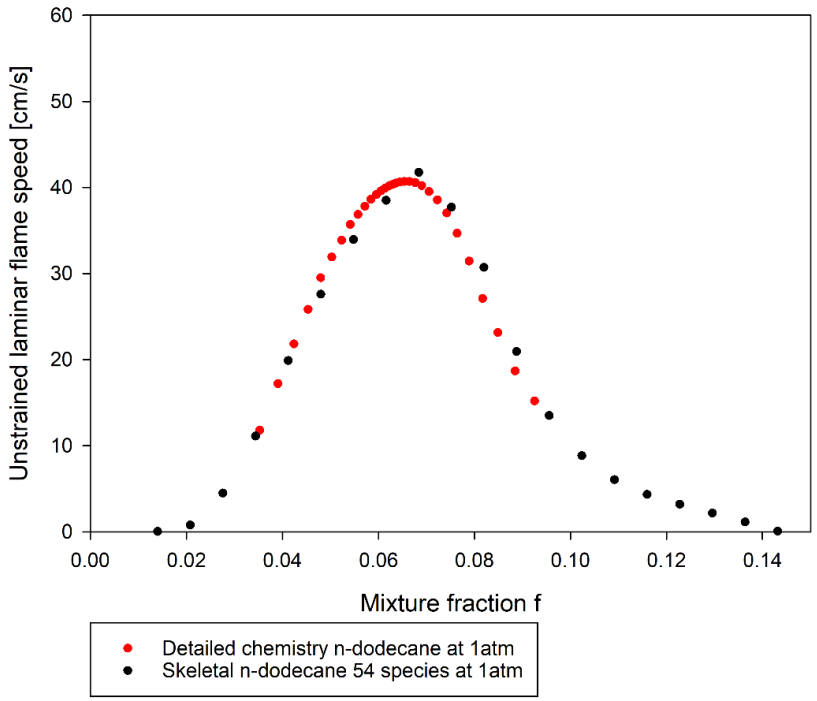

Figure 5.2 nC12H26 unstrained laminar flame speed comparison

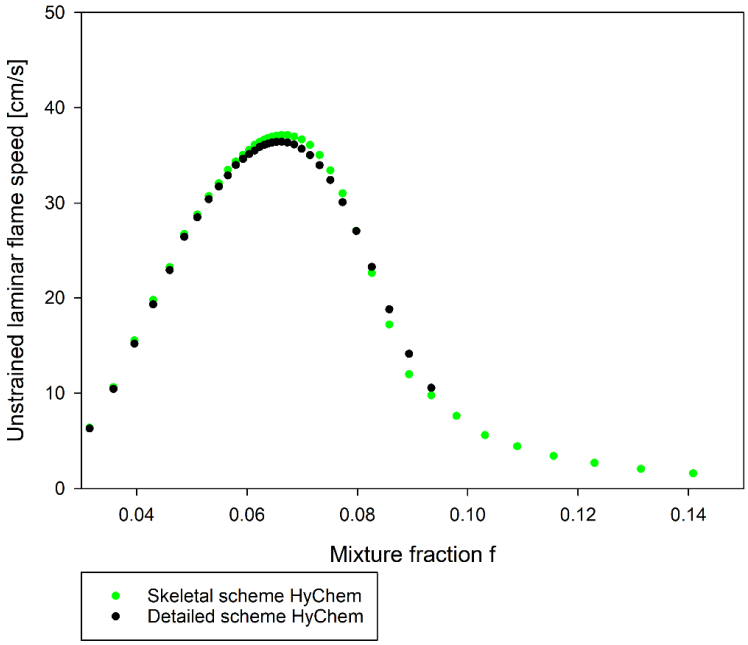

Figure 5.3 HyChem unstrained laminar flame speed comparison

5.5 Boundary conditions and meshes

The boundary conditions used were the same as the isothermal case discussed in Chapter 4, except the boundary conditions of spray and partially premixed combustion model parameters.

The spray boundary conditions are tabulated in Table 5.2.

Table 5.2 Spray boundary conditions

Injection type	Hollow cone
Injection velocity [m/s]	30
Cone angle [degree]	40
Fuel mass flow rate [g/s]	0.951
Primary atomisation model	Rosin–Rammler distribution
Minimum diameter [mm]	0.001
SMD [mm]	0.05
Maximum diameter [mm]	0.1
Spread parameter	3.5
Drag model	Spherical droplet

The liquid fuel properties of Jet A-1 kerosene used are reported in [108]. The physical properties are valid at 298.15 K and 1 bar. The properties of density and specific heat capacity are given in a range from 220 K to 684 K.

The meshes and results from Chapter 4 were used in this chapter. The converged steady-state cold flow solution was used as the initial condition in this chapter.

5.6 Results

Figures 5.4 to 5.15 show velocity magnitude, axial velocity, temperature, and mass fraction of the important species contour computed by steady-state RANS with a poly-dispersed spray and using the same grid from Chapter 4. The characteristics of the flow features showed a similarity with the isothermal case, and the inner and outer recirculation zones are presented in the results. The reaction zone embedded in the inner recirculation zone followed the spray injection pattern and showed a conical shape where a low velocity region was used to stabilise the flame. Two outer recirculation zones were strongly affected by the high velocity of the cold air stream, and the size of the recirculation zones was larger than the isothermal case. The mass fraction of n-dodecane shows that the liquid fuel evaporated into a gas vapour that was ready to burn in the computational domain. The mass fraction of OH radicals is a metric to show the important combustion characteristics, such as ignition delay and flame lift-off length. The mass fraction of CH_2O radicals is an essential intermediate species used to define the first combustion stage at relatively low temperatures. Both

skeletal n-dodecane and HyChem kinetic mechanisms were able to reproduce the same temperature field as well as the mass fraction of the important species. Figures 5.16 to 5.19 compare both kinetic schemes with the experimental data in terms of three velocity component profiles and temperature.

As shown in these figures, the prediction of the maximum and minimum axial and radial velocity magnitudes was reasonably matched, and the profile of the curve was reasonably well predicted. However, in Figure 5.16, when X = 60mm, the maximum value of the axial velocity was underpredicted. These discrepancies show that although the geometry is simple, the flow features of swirling flow are complicated. In addition, the swirl velocity components at X = 10mm and X = 30mm were overpredicted, but the shape of the curve was reasonably well predicted. In general, the prediction of three velocity components can be reproduced in the context of steady-state RANS using the SST k-omega model, and it is useful to guide the combustor designer about the aerothermal and critical swirler design.

The temperature field depicted in Figure 5.19 showed good agreement with the experimental data. The only discrepancy was that the temperature downstream of the burner was overpredicted. The assumption of an adiabatic wall boundary condition and no radiative heat transfer assumption may contribute to the discrepancy.

Figures 5.7 to 5.8 and 5.13 and 5.15 show the species concentrations of n-dodecane, OH, and CH2O radical contours for Yao-54 and HyChem, respectively. Since the measurement of species concatenation is not reported in the experimental work, there is no direct comparison between modelling and experimental work. However, the mass fraction of OH and CH2O can be used as a flame indicator, and it showed good agreement with the temperature contour. The high concentration region of OH and CH2O followed the shear layers of the flow and a cone-shaped flame that sits between the shear layers. In addition, the concentration of n-dodecane followed the shear layers, which implies that the liquid fuel first evaporated and then the droplets followed the shear layers of the flow. There was minimal concentration of n-dodecane at the combustor outlet, which suggests that all the fuel was burnt completely inside the computational domain, implying that combustion efficiency was high.

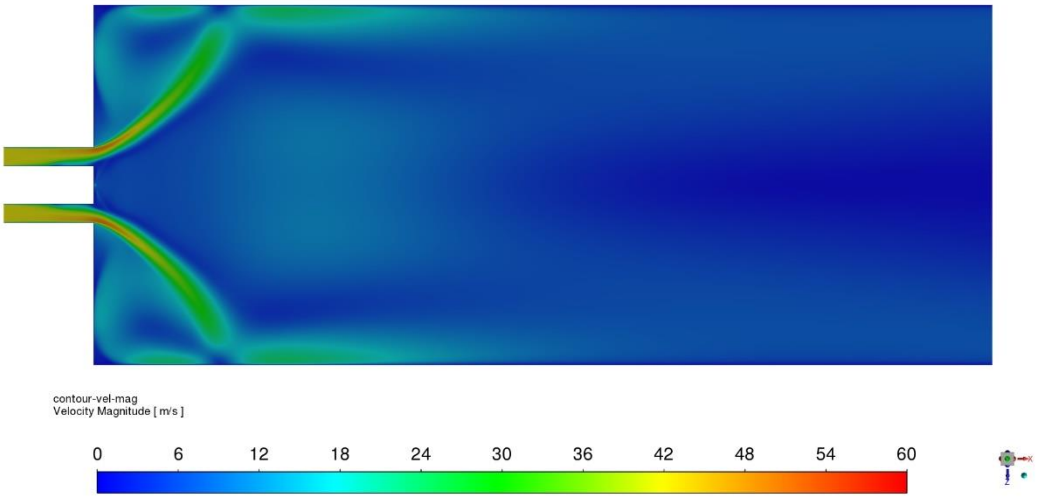

Figure 5.4 Velocity magnitude contour of Yao-54 scheme

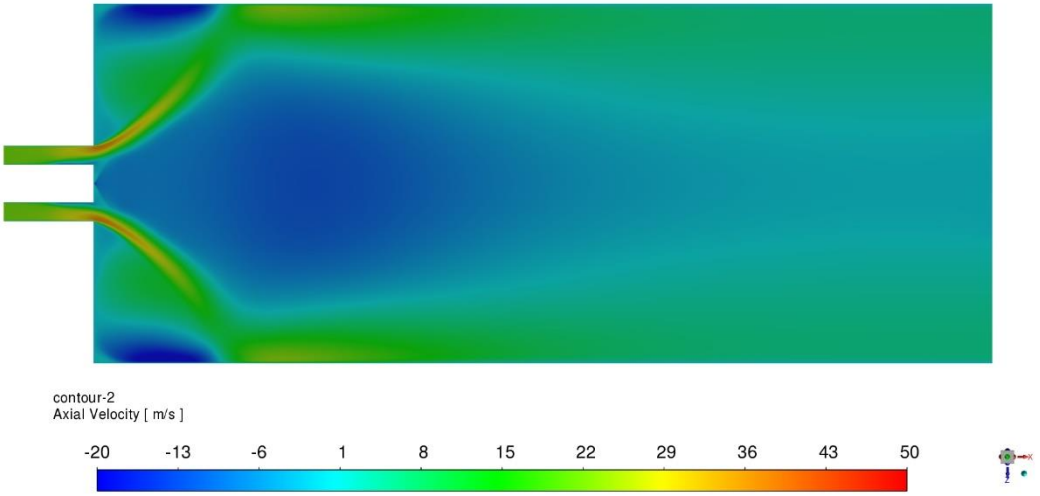

Figure 5.5 Axial velocity contour of Yao-54 scheme

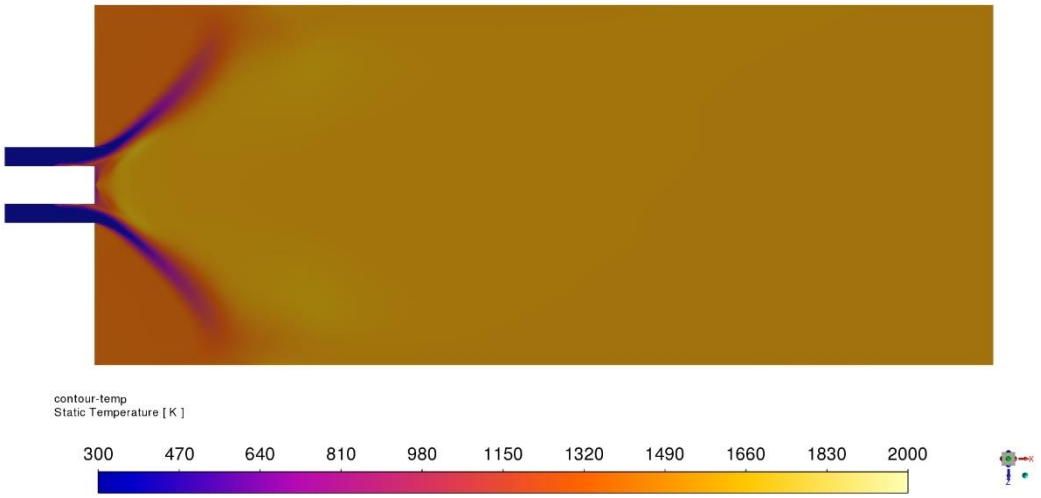

Figure 5.6 Temperature contour of Yao-54 scheme

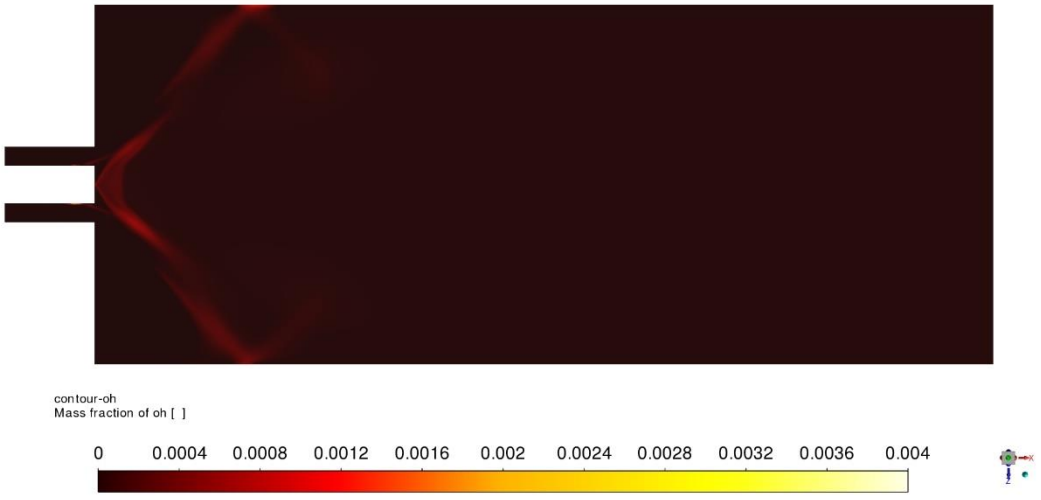

Figure 5.7 Mass fraction OH radical of Yao-54 scheme

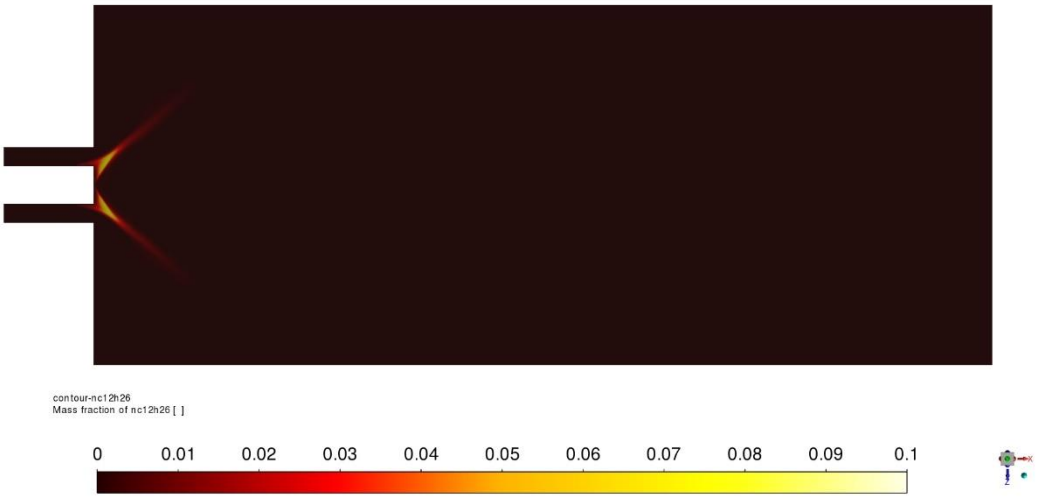

Figure 5.8 Mass fraction of n-dodecane of Yao-54 scheme

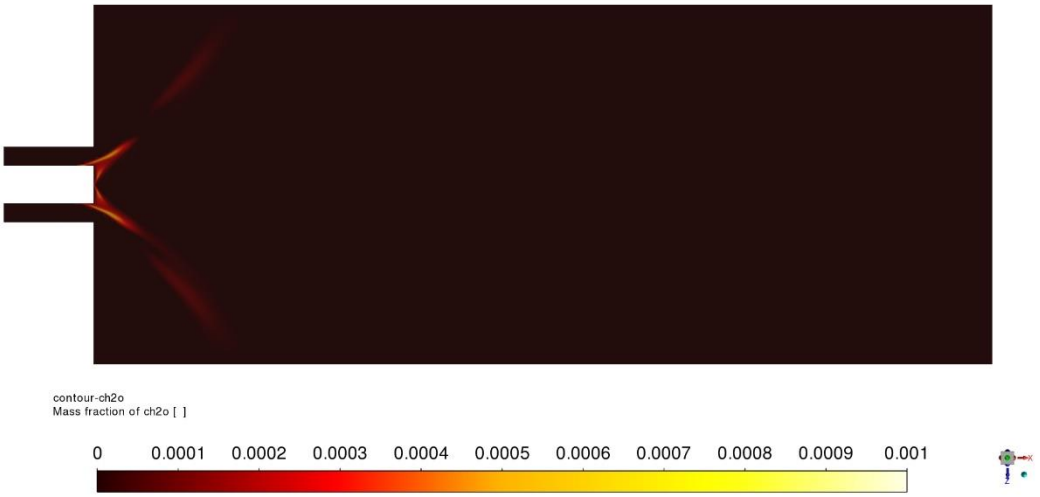

Figure 5.9 Mass fraction of CH_2O radical of Yao-54 scheme

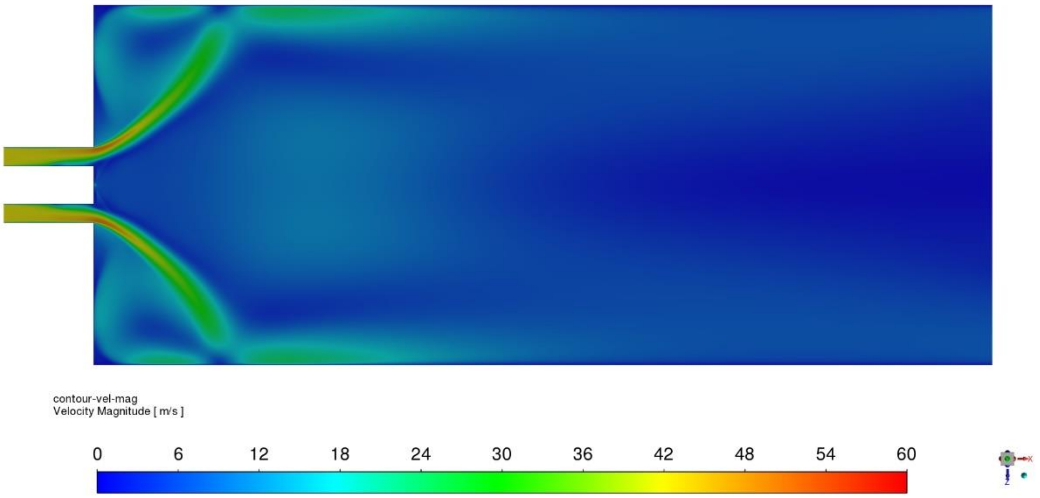

Figure 5.10 Velocity magnitude contour of HyChem scheme

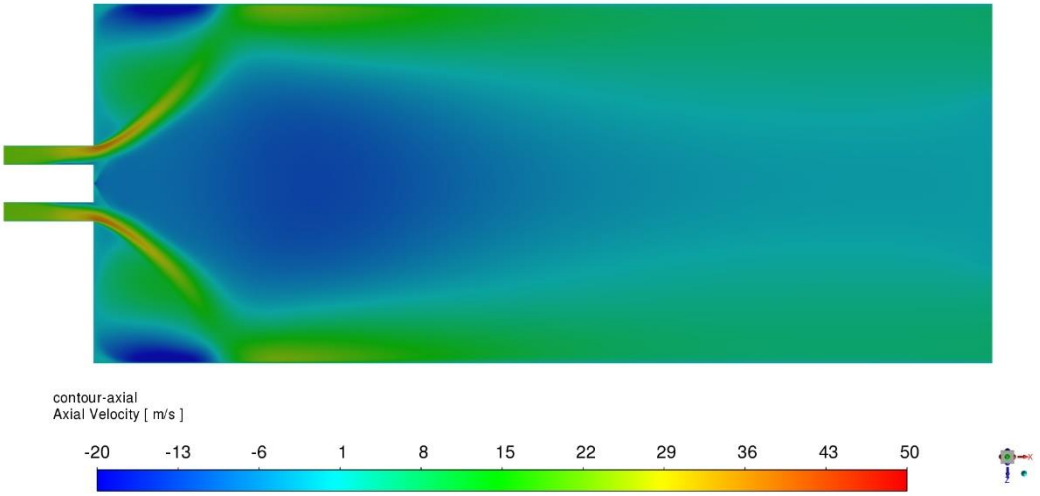

Figure 5.11 Axial velocity contour of HyChem scheme

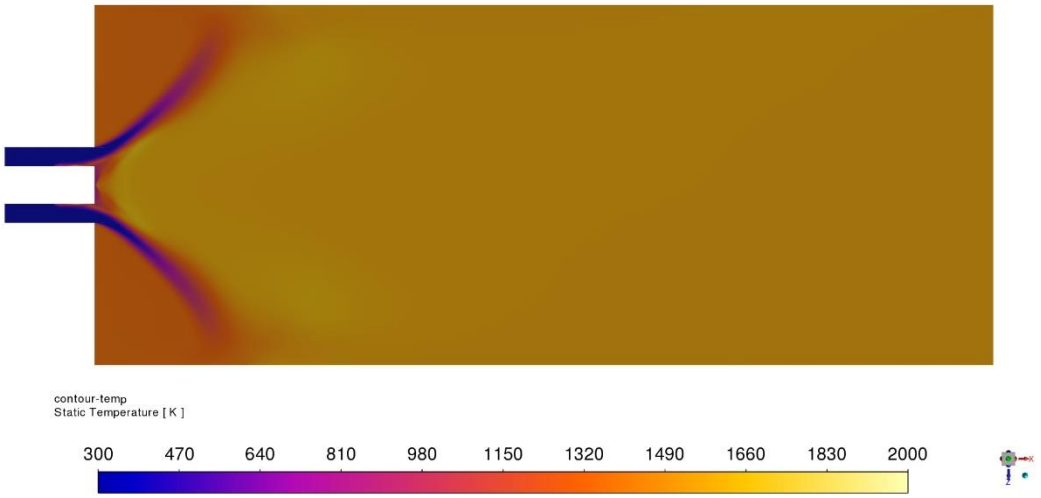

Figure 5.12 Temperature contour of HyChem scheme

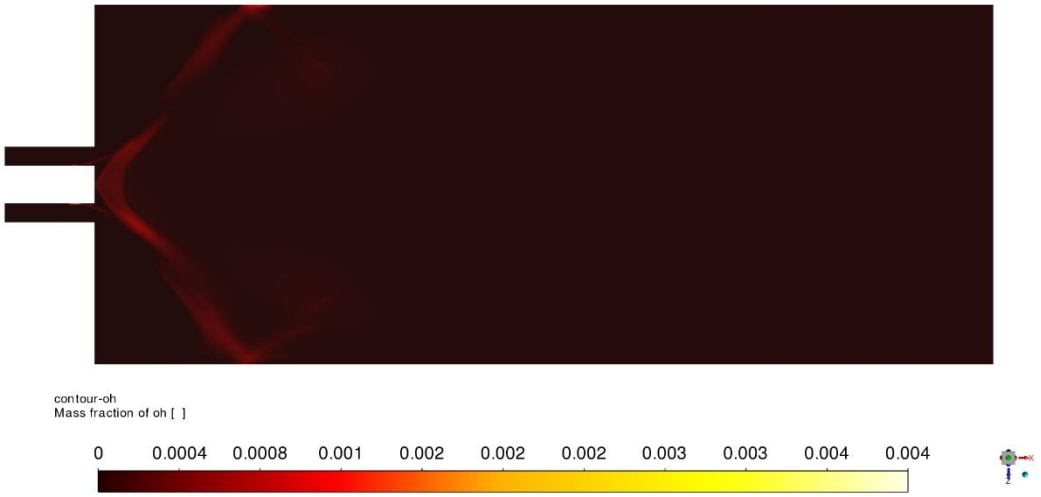

Figure 5.13 Mass fraction of OH radical of HyChem scheme

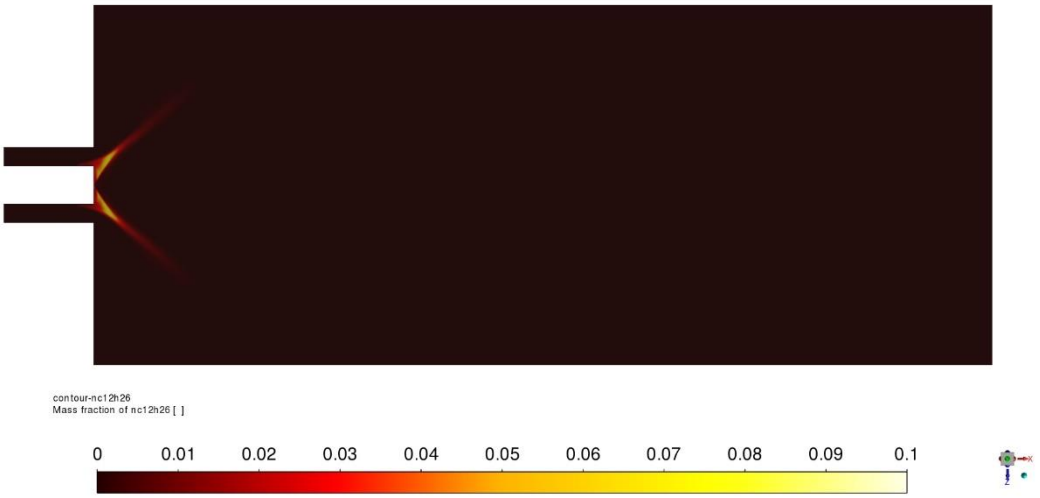

Figure 5.14 Mass fraction of n-dodecane of HyChem scheme

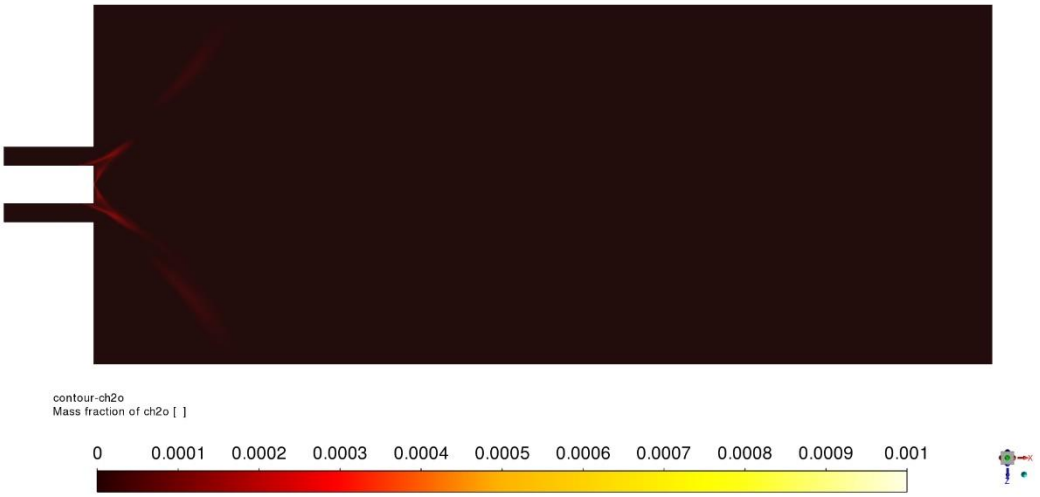

Figure 5.15 Mass fraction of CH_2O radical of HyChem scheme

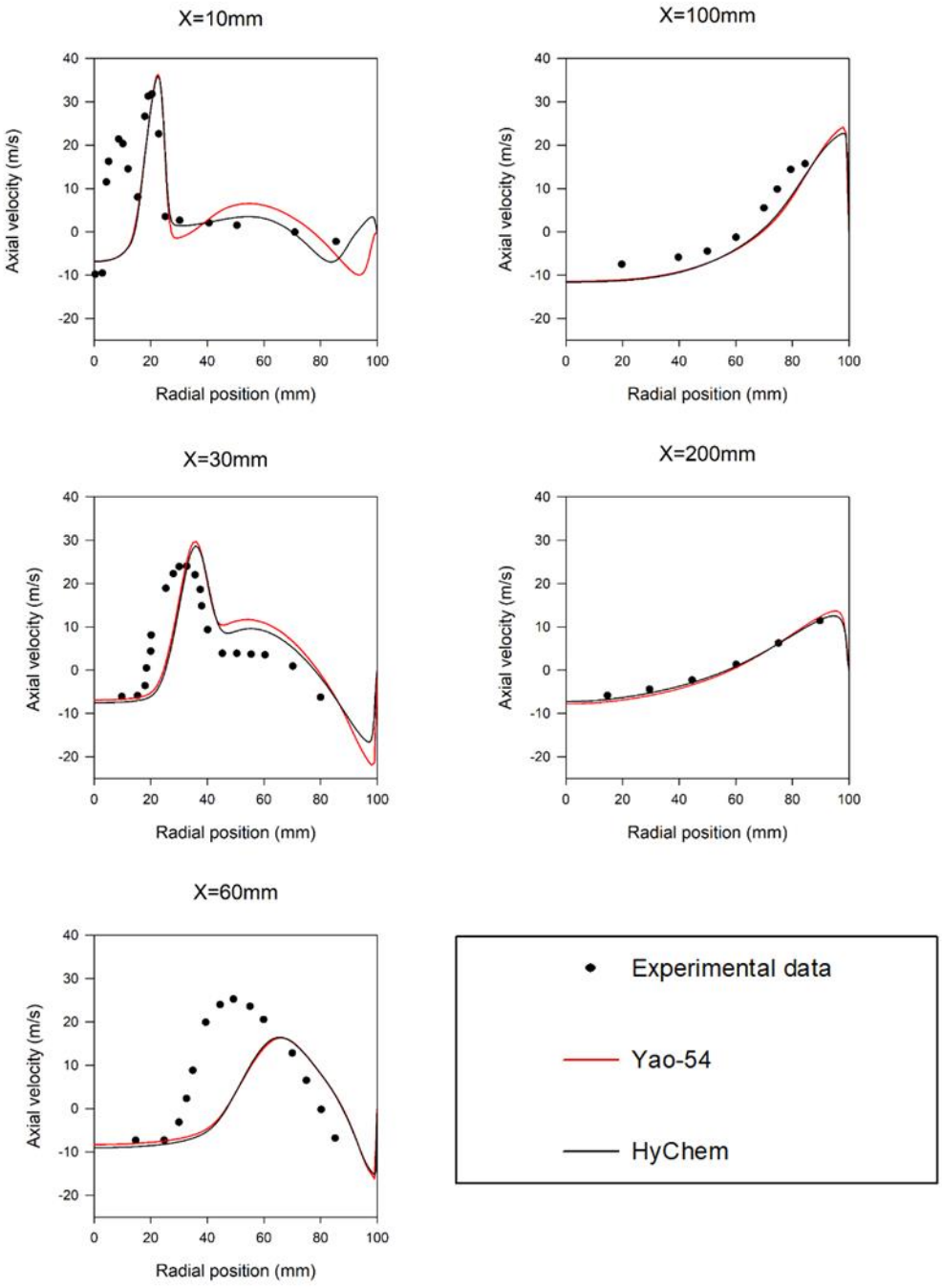

Figure 5.16 Axial velocity profiles of the Yao-54 and HyChem schemes

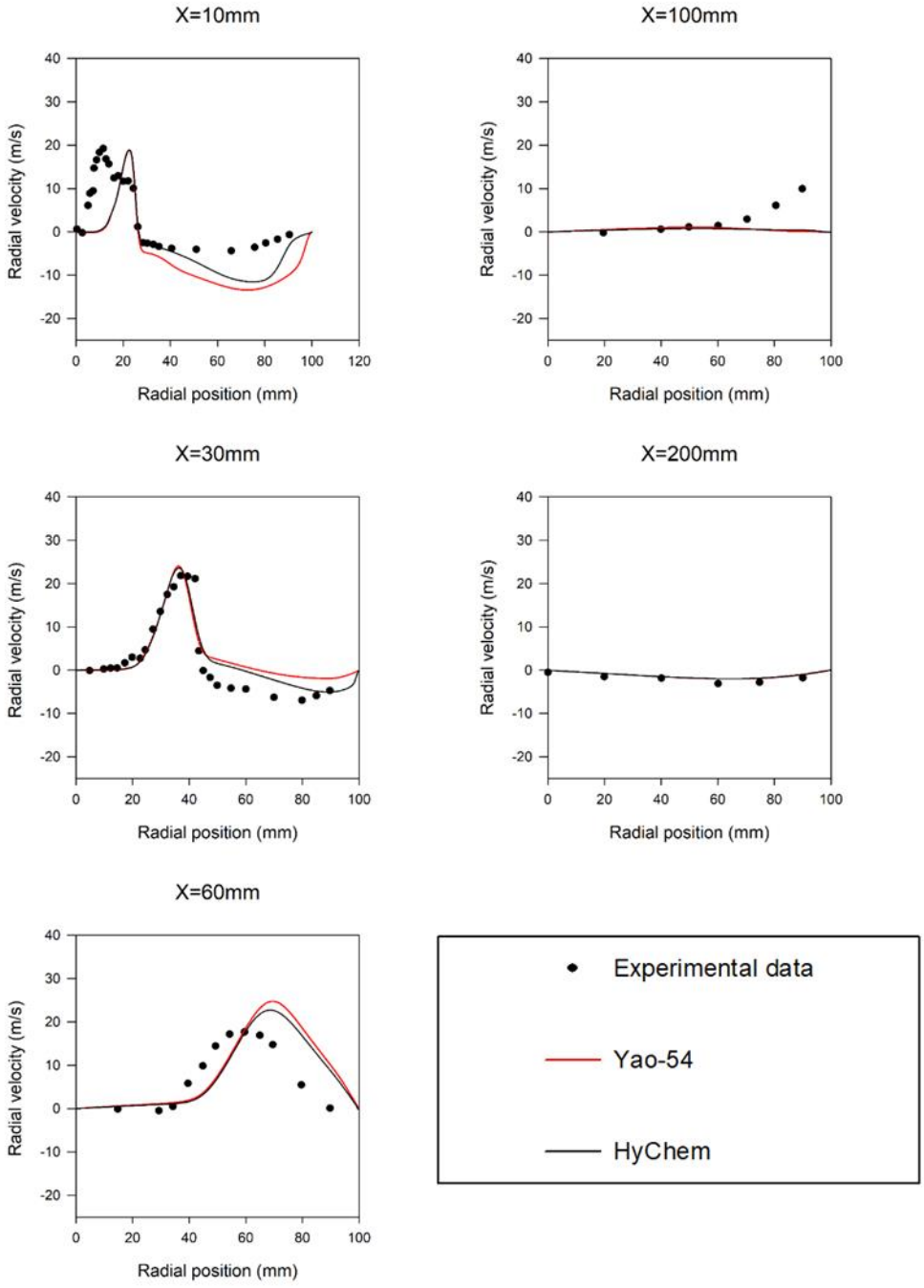

Figure 5.17 Radial velocity profiles of the Yao-54 and HyChem schemes

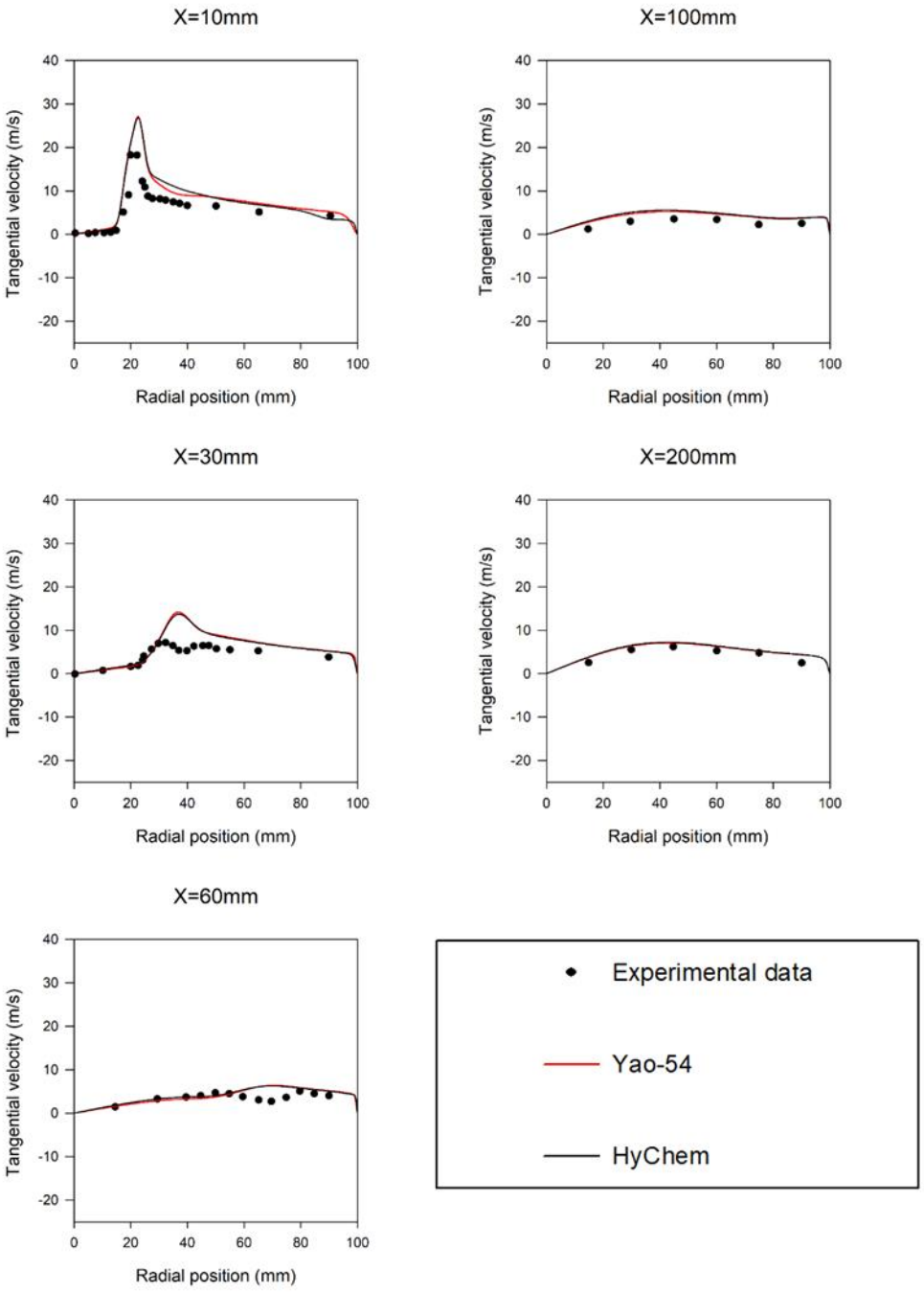

Figure 5.18 Swirl velocity profiles of the Yao-54 and HyChem schemes

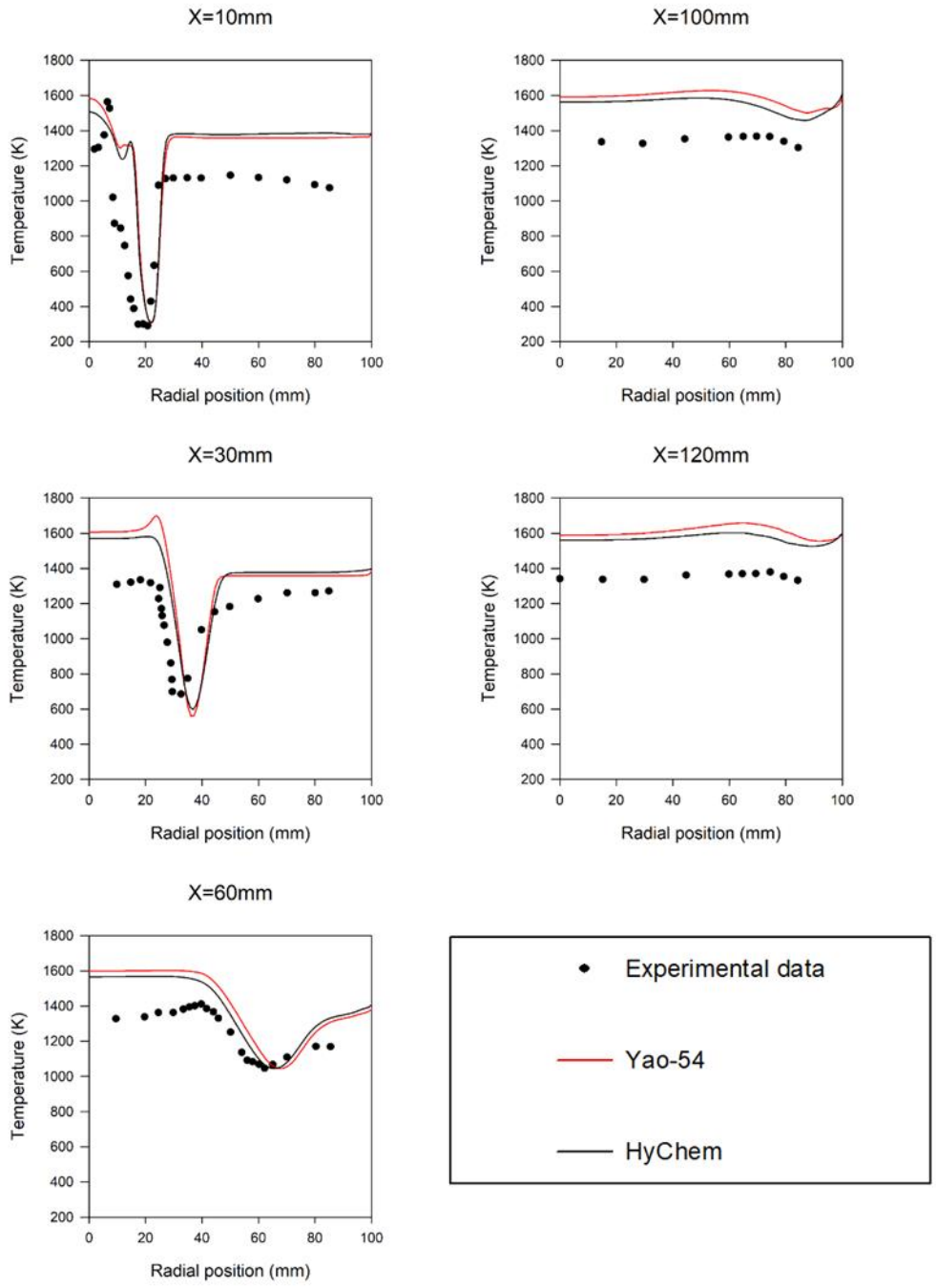

Figure 5.19 Temperature profiles of the Yao-54 and HyChem schemes

5.7 Comparison between steady-state and transient simulation in turbulent spray flames

As discussed in Chapter 4, transient simulation reproduces velocity profiles closer to experimental results than steady-state simulation. Transient simulation was studied to investigate the modelling performance in turbulent spray flames in a lab-scaled burner. The steady-state solutions computed in Section 5.6 were used as the initial conditions of the transient simulation. A time step size to 5×10^{-6}s was chosen to satisfy $CFL \leq 1$. Three flow-through times of 36 ms were computed to give the transient solutions. The comparison between steady-state and transient simulation in turbulent spray flames is discussed below.

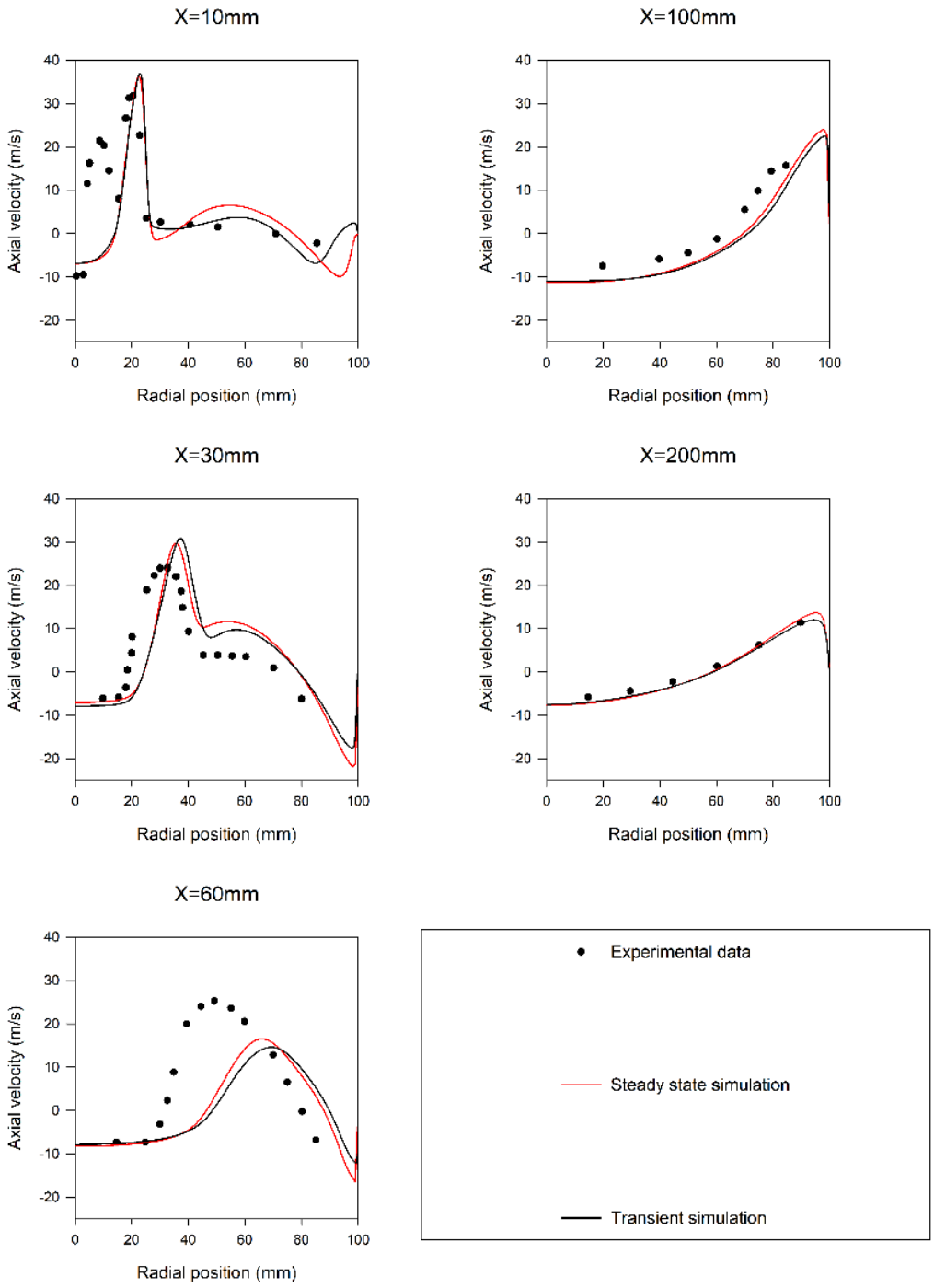

Figure 5.20 Comparison of axial velocity profiles

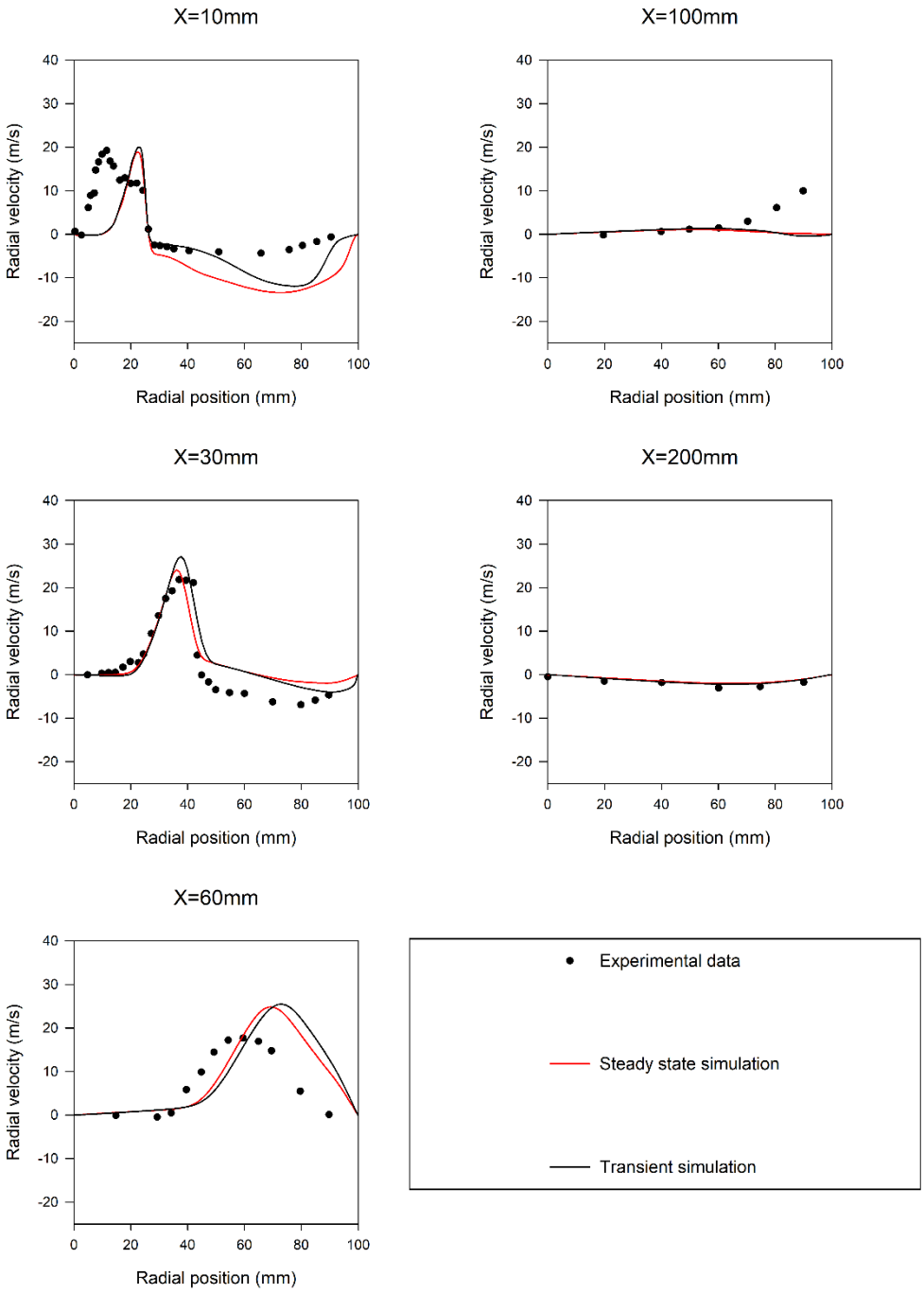

Figure 5.21 Comparison of radial velocity profiles

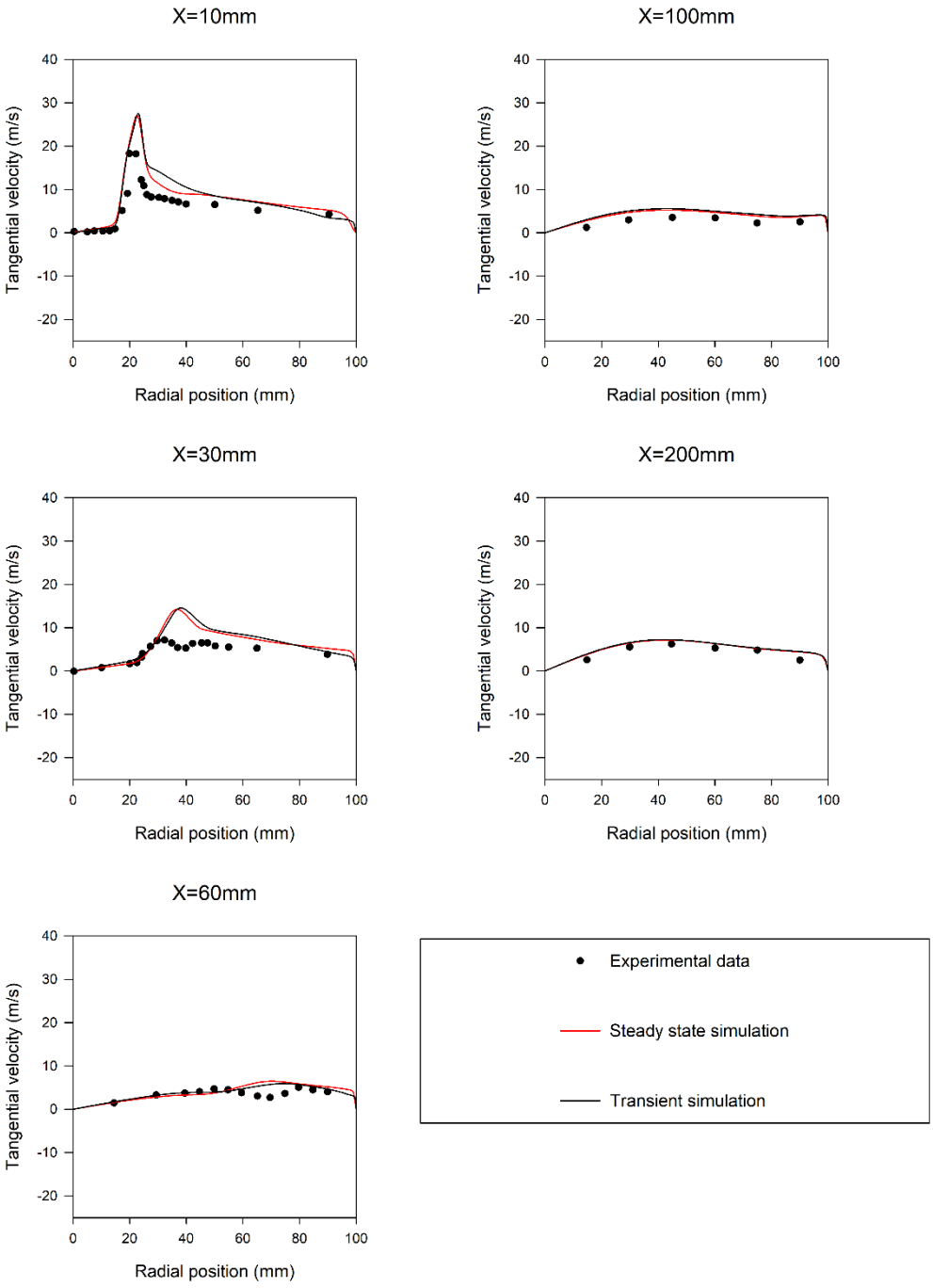

Figure 5.22 Comparison of tangential velocity profiles

Figures 5.22–5.24 show the comparison between steady-state and transient simulation in axial, radial, and tangential velocity. The results of transient and steady-state simulation generally have good agreement.

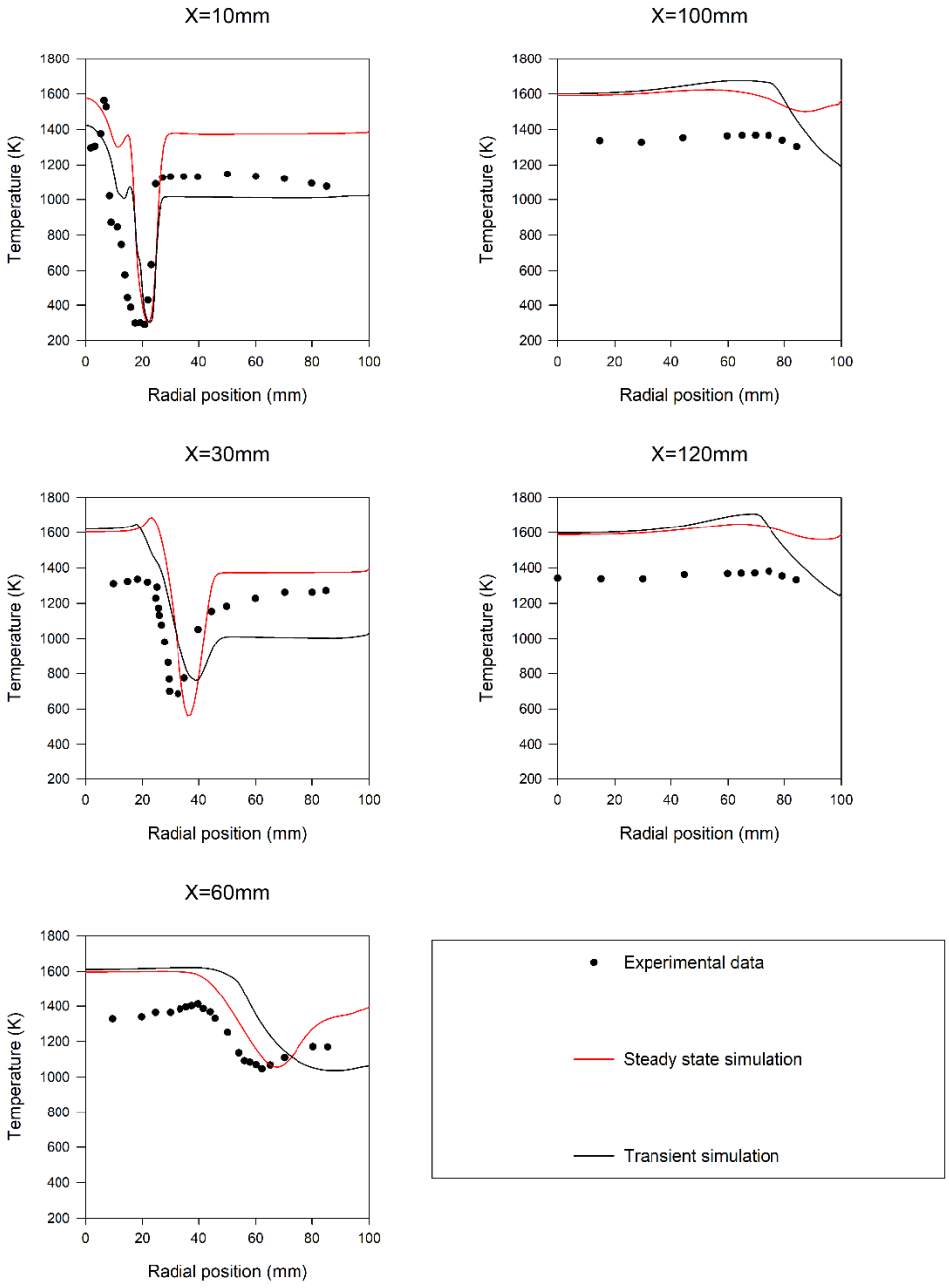

Figure 5.23 Comparison of temperature profiles

Figure 5.23 shows the temperature profiles. Transient simulation underpredicted the temperature profiles at axial directions of 10 mm and 30 mm, where steady-state simulation overpredicted the temperature profiles. Both steady-state simulation and transient RANS simulations overpredicted the temperature profiles at axial directions of 60 mm, 100 mm, and 200 mm. Based on the results shown in Figures 5.20 to 5.23, the modelling approach in this thesis relies on steady-state simulation because of its less expensive computational resources combined with reasonable accuracy.

5.8 Summary

This chapter presents an investigation of turbulent spray flame in a lab-scale burner under an equivalence ratio of 0.53. Two different mechanisms were computed in simulating this configuration, and the results showed good agreement in terms of temperature fields and velocity fields. The lab-scaled burner included all the physics inside a realistic combustor. The axial swirler generated swirling flow fields for the flame stabilisation mechanism. The liquid fuel first underwent atomisation, followed by evaporation and finally combustion. Hence, the modelling techniques in the spray combustion and droplet injection method have also been validated in this chapter and can be further applied to model a realistic micro gas turbine combustor with reasonable accuracy.

The state-of-the-art turbulent combustion model – flamelet-generated manifold with Yao n-dodecane mechanism – has been developed as the modelling strategy for turbulent spray flame in a lab-scaled burner. The only difference between the realistic combustor and the lab-scaled burner was the ambient pressure; however, the n-dodecane mechanism was valid in the pressure range from 1-80 bar. The mixture properties were calculated from the thermodynamics data using the Yao mechanism.

Moreover, Section 5.7 compared steady-state and transient CFD modelling. The results suggest that the steady state can be used in modelling reacting flow conditions in designing and developing the novel combustor discussed in the following chapter. The following chapter will focus on the basic calculation and optimisation process of the combustor, using the modelling techniques developed in this chapter.

Chapter 6 Optimisation of 30kW Micro Gas Turbine Combustor

6.1 Introduction

A combustion chamber or combustor is one of the crucial components in modern gas turbine engines. It converts the chemical energy from fuel by combustion to burnt gases, then turns into mechanical energy. The combustion process in the combustion chamber is very complex, including gas flow and fuel–air mixing, liquid atomisation and evaporation, chemical reactions, radiation and convection of hot gases, and various phenomena such as heat and mass transfer. Due to the advancement of fundamental studies in combustion, such as laminar flame speed measurement, chemical kinetic mechanism development, and model development for turbulent combustion, the design cycle of a combustor is shorter, and computational fluid dynamics (CFD) is widely used as a design tool in combination with experimental measurements. Section 6.2 presents a basic calculation for the important aerodynamic components, such as swirler and air-to-fuel ratio (AFR), to design the baseline combustor. Section 6.3 presents the modelling methodology developed in the previous chapter and applied to the novel combustor. Sections 6.4 and 6.5 present the CFD simulation results of the baseline design and the optimised design. Section 6.6 discusses the experimental investigation of the combustor to prove the baseline design concept.

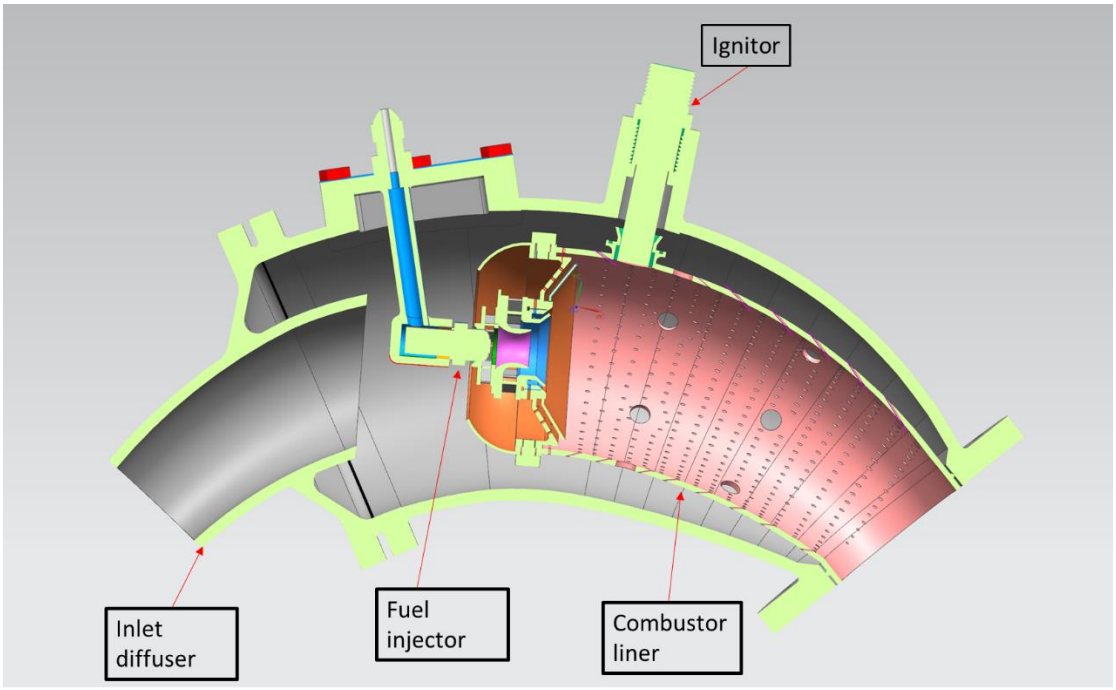

Figure 6.1 Novel combustor CAD model

6.2 Baseline design calculation

6.2.1 Overall effective area

The overall effective area is calculated to meet the total pressure drop constraint, and the equation to calculate the effective area is written as:

$$C_d A_h = \frac{\dot{m}_a}{\rho_a u_j} \tag{6.1}$$

where C_d is the discharge coefficient, A_h is the area of the flametube, $\dot{m}_a$ is the air mass flow rate, ρ_a is the air density, and u_j is the jet velocity. The

target is set to the total pressure drop, less than 2%, and the value of $C_d A_h$ for one can of the flametube is calculated using Equation (6.1).

6.2.2 Reference velocity approach

The reference velocity approach is used to calculate the passage velocity (V_p) and the dome velocity (V_d) at the swirler region to meet the design constraints. For small-scale engines, the size of the combustor is relatively small compared to large-scale engine combustors; hence, the reference velocity for the passage and dome are smaller.

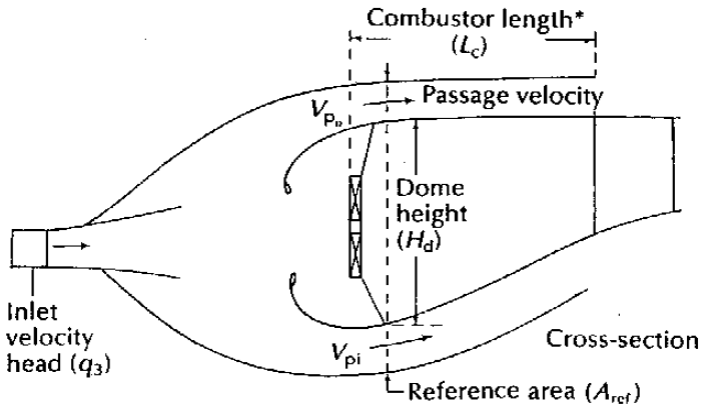

Figure 6.2 Reference area approach [109]

The reference velocity for passage and dome are calculated as 10.5 m/s and 2.36 m/s respectively to ensure the flame stabilisation and primary as well as dilution jet penetration performance.

6.2.3 Combustor air fuel distribution

Rich-burn quick-quench lean-burn (RQL) combustor architecture is one of the high technology readiness levels (TRL) combustor designs targeting low emissions in aeroengines [110]. The air mass flow distribution of the swirler was designed to ensure lean blowout performance; therefore, the swirler had an equivalence ratio of 1 at engine idle condition for stability. The flame tube/liner was separated into three different zones: primary zone (PZ), intermediate zone (IZ), and dilution zone (DZ). The primary zone air distribution was designed at an equivalence ratio near 1 to achieve high combustion efficiency. The combustion zone had an equivalence ratio between 0.6 and 0.8 to ensure combustion efficiency and hot spot generation downstream. The baseline design air mass flow distribution is listed in Table 6.1 below.

Table 6.1 Combustor air mass flow distribution

Component	Air mass flow (%)
Swirler	15.2
Primary holes	23.8
Dilution holes	22.3
Combustor dome	4.8
Liner effusion holes	33.9

The fuel flow rate is determined from the engine cycle calculation and diesel fuel lower heating value. The required fuel flow rate at the full load condition is calculated as 13.93 kg/hr.

6.2.4 Swirler design calculation

In the baseline design, flame stabilisation is achieved by a swirling flow in the primary zone. Swirling motion is generated by a radial swirler, air passes through the swirler blades, then it is imparted with tangential velocity, causing the air to rotate around the central axis of the swirler. In the baseline design, a radial swirler is used to generate swirl. A swirl number (S_N) is used to characterise the swirl intensity; in practice, the swirl number of a swirler needs to be greater than 0.6 to achieve a favourable swirl for flame stabilisation [20].

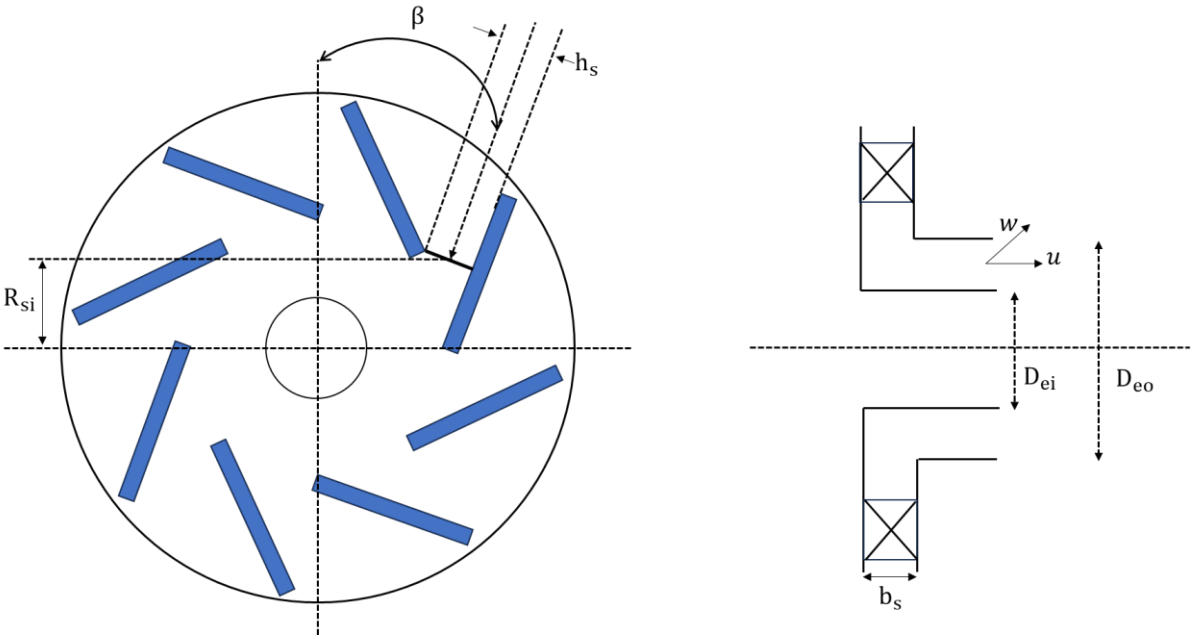

Figure 6.3 Radial swirler design

The swirl is defined as the ratio of axial flux of angular momentum to the axial flux of axial momentum [91]. The swirl number of the baseline swirler is derived from the tangential momentum flux ($G_{\varphi 0}$) at the swirler exit, which is written as:

$$G_{\varphi 0} = \int_{R_{ei}}^{R_{eo}} 2\pi r(wr)\rho u dr \tag{6.2}$$

where w is the tangential velocity, and R_{eo} and R_{ei} are the outer radius and inner radius, respectively.

The axial momentum flux (G_{x0}) at the swirler exit is written as:

$$G_{x0} = \int_{R_{ei}}^{R_{eo}} 2\pi r \rho u^2 dr \tag{6.3}$$

where u is the axial velocity.

The conservation of momentum applied is written as:

$$w_{si} R_{si} sin\beta = wr \tag{6.4}$$

The velocity between two swirler blades equals the exit velocity due to the conservation of mass, as follows:

$$u = \frac{\dot{m}_s}{\rho\pi(R_{eo}^2 - R_{ei}^2)} = w_{si} = \frac{\dot{m}_s}{\rho n h_s b_s} \tag{6.5}$$

Therefore, the swirl number of the radial swirler is defined as:

$$S_N = \frac{\pi(R_{eo}^2 - R_{ei}^2) R_{si} sin\beta}{n h_s b_s R_{eo}} \tag{6.6}$$

In the baseline design, a double radial swirler with a counter-rotating design was used to promote the evaporation effect and turbulent mixing effect [111]. The pressure swirl atomiser coupled with two swirlers is illustrated in Figure 6.3. The swirl cup design concept is widely used in modern gas turbine combustors due to its excellent fuel atomisation performance and uniform air fuel mixing, which prompt emission reduction [112].

An experimental investigation of the structure parameters of the venturi on the atomisation effect was conducted by Im et al. [113]. The length of the venturi tube correlates with the spray cone angle and droplet SMD. The longer venturi tube provides a greater spray cone angle and corresponds to smaller droplet SMD. The swirl numbers calculated using Equation 6.6 for primary and secondary swirlers are 0.24 and 0.70, respectively.

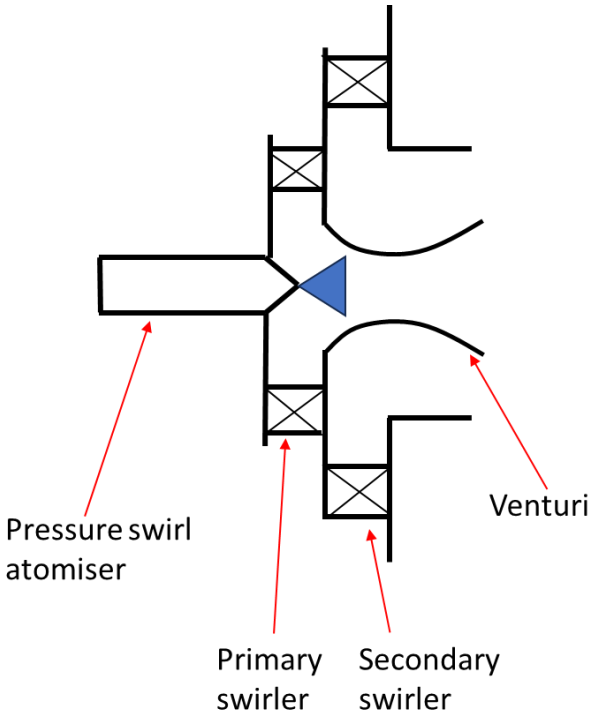

Figure 6.4 Swirl cup design concept

6.2.5 Injector and ignitor design calculation

The injector type is a pressure swirl-type injector [114], which is commonly used in aeroengine injectors to atomise the fuel and provide a hollow cone spray pattern. Figure 6.5 shows a schematic diagram of a pressure swirl

atomiser. The liquid is fed tangentially into an atomiser chamber, and air penetrates from the middle of the atomiser. The liquid undergoes a swirling motion, spreading out in the form of a conical sheet as it leaves the orifice, and a wider spray angle can be achieved to improve the atomisation performance.

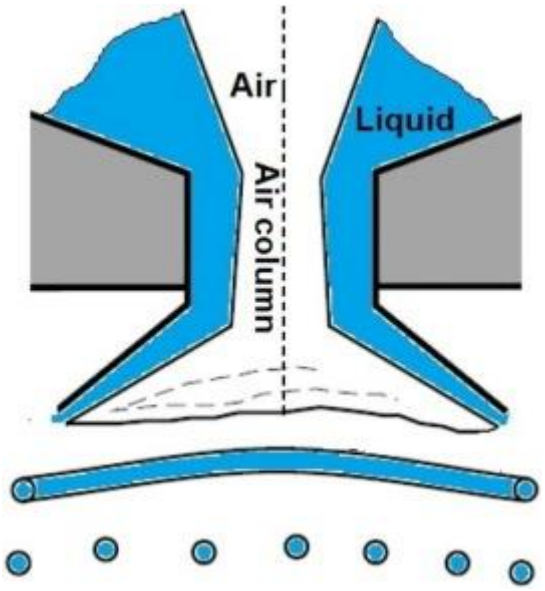

Figure 6.5 Pressure swirl atomiser [112]

The design nozzle parameters in operating condition are tabulated in the table below:

Table 6.2 Pressure swirl atomiser design parameters

Fuel pressure drop $[MPa]$	2.0
Fuel flow rate $[kg/hr]$	13.93
Flow number $[kg/hrMPa^{0.5}]$	11

Spray cone angle [degree]	80
Droplet SMD [μm]	30

The SUNTEC E7NC fuel pump was selected to pump the fuel from the fuel tank. The ignitor is a high energy device composed of 6 J energy with a 24V DC supply. The best ignition location is determined from the CFD results based on liquid fuel evaporation. The area of higher concentration of fuel vapour is chosen as the optimal location of the ignitor [115].

6.2.6. Liner design concept

Liner cooling is important for combustor life span and reliability. Combustor liners are one of the components in gas turbine engines that suffer from the high temperatures of hot burnt gases. In the baseline design, a multi-hole cooling design was used to protect the liner wall temperature. Nine rows of straight holes of 1 mm inclined 30 degrees along the wall were used to provide an air film near the liner wall of the convective heat transfer mechanism.

6.3 CFD Methodology

6.3.1 Geometry simplification

The combustor geometry was complicated, especially in the swirler area. There was also a large number of small holes for cooling purposes. Therefore, the computational domain was simplified before the grid generation process to reduce the computational grid size and the difficulties in modelling the combustor. The simplification is as follows:

- The ignitor was removed from the computational domain, and the ignition process was simplified to patch the computational domain as a progress variable of 1.
- The atomiser was simplified and modelled as a point injection of a hollow cone shape.
- The connection rod between the atomiser and the flange was simplified and assumed to have no effect aerodynamically.
- The computational domain was combined as one fluid body.

6.3.2 Computational grid generation

A grid independent study was first carried out to determine the most efficient and effective meshing for cold flow and reactive simulation. A low cell counts but accurate mesh is desirable, as the reacting flow simulation involves spray and chemistry reactions that add extra computational resources to the completion of the simulation. Table 6.3 shows the grid

parameters used to generate the mesh. The local refinement is targeted at the primary zone of the combustor, as there are steeper temperatures and density gradients of the flow field.

Table 6.3 Grid generation parameters

Min size (mm)	0.2
Max size (mm)	1.2
No. of inflation layers	4

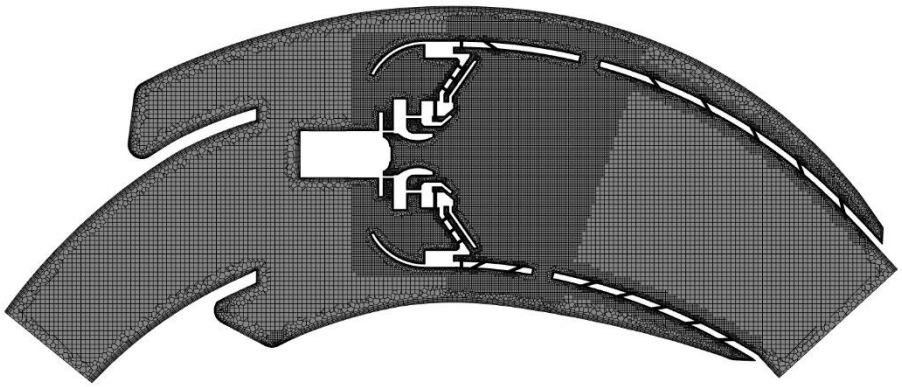

Figure 6.6 Mesh 1 (coarse)

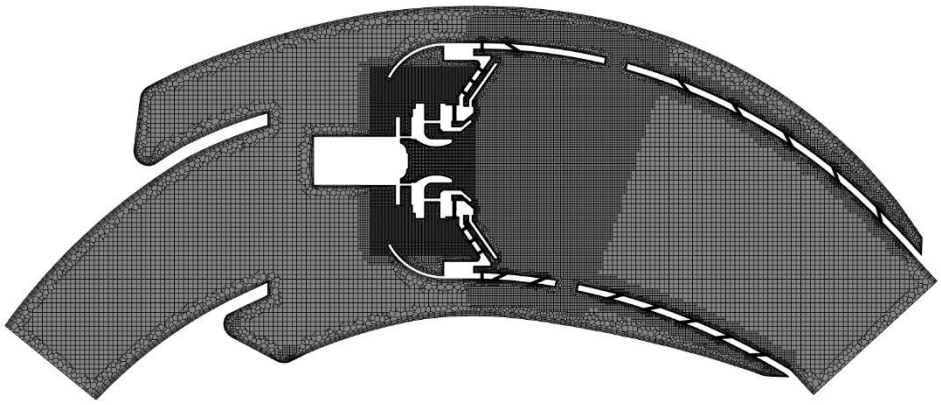

Figure 6.7 Mesh 2 (medium)

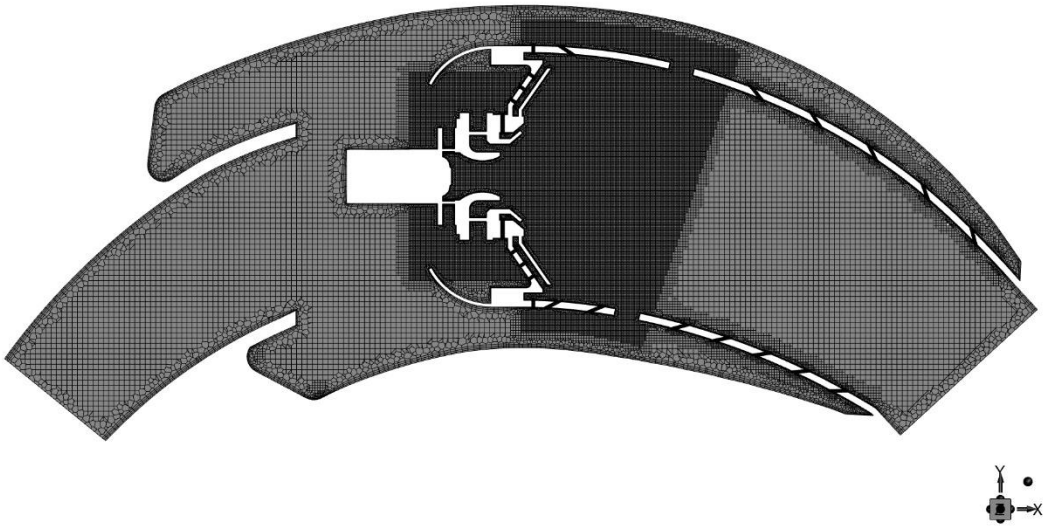

Figure 6.8 Mesh 3 (fine)

Mesh 1 used a local refinement size of 0.5 mm at the spray nozzle and possible flame location. Mesh 2 used a local refinement size of 0.5 mm, including the swirler area as well as the spray nozzle, and a size of 1 mm at the primary zone. Mesh 3 used a local refinement size of 0.5 mm at both swirler, spray nozzle, and primary zone regions. The computational domain was complicated by the swirler geometry and effusion holes at the liner wall and combustor dome; therefore, a hybrid meshing technique was used to balance the computational time and accuracy. In 3D CFD simulations with complex geometry, unstructured grids often use tetrahedron, pyramid, polyhedron, hexahedron, and wedge elements to represent a computational domain. Grid 1 was generated using poly-hexcore meshing in combination with prism layer mesh. Three layers of prism layer mesh were used near the wall to capture the steep gradient of boundary layer. Polyhedral elements were used to transit from prism layer mesh into hexahedral elements. The hexahedral element has the advantage of low numerical diffusion as well as reducing the total number of grid sizes. Local refinement areas of 0.5 mm cell size and 1 mm cell size were applied to the swirler region and primary zone region, respectively, to capture large temperatures and density gradients. Mesh 1 had 4 million cells, Mesh 2 had 7 million cells, and Mesh 3 had 14 million cells.

6.3.3 Turbulence model and boundary conditions

The cold flow condition was modelled prior to reactive flow conditions using the SST k-omega turbulence model, as suggested from the previous investigation on swirling spray flame in Chapter 5. The inlet condition uses a mass flow rate of 150g/s, temperature of 442 K. The turbulence condition of inlet is set as the hydraulic diameter of the inlet nozzle of 40 mm and assumed 5% of turbulence intensity. The outlet was selected as a static pressure of 374902.5 Pa.

6.3.4 Modelling assumptions and numerical schemes

The modelling assumptions are followed by the discussion in Section 3.11.3. The computational investigation of the combustor was simulated using steady-state RANS with the pressure-based code Ansys Fluent. A second-order upwind scheme was used for spatial discretisation. SIMPLE was used for pressure-velocity coupling.

6.3.5 Combustion modelling

Turbulent combustion was simulated using a tabulated chemistry model based on a set of 1D diffusion laminar flamelet configurations. Mixture fraction f and progress variable c were used to describe the mixing of reactants and the global reaction progress. The progress variable was defined as $Y_c = Y_{CO} + Y_{CO_2}$ as suggested by [116]. The unstrained laminar

flame speed was calculated using a CHEMKIN solver using the 54-species skeletal n-dodecane mechanism, which was used in Chapter 5 to investigate swirling spray flames and successfully applied to 3D CFD simulation of diesel spray under diesel engine conditions [101]. The initial scalar dissipation was specified as 1E-4 to capture the lower branch of the extinction S-curve, and the extinction scalar dissipation was calculated by the solver as 211 s^{-1}. The unstrained laminar flame speed is shown in Figure 6.9, and a 3D visualisation of the look-up table is shown in Figure 6.10.

Table 6.4 scalar dissipation rate of initial and extinction value

Initial scalar dissipation [s^{-1}]	1E-4
Extinction scalar dissipation [s^{-1}]	211

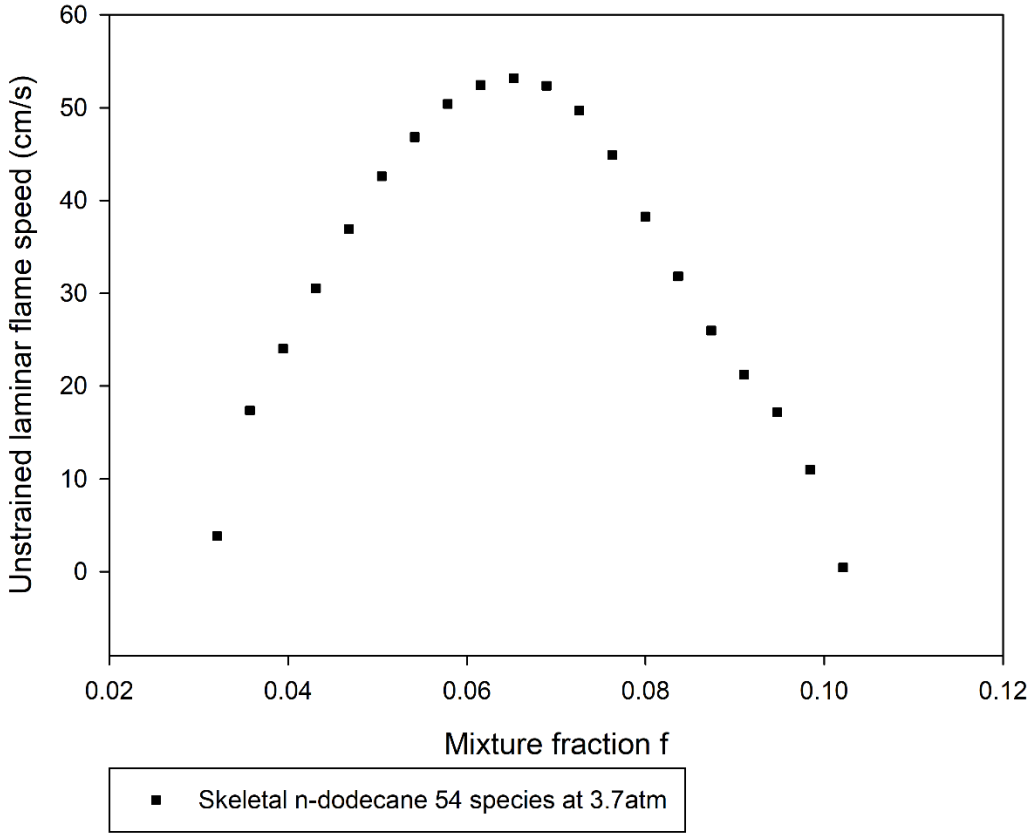

Figure 6.9 Unstrained laminar flame speed at 3.7atm

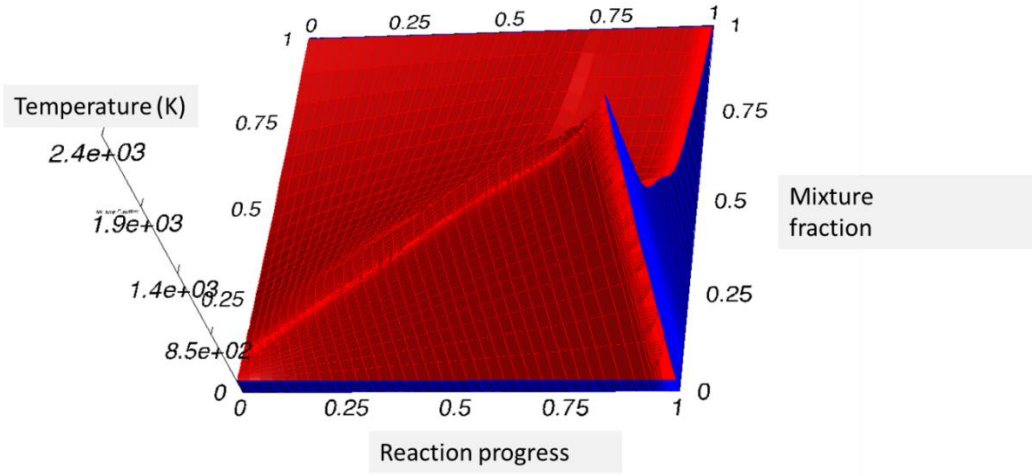

Figure 6.10 3D visualisation of PDF look-up table

The PDF look-up table is a non-adiabatic type with a 5-dimensional table, and the parameters used to compute the table are shown in Table 6.5.

Table 6.5 PDF look-up table control variables

Number of fmean grid points	100
Number of cmean grid points	100
Number of enthalpy grid points	23
Number of fvar grid points	50
Number of cvar grid points	50
Number of species	54

6.3.6 Spray modelling

The atomisation modelling was simplified to avoid the simulation of the inner structure of the atomiser, as it is extremely difficult and computationally expensive. This simplification has been successfully examined in the literature [117]. The pressure swirl atomiser was modelled using the Euler–Lagrange (E–L) approach described in Chapter 3. The Euler frame of reference applies to the continuous phase, which is air, and

the Lagrangian frame applies to liquid droplets. The E–L approach requires a set of boundary conditions for point injection, such as droplet velocity and droplet SMD. Therefore, analytical calculations were first computed using the linearised instability sheet atomisation (LISA) model [118]. The total velocity U was then calculated using the equation:

$$U = k_v \sqrt{\frac{2\Delta p}{\rho_l}} \tag{6.7}$$

where Δp is the fuel pressure ρ_l is the liquid density, and k_v is the discharge coefficient, which is equal to 0.7 suggested by [119].

The set of boundary conditions are listed in Table 6.6.

Table 6.6 Spray boundary conditions

Injection velocity [m/s]	40
Cone angle [deg]	40
Outer radius [mm]	0.4
Fuel flowrate [g/s]	3.896444
SMD [microns]	30
Min d [microns]	1
Max d [microns]	100
Spread diameter	3.5

No. of diameters	100

6.3.7 NOx modelling

The three principal pollutants that are produced from fossil fuel combustion are nitric oxide (NO), nitrogen dioxide (NO_2), and nitrous oxide (N_2O) [120]. Nitric oxide and nitrogen dioxide are collectively referred to as NOx emissions. Numerous modelling techniques accounting for NOx and soot have been developed; for example, numerical modelling of practical combustion systems and predicting NOx emissons with an integrated CFD-based approach is reported in [120]. A detailed review of NOx and soot modelling in diesel engines is discussed in [121]. Modelling NOx and soot formation by the eddy dissipation concept is reported and discussed in [122].

Since most liquid fuels produced from petroleum have practically no nitrogen content [19], NOx formation can be assumed to be thermal NOx dominant. Thermal NOx formation is known as the extended Zeldovich mechanism, which is described as follows:

$$O + N_2 \leftrightarrow N + NO \quad (6.8)$$

$$N + O_2 \leftrightarrow O + NO \quad (6.9)$$

$$N + OH \leftrightarrow H + NO \quad (6.10)$$

The NO species transport equation is used to predict the concentration of NO, taking into account convention, diffusion, production, and consumption of NO and related species. The governing equation is written as follows:

$$\frac{\partial}{\partial t}(\rho Y_{NO}) + \nabla \cdot (\rho \vec{v} Y_{NO}) = \nabla \cdot (\rho D \nabla Y_{NO}) + S_{NO} \tag{6.11}$$

where Y_{NO} is the mass fraction of NO in the gas phase, D is the effective diffusion coefficient, and the S_{NO} is the source term to be determined from the mechanisms (6.8) to (6.10). The reaction rate of mechanisms (6.8) to (6.10) has been measured and reported in [123].

6.4 Results

6.4.1 Grid independent study

Figure 6.11 shows the five different cross-section planes used for comparison in a grid independent study. Plane 1 defines the mixing field inside the combustor, whereas Plane 2 shows the fields after the primary holes. Planes 3 and 4 show the fields between the dilution holes, and finally Plane 5 shows the 5 mm before the outlet plane.

Figures 6.12 to 6.14 show the grid independent study results in terms of velocity, temperature, total pressure drop, and pattern factor at the

combustor outlet. The pattern factor is defined as the temperature uniformity at the outlet plane. In Figure 6.12, Mesh 1 shows the discrepancies in cross-section Plane 2, and the reason for that would be insufficient mesh refinement in Mesh 1 to capture the flow appropriately. Good agreements were achieved with Meshes 2 and 3. In Figure 6.13, Mesh 1 shows the temperature has reached over 2000 K in Plane 2, whereas the results of Mesh 2 and Mesh 3 were in good agreement, in a range between 1300 K and 1700 K. This further shows that Mesh 1 has insufficient mesh density to capture the flow field and temperature field inside the combustor. Figure 6.13 also shows that Mesh 1 overpredicted in pattern factor, and underpredicted the velocity magnitude and static temperature at the outlet plane. Therefore, Mesh 2 was considered the most efficient mesh density for this study, and the rest of the work was carried out using the local refinement size and global cell size of Mesh 2.

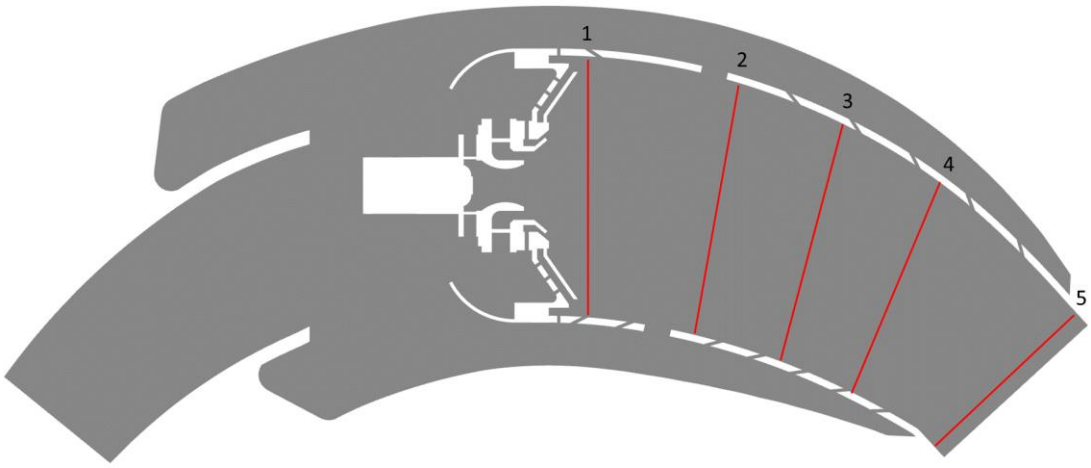

Figure 6.11 Mesh cross-section plane

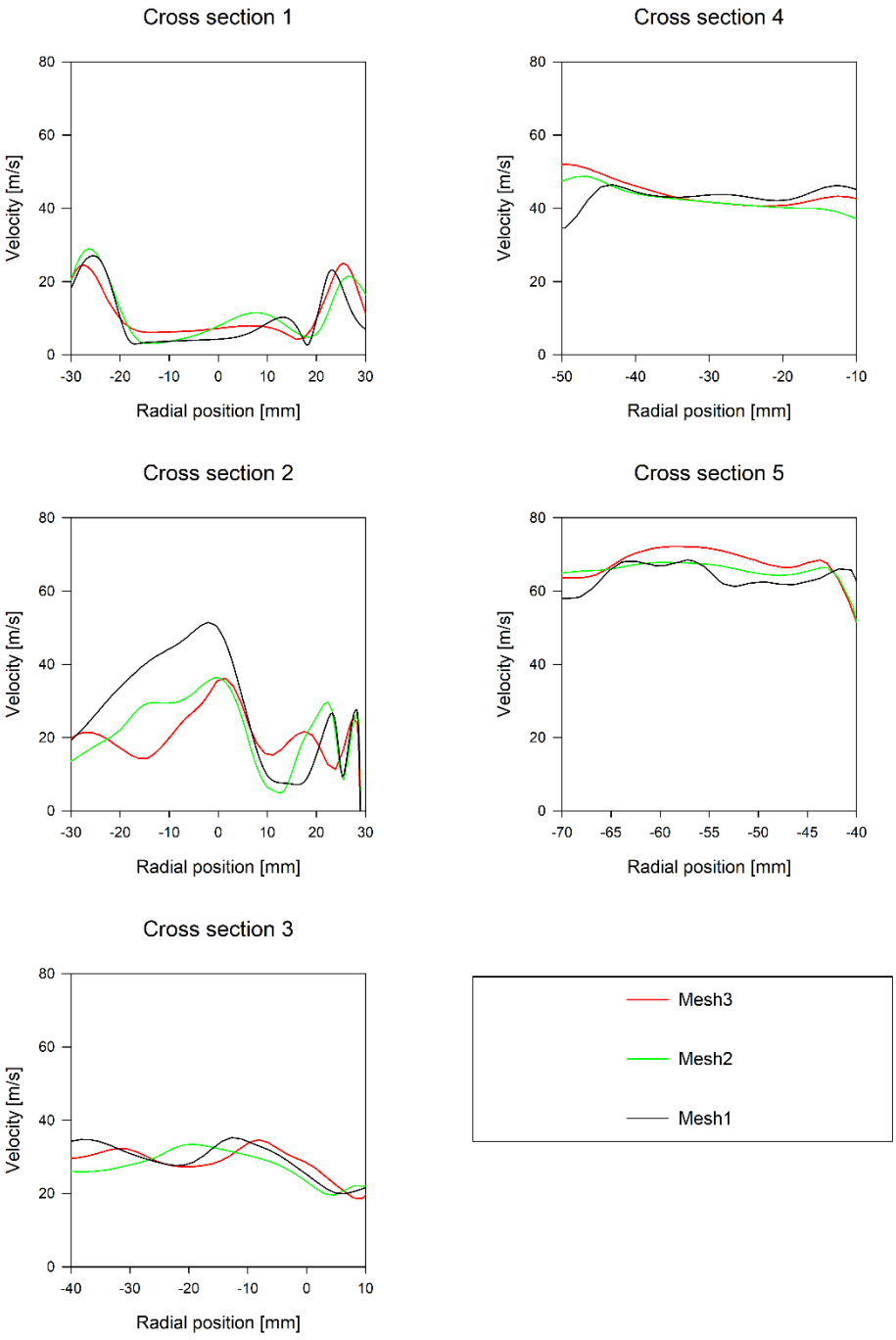

Figure 6.12 Grid independent study – velocity profiles

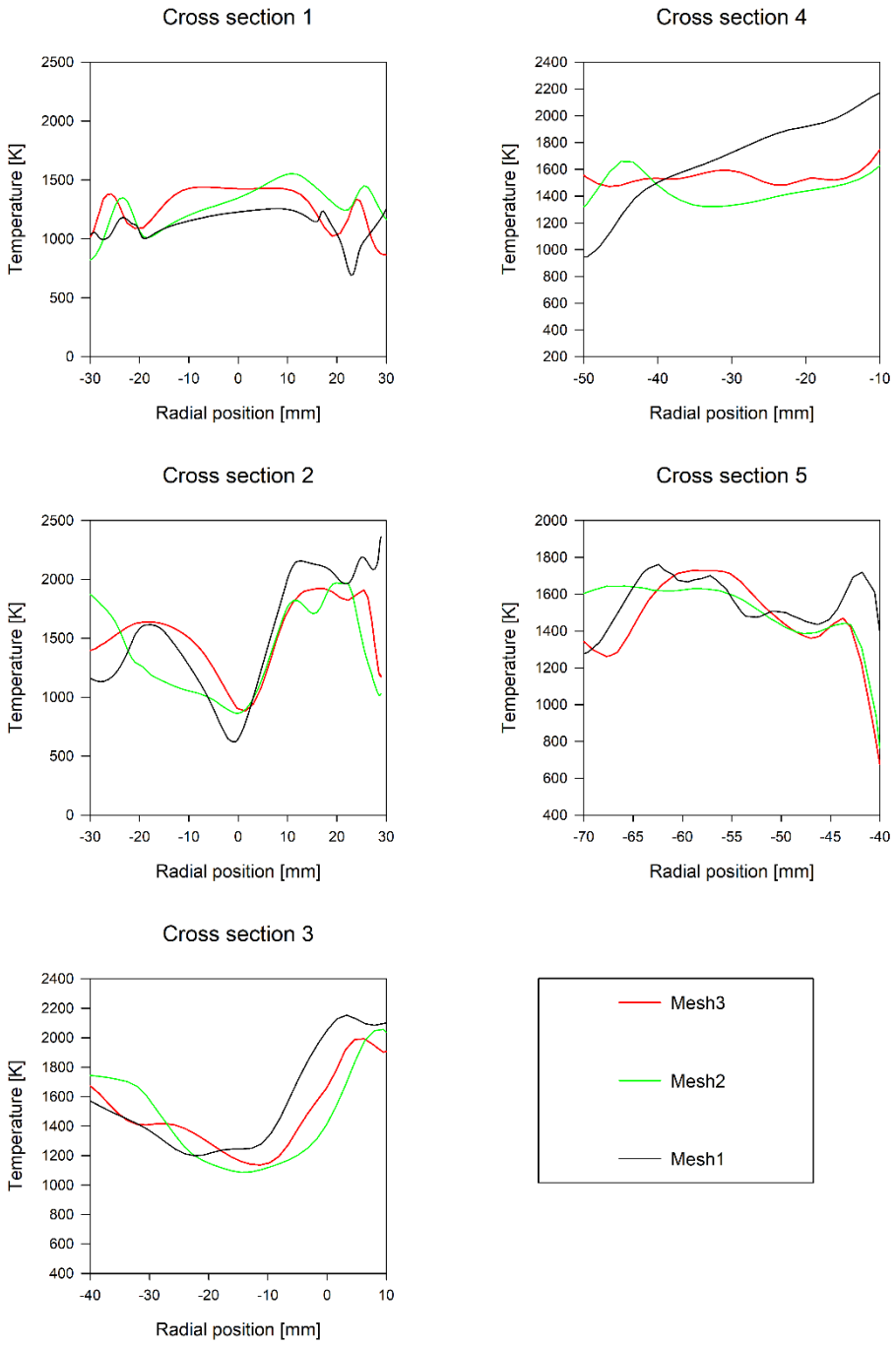

Figure 6.13 Grid independent study – temperature profiles

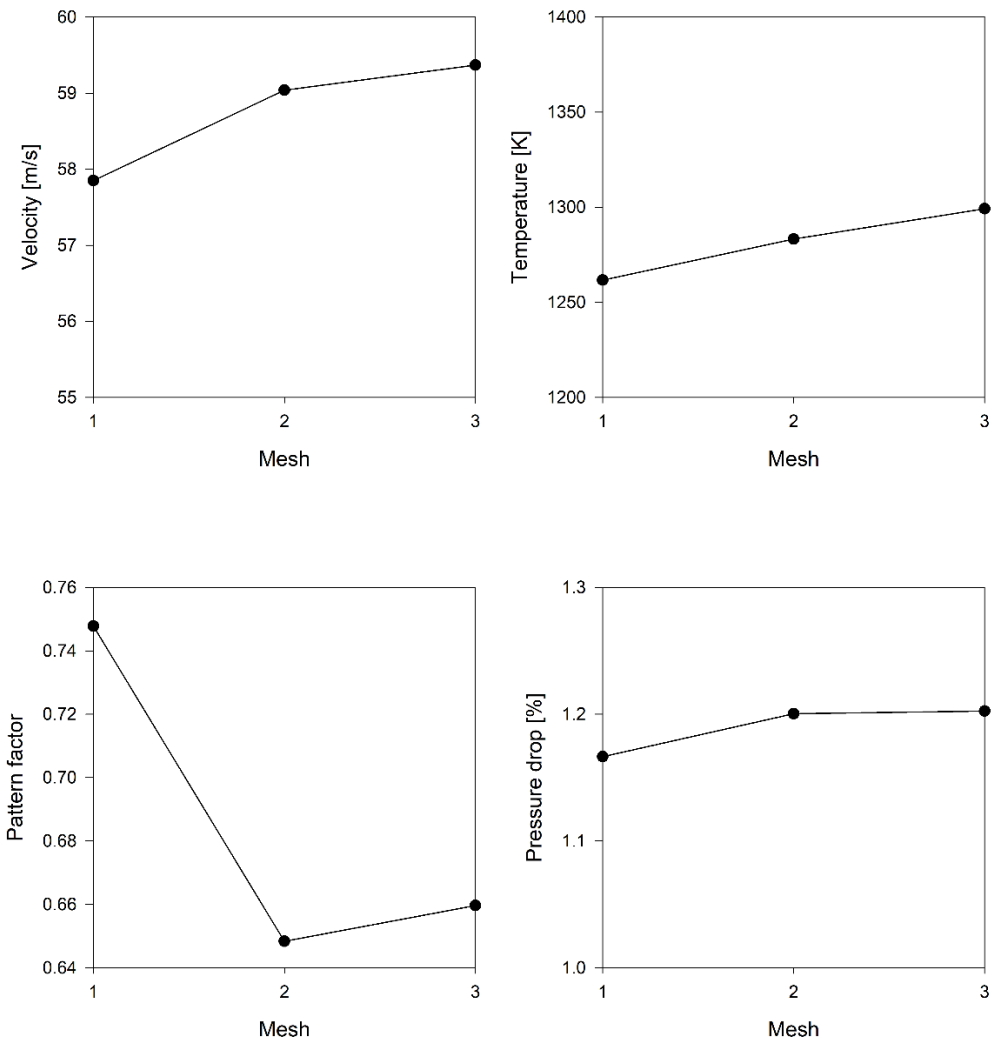

Figure 6.14 Grid independent study – outlet plane

6.4.2 Baseline reacting results

Figures 6.15 to 6.23 show the reacting CFD results of the baseline design. Figure 6.15 shows the velocity contour of the reacting flow; the flow accelerates due to the combination of heat release leading to the gas expansion effect. The primary jet penetration effect is stronger, and the velocity at the outlet is also higher than non-reacting conditions. Figure 6.16 shows the temperature contour; it can be seen that the flame is anchored in the primary zone and high-temperature spots exist after the primary jet. Figure 6.17 shows the mass fraction of n-dodecane, and it is observed that it follows the shear layer and that a high concentration of n-dodecane appears to have a V-shape. Figure 6.18 shows the mass fraction of the hydroxy (OH) radical, which is a flame indicator. It can also explain the possibility of high-temperature spots from Figure 6.19. A mass fraction of CO can be used as an indicator of combustion incompetence, which is shown in Figure 6.20, with a high concentration of CO located after the primary zone observed, which is an intermediate in combustion of carbon-containing fuels. CO is also a toxic product that is treated as a pollutant; therefore, further optimisation is needed to reduce the CO after the primary zone. Finally, Figure 6.21 illustrates the acetylene (C_2H_2), which can be considered a precursor to soot formation. This shows the high concentration of acetylene located inside the primary zone. Table 6.7 shows the mass-weighted average results at the outlet plane. The mass-weighted average temperature at the outlet is 1223.42 K, which lies in an acceptable range of the design

parameter. Pattern factor is used to quantitatively measure the non-uniformity of the outlet temperature distribution, which uses the expression in [124]:

$$Pattern\ factor\ (PF) = \frac{T_{outlet,max} - T_{outlet,avg}}{T_{outlet,avg} - T_{inlet}} \tag{6.8}$$

where T_{inlet}, $T_{outlet,max}$ and $T_{outlet,avg}$ are temperature at the combustor inlet, local maximum temperature, and local average temperature at the combustor outlet, respectively.

Table 6.7 Baseline combustor results at the outlet plane

Mass-weighted average	Value
Mass fraction of CO	3.84×10^{-3}
Mass fraction of OH	1.66×10^{-4}
Mass fraction of C_2H_2	1.08×10^{-4}
Mass fraction of $nC_{12}H_{26}$	1.83×10^{-3}
Mass fraction of NO	1.63×10^{-5}
Temperature [K]	1223
Pattern factor [-]	0.85
Total pressure drop [%]	1.45

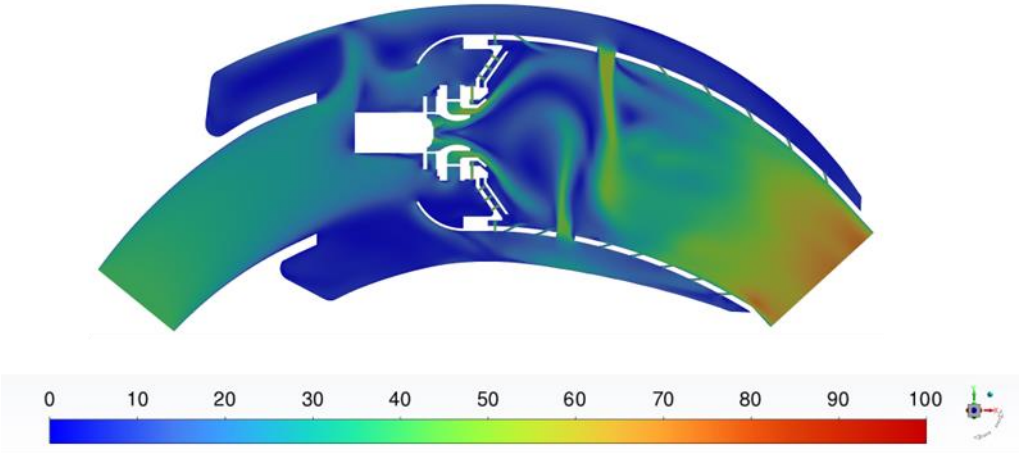

Figure 6.15 Velocity contour of the mid-section plane (z = 0)

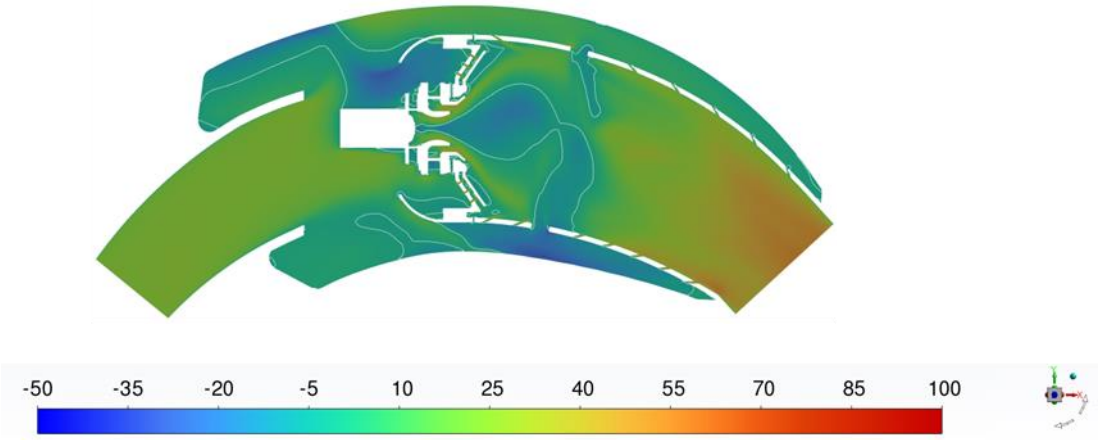

Figure 6.16 Axial velocity contour of mid-section plane (z = 0);
the white iso-contour line shows the axial velocity of 0 m/s

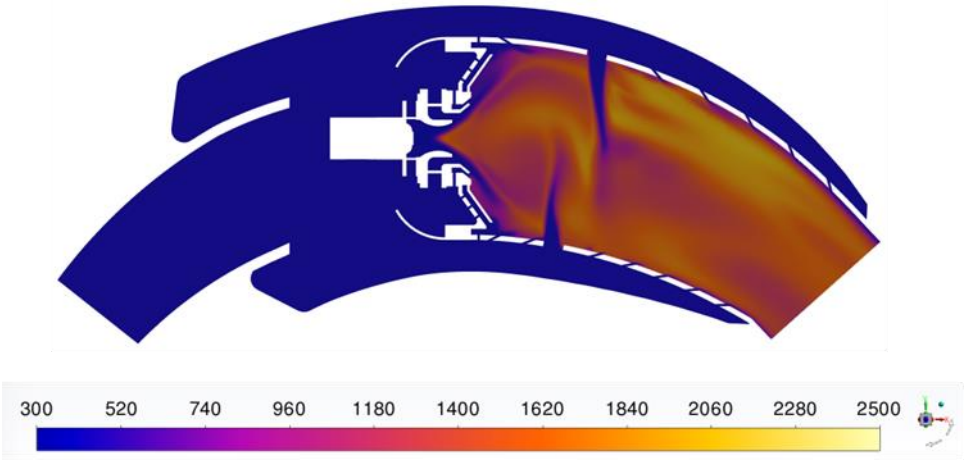

Figure 6.17 Temperature contour of mid-section plane (z = 0)

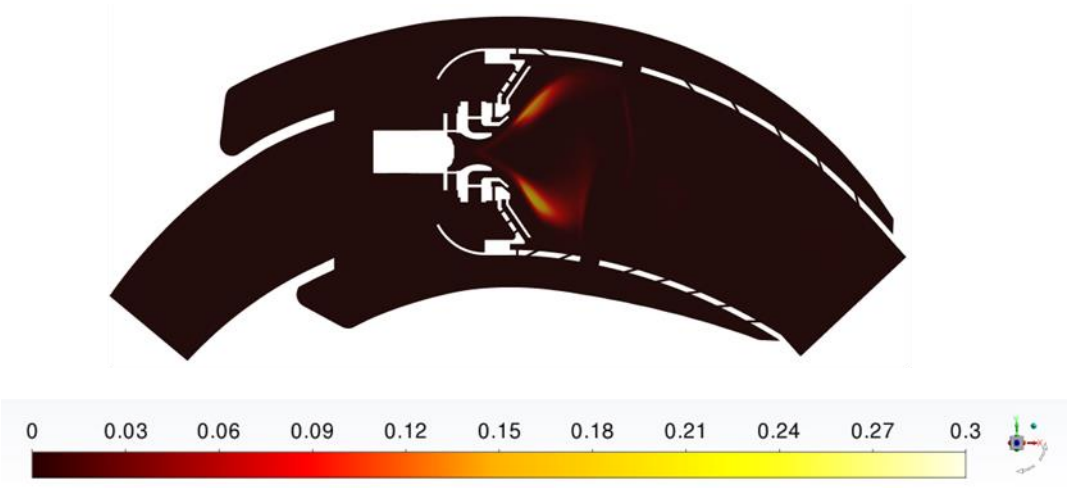

Figure 6.18 Mass fraction of n-dodecane of mid-section plane (z = 0)

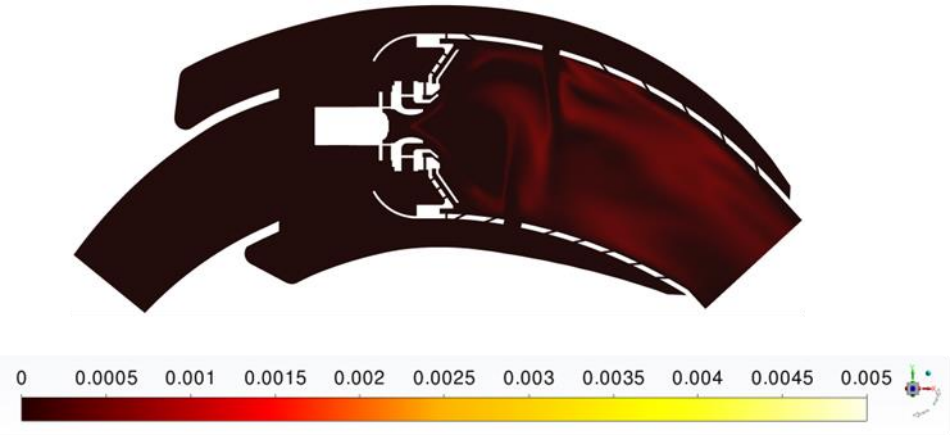

Figure 6.19 Mass fraction of OH radical of the mid-section plane (z = 0)

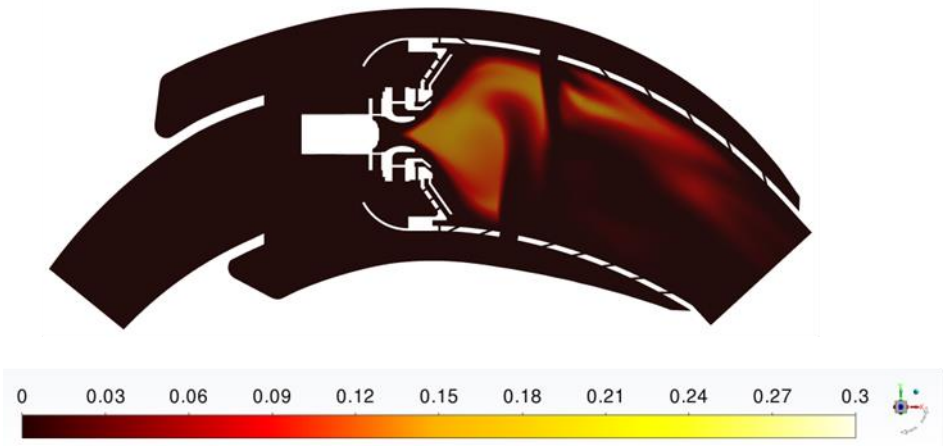

Figure 6.20 Mass fraction of CO of the mid-section plane (z = 0)

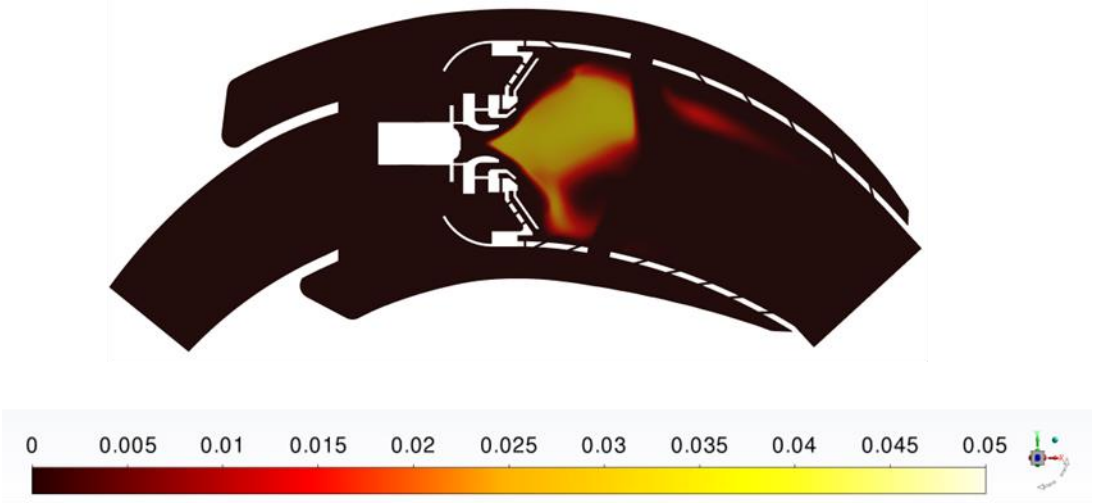

Figure 6.21 Mass fraction of C_2H_2 of the mid-section plane (z = 0)

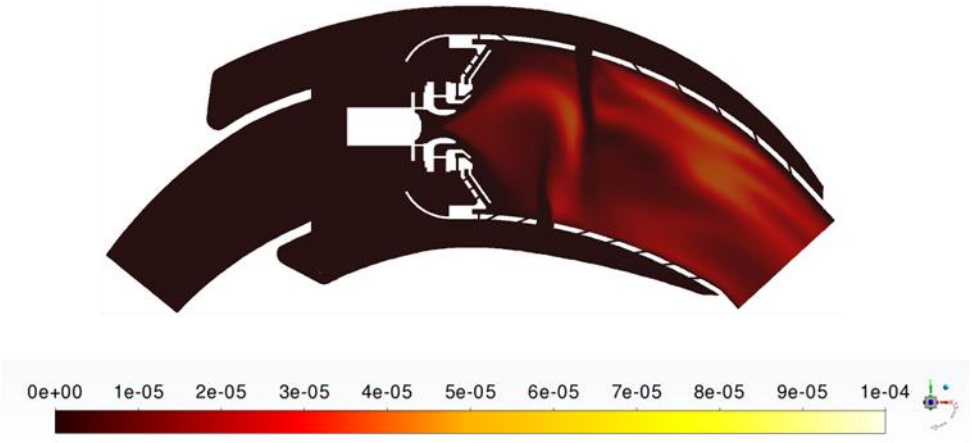

Figure 6.22 Mass fraction of NO of the mid-section plane (z = 0)

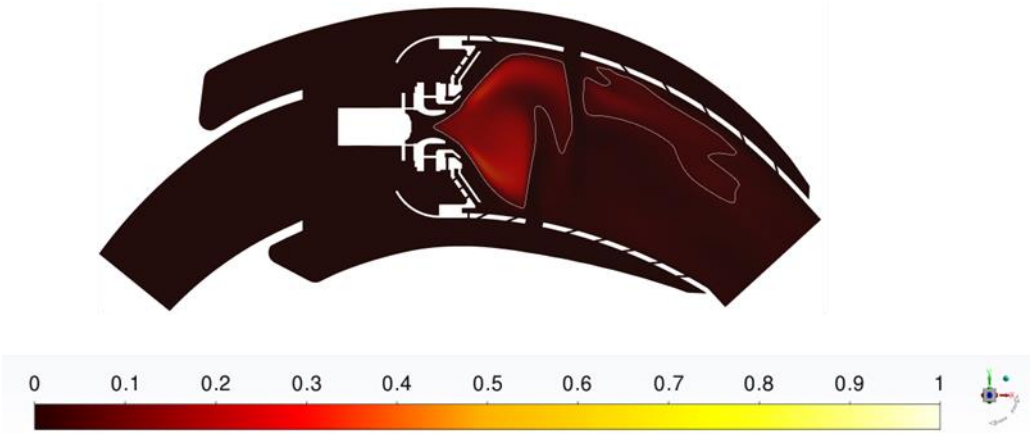

Figure 6.23 Contour of mixture fraction of the mid-section plane (z = 0); the white iso-contour shows the stoichiometric mass fraction value (Y_{st} = 0.06246)

6.4.3 Effect of boundary conditions

As shown in Table 1.3, the combustor is designed to operate at a pressure ratio of 3.7, and the air mass flow rate from the compressor is 150g/s. Two boundary conditions in CFD can be used to solve this problem. The velocity inlet is intended for incompressible flows with an assumption that the velocity profile is uniform and can be computed from the mass flow rate and the area of the domain. Therefore, the static pressure adjusts to accommodate the prescribed velocity distribution, and the total pressure also varies. Another type of boundary condition for inlet is pressure inlet; the total pressure is prescribed at the inlet, so the mass flow rate varies accordingly. Table 6.8 shows the two boundary conditions.

Table 6.8 Two types of boundary conditions used in CFD

	Inlet	Outlet
BC1	Mass flow rate of 150 g/s	Static pressure of 374902.5 Pa
BC2	Total pressure of 374902.5 Pa	Static pressure of 374902.5 Pa

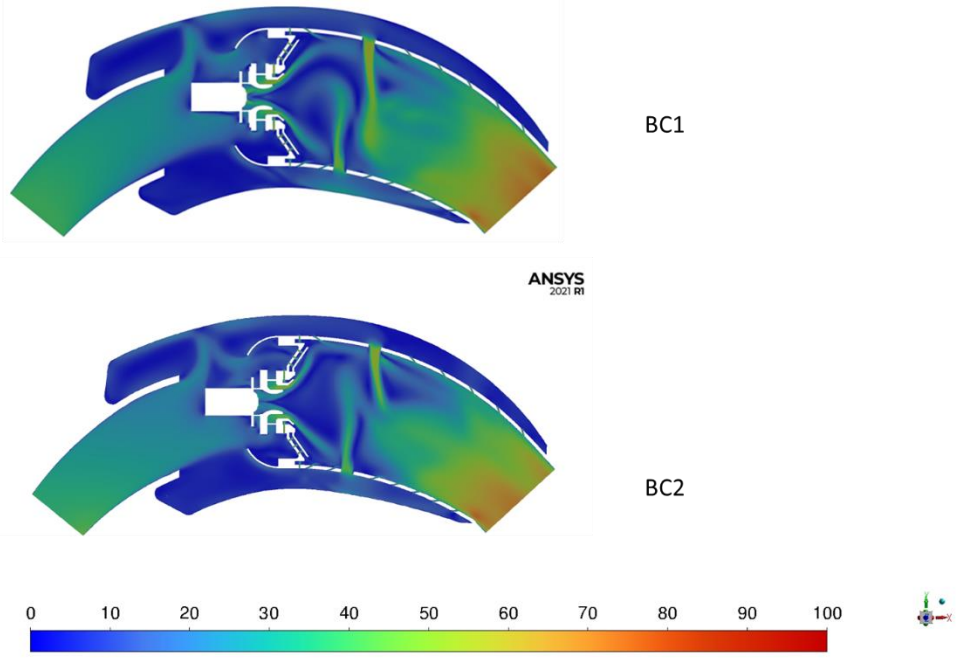

Figure 6.24 Velocity magnitude for BC1 and BC2

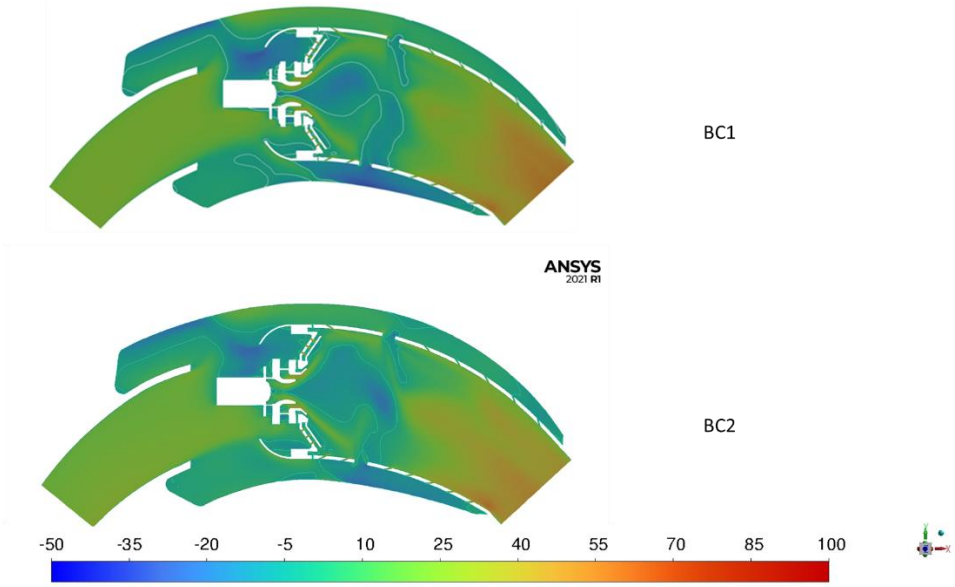

Figure 6.25 Axial velocity for BC1 and BC2

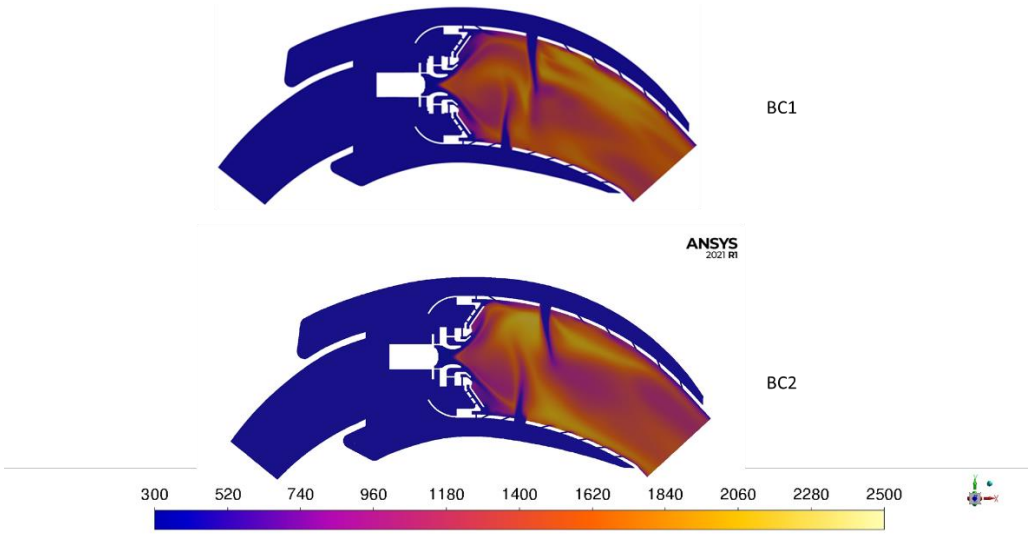

Figure 6.26 Temperature for BC1 and BC2

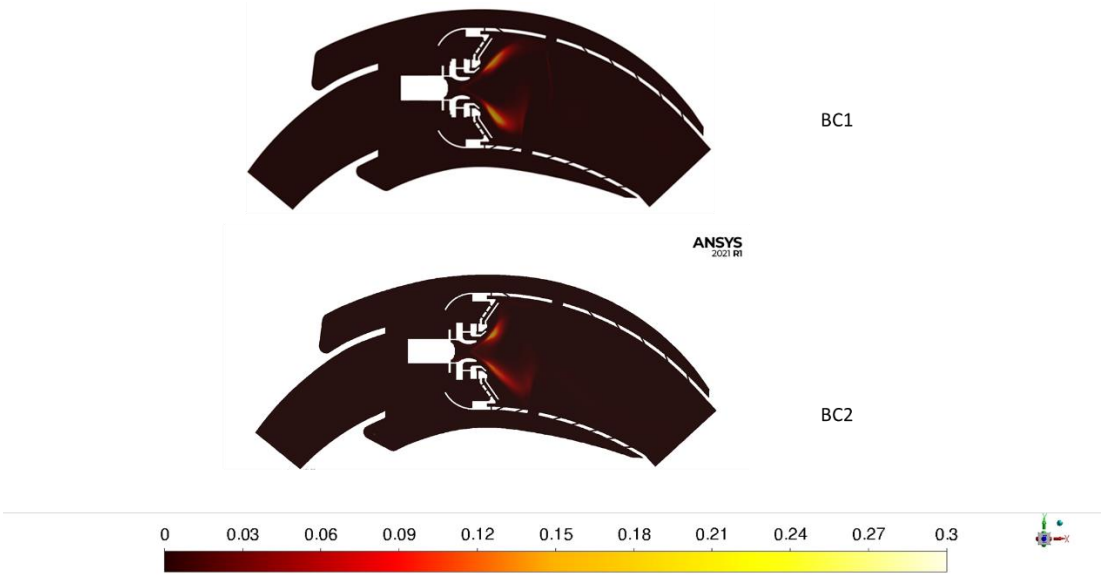

Figure 6.27 Mass fraction of n-dodecane for BC1 and BC2

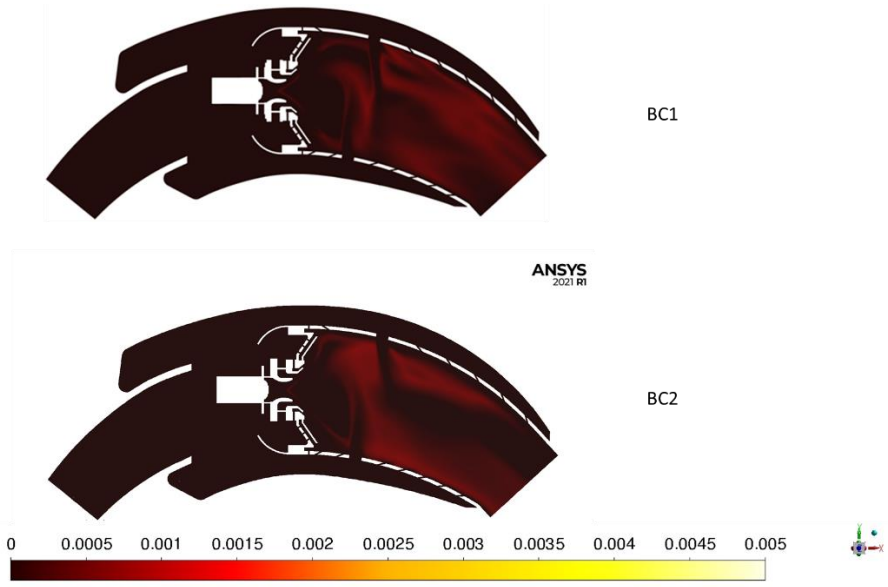

Figure 6.28 Mass fraction of OH for BC1 and BC2

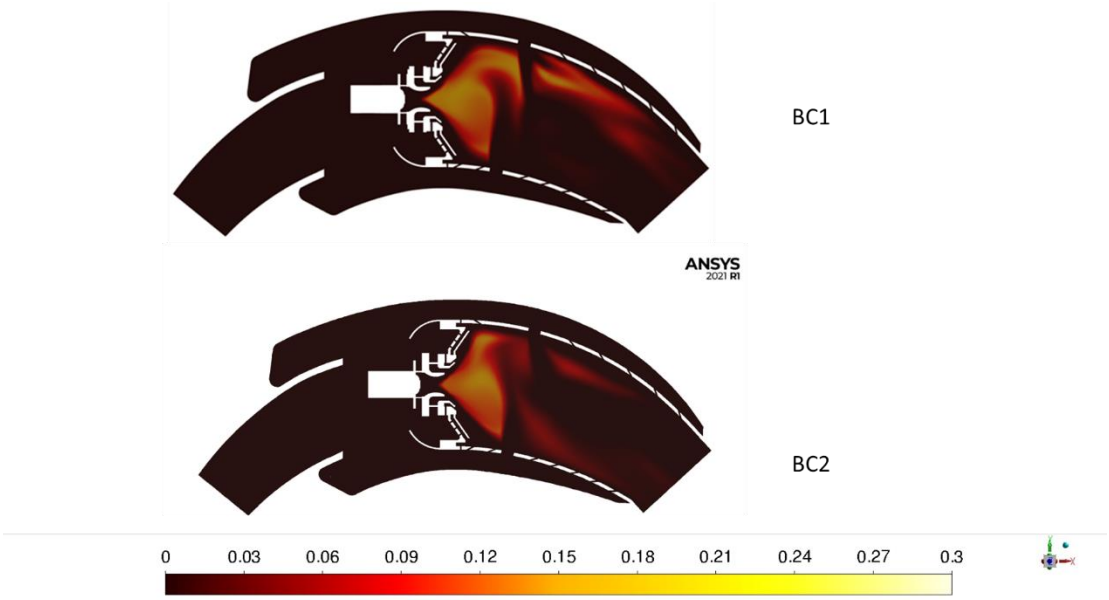

Figure 6.29 Mass fraction of CO for BC1 and BC2

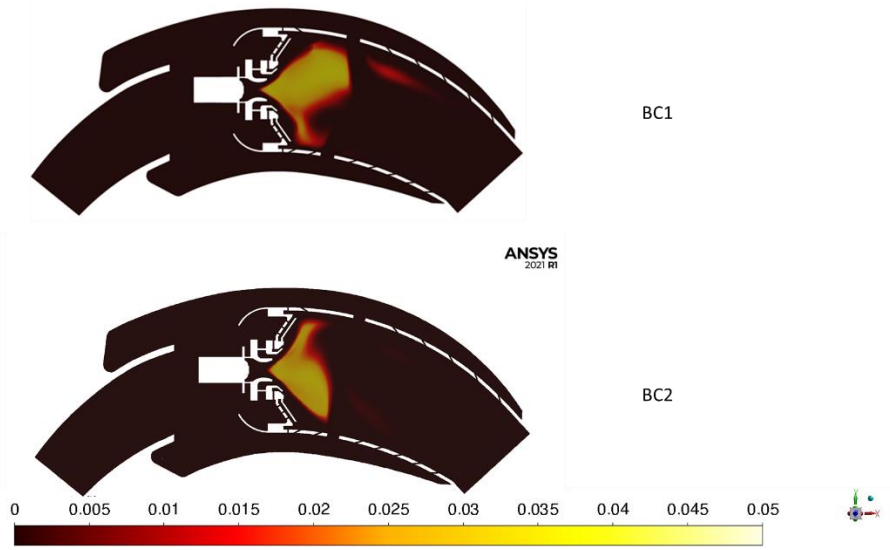

Figure 6.30 Mass fraction of C2H2 for BC1 and BC2

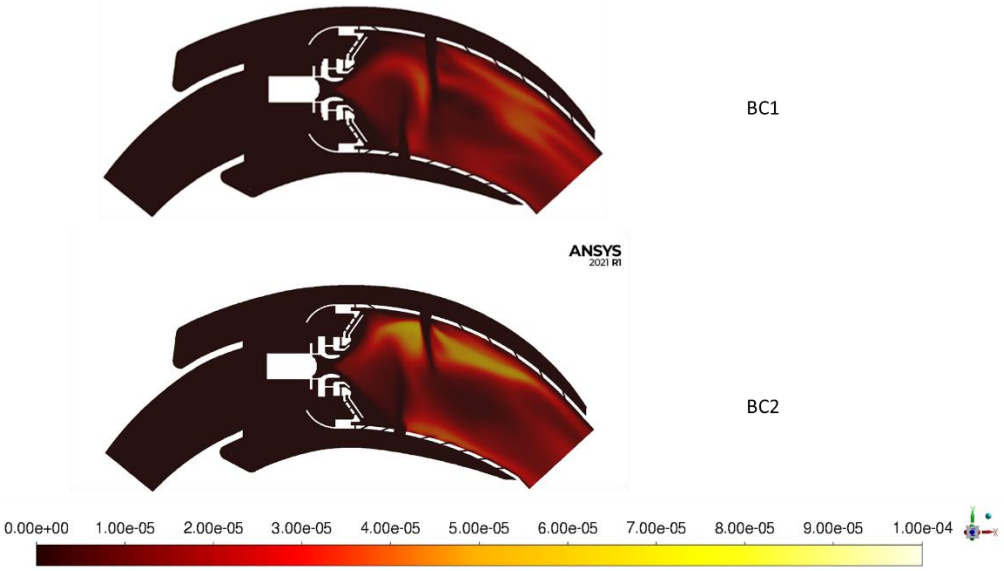

Figure 6.31 Mass fraction of NO for BC1 and BC2

Table 6.9 Results comparison for BC1 and BC2 at combustor outlet

	BC1	BC2	% difference
Mass outlet [g/s]	150	147	−2.3
Mass fraction of OH at outlet [-]	1.66×10^{-4}	2.7×10^{-3}	−8.7
Mass fraction of n-dodecane at outlet [-]	1.83×10^{-3}	1.42×10^{-3}	−22.6
Mass fraction of CO at outlet [-]	3.84×10^{-3}	2.70×10^{-3}	−29.6
Mass fraction of C2H2 at outlet [-]	1.08×10^{-4}	3.48×10^{-5}	−67.8
Mass fraction of NO at outlet [-]	1.63×10^{-5}	1.73×10^{-5}	5.9
Temperature at outlet [K]	1223	1232	0.7
Pattern factor [-]	0.85	1.10	29.9
Total pressure drop [%]	1.45	1.29	−0.2

Figures 6.24 to 6.31 shows the velocity and mass fraction of important species and the temperature fields of two boundary conditions. Table 6.9

compares the values at the combustor outlet. The 2.3% difference in terms of the mass flow resulted in large discrepancies in the species mass fraction at the outlet. However, the percentage error of the total pressure drop was 0.2% and the percentage error of the average temperature at the outlet was 0.7%. As the mass flow rate from the air compressor is also an important parameter to consider, BC1 will be used in the following section for the design parametric study.

6.5 Design parametric analysis

The combustor was simulated and the baseline results of the reacting CFD were discussed in Section 6.4. In the design of an RQL combustor for low emissions, the structural parameters and operating conditions have a significant impact [125]; hence, it was important to investigate the influence of structural parameters and operating conditions by using the combustion models developed in the previous chapters. The objectives were to lower the value of n-dodecane, species of carbon monoxide (CO), hydroxyl (OH), acetylene (C_2H_2), nitric oxide (NO), and pattern factor at the outlet to improve combustion efficiency and pollutant reduction.

In this section, the focus is on investigating the influence of the diameter of primary holes, the number of primary holes, and the locations of the primary holes on combustion species, pattern factor, and NO concentration. [126] and [127] highlighted that primary holes are important in controlling

NOx emissions because primary holes introduce air into the combustor that interacts with swirling flows, which has a beneficial effect on NOx emissions and a flame stabilisation mechanism. The experimental and numerical analysis of a confined combustor has been investigated, and the local equivalent ratio has an impact on the outlet temperature and recirculation zone, as reported in [128]. Wang et al. [129] have shown numerically that dilution holes have a major impact on outlet temperature distribution control and pattern factor.

Hence, the parametric analysis focused on the effect of primary hole size, the number of primary holes, and the locations of primary holes to understand the combustor performance as well as emissions prediction of this novel shape burner regarding the aerodynamic effect.

Agrawal [130] listed the diesel fuel operating fuel temperature range from ambient up to 380 K in stationary generator turbines, automotive diesel engines, and marine diesel engines. It is suggested in [131] and [132] that preheated liquid fuel shows significant improvement in fuel atomisation due to its density: surface tension and viscosity decrease as temperature rises.

From the engine cycle efficiency point of view, a heat exchanger is a promising approach to increase the overall cycle efficiency because of the low-pressure ratio in micro gas turbine engines [133]. The hot burnt gas mixtures pass through the heat exchanger and re-enter into the combustor at the inlet. Serval studies have investigated increased inlet temperature to

combustion performance and emission prediction [134], [135]. Therefore, an air temperature of 700 K was chosen to understand the combustor performance and emission prediction of this novel combustor. The reduction in fuel flow rate was calculated using Equation 6.9 and Equation 6.10, assuming the diesel lower heating value (LHV) of 43MJ/kg:

$$Q_{in} = \dot{m} c_p \Delta T \tag{6.9}$$

$$Q_{in} = \dot{m}_f \times LHV \tag{6.10}$$

where Q_{in} is the heat addition due to combustion, $\dot{m}$ is air mass flow from the compressor, c_p is the specific heat capacity, ΔT is the temperature difference between compressor outlet and turbine inlet, and $\dot{m}_f$ is the fuel flow rate.

Hence, fuel temperature and air temperature were the two operational factors chosen to understand the operational effects on combustor performance and emission prediction. The parameters and operating conditions parameters were studied using the experimental methodology design described in the following section.

6.5.1 Design of experiment (DoE)

From the literature, key parameters of the structural and operational change affecting combustor performance and emissions were identified. Design of experiment is a systematic approach to investigate the impact of multiple different factors on a response. Seok applied CFD and two DoE, which are fractional factorial design and response surface method (RSM), to minimise the resistance of the bow shape of a tanker hull [136]. The factorial design was successfully utilised to reduce the number of geometry configurations from more than 1000 to 84 in a study of the NASA Crew Exploration Vehicle (CEV) [137]. A full factorial design with CFD spray modelling has been used to identify the effects of vapour and liquid penetration by four different factors [138]. A type of DoE, which is a four-factor Latin hypercube space-filling design with CFD, has been used to study forces and moments acting on a missile through various speeds and angles of attack [139]. DoE with CFD was shown to be efficient and beneficial for studying a large number of factors. It is important to carefully select useful factors and to consider the range of levels.

In this thesis, 2-level fractional factorial design together with the CFD modelling presented in the previous section was used to investigate the effect of five factors on the major species concentration, temperature, pattern factor, and total pressure drop across the combustor.

In general, reacting CFD simulation requires considerable computational resources, as the solver needs to solve N-S equations plus the transport

equation for mixture fraction and progress variable. Therefore, due to a limited budget and resources, fractional factorial design with resolution V was used to study five factors for the purpose of reducing the number of experimental runs by 50%, and there were no main effects or 2-factor interactions aliased with any other main effect or 2-factor interactions. The design parameters and the DoE layout are presented in Tables 6.10 and 6.11.

Table 6.10 The design parameters and level of the combustor

Parameter	Unit	Level (-1)	Level (+1)
Primary holes diameter (A)	mm	7.8 (baseline)	9
Number of primary holes (B)	-	6 (baseline)	10
The streamwise distance of primary holes (C)	mm	0 (baseline)	15
Fuel temperature (D)	K	341 (baseline)	380
Air temperature (E)	K	442 (baseline)	700

Table 6.11 Design of Experiment of five different factors

Run	A	B	C	D	E
1	7.8	10	0	380	700
2	7.8	6	15	341	442
3	7.8	10	15	380	442
4	9	6	15	380	442
5	7.8	10	0	341	442
6	7.8	6	0	380	442
7	9	10	0	341	700
8	9	10	15	341	442
9	9	10	0	380	442
10	7.8	6	0	341	700
11	7.8	6	15	380	700
12	7.8	10	15	341	700
13	9	10	15	380	700
14	9	6	0	341	442
15	9	6	0	380	700
16	9	6	15	341	700

Table 6.12 Results of DoE; Y denotes species mass fraction, T is temperature, PF is pattern factor and dP is the total pressure drop

Run	Y_{CO} [-]	$Y_{C_2H_2}$ [-]	Y_{OH} [-]	$Y_{nC_{12}H_{26}}$ [-]	Y_{NO} [-]	T [K]	PF [-]	dP [%]
1	3.52×10^{-4}	1.42×10^{-5}	5.10×10^{-6}	2.17×10^{-4}	1.22×10^{-5}	1.24×10^{3}	0.42	1.82
2	1.03×10^{-3}	2.00×10^{-5}	1.22×10^{-4}	1.23×10^{-3}	1.19×10^{-5}	1.26×10^{3}	0.94	0.76
3	2.43×10^{-3}	3.13×10^{-5}	1.86×10^{-4}	1.14×10^{-3}	1.15×10^{-5}	1.24×10^{3}	0.96	0.98
4	1.81×10^{-3}	2.74×10^{-5}	1.54×10^{-4}	1.45×10^{-3}	1.07×10^{-5}	1.24×10^{3}	0.83	0.79
5	1.41×10^{-3}	2.19×10^{-5}	1.20×10^{-4}	1.12×10^{-3}	1.40×10^{-5}	1.26×10^{3}	0.77	0.39
6	1.03×10^{-3}	1.88×10^{-5}	1.09×10^{-4}	1.10×10^{-3}	1.56×10^{-5}	1.26×10^{3}	0.55	0.38
7	8.09×10^{-5}	3.50×10^{-6}	3.40×10^{-6}	2.11×10^{-4}	1.05×10^{-5}	1.28×10^{3}	0.70	1.04
8	3.60×10^{-3}	5.56×10^{-5}	1.88×10^{-4}	1.54×10^{-3}	1.00×10^{-5}	1.20×10^{3}	1.08	0.6
9	2.04×10^{-3}	3.42×10^{-5}	1.30×10^{-4}	1.33×10^{-3}	1.40×10^{-5}	1.24×10^{3}	0.89	0.66
10	2.10×10^{-4}	9.10×10^{-6}	4.60×10^{-6}	3.58×10^{-4}	1.27×10^{-5}	1.28×10^{3}	0.48	1.88
11	4.24×10^{-4}	1.77×10^{-5}	8.10×10^{-6}	3.43×10^{-4}	1.17×10^{-5}	1.28×10^{3}	0.61	1.96
12	4.85×10^{-4}	1.84×10^{-5}	1.30×10^{-5}	3.58×10^{-4}	9.00×10^{-6}	1.28×10^{3}	0.93	1.54
13	4.63×10^{-4}	1.91×10^{-5}	8.80×10^{-6}	3.57×10^{-4}	1.12×10^{-5}	1.28×10^{3}	0.42	1.43
14	1.73×10^{-3}	2.26×10^{-5}	1.44×10^{-4}	1.49×10^{-3}	1.41×10^{-5}	1.23×10^{3}	0.86	0.55
15	3.45×10^{-4}	1.47×10^{-5}	6.00×10^{-6}	3.93×10^{-4}	1.43×10^{-5}	1.28×10^{3}	0.49	1.81
16	5.98×10^{-4}	2.50×10^{-5}	1.00×10^{-5}	3.40×10^{-4}	1.04×10^{-5}	1.27×10^{3}	0.65	1.72

Table 6.12 presents the recorded CFD results at the combustor outlet. Minitab software was used to identify the factors that influence the mean major species concentration, temperature, pattern factor. and total pressure drop across the combustor. The following sections use a main effect plot and interaction plot to determine which factor has the most significant impact.

6.5.2 Effect of mass fraction of CO on factors

In this section, the main effects and interaction effects of five factors on the mass-weighted averaged mass fraction of carbon monoxide (CO) at the combustor outlet are investigated. Carbon monoxide is a by-product during incomplete combustion of fuels due to the insufficient presence of oxygen. The first step in the analysis involved checking the data for normality assumptions, followed by a Pareto plot of effects to identify the most important main and interaction effects. Moreover, a main effect and an interaction plot were used to analyse the interaction between the factors.

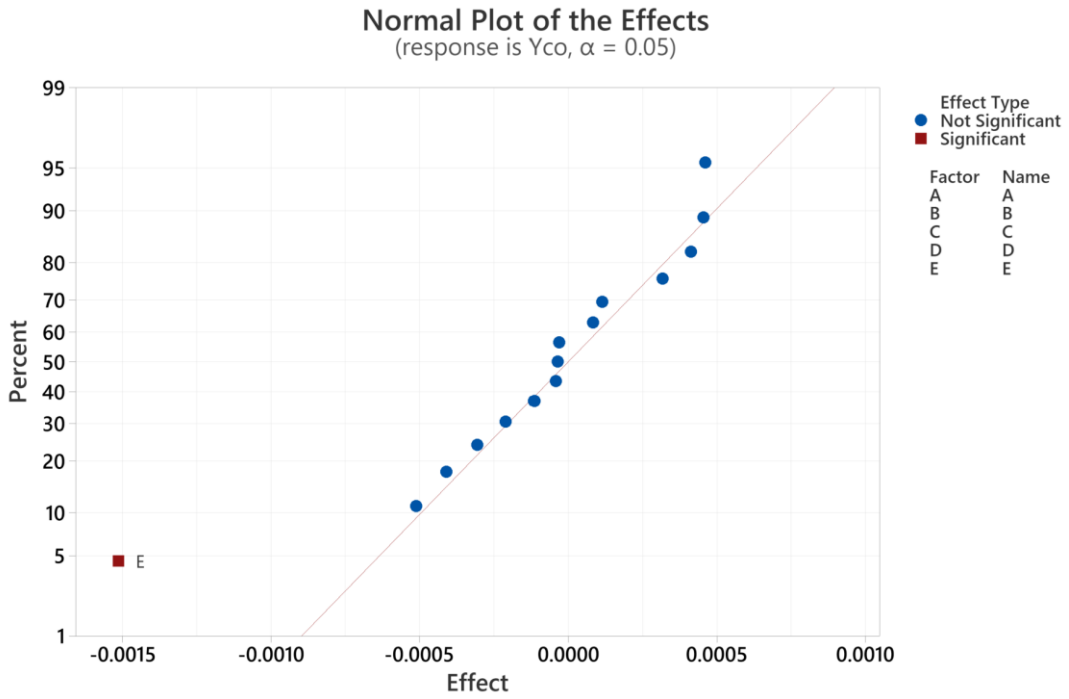

Figure 6.32 Normal plot of the effects for the mass fraction of CO

Figure 6.32 suggests that the data followed a normal distribution. The Pareto plot shows the effects in decreasing order of the absolute value of the standardised effects and draws a reference line on the chart. Any effect that extends the reference lines appears to be statistically significant. Figure 6.33 shows that the main effect of factor E is statistically significant at the 5% significance level. None of the interactions appear to be statistically significant.

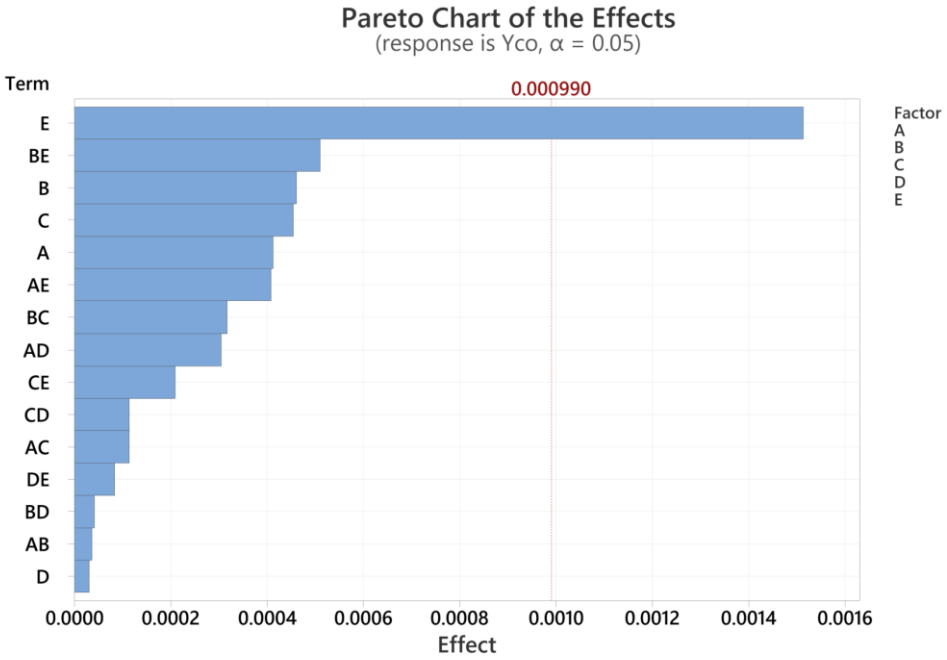

Figure 6.33 Pareto chart of the effects for the mass fraction of CO

Figure 6.34 shows that Factor E, which is the air temperature, had the most significant effect, as the gradient of the curve is the largest compared to the other factors. In addition, the mass fraction of CO decreased as the air temperature increased. Factors A (diameter of primary holes), B (number of primary holes) and C (streamwise distance of primary holes) showed secondary effects. The mass fraction of CO increased as the geometric parameters increased. Factor D, which is the fuel temperature, showed little effect on the mass fraction of CO at the combustor outlet.

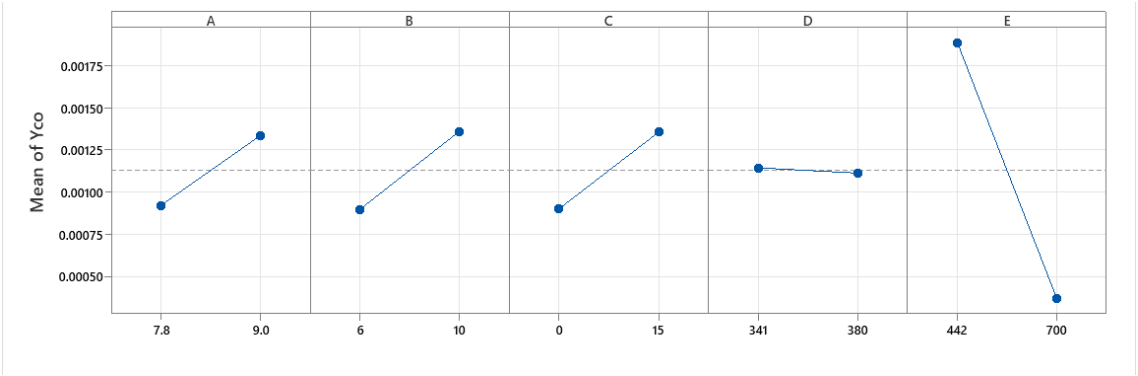

Figure 6.34 Main effects plot for the mass fraction of CO

Figure 6.35 shows the interaction plot for the mass fraction of CO on the five factors. The more parallel the line for each factor, the more they interact with each other. There are minimal interactions between Factors AB, AC, BD, CE, DC, and DE. On the other hand, there is an interaction, such that for Factors D and A, when the larger diameter of the primary hole produces less CO than when the fuel temperature is 341 K. However, at a fuel temperature of 380 K, the mass fraction CO is almost the smallest, regardless of the diameter of primary holes. There is no noticeable interaction between Factor E and other factors. The combination of Factor E with the other factors can drive the mass fraction of CO to decrease, and the higher fuel temperature (D) and large diameter of primary holes (A) can reduce the mass fraction of CO.

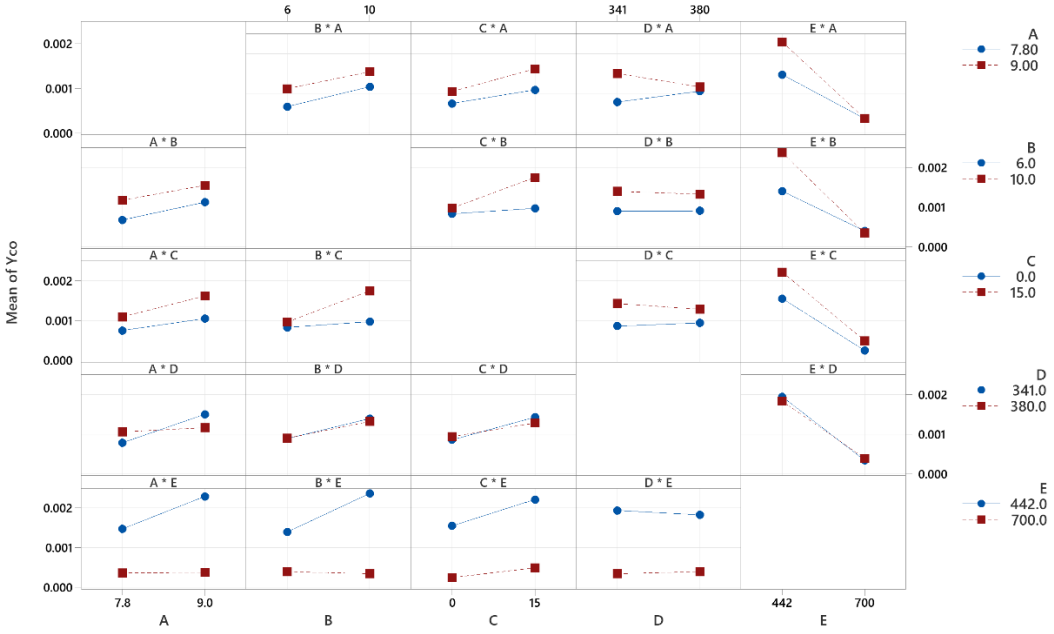

Figure 6.35 Interaction plot for the mass fraction of CO

6.5.3 Effect of mass fraction of C2H2 on factors

In order to identify the significant main effects and interaction effects, the normal plot and Pareto chart were used. In a normal plot, those effects that fall off the straight line are deemed to be statistically significant and those that fall along the straight line are deemed to be statistically insignificant. Figures 6.36 and 6.37 show that the main effect of Factor E is statistically significant at the 5% significance level.

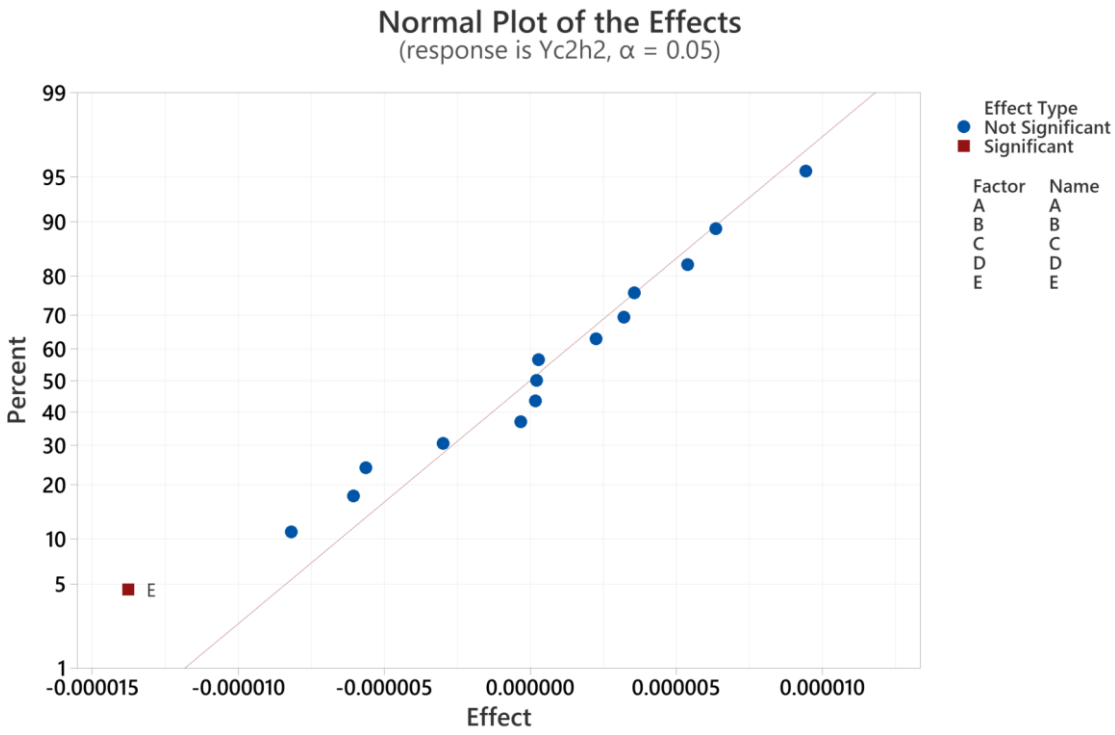

Figure 6.36 Normal plot of the effects for mass fraction of C2H2

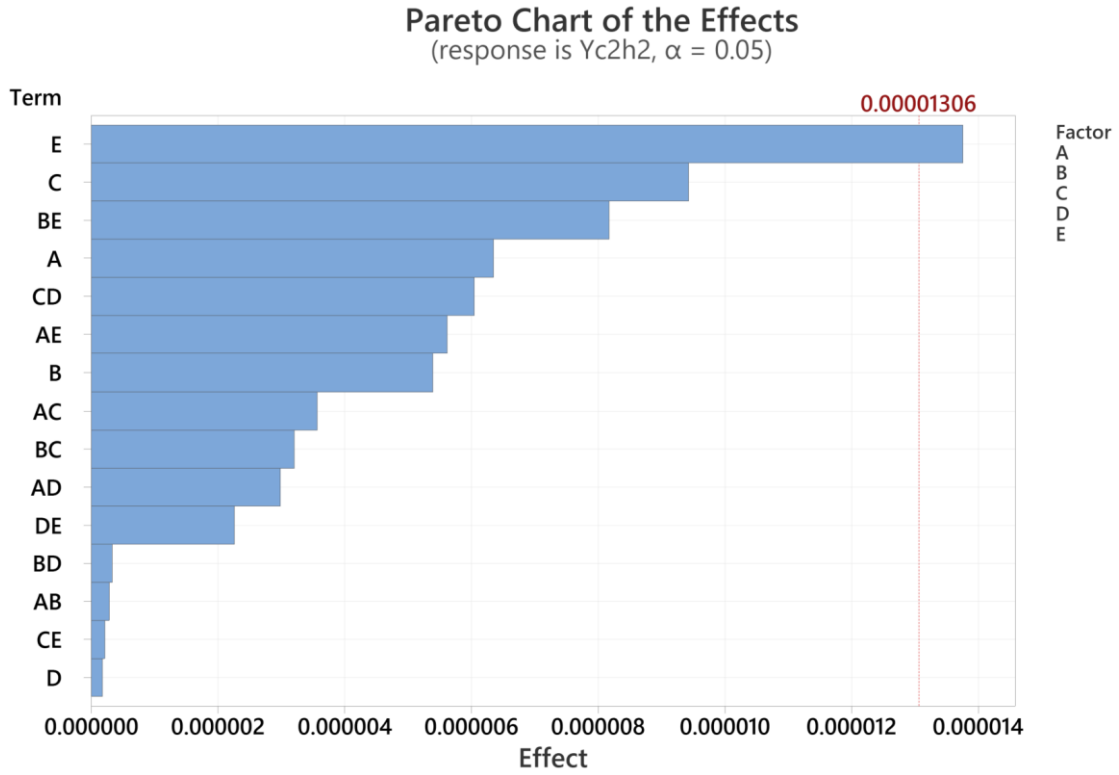

Figure 6.37 Pareto chart of the effects for mass fraction of C2H2

In Figure 6.38, the main effect of factors for the mass fraction of acetylene (C2H2) at the combustor outlet can be illustrated. The acetylene (C2H2) can be considered a soot precursor in hydrocarbon flames [140]. The figures show aa similar trend as Figure 6.32. The mass fraction of C2H2 at the combustor outlet decreased with the increase in air inlet temperature (factor E). The mass fraction of C2H2 increases with the increases in factors A, B, and C. Factor D, which is fuel temperature, has little influence on the mass fraction of C2H2.

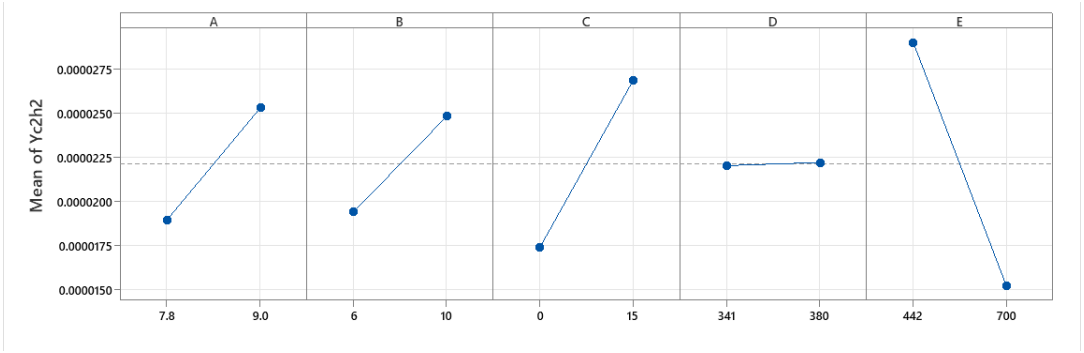

Figure 6.38 Main effects plot for mass fraction of C2H2

Figure 6.39 shows the interaction plot for the mass fraction of C2H2. There are few interactions between Factors AB, BD, and CE. Although the main effect plot shows that the factor had very little effect on the mass fraction of C2H2, the most significant interaction that could be observed was in Factors AD and CD. The lines crossed over each other, which means the fuel temperature of 341 K produces more mass fraction of C2H2 at the combustor outlet with the increased level of Factors A (diameter of primary holes) and C (streamwise distance of primary holes).

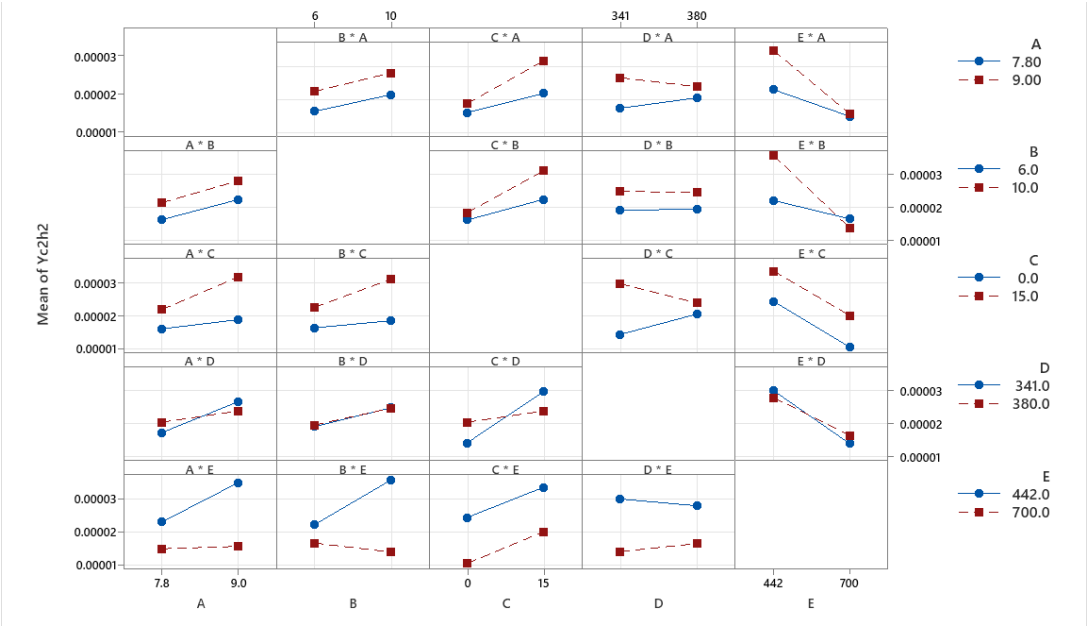

Figure 6.39 Interaction plot for mass fraction of C2H2

6.5.4 Effect of mass fraction of OH on factors

It can be seen in Figure 6.40 that all the points on the normal plot come close to forming a straight line, which implies that the data are normal. Figures 6.40 and 6.41 show that the main effects of Factor E are statistically significant at the 5% significance level.

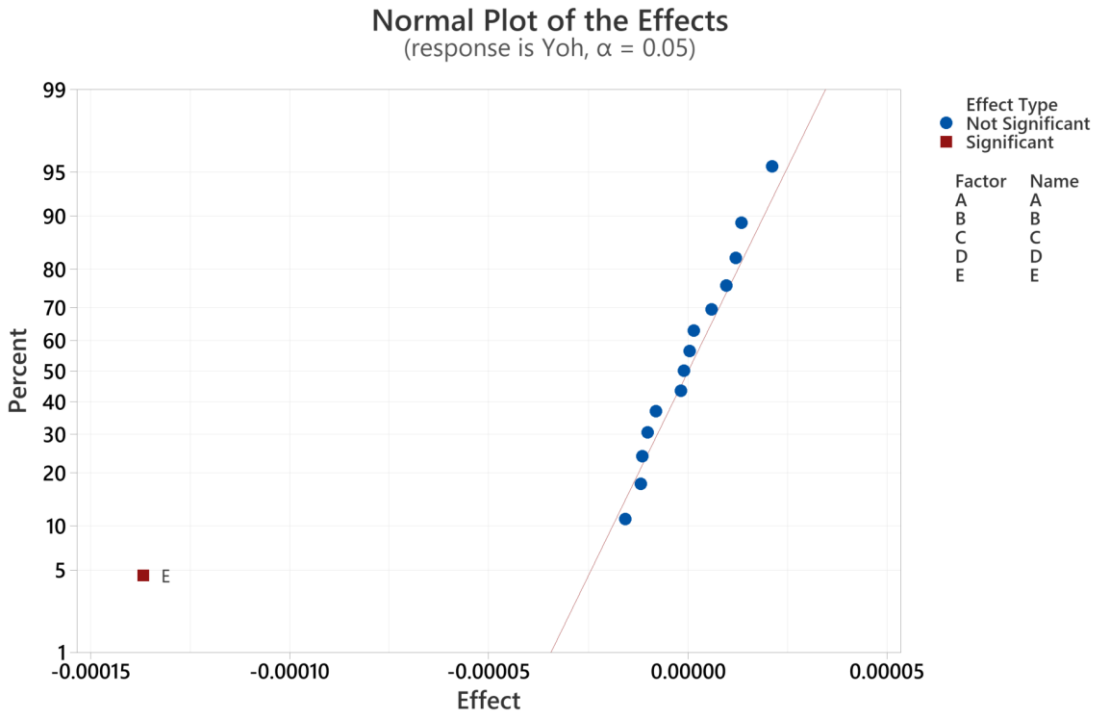

Figure 6.40 Normal plot of the effects of mass fraction of OH

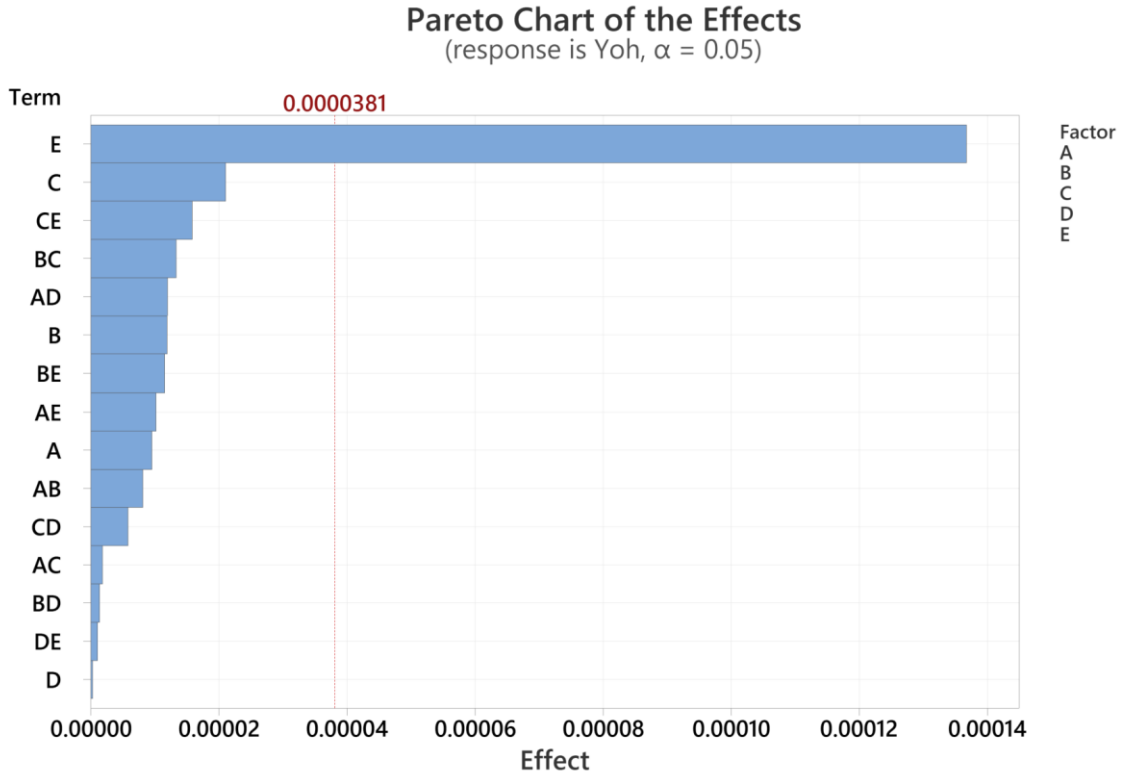

Figure 6.41 Pareto chart of the effects of mass fraction of OH

In Figure 6.42 we can see the main effects plot for mass fraction of hydroxyl radical (OH) at the combustor outlet. The mass fraction of OH product imaging can characterise local heat release rate (HRR) in [141]. The OH radical characterisation has been widely used to characterise the flame HRR; hence, the mass fraction of OH was chosen to become one of the factors to monitor and optimise the combustor. Factor E (air inlet temperature) had the most significant effects on the mass fraction of OH at the combustor outlet. The mass fraction of OH decreased with increasing air temperature. For Factors A (primary hole diameter), B (number of primary holes), and C (streamwise direction of primary holes), the geometric feature

of the combustor had little effect on the mass fraction of OH. Factor D (fuel temperature) showed no effect on the mass fraction of OH.

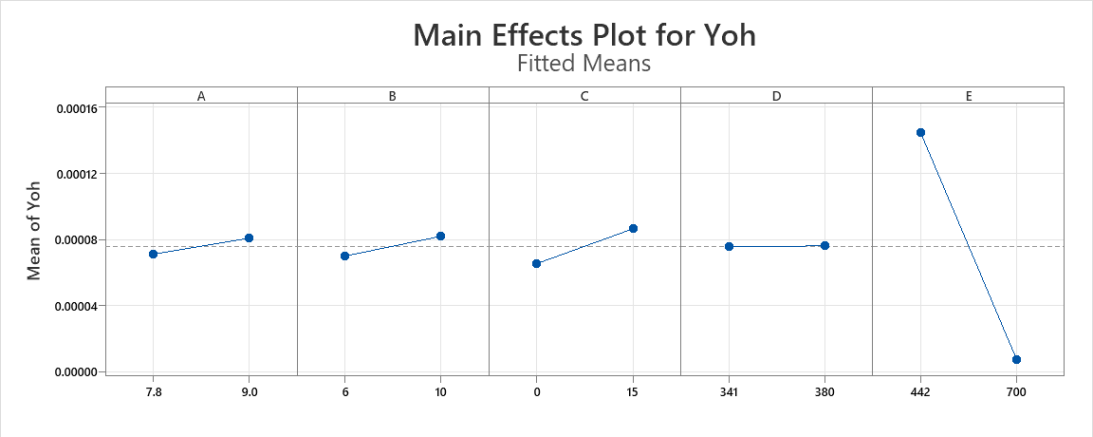

Figure 6.42 Main effects plot for mass fraction of OH

Figure 6.43 shows the interaction plot for mass fraction of OH. There were few interactions between each factor, as the lines are almost parallel to each other. There was a cross-over in Factor AD; nevertheless, the effect on the mass fraction of OH was small. In conclusion, Factor E, which is the air temperature, had the most significant effect in decreasing the mass fraction of OH at the combustor outlet, which contributed to a more even pattern factor.

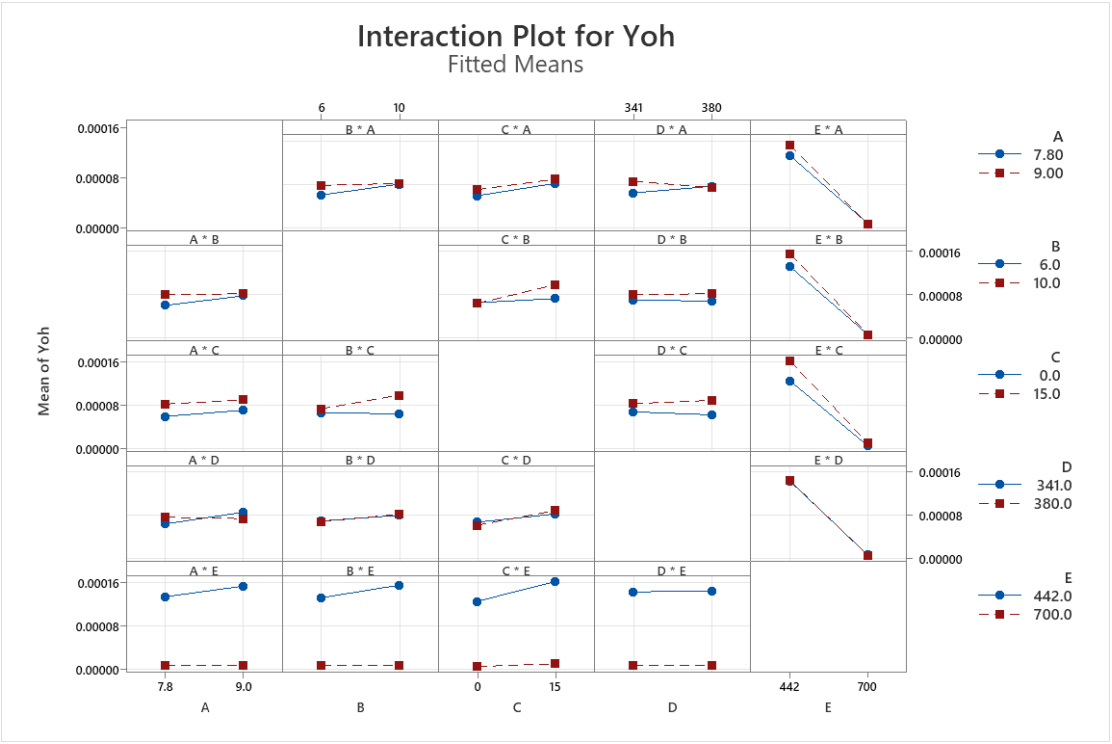

Figure 6.43 Interaction plot for mass fraction of OH

6.5.5 Effect of mass fraction of n-dodecane on factors

The data normality assumptions and the most important effects were confirmed and identified in Figures 6.44 and 6.45, where the main effect of Factors A and E and the interaction AE are deemed to be statistically significant at the 5% significance level.

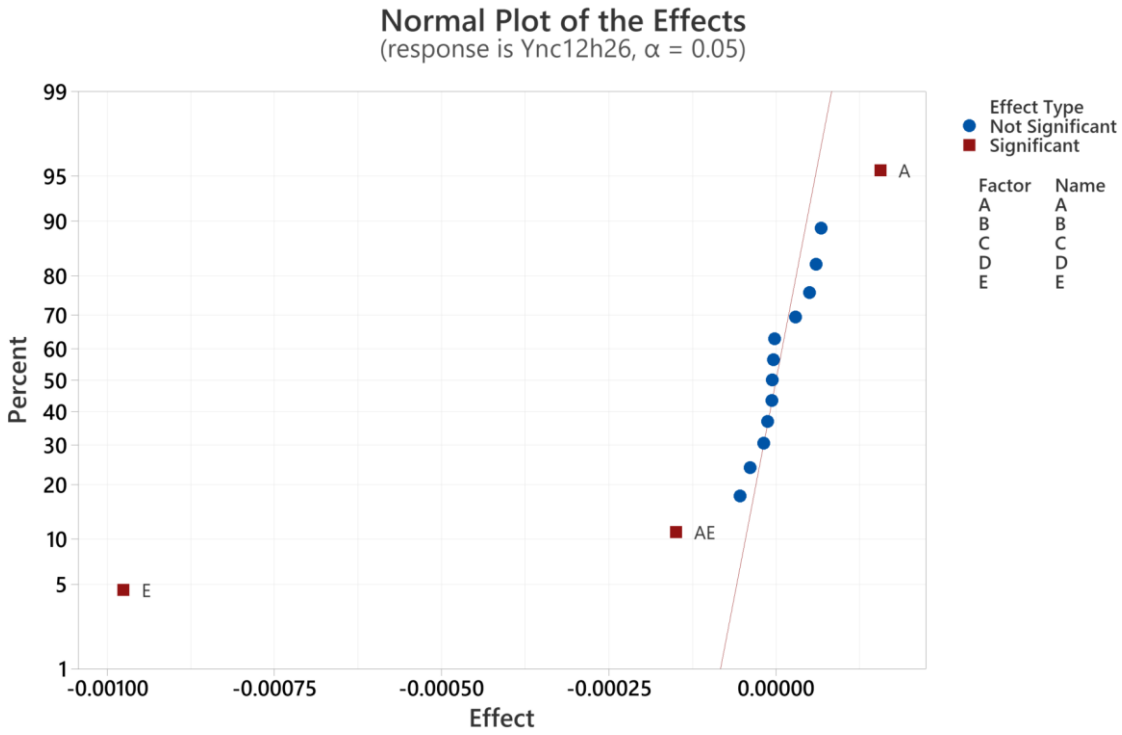

Figure 6.44 Normal plot of the effects of mass fraction of n-dodecane

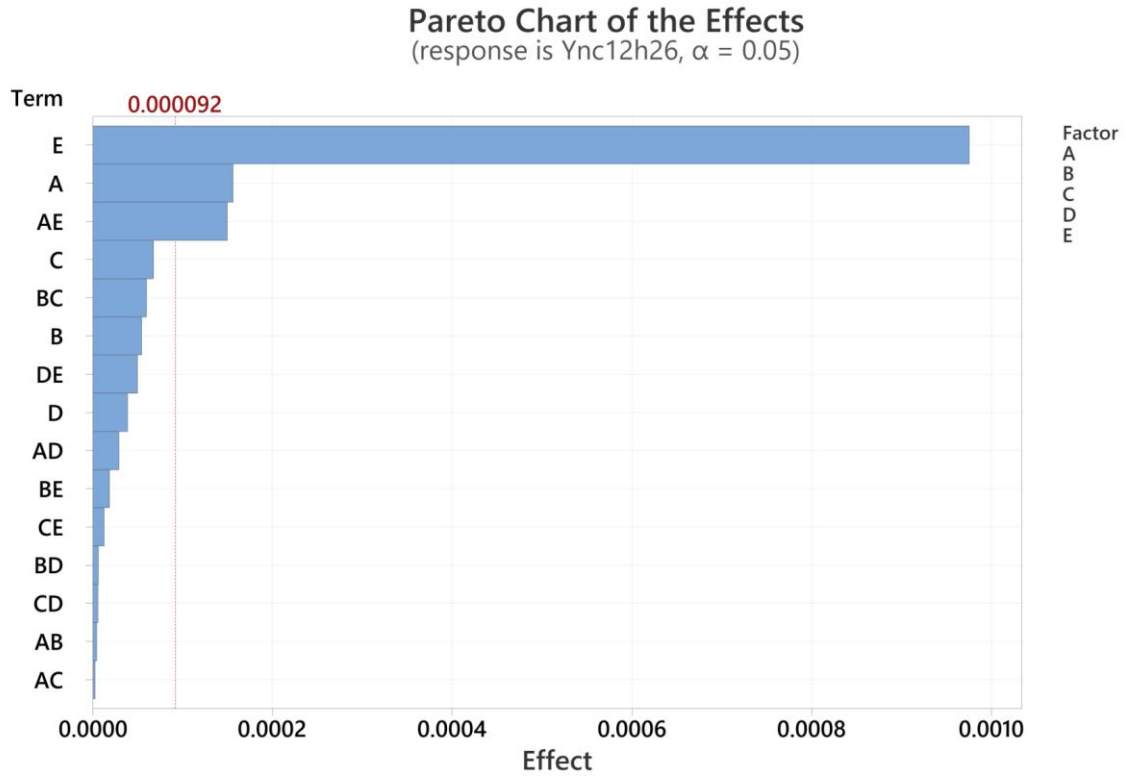

Figure 6.45 Pareto chart of the effects of mass fraction of n-dodecane

In Figure 6.46, the main effects plot for mass fraction of n-dodecane illustrates that Factor E (air inlet temperature) also had the most significant effect on the mass fraction of n-dodecane at the combustor outlet. N-dodecane can be considered as the quantity of unburnt hydrocarbons (UHC) at the combustor outlet. The mass fraction of n-dodecane increased with the geometric features, which are Factor A (primary hole diameter) and Factor C (streamwise location of the primary holes), but the effect was small compared to Factor E. On the other hand, the mass fraction of n-dodecane decreased with Factors B (number of primary holes) and D (fuel temperature). The effect was insignificant compared to Factor E.

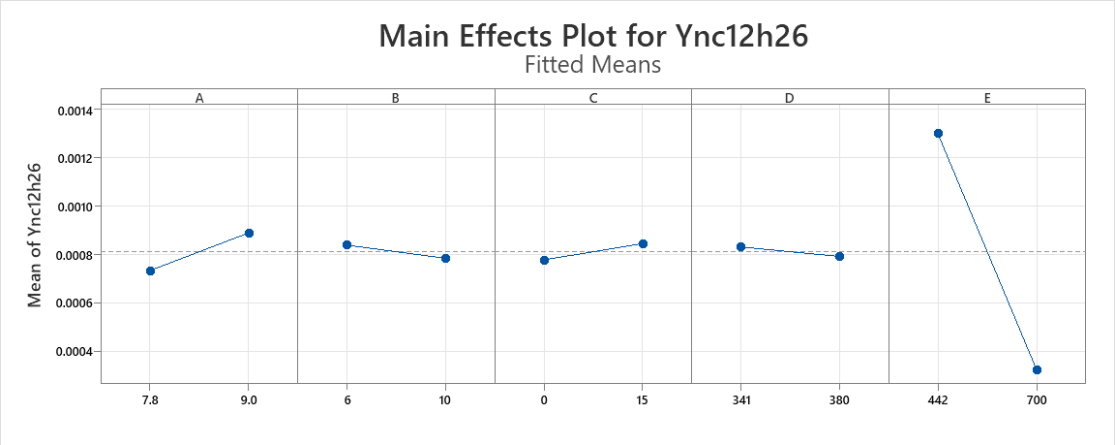

Figure 6.46 Main effects plot for mass fraction of n-dodecane

Figure 6.47 shows the interaction plot for mass fraction of n-dodecane. The interaction plot shows that the interaction between each factor was not significant, as the gradient of the lines is almost parallel to each other. Factor E (air temperature) had the most significant effect on the reduction of mass fraction of n-dodecane at the combustor outlet.

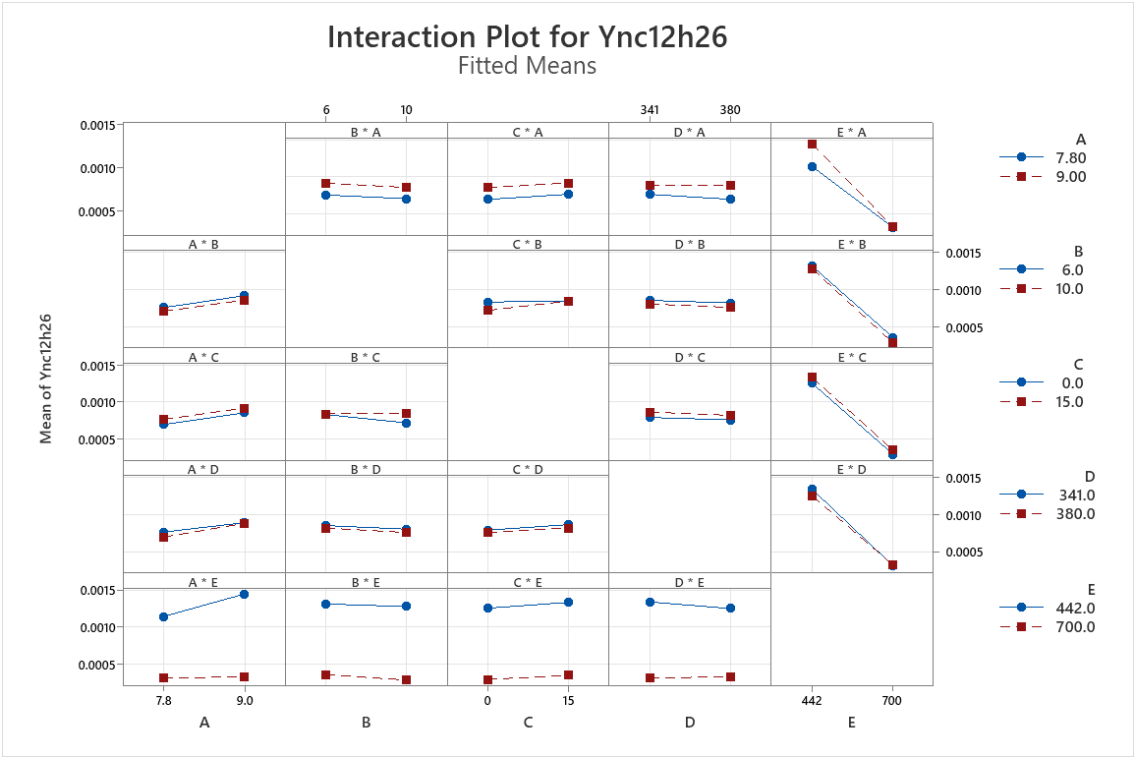

Figure 6.47 Interaction plot for mass fraction of OH

6.5.6 Effect of mass fraction of NO on factors

Similarly, the normal plot and Pareto chart were used to check whether the data normality assumptions were valid, and to identify the most significant main and interaction effects that influenced the mass fraction of NO at the combustor outlet. In Figures 6.48 and 6.49, the main effect of Factor C was statistically significant at the 5% significance level.

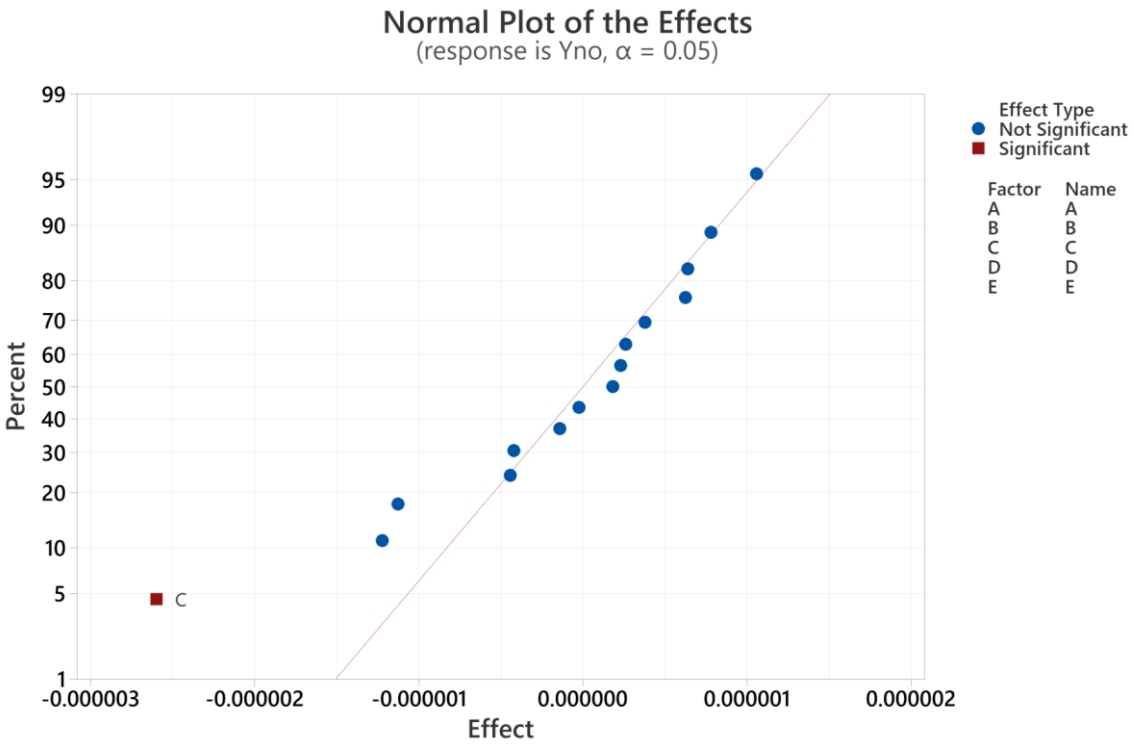

Figure 6.48 Normal plot of the effects of mass fraction of NO

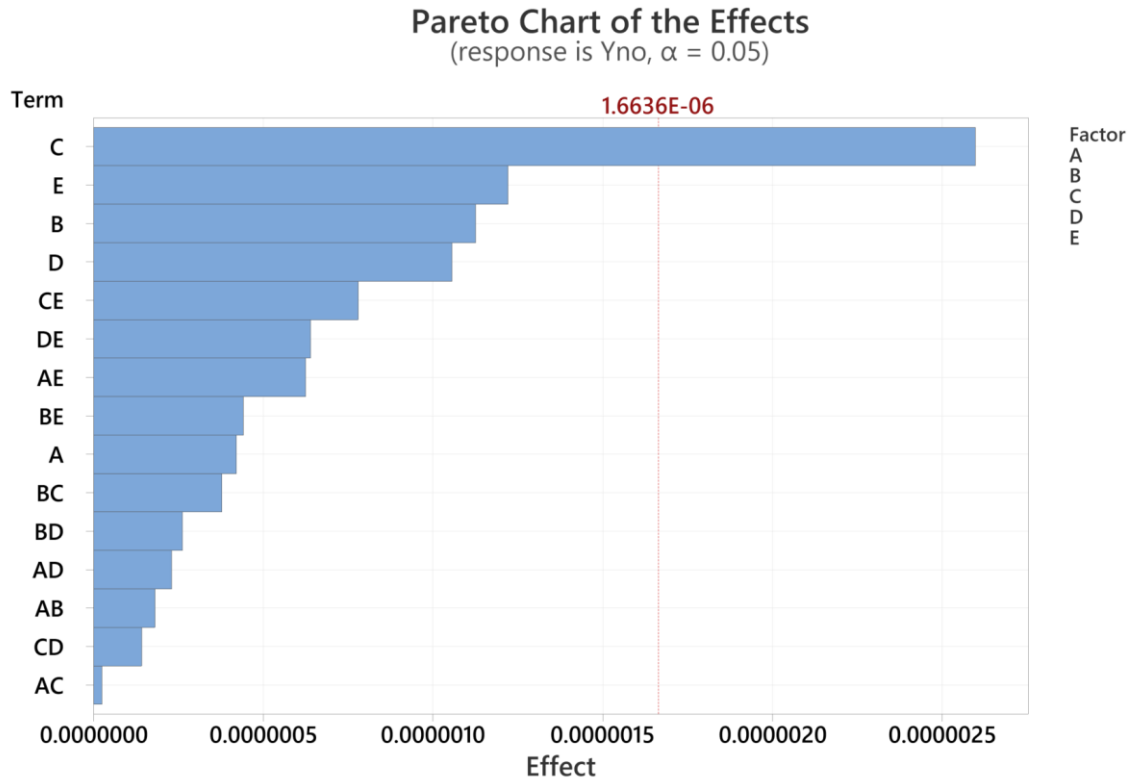

Figure 6.49 Pareto chart of the effects of mass fraction of NO

Nitric oxide (NO) emission is known as an indirect greenhouse gas, which is a growing concern for greenhouse gas emissions and pollutants [142]. Therefore, the mass fraction of NO at the combustor outlet had to be minimised to comply with the regulations in Table 1.2 in Chapter 1. Figure 6.50 illustrates the main effects plot for mass fraction of NO. The mass fraction of NO decreased with increasing Factors A (primary hole diameter), B (number of primary holes), C (streamwise location of primary holes), and E (air temperature). In contrast, the mass fraction of NO increased with the higher fuel temperature shown in Factor D. Factor C showed the most

significant effect in the reduction of the mass fraction of NO at the combustor outlet, as the gradient of the line was the largest.

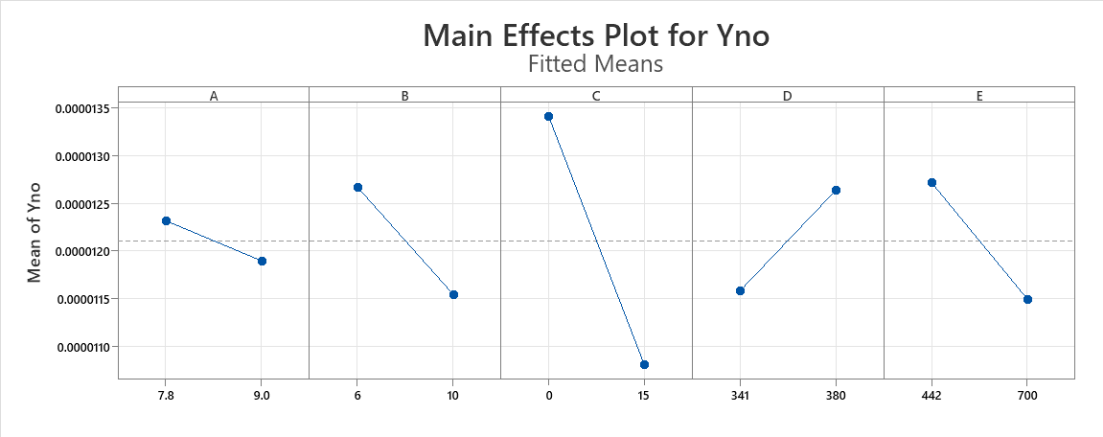

Figure 6.50 Main effects plot for mass fraction of NO

Figure 6.51 shows the interaction plot for mass fraction of NO. There were no significant interaction effects from Factor A to Factor E. Therefore, Factors C and E can be considered the most significant effect contribution to the reduction of mass fraction of NO.

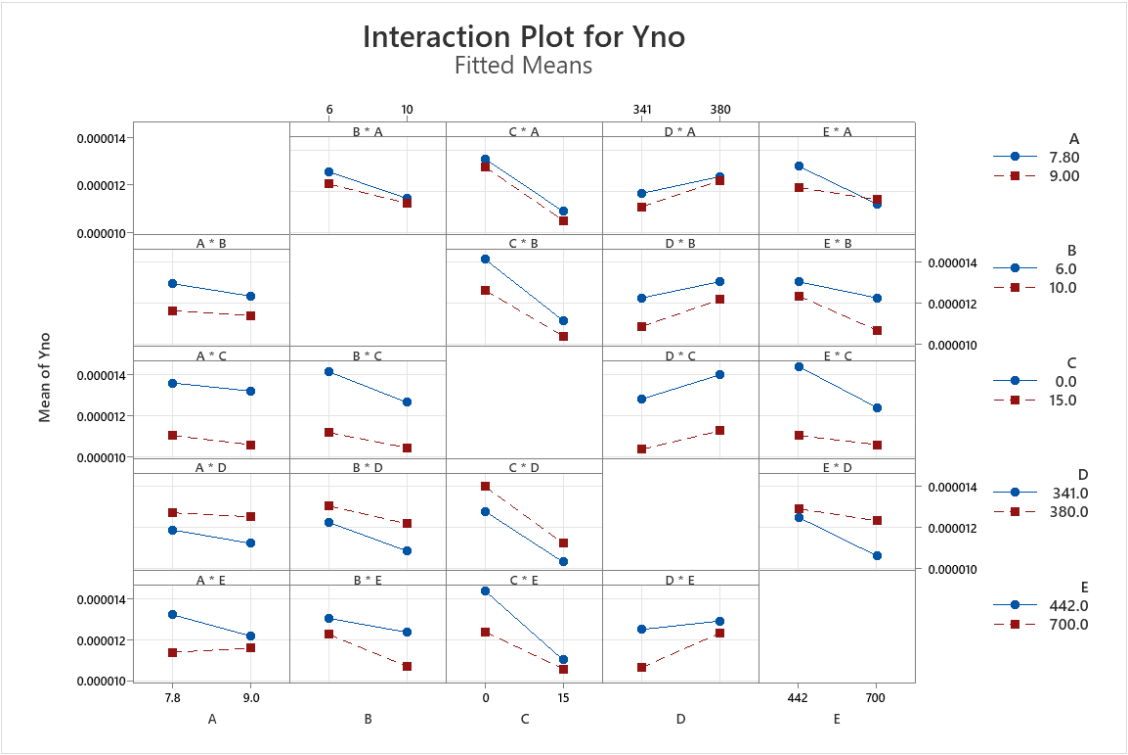

Figure 6.51 Interaction plot for mass fraction of NO

6.5.7 Effect of combustor outlet temperature on factors

In Figure 6.52, the normal plot shows that the data were fairly normal, as the insignificant data followed along the straight line. In Figures 6.52 and 6.53, the main effect of Factor E was statically significant at the 5% significance level.

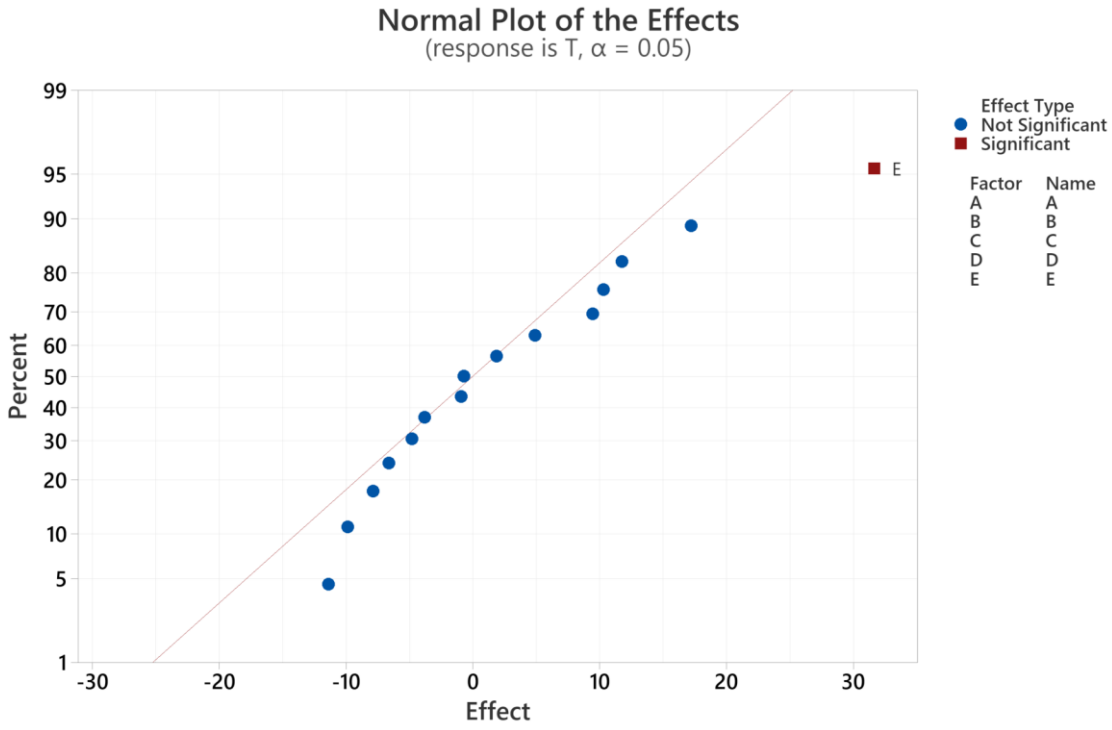

Figure 6.52 normal plot of the effects of outlet temperature.

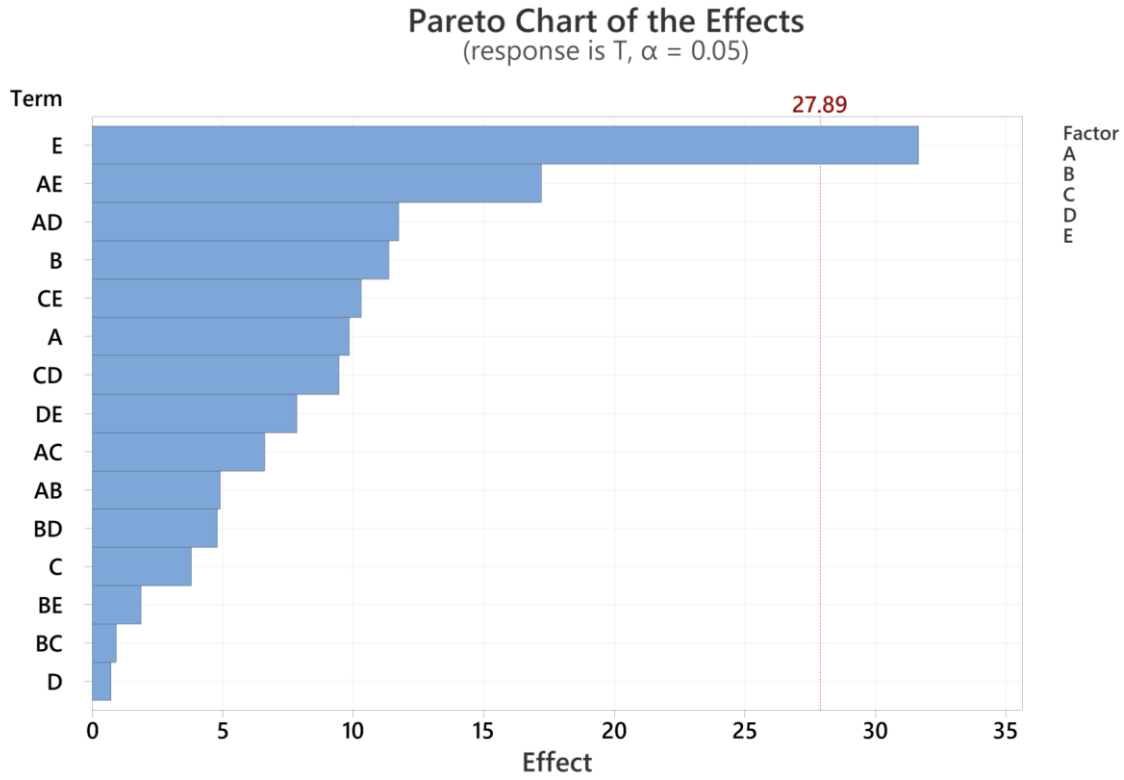

Figure 6.53 Pareto chart of the effects of outlet temperature

The temperature profile at the combustor outlet is critical to the operating reliability and lifetime of the turbine [143]. In this study, the impact of increasing air temperature at the combustor inlet resulted in a reduction in the fuel flow rate. The mean temperature of the factor was 1273 K, which is the same as the requirement for temperature in Table 1.3. In Figure 6.54, the change in geometric features of the combustor (Factors A–C) and fuel temperature (Factor D) led to a reduction in combustor outlet temperature. Factor E (air temperature) had the most significant effect for combustor outlet temperature, as shown by the line, which is the steepest.

Figure 6.54 Main effects plot for mass fraction of outlet temperature

In Figure 6.55, the interaction plot for combustor outlet temperature is presented. There were few interactions between each factor except Factors AD, BD, and CD. Two lines were crossed over, which implies that there are strong interactions between Factors A and D, Factors B and D, and Factors C and D. However, there were no significant interactions between Factor E and other factors. Hence, Factor E can be considered to have the most significant effect on temperature at the combustor outlet.

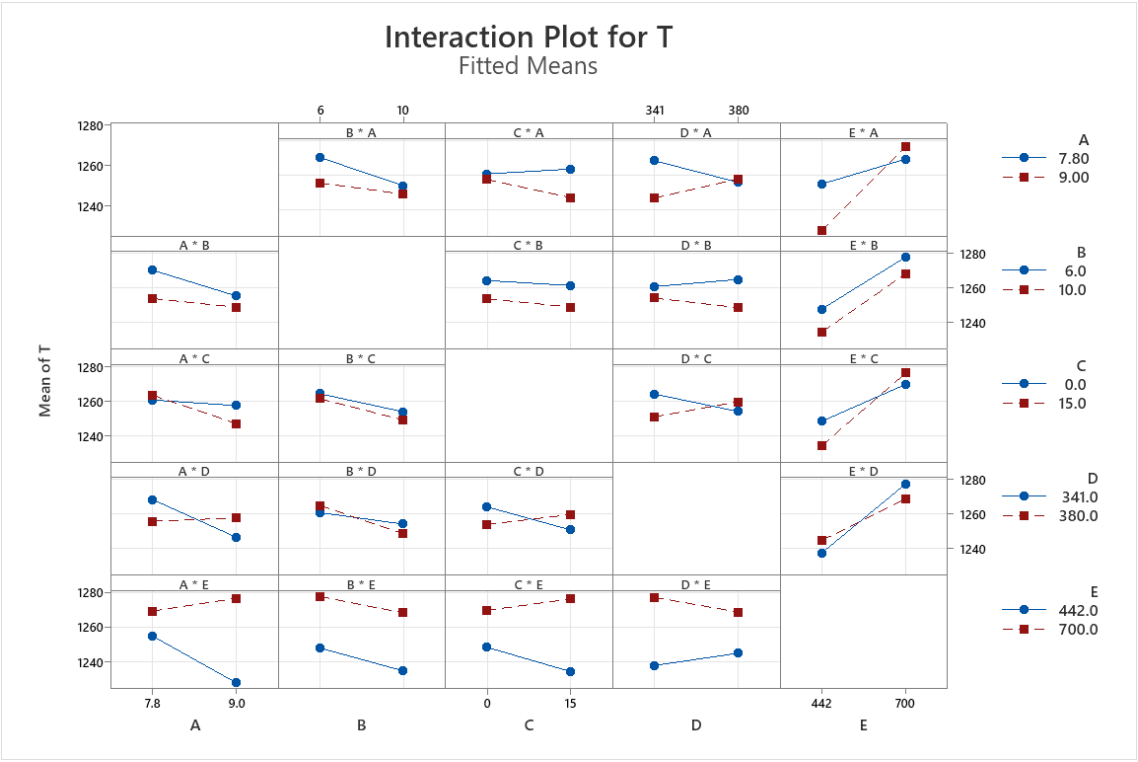

Figure 6.55 Interaction plot for combustor outlet temperature

6.5.8 Effect of pattern factor on factors

To identify the significant main effects and interaction effects, the normal plot in Figure 6.56 was used to illustrate that all the points on the normal plot cαme close to forming a fairly straight line. In Figure 6.57, the Pareto chart was used to identify the main effects of Factors C, D, E, and one interaction effect AC was deemed to be statistically significant at the 5% significance level.

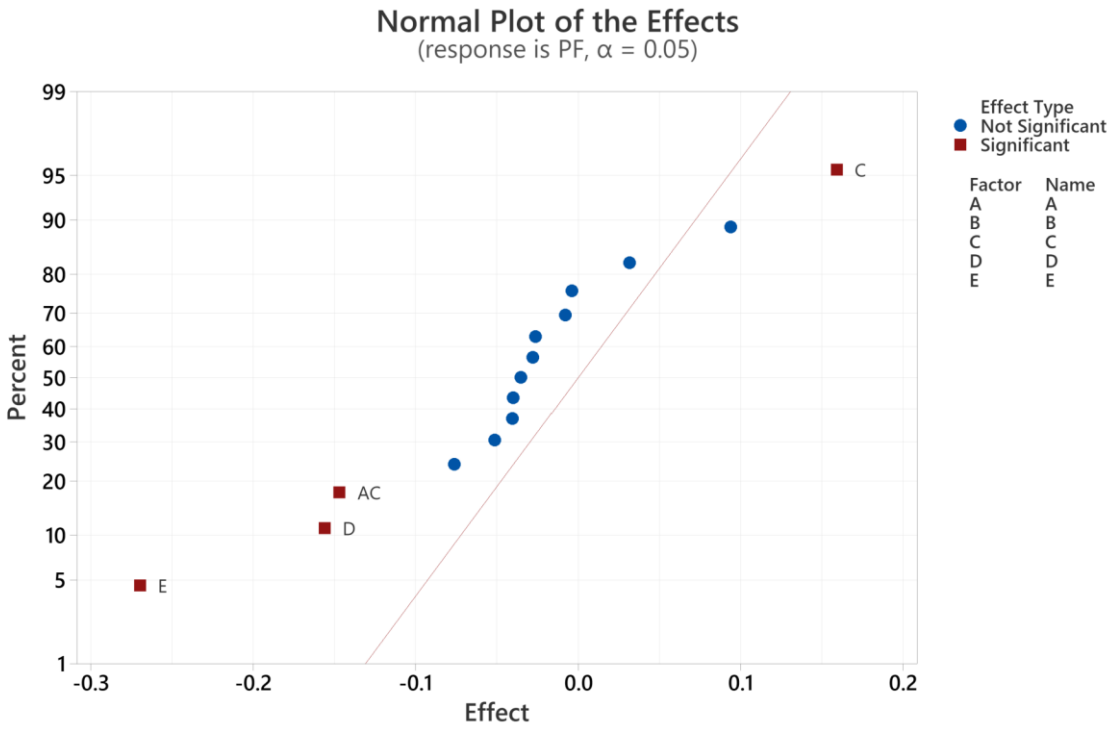

Figure 6.56 Normal plot of the effects of pattern factors

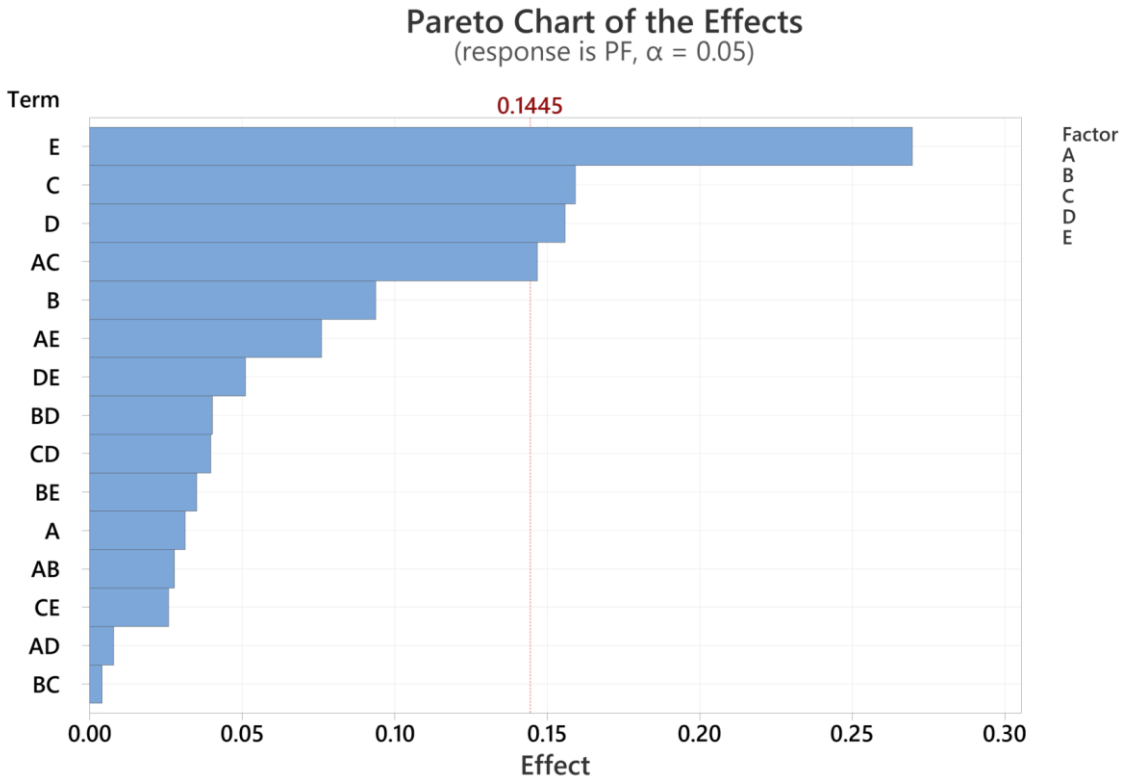

Figure 6.57 Pareto chart of the effects of pattern factor

As discussed in Section 6.5.7, the temperature profile is an important factor in determining turbine life. Pattern factor is a parameter used to describe the uniformity of turbine inlet temperature. A higher pattern factor indicates less non-uniformity of turbine inlet temperature, which may lead to very irregular hot spots at the combustor outlet [144]. In Figure 6.44, the increase in geometric features (Factors A, B and C) of the combustor increased the pattern factor. The increase in operational conditions (Factors D and E) reduced the pattern factor. The most significant effect of the pattern factor is Factor E (air temperature).

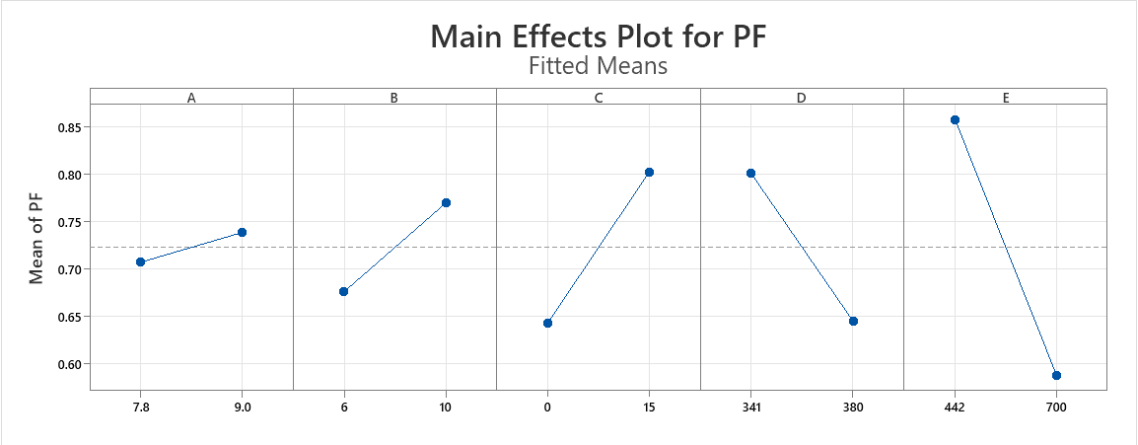

Figure 6.58 Main effects plot for mass fraction of pattern factor

Figure 6.45 shows the interaction plot for the pattern factor. There was a significant interaction between Factors A and C. In addition, there was little interaction between Factors E and A. Considering Figures 6.44 and 6.45, the operational conditions, which are Factor E (air temperature) and Factor D (fuel temperature), contributed to a significant reduction in pattern factor.

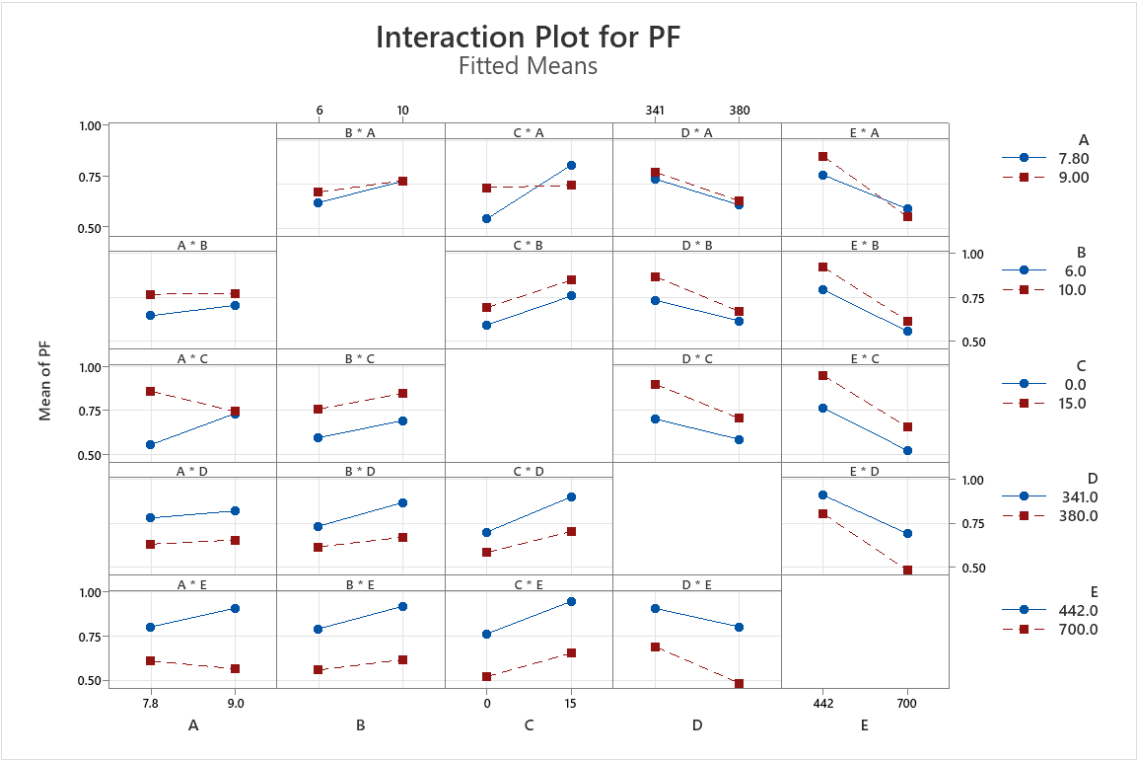

Figure 6.59 Interaction plot for pattern factor

6.5.9 Effect of total pressure drop on factors

In Figures 6.60 and 6.61, the normal plot shows the data were fairly normal, as all the points came close to forming a straight line. Moreover, the main effect of Factor E was statistically significant at the 5% significance level.

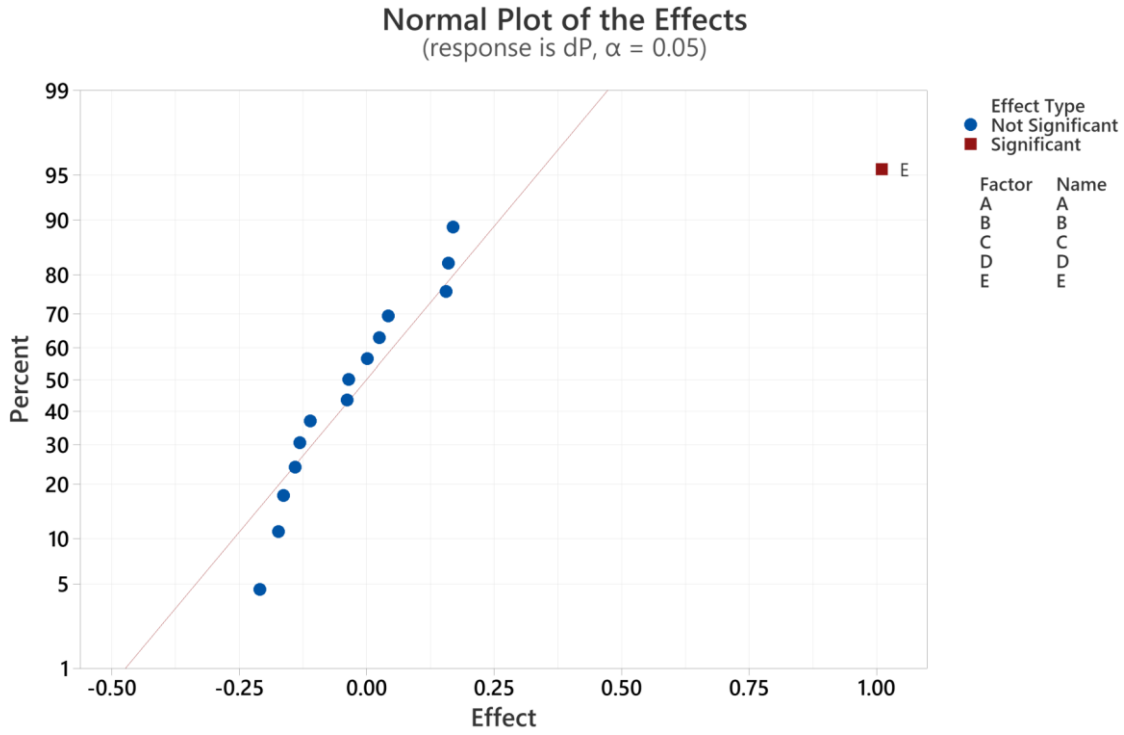

Figure 6.60 Normal plot of the effects of total pressure drop

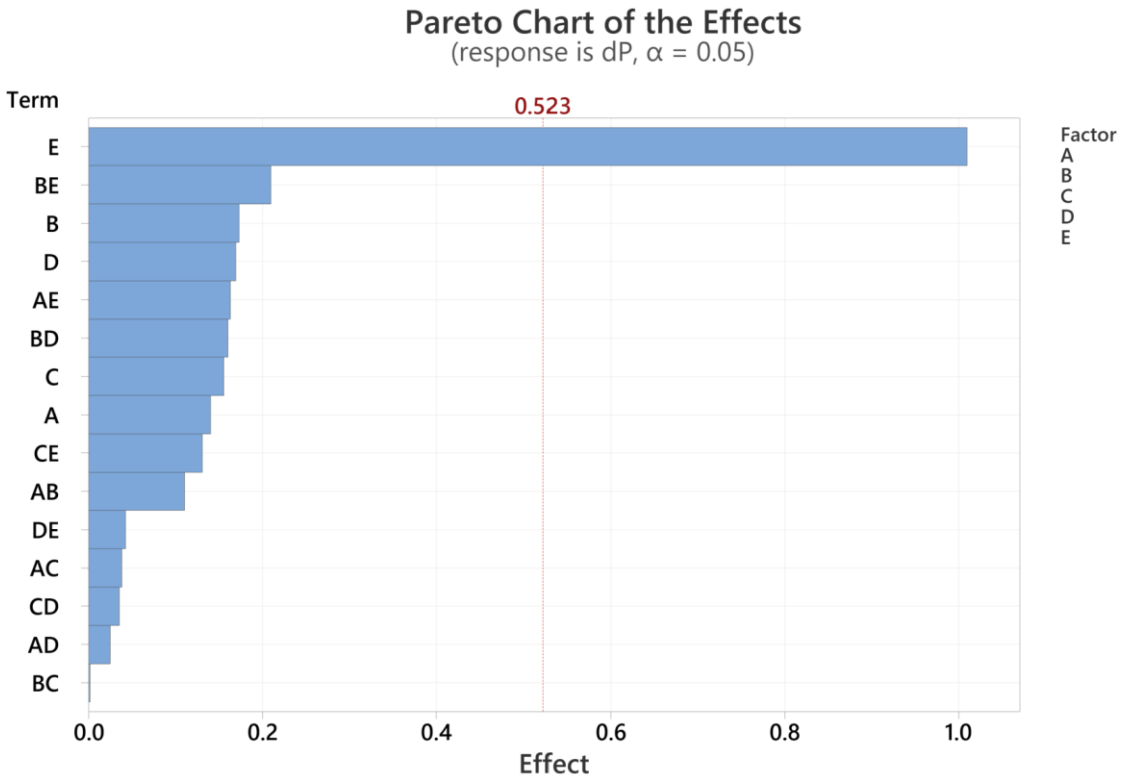

Figure 6.61 Pareto chart of the effects of total pressure drop

Total pressure is measured by the difference between the combustor inlet total pressure and outlet total pressure, reflecting the fluid dynamic characteristics and the energy-conversion intensity. The increase in air temperature (Factor E) increased with total pressure drop, because higher temperature leads to higher air velocity, causing greater flow resistance.

Factor E showed the most significant effect for the total pressure drop in Figure 6.62.

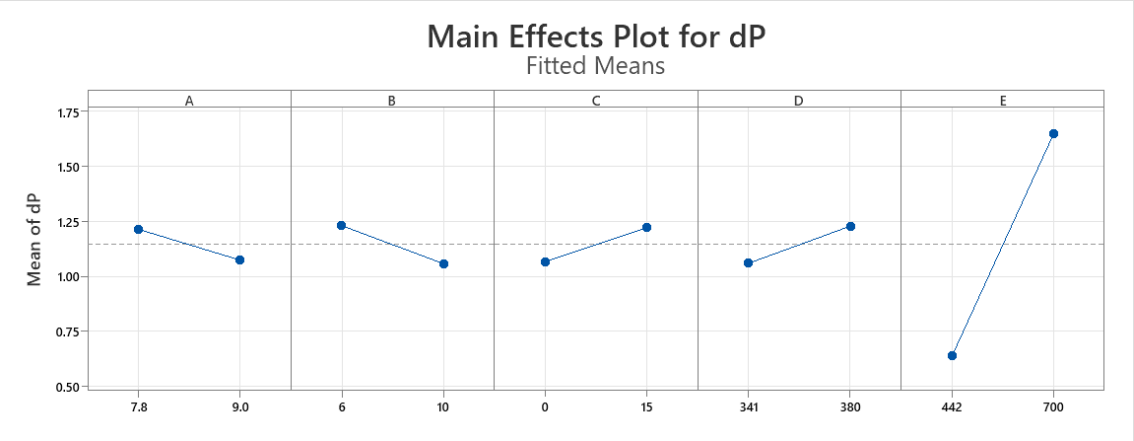

Figure 6.62 Main effects plot for mass fraction of total pressure drop

Figure 6.63 shows the interaction plot for total pressure drop across the combustor. The majority of the interactions between each factor were insignificant, as shown by the lines, which are almost parallel to each other. In short, Factor E had the most significant effect on total pressure drop across the combustor as the higher air velocity, which resulted in higher flow resistance, dominated.

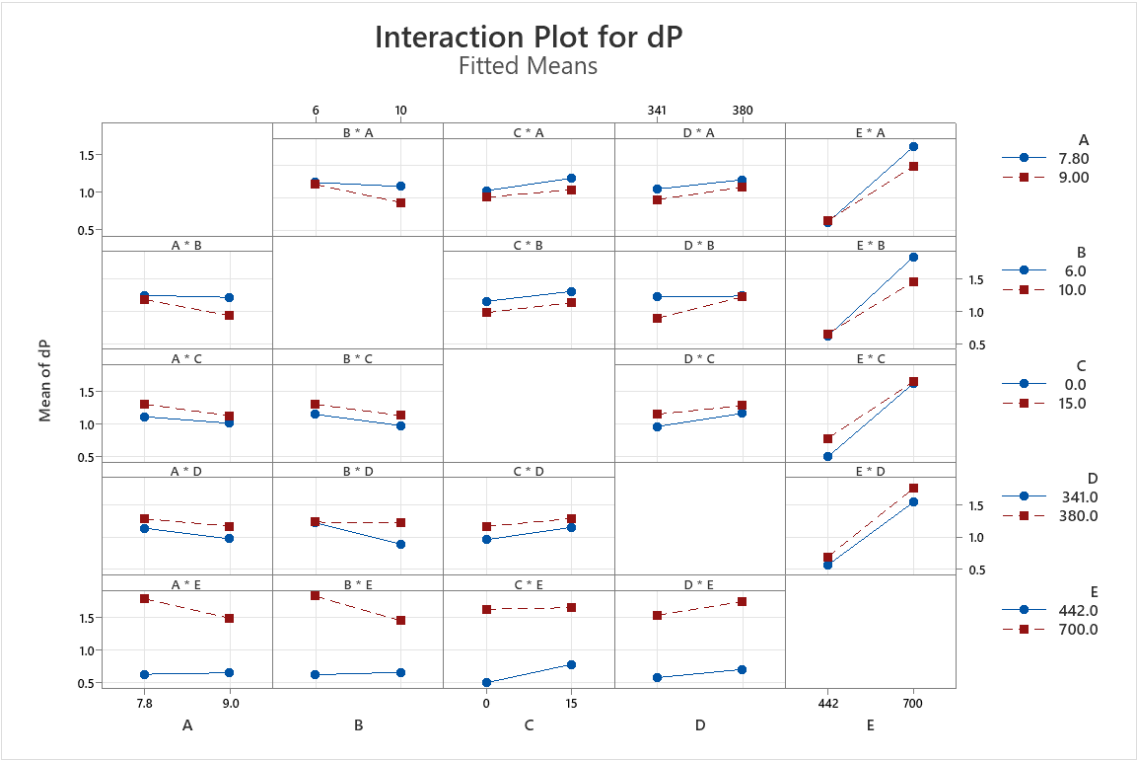

Figure 6.63 Interaction plot for total pressure drop

6.5.10 Combustor optimisation

Figures 6.32 and 6.63 show the five factors related to the different emission parameters and operational parameters at the combustor outlet. An optimisation of the baseline combustor was studied using the response optimisation with the goal function targeting the response of mass fractions of CO, C2H2, OH, n-dodecane, and NO as well as outlet temperature, pattern factor, and total pressure drop across the combustor. The response optimiser was used to search for optimal responses based on the requirements defined for each response, which was computed using statistical software Minitab. The optimisation requirements were set to minimise the mass fraction of CO, C2H2, OH, nC12H26, NO, PF, and dP, and the temperature target to 1273 K. The optimal combustor design parameters and the predicted emissions and temperature are shown in Table 6.13 and Table 6.14, respectively.

Table 6.13 Response optimiser results

Factor	A [mm]	B [-]	C [-]	D [K]	E [K]
Parameter	8.43	10	0	348	700

Table 6.14 Response optimiser prediction

$\mathbf{Y_{co}}$ [-]	$\mathbf{Y_{C_2H_2}}$ [-]	$\mathbf{Y_{OH}}$ [-]	$\mathbf{Y_{nC_{12H_{26}}}}$ [-]	$\mathbf{Y_{NO}}$ [-]	T [K]	PF [-]	dP [%]
2.57 $\times 10^{-5}$	4.80 $\times 10^{-6}$	0	2.25 $\times 10^{-4}$	1.09 $\times 10^{-5}$	1273	0.62	1.31

6.5.11 Comparison between baseline and optimised combustor design

In this section, the results CFD simulation is presented using the geometric and operational parameters in Table 6.13 and the strategies developed in Section 6.3.

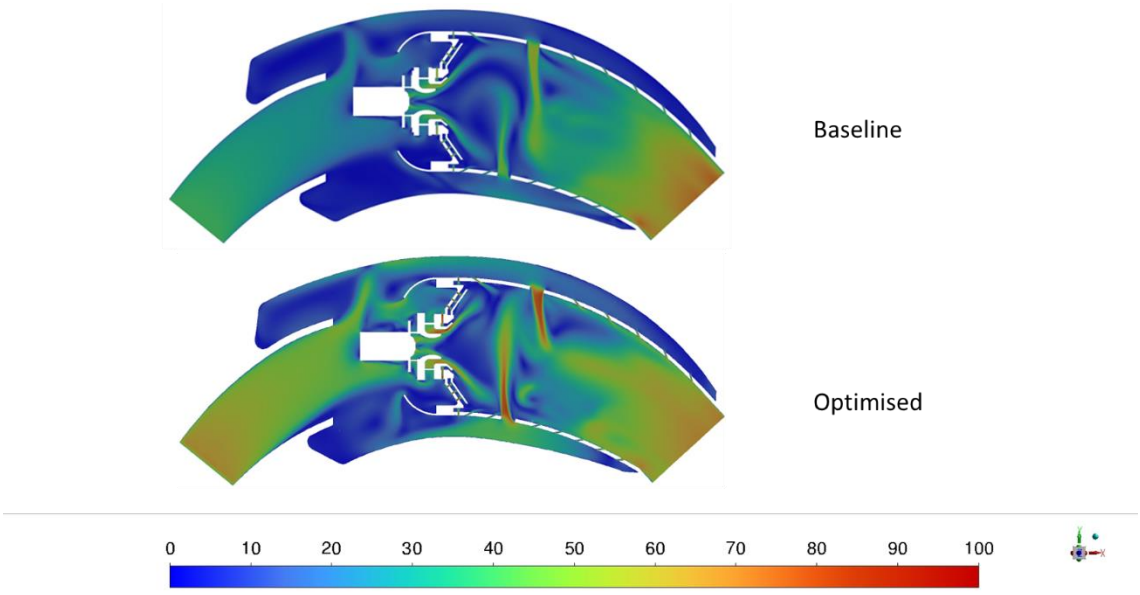

Figure 6.64 Velocity magnitude of baseline and optimised combustor

Figure 6.64 compares the velocity magnitude of the baseline and optimised combustor. The flow velocity of the optimised combustor is higher than the baseline as the air temperature is 700K at the combustor inlet. Hence, the shear layers are deflected outward, and the primary jets penetrate more deeply into the liner, resulting in better fuel and air mixing.

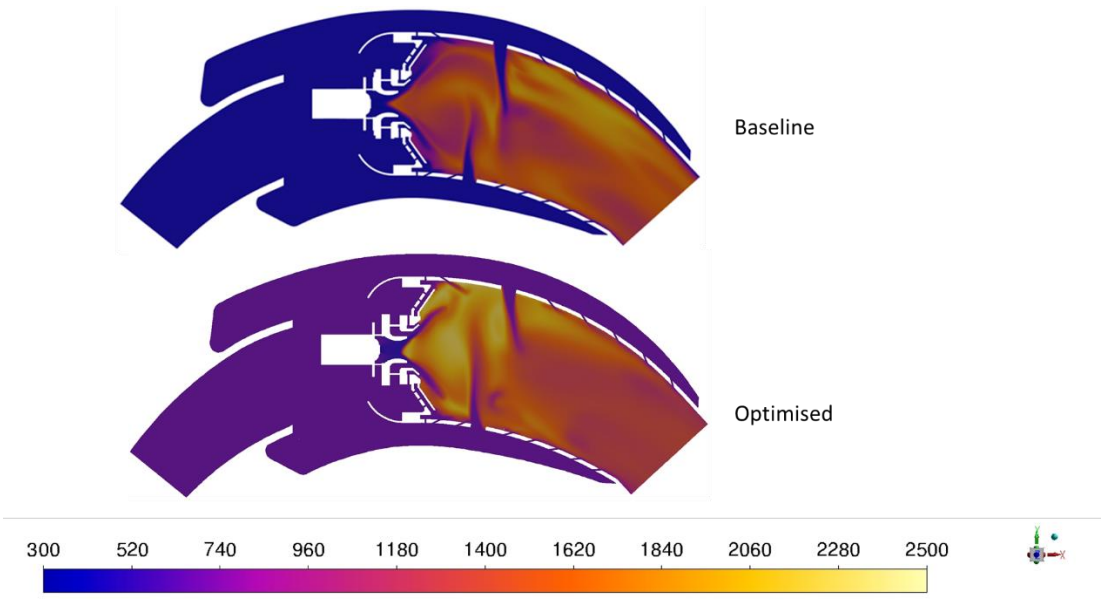

Figure 6.65 Temperature of baseline and optimised combustor

In Figure 6.65, the temperature contour revealed that the higher possibilities of the completed combustion happened within the primary zone at the optimised combustor. The high-temperature regions after the primary zone were reduced in the optimised combustor. In addition, the mass-averaged temperature at the combustor outlet was 1276 K when the combustor was optimised for higher thermal efficiency.

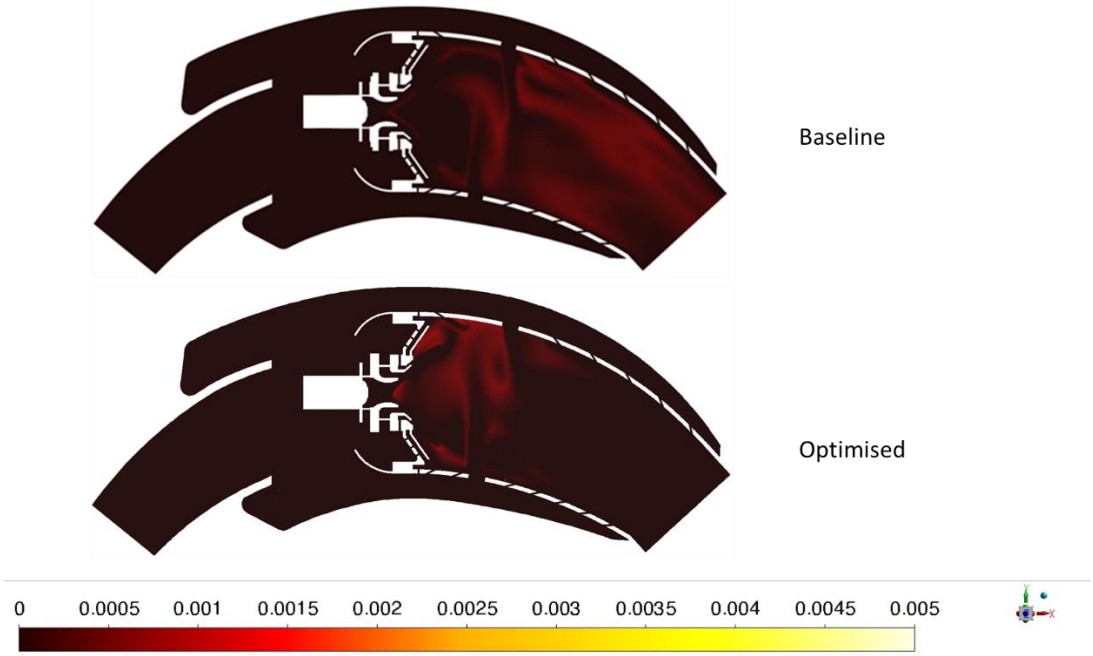

Figure 6.66 Mass fraction of OH of baseline and optimised combustor

In Figure 6.66, the optimised design showed a lower concentration of hydroxyl radical (OH) after the primary zone compared to the baseline design, which implies that the flame cannot reach towards the combustor outlet and the thermal field uniformity (pattern factor) is reduced.

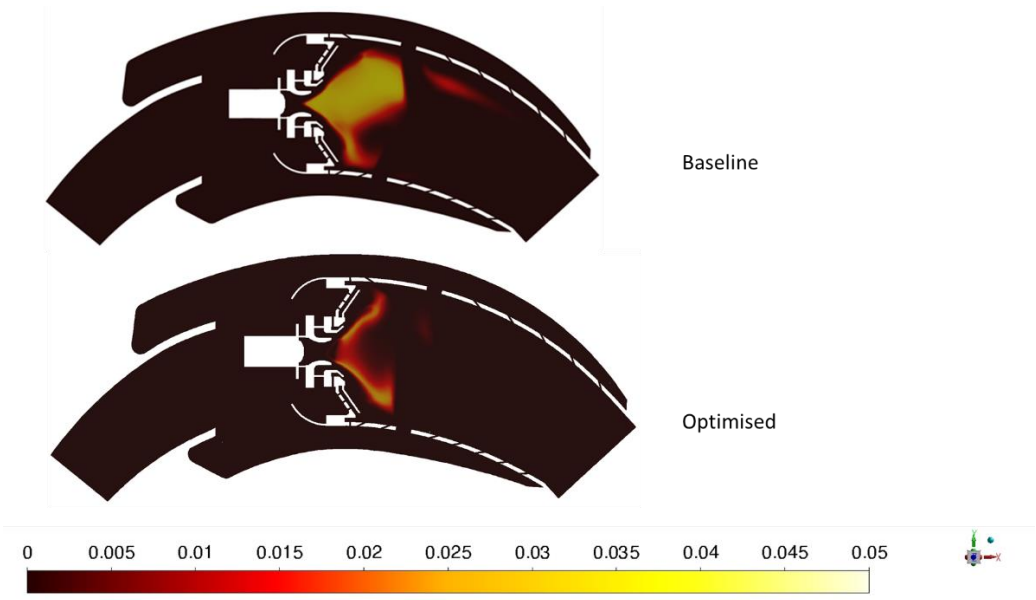

Figure 6.67 Mass fraction of C2H2 of baseline and optimised combustor

Figure 6.67 compares the mass fraction of acetylene (C2H2) between baseline and the optimised combustor. It can be seen that the concentration of acetylene decreased significantly in the primary zone at the optimised combustor. On the other hand, there is a very low concentration of acetylene after the primary zone at the optimised combustor; therefore, the soot caused by incomplete combustion can be reduced with the optimised design.

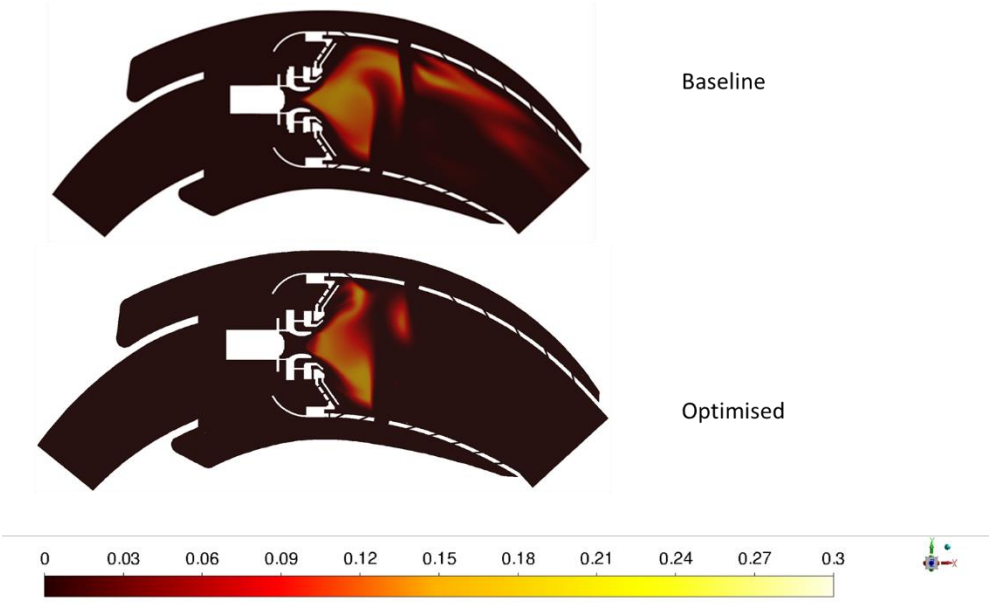

Figure 6.68 Mass fraction of CO of baseline and optimised combustor

Figure 6.68 shows the mass fraction of the carbon monoxide (CO) contour. The optimised combustor showed lower concentrations of carbon monoxide in the primary zone and very low concentrations of carbon monoxide after the primary zone. The optimised design also showed that carbon monoxide had been converted into carbon dioxide (CO_2) after the primary zone and the combustion incompleteness was reduced.

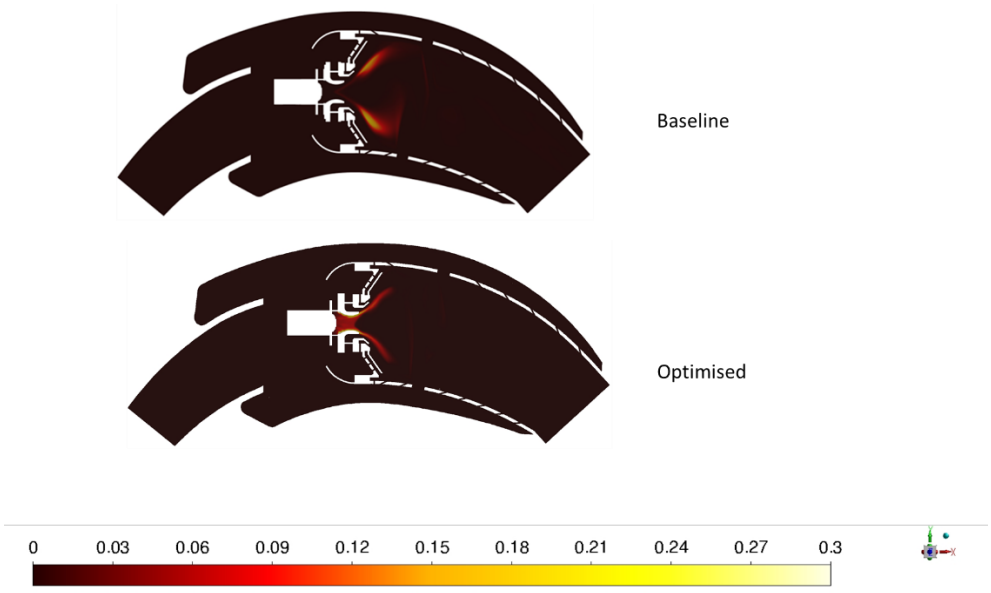

Figure 6.69 Mass fraction of n-dodecane of baseline and optimised combustor

Figure 6.69 shows that the air temperature increased to 700 K in the optimised design, implying that the atomisation performance of the liquid fuel was enhanced. The concentration of fuel vapour (n-dodecane was used as the diesel fuel surrogate) increased, especially in the region of venturi in the swirl cup. The fuel vapour followed the shear layers after exiting the venturi in the swirl cup, and combustion happened in the primary zone.

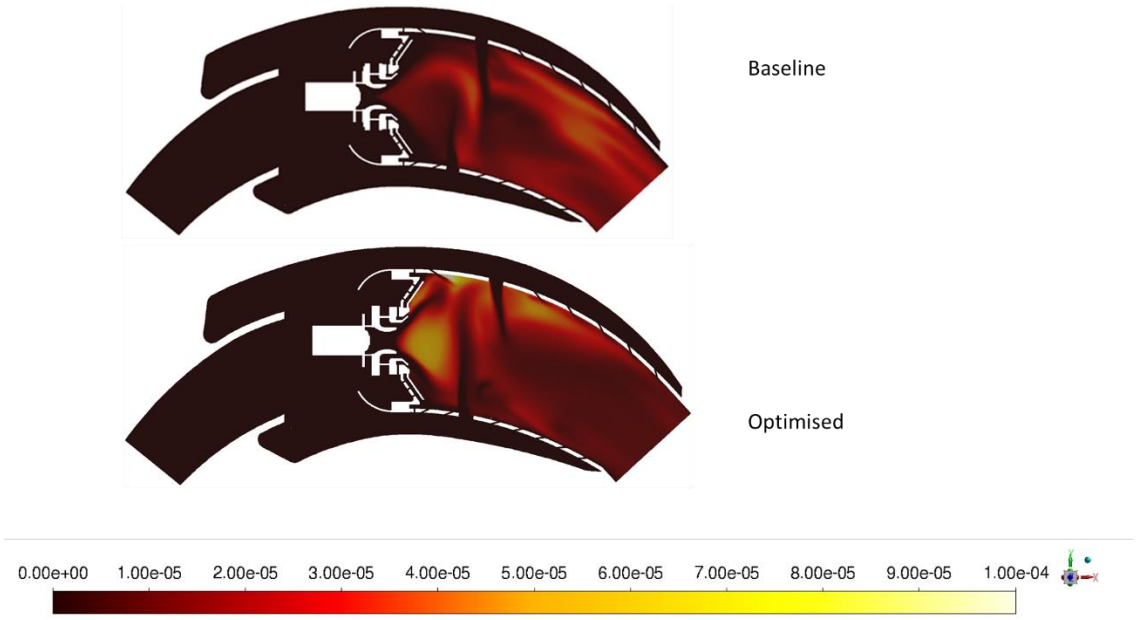

Figure 6.70 Mass fraction of NO of baseline and optimised combustor

Figure 6.70 shows a comparison between the baseline and the optimised combustor of mass fraction of nitric oxide (NO). The higher concentration of NO accumulated primarily in the primary zone, and the concentration of NO after the primary zone was reduced in the optimised design.

Figures 6.64 to 6.70 show the significant improvement in the aerodynamic effect and pollutants of the optimised design over the baseline design. The comparison between the DoE prediction and the CFD calculation at the combustor outlet parameters is shown in Table 6.15.

Table 6.15 Comparison between DoE prediction and CFD calculation at the combustor outlet

	Y_{co} [-]	$Y_{C_2H_2}$ [-]	Y_{OH} [-]	$Y_{nC_{12}H_{26}}$ [-]	Y_{NO} [-]	T [K]	PF [-]	dP [%]
DoE	2.57×10^{-5}	4.80×10^{-6}	0	2.25×10^{-4}	1.09×10^{-5}	1273	0.62	1.31
CFD	4.49×10^{-4}	1.80×10^{-5}	8.29×10^{-6}	2.91×10^{-4}	1.13×10^{-5}	1276	0.50	1.56
Difference [%]	94.28	73.33	-	22.68	3.54	0.24	-24	0.25

In Table 6.15, the mass fractions of major species, temperature-related parameters, and total pressure drop are compared between the DoE prediction and the CFD calculation. The results suggest that DoE prediction is acceptable in predicting the value of mass fractions of NO, temperature, and total pressure drop across the combustor. The percentage error for mass fraction of NO is 3.54%, temperature 0.24%, and total pressure drop 0.25%. The DoE overpredicted the species concentration of CO, C2H2, nC12H26, and pattern factor because the chemical reaction follows the Arrhenius equation, which has non-linearity in its nature; therefore, it is difficult to predict by DoE. However, it is useful to apply DoE to predict the temperature, the concentration of NO, and total pressure drop across the combustor, which are the important design parameters that need to be determined in the early design phase.

Table 6.16 Comparison between baseline and optimised design

	Baseline	Optimised	Difference [%]
Mass fraction of CO [-]	3.84×10^{-3}	4.49×10^{-4}	-88
Mass fraction of OH [-]	1.66×10^{-4}	8.29×10^{-6}	-95
Mass fraction of C_2H_2 [-]	1.08×10^{-4}	1.80×10^{-5}	-83
Mass fraction of $nC_{12}H_{26}$ [-]	1.83×10^{-3}	2.91×10^{-4}	-84
Mass fraction of NO [-]	1.63×10^{-5}	1.13×10^{-5}	-31
Temperature [K]	1223	1276	4
Pattern factor [-]	0.85	0.50	-41
Total pressure drop [%]	1.45	1.56	0.1

Finally, Table 6.16 shows the value at the combustor outlet between baseline and optimised design. The DoE with CFD methodology showed that the thermal and pollutant performance of the optimised combustor was vastly enhanced. The mass fractions of major species all reduced significantly at the combustor outlet to minimise the pollutants, reducing

the chance of hot spots burning the turbine blades. The temperature at the outlet also increased to around 1276 K to maximise the thermal performance. The pattern factor also decreased to increase the temperature uniformity at the combustor outlet. The total pressure drop increased by only 0.1%, prompting better air fuel mixing, but not increasing the specific fuel consumption rate significantly. The CFD calculation of NO at the combustor outlet is around 11 parts per million (ppm), which shows potential compliance with the UK regulation shown in Table 1.2.

6.6 Experimental investigation

The engine firing test was conducted with one combustor each time to ensure the combustor could successfully fire before the development work, such as emissions and outlet temperature measurement, began. The test rig was set up with the help of Dr Guang Pu from Birmingham High Performance Turbomachinery Limited and Dr Jianchen Wang from Beihang University.

The test rig consisted of compressor, turbine, combustor, and discharge nozzle, as shown in Figures 6.71 and 6.72. The fuel delivery system included a fuel tank, fuel pump, battery and ignition system, as shown in Figure 6.73. Market diesel fuel was used in this experiment. The firing test procedure was to first switch on the fuel pump and the fuel through atomiser flow into the combustor. After that, the pressure valve was

adjusted to increase the pressure, while the operating pressure and the value was monitored by a pressure gauge. Finally, the fuel ignition switch was turned on to ignite. The pressure and fuel flow rate used in this test were based on the results in previous testing. After the fuel shut-down process, the air kept being delivered to purge the combustor and avoid the fuel coking effect.

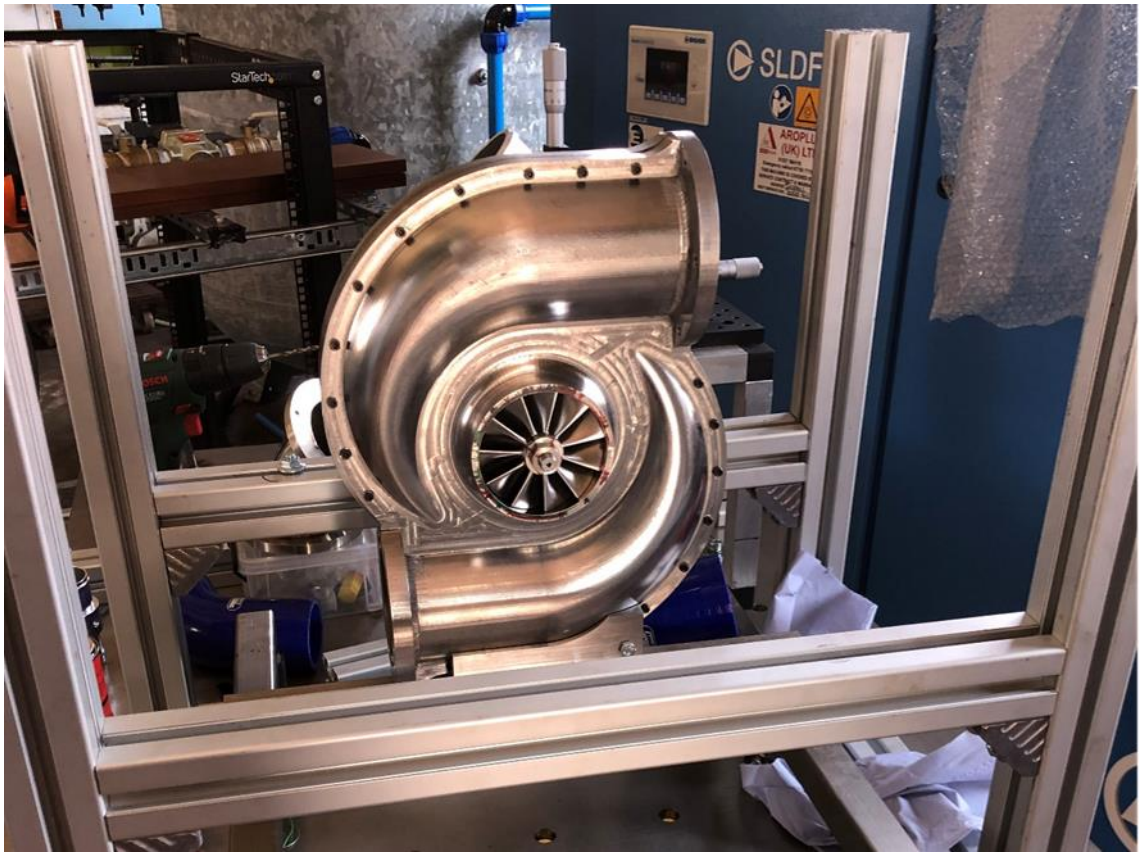

Figure 6.71 Compressor and turbine assembly – cross section

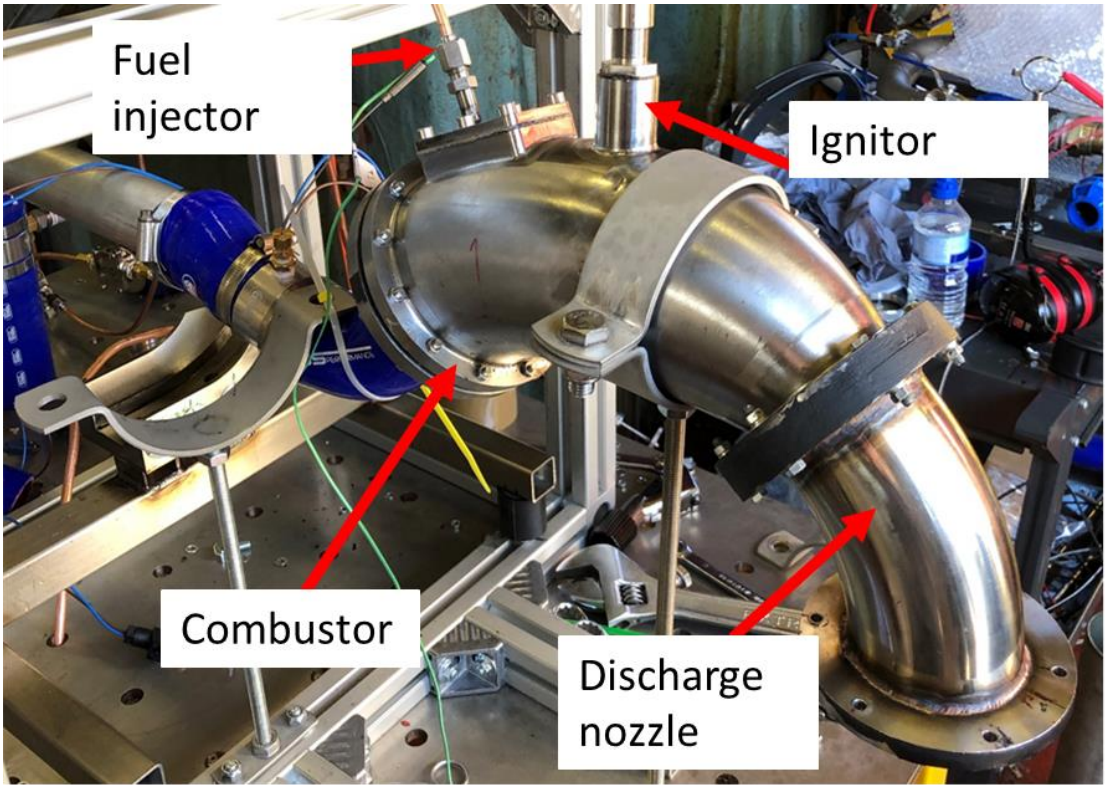

Figure 6.72 Combustor assembly and discharge nozzle

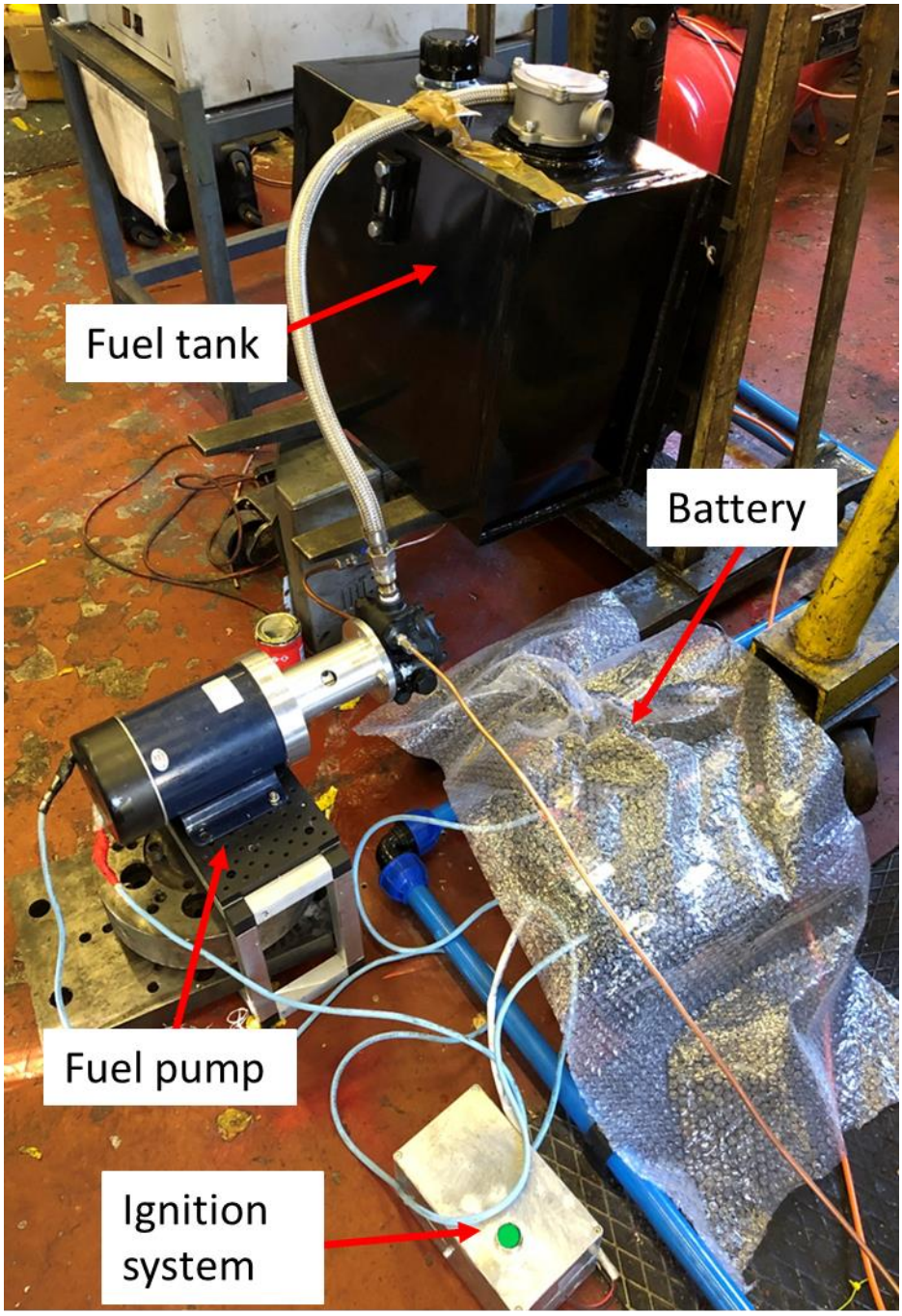

Figure 6.73 Fuel delivery system and ignition system

Figure 6.74 shows the combustor's weak extinction limit graph. The successful ignition region was determined based on the recorded pressure and fuel flow rate. After the successful combustor ignition process, the fuel flow rate decreased until the failure of combustion ignition occurred. The experimental investigation successfully demonstrated that the novel combustor was able to ignite and operate in the engine configuration. The baseline CFD condition is shown by the red square in Figure 6.74, which lies inside the successful ignition region. The optimised design is shown in purple, which is outside the successful ignition region. Since the air inlet temperature was increased from 442 K to 700 K, the weak extinction limit of the optimised design needed to be determined in another experimental run. Following the curve of the experimental results, the higher total pressure drop gave a lower value of FAR, which resulted in a better weak extinction performance.

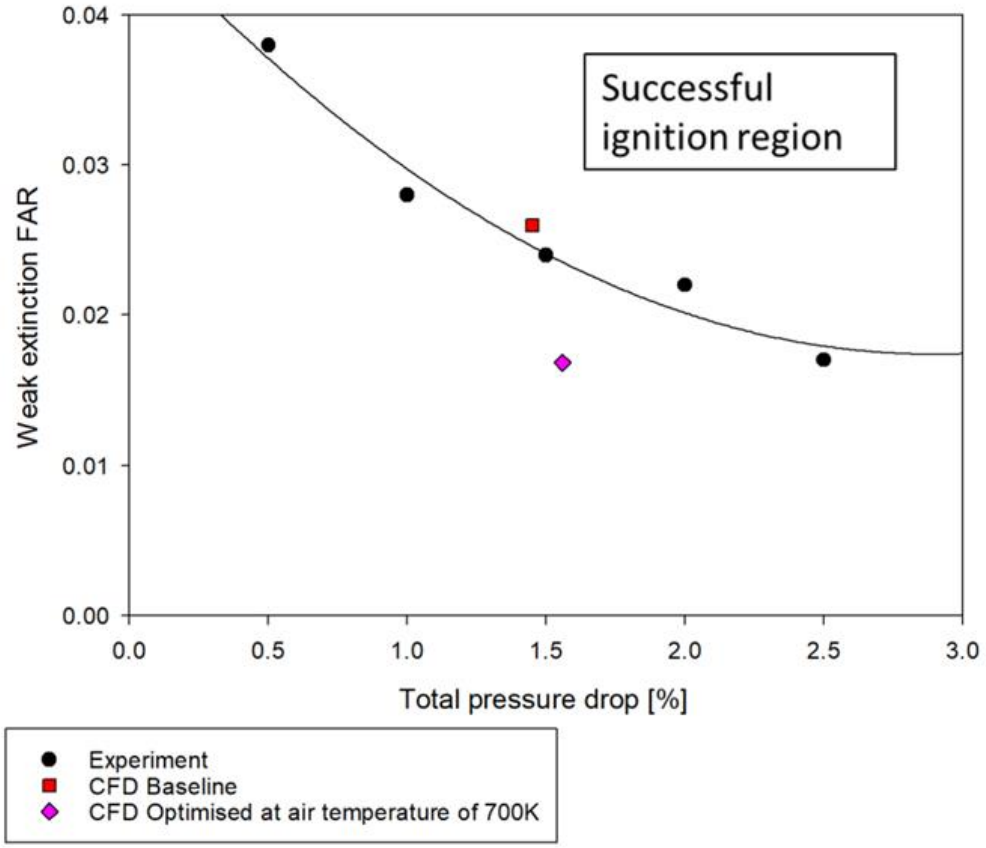

Figure 6.74 Combustor weak extinction limit

6.7 Summary

This chapter presented the process of developing the micro gas turbine combustor for a 30 kW engine. The design concept of some important components was calculated using empirical formulae. The reacting CFD simulation of the baseline design was carried out to assess the combustor performance and emissions at the combustor outlet. The numerical investigation of combustor design parameters was carried out by analysing the CFD results of different design variations and comparing them with the baseline design. The influence of primary holes in terms of the diameter of holes, the number of holes used, and the location of these holes on the outlet, the temperature distribution, and the combustion major species were explored.

In addition, an experimental investigation was conducted to show the feasibility of the baseline design concept and ignition performance. Due to the difficulty of utilising detailed measurement techniques of flame structure and internal combustor flow fields, detailed measurements were not taken in this project.

The design concept and the results of the reacting CFD simulation demonstrated that the proposed combustor design concept has the potential to achieve excellent performance and is sufficiently compact for a small-scale engine power range up to 30 kW.

Chapter 7 Conclusions and Further Research Suggestions

7.1 Overview

Chapter 1 presented background research into micro gas turbines and combustor technologies of the leading micro gas turbines market. The associated regulations in ground-based gas turbines and combustor design considerations were also summarised and discussed. The research goals were set in relation to how DoE with CFD can help in designing and developing a combustor.

In Chapter 2, the physics of micro gas turbine combustors was presented. Low emission combustion technologies were reviewed. The fundamental knowledge in combustion and multiphase phase flow physics inside the combustor were discussed.

Chapter 3 presented the modelling methodology of turbulent combustion. The state-of-the-art turbulence modelling in the RANS context as well as the reduced-order method of the flamelet model were discussed. The special treatment accounting for turbulent spray flames was also discussed. The modelling assumptions were discussed for developing the reacting CFD modelling in the following chapters.

Chapter 4 investigated the isothermal CFD modelling strategies developed in Chapter 3 in modelling the non-reacting swirling flows in a lab-scaled burner to mimic the swirling flow physics inside a real micro gas turbine combustor. The results from the isothermal CFD model were then compared to experimental data, which showed agreement across the key parameters. The validated isothermal CFD model was then used to model the reacting conditions.

Chapter 5 focused on reacting CFD modelling in a swirling spray flame of kerosene in a lab-scale burner. The results from the reacting CFD model were then compared to experimental data, which showed agreement in velocity and temperature profiles. The validated reacting CFD model was then used to design and optimise the proposed novel combustor.

Chapter 6 presented the design calculations covering the swirler, injector, and liner size, which helped in the early design phase of the combustor. The baseline design was analysed and modelled using the reacting CFD methodology developed in previous chapters. Optimisation was achieved with the use of DoE and a reacting CFD model. The results showed that the optimised combustor reduced pollutant emissions significantly and the thermal performance was maximised.

7.2 Review of research objectives

The aims of this research were to design and improve the performance of combustors and to develop a modelling strategy of turbulent swirling spray flames when designing a micro gas turbine combustor. These were achieved, filling a gap in related research. The modelling strategy can be applied to early-stage combustor design work and can reduce the cost and resources of conducting experimental verification. The key conclusions of this research are presented below, relating the key results to each objective:

1. Simulate and analyse the performance and limitations of popular turbulence models in swirling flow dynamics in a swirl-stabilised burner.

- For the investigation into the turbulent swirling flow dynamics, five different turbulent models were used to simulate and compare with the experimental data from a lab-scale burner under isothermal conditions in Chapter 4. The k-omega SST turbulence model showed that the velocity profiles were reproduced, and transient phenomena of precessing vortex core (PVC) were captured.

2. Simulate and analyse the performance and limitations of the state-of-the-art turbulent combustion model in spray combustion in a swirl-stabilised burner.

- The state-of-the-art flamelet model – flamelet-generated manifold (FGM) – was used to model the swirling spray flame of kerosene in a lab-scaled burner in Chapter 5. The reacting CFD model reproduced the velocity and temperature profiles in good agreement with the experimental data. The limitations in spray combustion in a swirl-stabilised burner were computationally demanding, as the droplets inside the combustor are massive and the radiative properties of the mixtures are unknown.

3. Investigate the state-of-the-art low emissions combustor design configurations and the design calculation to design a novel combustor in a micro gas turbine application.

- Through background research in Chapters 1 and 2, it was established that low emissions combustor design used RQL and LPP combustion technologies.
- The design calculations for radial swirler, combustor effective area, and injector were proposed in Chapter 6.
- The reacting CFD modelling and experimental investigation showed that the baseline combustor was applicable in low emission micro gas turbines.

4. Develop a modelling strategy for spray combustion in a swirl-stabilised combustor and assess the trade-off between combustor performance and emissions through different design parameters.

- Reacting CFD modelling strategies developed in Chapters 4 and 5 were used to model the baseline novel combustor and assess the combustor performance and emissions prediction.
- DoE and reacting CFD modelling were used to investigate the geometric and operational effects on combustor performance and emissions prediction.
- The baseline combustor was optimised using the results of DoE, and the optimised combustor showed that the emissions were reduced by more than 30%, with only a 0.1% increase in total pressure drop.

7.3 Further research suggestions

The following topics are suggested for future research:

1. Experimental measurements in a more representative testing environment

Due to the absence of equipment and techniques for detailed measurement, the CFD simulation is an alternative tool to analyse and provide design feasibility and optimisation ideas. Future work should focus on validating the CFD using the data from detailed measurements of the designed combustor, such that it can be more reliably used as a design tool.

2. High-fidelity simulation tools, such as large eddy simulation (LES)

Due to the complicated nature of combustors and the related combustion instability problem inside a combustor, which is transient in nature, a time-resolving simulation such as LES would be useful to resolve the transient characteristics and provide insight into flashback and combustion instability problems. In addition, with the use of unsteady CFD simulation, the modelling results can match the weak extinction graph shown in Figure 6.74, which is a huge saving for early-stage combustor design work.

3. More representative chemical kinetics schemes for diesel fuel are needed and account for NOx production as well as the soot effect

A practical diesel fuel composition is extremely complicated, and so far in the literature single or up to three-component surrogate fuels have been used to represent a practical diesel fuel. Since the fuel surrogate physical properties significantly affect the spray evaporation and atomisation effect, a more representative fuel and mechanism development work would be most advantageous in CFD modelling. A mechanism with soot modelling capability is important to understand the complex soot formation processes inside a combustor. A more compact kinetic mechanism that can accurately predict some major combustion species and pollutants would be beneficial in simulating the complex geometry of 3D CFD.

Bibliography

[1] Marco Antônio Rosa do, N., Lucilene de Oliveira, R., Eraldo Cruz dos, S., Eli Eber Batista, G., Fagner Luis Goulart, D., Elkin Iván Gutiérrez, V., & Rubén Alexis Miranda, C. (2013). Micro Gas Turbine Engine: A Review. In B. Ernesto (Ed.), Progress in Gas Turbine Performance (pp. Ch. 5). IntechOpen.

[2] Chiaramonti, D., Rizzo, A. M., Spadi, A., Prussi, M., Riccio, G., & Martelli, F. (2013). Exhaust emissions from liquid fuel micro gas turbine fed with diesel oil, biodiesel and vegetable oil. Applied energy, 101, 349-356.

[3] C. Soares (2011), Microturbines: Applications for Distributed Energy Systems, Elsevier.

[4] Amanda S. Nascimento, Cecília M. F. Rubira, Rachel Burrows, and Fernando Castor. (2013). A systematic review of design diversity-based solutions for fault-tolerant SOAs. In Proceedings of the 17th International Conference on Evaluation and Assessment in Software Engineering (EASE '13). Association for Computing Machinery, New York, NY, USA, 107–118.

[5] Li, J., & Li, Y. (2023). Micro gas turbine: Developments, applications, and key technologies on components. Propulsion and Power Research, 12(1), 1-43.

[6] Capstone Turbine Corporation, URL: https://www.capstoneturbine.

com [cited 05 October 2023].

[7] Bladon, URL: https://www.bladonmt.com [cited 05 October 2023].

[8] Yinger, Robert J. Behavior of Capstone and Honeywell microturbine generators during load changes. United States.

[9] ETGROUP, Micro-Gas Turbine, URL: https://www.etgroup.nl/en/

micro-gas-turbine [cited 05 October 2023].

[10] Lieuwen, T., & Yang, V. (Eds.). (2013). Gas Turbine Emissions (Cambridge Aerospace Series). Cambridge: Cambridge University Press. doi:10.1017/CBO9781139015462

[11] Bilger, R. W. (2011). The role of combustion technology in the 21st century. In Turbulent Combustion Modelling: Advances, New Trends and Perspectives (pp. 3-18). Dordrecht: Springer Netherlands.

[12] Research Centre for High Performance Turbomachinery, URL: https://www.birmingham.ac.uk/research/activity/mechanical-engineering/turbomachinery [cited 12 March 2024].

[13] Parente, J., Mori, G., Anisimov, V. V., & Croce, G. (2004). Micro Gas Turbine Combustion Chamber Design and CFD Analysis. ASME Turbo Expo 2004: Power for Land, Sea, and Air,

[14] Gosselin, P., DeChamplain, A., Kalla, S., & Kretschmer, D. Three-dimensional CFD analysis of a gas turbine combustor. In 36th AIAA/ASME/SAE/ASEE Joint Propulsion Conference and Exhibit. https://doi.org/10.2514/6.2000-3466

[15] Lai, M. K., Reynolds, R. S., & Armstrong, J. (2002). CFD-Based, Parametric, Design Tool for Gas Turbine Combustors From Compressor Deswirl Exit to Turbine Inlet. ASME Turbo Expo 2002: Power for Land, Sea, and Air,

[16] FULLER, E., & SMITH, C. Integrated CFD modeling of gas turbine combustors. In 29th Joint Propulsion Conference and Exhibit. https://doi.org/10.2514/6.1993-2196

[17] Cameretti, M. C., & Tuccillo, R. (2005). A CFD Based Off-Design Study of Micro-Gas Turbines Combustors. ASME Turbo Expo 2005: Power for Land, Sea, and Air,

[18] M. A. R. do Nascimento, L. de Oliveira Rodrigues, E. C. dos Santos, E. E. B. Gomes, F. L. G. Dias, E. I. G. Velásques, and R. A. M. Carrillo. (2013). Progress in Gas Turbine Performance, Prog. Gas Turbine Perform., pp. 107–142.

[19] Boyce, M. P. (2012). 2 - Advanced industrial gas turbines for power generation. In A. D. Rao (Ed.), Combined Cycle Systems for Near-Zero Emission Power Generation (pp. 44-102). Woodhead Publishing.

[20] Lefebvre, A.H. and Ballal, D.R. (2010) Gas turbine combustion: Alternative fuels and emissions. Boca Raton, FL: CRC.

[21] Irvin G., Richard A. Y., Nick G. G. (2014). Combustion: Academic Press

[22] Lieuwen, T. (2021). Hydrodynamic Flow Stability II: Common Combustor Flow Fields. In Unsteady Combustor Physics (pp. 113-175). Cambridge: Cambridge University Press. doi:10.1017/9781108889001.005

[23] Bilger, R. W. (1978). The effect of admixing fresh emissions on the photostationary state relationship in photochemical smog. Atmospheric Environment (1967), 12(5), 1109-1118.

[24] Burke, S. P., & Schumann, T. E. W. (1928). Diffusion Flames. Industrial & Engineering Chemistry, 20(10), 998-1004

[25] Chung K. Law. (2006). Combustion Physics: Cambridge University Press

[26] Sivathanu, Y. R., & Faeth, G. M. (1990). Generalized state relationships for scalar properties in nonpremixed hydrocarbon/air flames. Combustion and Flame, 82(2), 211-230

[27] Peters, N. (2000). Turbulent Combustion. Cambridge: Cambridge University Press.

[28] Turns, S. R., & Haworth, D. C. (2021). An introduction to combustion: Concepts and applications. New York, NY u.a: McGraw-Hill.

[29] Veynante, D., & Vervisch, L. (2002). Turbulent combustion modeling. Progress in energy and combustion science, 28(3), 193-266.

[30] Bilger, R. W. (2000). Future progress in turbulent combustion research. Progress in Energy and Combustion Science, 26(4), 367-380

[31] Candel, S., Durox, D., Schuller, T., Bourgouin, J.-F., & Moeck, J. P. (2014). Dynamics of Swirling Flames. Annual Review of Fluid Mechanics, 46(1), 147-173

[32] Lyons, K. M. (2007). Toward an understanding of the stabilization mechanisms of lifted turbulent jet flames: Experiments. Progress in Energy and Combustion Science, 33(2), 211-231.

[33] Massey, J. C. (2019). Analyses of Bluff Body and Swirl-Stabilised Flames Using Large Eddy Simulation

[34] Kuo, K. K., & Acharya, R. (n.d.). Fundamentals of Turbulent and Multiphase Combustion. John Wiley & Sons.

[35] Bouali, Z., Mura, A., & Reveillon, J. (2022). Liquid Fuel Combustion. In N. Swaminathan, X.-S. Bai, N. E. L. Haugen, C. Fureby, & G. Brethouwer

(Eds.), Advanced Turbulent Combustion Physics and Applications (pp. 328–366). chapter, Cambridge: Cambridge University Press.

[36] Jenny, P., Roekaerts, D., & Beishuizen, N. (2012). Modeling of turbulent dilute spray combustion. Progress in Energy and Combustion Science, 38(6), 846-887.

[37] Sirignano WA. (1983). Fuel droplet vaporization and spray combustion theory. Prog Energy Combust Sci; 9: 291–322

[38] Williams A (1990). Combustion of liquid fuel sprays. Butterworths (Canada) Limited.

[39] J. L. Holechek, H. M. E. Geli, M. N. Sawalhah and R. Valdez. 2022, A Global Assessment: Can Renewable Energy Replace Fossil Fuels by 2050? Sustainability 2022 Vol. 14 Issue 8 Pages 4792.

[40] Masri, A. R. (2016). Turbulent Combustion of Sprays: From Dilute to Dense. Combustion Science and Technology, 188(10), 1619-1639

[41] Pope, S. B. (2000). Turbulent flows. Cambridge: Cambridge University Press.

[42] A. N. Kolmogorov. (1991). The Local Structure of Turbulence in Incompressible Viscous Fluid for Very Large Reynolds Numbers . Proceedings: Mathematical and Physical Sciences 1991 Vol. 434 Issue 1890 Pages 9-13

[43] ANSYS Inc. (2021). FLUENT Theory Guide

[44] B. E. Launder and B. I. Sharma. (1974). Application of the energy-dissipation model of turbulence to the calculation of flow near a spinning disc. Letters in Heat and Mass Transfer 1974 Vol. 1 Issue 2 Pages 131-137
[45] D. C. Wilcox. 1994. Simulation of Transition with a Two-Equation Turbulence Model. AIAA Journal 1994 Vol. 32 Issue 2 Pages 247-255

[46] T-H. Shih, W. Liou, A. Shabbir, Z. Yang, and J. Zhu. 1995. A New k-ϵ Eddy-Viscosity Model for High Reynolds Number Turbulent Flows. NASA Technical Memorandum 106721 ICOMP-94--21; CMOTr-94—6

[47] V. Yakhot and S. A. Orszag. 1986. Renormalization group analysis of turbulence. I. Basic theory. Journal of Scientific Computing 1986 Vol. 1 Issue 1 Pages 3-51

[48] Versteeg, H. and Malalasekera, W. (2007). Introduction to Computational Fluid Dynamics: The Finite Volume Method. 2nd ed. Pearson.

[49] F. R. Menter. 1994. Two-equation eddy-viscosity turbulence models for engineering applications. AIAA Journal 1994 Vol. 32 Issue 8 Pages 1598-1605

[50] M. M. Gibson and B. E. Launder. 1978. Ground effects on pressure fluctuations in the atmospheric boundary layer. Journal of Fluid Mechanics 1978 Vol. 86 Issue 3 Pages 491-511

[51] B. E. Launder. 1989. Second-Moment Closure: Present... and Future?. Inter. J. Heat Fluid Flow. 10(4). 282–300..

[52] B. E. Launder, G. J. Reece, and W. Rodi. 1974. Progress in the Development of a Reynolds-Stress Turbulence Closure. J. Fluid Mech. 68(3). 537–566.

[53] Hanjalić, K., and Launder, B., 2011. Modelling Turbulence in Engineering and the Environment: Second-Moment Routes to Closure. Cambridge: Cambridge University Press

[54] F. Menter and Y. Egorov. 2005. A Scale Adaptive Simulation Model using Two-Equation Models. In: 43rd AIAA Aerospace Sciences Meeting and Exhibit American Institute of Aeronautics and Astronautics

[55] Johansson, S.H., Davidson, L. and Olsson, E. 1993, Numerical simulation of vortex shedding past triangular cylinders at high Reynolds number using a k-ε turbulence model. Int. J. Numer. Meth. Fluids, 16: 859-878.

[56] G. Patnaik, J. P. Boris and T. R. Young. 2007, Large-scale urban simulations. In: Implicit Large Eddy Simulation: Computing Turbulent Fluid Dynamics 2007 Vol. 9780521869829

[57] M. Strelets. 2001, Detached eddy simulation of massively separated flows. 39th Aerospace Sciences Meeting and Exhibit

[58] A. Travin, M. Shur, M. Strelets and P. Spalart. 2000. Detached-Eddy Simulations Past a Circular Cylinder. Flow, Turbulence and Combustion, 63, 293-313

[59] Argyropoulos, C. D., & Markatos, N. C. (2015). Recent advances on the numerical modelling of turbulent flows. Applied Mathematical Modelling, 39(2), 693-732.

[60] Gupta, A. K., Lilley, D. G., & Syred, N. (1984). Swirl flows. Tunbridge Wells.

[61] Guo, B., Langrish, T. A., & Fletcher, D. F. (2001). Simulation of turbulent swirl flow in an axisymmetric sudden expansion. AIAA journal, 39(1), 96-102.

[62] Jochmann, P., Sinigersky, A., Hehle, M., Schäfer, O., Koch, R., & Bauer, H. J. (2006). Numerical simulation of a precessing vortex breakdown. International Journal of Heat and Fluid Flow, 27(2), 192-203.

[63] Saqr, K. M., Shehata, A. I., Taha, A. A., & ElAzm, M. M. A. (2016). CFD modelling of entropy generation in turbulent pipe flow: Effects of temperature difference and swirl intensity. Applied Thermal Engineering, 100, 999-1006.

[64] Brown, G. J., Fletcher, D. F., Leggoe, J. W., & Whyte, D. S. (2020). Application of hybrid RANS-LES models to the prediction of flow behaviour in an industrial crystalliser. Applied Mathematical Modelling, 77, 1797-1819.

[65] Brown, G. J., Whyte, D. S., & Fletcher, D. F. (2014). Dynamic flow modelling in precipitator vessels–A study of turbulence modelling approaches. Applied mathematical modelling, 38(17-18), 4163-4174.

[66] Bradley, D., 1996. Turbulent Reacting Flames. Academic Press, 1994. 647 pp. ISBN 0 12 447945 6. Journal of Fluid Mechanics, 321, pp.442–443

[67] Favre, A. 1971 Statistical equations for turbulent fluctuations in compressible flows - rates and temperatures. C. R. Ae. Se. Serie A 273(22), 1087 1092

[68] Williams, F. A. (1985). Combustion Theory: CRC Press

[69] Thierry Poinsot, Denis Veynante. (2011). Theoretical and Numerical Combustion: CNRS.

[70] K.Kuo, Principles of Combustion, 2nd Edition. (2005): PEARSON

[71] Peters, N. (1984). Laminar diffusion flamelet models in non-premixed turbulent combustion. Progress in Energy and Combustion Science, 10(3), 319-339.

[72] Peters, N. (1988). Laminar flamelet concepts in turbulent combustion. Symposium (International) on Combustion, 21(1), 1231-1250.

[73] Oijen, J. A. V., & Goey, L. P. H. D. (2000). Modelling of Premixed Laminar Flames using Flamelet-Generated Manifolds. Combustion Science and Technology, 161(1), 113-137

[74] Bao, H., Akargun, H. Y., Roekaerts, D., & Somers, B. (2023). The inclusion of scalar dissipation rate in modeling of an n -dodecane spray flame using flamelet generated manifold. Combustion and Flame, 249, 112610

[75] Kong, F., Li, T., Cheng, C., Shan, C., & Xu, B. (2022). Modeling of spray flame in gas turbine combustors with LES and FGM. Fuel, 325, 124756.

[76] Li, K., Rahnama, P., Novella, R., & Somers, B. (2023). Combining flamelet generated manifold and machine learning models in simulation of a non-premixed diffusion flame. Energy and AI, 14, 100266.

[77] Füzesi, D., Wang, S., Józsa, V., & Chong, C. T. (2023). Ammonia-methane combustion in a swirl burner: Experimental analysis and numerical modeling with Flamelet Generated Manifold model. Fuel, 341, 127403

[78] Bonniot, C., & Borghi, R. (1979). Joint probability density function in turbulent combustion. Acta Astronautica, 6(3), 309-327.

[79] Wu, H., See, Y. C., Wang, Q., & Ihme, M. (2015). A Pareto-efficient combustion framework with submodel assignment for predicting complex flame configurations. Combustion and Flame, 162(11), 4208-4230

[80] Baba, Y., & Kurose, R. (2008). Analysis and flamelet modelling for spray combustion. Journal of Fluid Mechanics, 612, 45-79

[81] Luo, Y., Wen, X., Wang, H., Luo, K., & Fan, J. (2018). Evaluation of different flamelet tabulation methods for laminar spray combustion. Physics of Fluids, 30(5).

[82] Ma, L., & Roekaerts, D. (2016). Modeling of spray jet flame under MILD condition with non-adiabatic FGM and a new conditional droplet injection model. Combustion and Flame, 165, 402-423

[83] Ma, L., & Roekaerts, D. (2017). Numerical study of the multi-flame structure in spray combustion. Proceedings of the Combustion Institute, 36(2), 2603-2613

[84] Wehrfritz, A., Kaario, O., Vuorinen, V., Somers, B., (2016). Large Eddy Simulation of n-dodecane spray flames using Flamelet Generated Manifolds. Combustion and Flame 167, 113–131.

[85] Tyliszczak, A., Cavaliere, D. E., & Mastorakos, E. (2014). LES/CMC of Blow-off in a Liquid Fueled Swirl Burner. Flow, Turbulence and Combustion, 92(1), 237-267

[86] A. D. Gosman and E. Ioannides. (1983). Aspects of computer simulation of liquid-fuelled combustors. J.Energy. 7(6). 482–490

[87] W. E. Ranz and W. R. Marshall, Jr. (1952). Vaporation from Drops, Part I. Chem. Eng. Prog. 48(3). 141–146. March.

[88] W. E. Ranz and W. R. Marshall, Jr. (1952). Evaporation from Drops, Part I and Part II. Chem. Eng. Prog. 48(4). 173–180. April

[89] S. S. Sazhin. (2006). Advanced Models of Fuel Droplet Heating and Evaporation. Progress in Energy and Combustion Science. Elsevier Science. 32. 162–214. 2006

[90] D.-H. Sheen. 1993, Swirl-Stabilised Turbulent Spray Flames in an Axisymmetric Model Combustor, Imperial College, London..

[91] Syred, N. (2006). A review of oscillation mechanisms and the role of the precessing vortex core (PVC) in swirl combustion systems. Progress in Energy and Combustion Science, 32(2), 93-161.

[92] Sheen, H., Chen, W., & Wu, J. (1997). Flow patterns for an annular flow over an axisymmetric sudden expansion. Journal of Fluid Mechanics, 350, 177-188. doi:10.1017/S0022112097006794

[93] Vignat, G., Durox, D., & Candel, S. (2022). The suitability of different swirl number definitions for describing swirl flows: Accurate, common and (over-) simplified formulations. Progress in Energy and Combustion Science, 89, 100969

[94] Syred, N. (2006). A review of oscillation mechanisms and the role of the precessing vortex core (PVC) in swirl combustion systems. Progress in Energy and Combustion Science, 32(2), 93-161.

[95] Zhang, Y., & Vanierschot, M. (2021). Modeling capabilities of unsteady RANS for the simulation of turbulent swirling flow in an annular bluff-body combustor geometry. Applied Mathematical Modelling, 89, 1140-1154

[96] Guo, S., Wang, J., Zhang, W., Lin, B., Wu, Y., Yu, S., Li, G., Hu, Z., & Huang, Z. (2019). Investigation on bluff-body and swirl stabilized flames near lean blowoff with PIV/PLIF measurements and LES modelling. Applied Thermal Engineering, 160, 114021

[97] Jeong, J., & Hussain, F. (1995). On the identification of a vortex. Journal of Fluid Mechanics, 285, 69-94. doi:10.1017/S0022112095000462.

End of chapter 4

[98] Hussien, A., & Devaud, C. B. (2022). Simulations of partially premixed turbulent ethanol spray flames using doubly conditional source term estimation (DCSE). Combustion and Flame, 239, 111651

[99] Sula, C., Grosshans, H., & Papalexandris, M. V. (2023). Numerical study of spray combustion of a biodiesel surrogate fuel using the LES-FGM approach. Combustion and Flame, 249, 112611

[100] Kong, F., Li, T., Cheng, C., Shan, C., & Xu, B. (2022). Modeling of spray flame in gas turbine combustors with LES and FGM. Fuel, 325, 124756.

[101] Yao, T., Pei, Y., Zhong, B.-J., Som, S., Lu, T., & Luo, K. H. (2017). A compact skeletal mechanism for n-dodecane with optimized semi-global low-temperature chemistry for diesel engine simulations. Fuel, 191, 339-349

[102] Ong, J. C., Pang, K. M., Bai, X.-S., Jangi, M., & Walther, J. H. (2021). Large-eddy simulation of n-dodecane spray flame: Effects of nozzle diameters on autoignition at varying ambient temperatures. Proceedings of the Combustion Institute, 38(2), 3427-3434.

[103] Wang, L.-Y., Bauer, C. K., & Gülder, Ö. L. (2019). Soot and flow field in turbulent swirl-stabilized spray flames of Jet A-1 in a model combustor. Proceedings of the Combustion Institute, 37(4), 5437-5444.

[104] BABA, Y., & KUROSE, R. (2008). Analysis and flamelet modelling for spray combustion. Journal of Fluid Mechanics, 612, 45-79.

[105] Fiorina, B., Baron, R., Gicquel, O., Thevenin, D., Carpentier, S., & Darabiha, N. (2003). Modelling non-adiabatic partially premixed flames using flame-prolongation of ILDM. Combustion Theory and Modelling, 7(3), 449-470.

[106] Mohaddes, D., Xie, W., & Ihme, M. (2021). Analysis of low-temperature chemistry in a turbulent swirling spray flame near lean blow-out. Proceedings of the Combustion Institute, 38(2), 3435-3443.

[107] Xu, R., Wang, K., Banerjee, S., Shao, J., Parise, T., Zhu, Y., Wang, S., Movaghar, A., Lee, D. J., Zhao, R., Han, X., Gao, Y., Lu, T., Brezinsky, K., Egolfopoulos, F. N., Davidson, D. F., Hanson, R. K., Bowman, C. T., & Wang, H. (2018). A physics-based approach to modeling real-fuel combustion

chemistry – II. Reaction kinetic models of jet and rocket fuels. Combustion and Flame, 193, 520-537.

[108] Rachner, Michael (1998) Die Stoffeigenschaften von Kerosin Jet A-1. DLR-Mitteilungen 98-01 (1).

[109] Mellor A. M. (1990). Design of Modern Turbine Combustors: Academic Press

[110] Liu, Y., Sun, X., Sethi, V., Nalianda, D., Li, Y.-G., & Wang, L. (2017). Review of modern low emissions combustion technologies for aero gas turbine engines. Progress in Aerospace Sciences, 94, 12-45

[111] Mongia, H. (2003). Recent Advances in the Development of Combustor Design Tools. In 39th AIAA/ASME/SAE/ASEE Joint Propulsion Conference and Exhibit.

[112] Lefebvre, A. H. (1980). Airblast atomisation. Progress in Energy and Combustion Science, 6(3), 233-261

[113] Im, K.-S., Kim, H., Lai, M.-C., & Tacina, R. (2001). Parametric Study of the Swirler/Venturi Spray Injectors. Journal of Propulsion and Power, 17(3), 717-727.

[114] Najafi, S. M. A., Mikaniki, P., & Ghassemi, H. (2021). Numerical simulation of heavy fuel oil atomization using a pulsed pressure-swirl injector. Chinese Journal of Chemical Engineering, 32, 61-69

[115] Wang, X., Huang, Y., Liu, Y., & Sun, L. (2022). Effect of the ignition location on lean light-off limits for a gas turbine combustor. Combustion and Flame, 245, 112295.

[116] Fiorina, B., Gicquel, O., Vervisch, L., Carpentier, S., & Darabiha, N. (2005). Approximating the chemical structure of partially premixed and diffusion counterflow flames using FPI flamelet tabulation. Combustion and Flame, 140(3), 147-160

[117] Schmidt, D. P., Nouar, I., Senecal, P. K., Rutland, J., Martin, J. K., Reitz, R. D., & Hoffman, J. A. (1999). Pressure-swirl atomization in the near field. SAE transactions, 471-484

[118] Han, Z., Parrish, S. E., Farrell, P. V., & Reitz, R. D. (1997). Modeling atomisation processes of pressure-swirl hollow-cone fuel sprays. Atomisation and sprays, 7(6).

[119] A. K. Lichtarowicz, R. K. Duggins, and E. Markland. (1965). Discharge Coefficients for Incompressible Non-Cavitating Flow Through Long Orifices. Journal of Mechanical Engineering Science. 7. 2.

[120] Falcitelli, M., Pasini, S., & Tognotti, L. (2002). Modelling practical combustion systems and predicting NOx emissions with an integrated CFD based approach. Computers & chemical engineering, 26(9), 1171-1183.

[121] Singh, R. K., & Agarwal, A. K. (2021). Soot and NOx modelling for diesel engines. In Engine Modeling and Simulation (pp. 195-217). Singapore: Springer Singapore.

[122] Magnussen, B. F. (1989, October). Modeling of NOx and soot formation by the eddy dissipation concept. In International Flame Research Foundation First Topic Oriented Technical Meeting (pp. 17-19).

[123] D. L. Baulch, D. D. Drysdall, D. G. Horne, and A. C. Lloyd. Evaluated Kinetic Data for High Temperature Reactions. 1,2,3. Butterworth. 1973.

[124] Torkzadeh, M. M., Bolourchifard, F., & Amani, E. (2016). An investigation of air-swirl design criteria for gas turbine combustors through a multi-objective CFD optimization. Fuel, 186, 734-749.

[125] McKinney, R., Cheung, A., Sowa, W., & Sepulveda, D. (2007, January). The Pratt & Whitney TALON X low emissions combustor: revolutionary results with evolutionary technology. In 45th AIAA aerospace sciences meeting and exhibit (p. 386)

[126] Marosky, A., Seidel, V., Bless, S., Sattelmayer, T., & Magni, F. (2012). Impact of Cooling Air Injection on the Primary Combustion Zone of a Swirl Burner. Journal of Engineering for Gas Turbines and Power, 134(12)

[127] Bassam Mohammad, S.-M. J., M. Gurhan Andac. Influence of the Primary Jets and Fuel Injection on the Aerodynamics of a Prototype Annular Gas Turbine Combustor Sector

[128] Li, D., Zhang, W., Hu, G., Jin, W., Wang, J., & Huang, Z. (2024). Investigation on unsteady formation and evolution of high-temperature zone in a staged swirl combustor. Applied Thermal Engineering, 242, 122465

[129] Wang, K., Li, F., Zhou, T., & Wang, D. (2024). Numerical simulations on the effect of swirler installation angle on outlet temperature distribution in gas turbine combustors. Applied Thermal Engineering, 240, 122252

[130] Agrawal, A. K. (2022). Liquid Fuel Atomisation and Combustion. In J. O'Connor, B. Noble, & T. Lieuwen (Eds.), Renewable Fuels: Sources,

Conversion, and Utilization (pp. 414–450). chapter, Cambridge: Cambridge University Press

[131] Corporan, E., Williams, V., Stouffer, S., Hendershott, T., & Monfort, J. (2023). High temperature fuel impacts on combustion characteristics of a swirl-stabilized combustor. Fuel, 335, 126993.

[132] Chong, C. T., Chiong, M. C., Ng, J. H., Tran, M. V., Valera-Medina, A., Józsa, V., & Tian, B. (2020). Dual-fuel operation of biodiesel and natural gas in a model gas turbine combustor. Energy & fuels, 34(3), 3788-3796

[133] Saravanamuttoo, H. I. H., Rogers, G. F. C., Cohen, H.,, Straznicky, P. V. (2009). Gas Turbine Theory. Harlow, England; New York: Pearson Prentice Hall. ISBN: 9780132224376

[134] Kumar, M., & Karmakar, S. (2023). Butyl butyrate, Jet A-1 and their blends: Combustion performance in the swirl stabilized burner at different inlet air temperature. Biomass and Bioenergy, 168, 106651.

[135] Altaher, M. A., Li, H., & Andrews, G. E. (2012, June). Co-firing of kerosene and biodiesel with natural gas in a low NOx radial swirl combustor. In Turbo Expo: Power for Land, Sea, and Air (Vol. 44670, pp. 557-567). American Society of Mechanical Engineers

[136] Seok, W., Kim, G. H., Seo, J., & Rhee, S. H. (2019). Application of the Design of Experiments and Computational Fluid Dynamics to Bow Design Improvement. Journal of Marine Science and Engineering, 7(7), 226. https://www.mdpi.com/2077-1312/7/7/226

[137] Rhew, R., & Parker, P. A Parametric Geometry Computational Fluid Dynamics (CFD) Study Utilizing Design of Experiments (DOE). In 2007 U.S. Air Force T&E Days. https://doi.org/10.2514/6.2007-1615

[138] Faritzon, Olle (2023) Design of experiment based on full factorial CFD spray modelling, Design of Experiment Based on Full Factorial CFD Spray Modelling. dissertation. Lunds universitet/Institutionen för energivetenskaper.

[139] Cleaver, T. A., Gutman, A. J., Martin, C. L., Reeder, M. F., & Hill, R. R. (2016). Using design of experiments methods for applied computational fluid dynamics: A case study. Quality Engineering, 28(3), 280–292. https://doi.org/10.1080/08982112.2015.1101645

[140] Marrodán, L., Fuster, M., Millera, Á., Bilbao, R., & Alzueta, M. U. (2018). Ethanol as a fuel additive: high-pressure oxidation of its mixtures with acetylene. Energy & Fuels, 32(10), 10078-10087.

[141] Paul, P. H., & Najm, H. N. (1998, January). Planar laser-induced fluorescence imaging of flame heat release rate. In Symposium (International) on Combustion (Vol. 27, No. 1, pp. 43-50). Elsevier.

[142] Sonwani, S., & Saxena, P. (Eds.). (2022). Greenhouse gases: sources, sinks and mitigation. Singapore:: Springer.

[143] Doll, U., Stockhausen, G., Heinze, J., Meier, U., Hassa, C., & Bagchi, I. (2017). Temperature measurements at the outlet of a lean burn single-sector combustor by laser optical methods. Journal of Engineering for Gas Turbines and Power, 139(2), 021507.

[144] Kocaman, O. C., Aksu, T., & Uslu, S. (2016). Large-Eddy Simulation of a Full Annular RQL Combustion Chamber & Fuel Distribution Effects on the Combustor Exit Temperature Profile. In 52nd AIAA/SAE/ASEE Joint Propulsion Conference (p. 4786).

[145] Dalla Barba, F., Wang, J., & Picano, F. (2021). Revisiting D2-law for the evaporation of dilute droplets. Physics of Fluids, 33(5).

[146] Yuan, R. (2015). Measurement in Swirl-Stabilised Spray Flames at Blow-Off, University of Cambridge, Ph.D. thesis.

[147] Felden, A., Esclapez, L., Riber, E., Cuenot, B., & Wang, H. (2018). Including real fuel chemistry in LES of turbulent spray combustion. Combustion and Flame, 193, 397-416.

[148] Xin, S., He, Y., Liu, T., Wu, Y., Wu, X., & Wang, Z. (2023). Temperature and flame structure imaging in kerosene swirl-stabilized spray flames at low air flow using TLAF and OH-PLIF. Journal of the Energy Institute, 109, 101294.

[149] Rault, T. M., Vishwanath, R. B., & Gülder, Ö. L. (2021). Impact of ethanol blending on soot in turbulent swirl-stabilized Jet A-1 spray flames in a model gas turbine combustor. Proceedings of the Combustion Institute, 38(4), 6431-6439.

[150] Eckel, G., Grohmann, J., Cantu, L., Slavinskaya, N., Kathrotia, T., Rachner, M., Le Clercq, P., Meier, W., & Aigner, M. (2019). LES of a swirl-stabilized kerosene spray flame with a multi-component vaporization model and detailed chemistry. Combustion and Flame, 207, 134-152.

[151] Puggelli, S., Bertini, D., Mazzei, L., & Andreini, A. (2016). Scale Adaptive Simulations of a Swirl Stabilized Spray Flame Using Flamelet Generated Manifold. Energy Procedia, 101, 1143-1150.

[152] Wang, L.-Y., Bauer, C. K., & Gülder, Ö. L. (2019). Soot and flow field in turbulent swirl-stabilized spray flames of Jet A-1 in a model combustor. Proceedings of the Combustion Institute, 37(4), 5437-5444.

[153] Malbois, P., Salaün, E., Vandel, A., Godard, G., Cabot, G., Renou, B., Boukhalfa, A. M., & Grisch, F. (2019). Experimental investigation of aerodynamics and structure of a swirl-stabilized kerosene spray flame with laser diagnostics. Combustion and Flame, 205, 109-122.

[154] Sun, C., Shi, Z., Li, Y., Lou, Y., Wei, G., & Yang, Z. (2023). Development of a Skeletal Mechanism of a Four-Component Diesel Surrogate Fuel Using the Decoupling Method. ACS omega, 8(39), 35904–35918.

[155] Zhang, Y., Jia, M., Wang, P., Chang, Y., Yi, P., Liu, H., & He, Z. (2019). Construction of a decoupling physical–chemical surrogate (DPCS) for practical diesel fuel. Applied Thermal Engineering, 149, 536-547.

[156] Al Qubeissi, M. (2018). Predictions of droplet heating and evaporation: An application to biodiesel, diesel, gasoline and blended fuels. Applied Thermal Engineering, 136, 260-267.

[157] Ra, Y., & Reitz, R. D. (2009). A vaporization model for discrete multi-component fuel sprays. International Journal of Multiphase Flow, 35(2), 101-117.

[158] Myong, K. J., Suzuki, H., Senda, J., & Fujimoto, H. (2008). Spray inner structure of evaporating multi-component fuel. Fuel, 87(2), 202-210.

[159] Xu, G., Jia, M., Li, Y., Chang, Y., & Wang, T. (2018). Potential of reactivity controlled compression ignition (RCCI) combustion coupled with variable valve timing (VVT) strategy for meeting Euro 6 emission regulations and high fuel efficiency in a heavy-duty diesel engine. Energy conversion and management, 171, 683-698.

[160] Tay, K. L., Yang, W., Zhao, F., Yu, W., & Mohan, B. (2017). Numerical investigation on the combined effects of varying piston bowl geometries and ramp injection rate-shapes on the combustion characteristics of a kerosene-diesel fueled direct injection compression ignition engine. Energy conversion and management, 136, 1-10.

[161] Li, Y., Jia, M., Chang, Y., Fan, W., Xie, M., & Wang, T. (2015). Evaluation of the necessity of exhaust gas recirculation employment for a methanol/diesel reactivity controlled compression ignition engine operated at medium loads. Energy Conversion and Management, 101, 40-51.

[162] Swaminathan, N., Bai, X., Haugen, N., Fureby, C., & Brethouwer, G. (Eds.). (2022). Advanced Turbulent Combustion Physics and Applications. Cambridge: Cambridge University Press. doi:10.1017/9781108671422

[163] Naoumov, V., Krioukov, V., Abdullin, A., & Demin, A. (2019). Chemical Kinetics in Combustion and Reactive Flows: Modeling Tools and Applications. Cambridge: Cambridge University Press. doi:10.1017/9781108581714

[164] Sultanian, B. (2018). Gas Turbines: Internal Flow Systems Modeling (Cambridge Aerospace Series). Cambridge: Cambridge University Press. doi:10.1017/9781316755686

[165] Ricart, L. M., Reltz, R. D., & Dec, J. E. (2000). Comparisons of diesel spray liquid penetration and vapor fuel distributions with in-cylinder optical measurements. J. Eng. Gas Turbines Power, 122(4), 588-595.

[166] Reitz, R. (1987). Modeling atomisation processes in high-pressure vaporizing sprays. Atomisation and Spray technology, 3(4), 309-337.

[167] Yi, P., Long, W., Jia, M., Tian, J., & Li, B. (2016). Development of a quasi-dimensional vaporization model for multi-component fuels focusing on forced convection and high temperature conditions. International Journal of Heat and Mass Transfer, 97, 130-145.

[168] Sazhin, S. S., Elwardany, A. E., Krutitskii, P. A., Deprédurand, V., Castanet, G., Lemoine, F., ... & Heikal, M. R. (2011). Multi-component droplet heating and evaporation: numerical simulation versus experimental data. International journal of thermal sciences, 50(7), 1164-1180.

[169] Singh, S., Reitz, R. D., & Musculus, M. P. (2006). Comparison of the characteristic time (CTC), representative interactive flamelet (RIF), and direct integration with detailed chemistry combustion models against optical diagnostic data for multi-mode combustion in a heavy-duty DI diesel engine. SAE transactions, 61-82.

[170] Pitz, W. J., & Mueller, C. J. (2011). Recent progress in the development of diesel surrogate fuels. Progress in Energy and Combustion Science, 37(3), 330-350.

[171] Li, Y., Jia, M., Chang, Y., Liu, Y., Xie, M., Wang, T., & Zhou, L. (2014). Parametric study and optimization of a RCCI (reactivity controlled compression ignition) engine fueled with methanol and diesel. Energy, 65, 319-332.

[172] Jia, M., Li, Y., Xie, M., & Wang, T. (2013). Numerical evaluation of the potential of late intake valve closing strategy for diesel PCCI (premixed charge compression ignition) engine in a wide speed and load range. Energy, 51, 203-215.

[173] Jia, M., Xie, M., & Wang, T. (2013). Numerical investigation of the influence of intake valve lift profile on a diesel premixed charge compression ignition engine with a variable valve actuation system at moderate loads and speeds. International Journal of Engine Research, 14(2), 151-179.

[174] Torelli, R., D'Errico, G., Lucchini, T., Ikonomou, V., & McDavid, R. M. (2015). A spherical volume interaction DDM approach for diesel spray modeling. Atomisation and Sprays, 25(4).

[175] Pei, Y., Mehl, M., Liu, W., Lu, T., Pitz, W. J., & Som, S. (2015). A multicomponent blend as a diesel fuel surrogate for compression ignition engine applications. Journal of Engineering for Gas Turbines and Power, 137(11), 111502.

[176] Xiwei, W. A. N. G., HUANG, Y., Yunfeng, L. I. U., Yufan, W. U., & Hongyan, W. A. N. G. (2023). An FV-EE model to predict lean blowout limits for gas turbine combustors with different structures and sprays. Chinese Journal of Aeronautics, 36(5), 145-156.

[177] Feng, Y., Li, X., Ren, X., Gu, C., Lv, X., Li, S., & Wang, Z. (2024). Influence of the turbulence model on the numerical predictions of cold turbulent flow in a heavy-duty gas turbine DLN combustor. International Journal of Thermal Sciences, 196, 108735.

[178] Pang, L., Zhao, N., Xu, H., Li, Z., Zheng, H., & Yang, R. (2023). Numerical simulations on effect of cooling hole diameter on the outlet temperature distribution for a gas turbine combustor. Applied Thermal Engineering, 234, 121308.

[179] Mahto, N., & Chakravarthy, S. R. (2022). Response surface methodology for design of gas turbine combustor. Applied Thermal Engineering, 211, 118449.

[180] Tamang, S., & Park, H. (2023). Numerical investigation of combustion characteristics for hydrogen mixed fuel in a can-type model of the gas

turbine combustor. International Journal of Hydrogen Energy, 48(30), 11493-11512.

[181] Ruan, C., He, Z., Feng, X., He, P., Gao, X., Zhang, L., ... & Lu, X. (2022). Experimental study of axial spark location effects on transient flame/flow dynamics during ignition in a kerosene-fueled gas turbine model combustor. Fuel, 323, 124336.

[182] Kong, F., Li, T., Cheng, C., Shan, C., & Xu, B. (2022). Modeling of spray flame in gas turbine combustors with LES and FGM. Fuel, 325, 124756.

[183] Nozari, M., Tabejamaat, S., Sadeghizade, H., & Aghayari, M. (2021). Experimental investigation of the effect of gaseous fuel injector geometry on the pollutant formation and thermal characteristics of a micro gas turbine combustor. Energy, 235, 121372.

[184] Liu, H., Zeng, Z., & Guo, K. (2023). Numerical analysis on hydrogen swirl combustion and flow characteristics of a micro gas turbine combustor with axial air/fuel staged technology. Applied Thermal Engineering, 219, 119460.

[185] Yan, P., Fan, W., & Zhang, R. (2023). Predicting the NOx emissions of low heat value gas rich-quench-lean combustor via three integrated learning algorithms with Bayesian optimization. Energy, 273, 127227.

[186] McKinney, R., Cheung, A., Sowa, W., & Sepulveda, D. (2007, January). The Pratt & Whitney TALON X low emissions combustor: revolutionary results with evolutionary technology. In 45th AIAA aerospace sciences meeting and exhibit (p. 386).

[187] Outcalt, S., Laesecke, A., & Freund, M. B. (2009). Density and speed of sound measurements of Jet A and S-8 aviation turbine fuels. Energy & fuels, 23(3), 1626-1633.

[188] Coordinating Research Council. (2004). Handbook of aviation fuel properties. Warrendale, PA: Society of Automotive Engineers.

[189] Fan, X., Xu, G., Liu, C., Wang, J., Lin, Y., & Zhang, C. (2020). Experimental investigations of the flow field structure and interactions between sectors of a double-swirl low-emission combustor. Journal of Thermal Science, 29, 43-51.

[190] Epstein, A. H. (2012). Aircraft engines' needs from combustion science and engineering. Combustion and Flame, 159(5), 1791-1792.

[191] Longwell, J. P., Frost, E. E., & Weiss, M. A. (1953). Flame stability in bluff body recirculation zones. Industrial & Engineering Chemistry, 45(8), 1629-1633.

[192] Ateshkadi, A., McDonell, V. G., & Samuelsen, G. S. (2000). Lean blowout model for a spray-fired swirl-stabilized combustor. Proceedings of the Combustion Institute, 28(1), 1281-1288.

[193] Polymeropoulos, C. E., & Das, S. (1975). The effect of droplet size on the burning velocity of kerosene-air sprays. Combustion and Flame, 25, 247-257.

[194] Gong, J. S., & Fu, W. B. (2007). The experimental study on the flow characteristics for a swirling gas–liquid spray atomizer. Applied thermal engineering, 27(17-18), 2886-2892.

[195] Pang, L., Zhao, N., Xu, H., Li, Z., Zheng, H., & Yang, R. (2023). Numerical simulations on effect of cooling hole diameter on the outlet temperature distribution for a gas turbine combustor. Applied Thermal Engineering, 234, 121308.

[196] Pang, L., Zhao, N., Xu, H., Li, Z., Zheng, H., & Yang, R. (2023a). Numerical simulations on effect of cooling hole diameter on the outlet temperature distribution for a gas turbine combustor. Applied Thermal Engineering, 234, 121308.

[197] Rashwan, S. S. (2018). The effect of swirl number and oxidizer composition on combustion characteristics of non-premixed methane flames. Energy & Fuels, 32(2), 2517-2526.

[198] Alajmi, A. E. S. E. T., Adam, N. M., Hairuddin, A. A., & Abdullah, L. C. (2019). Fuel atomisation in gas turbines: A review of novel technology. International Journal of Energy Research, 43(8), 3166-3181.

[199] Bazdidi-Tehrani, F., Teymoori, A., & Ghiyasi, M. (2022). Sensitivity Analysis of Pollutants and Pattern Factor in a Gas Turbine Model Combustor due to Changes in Stabilizing Jets Characteristics. Journal of Thermal Science, 31(5), 1622-1641.

[200] Xu, R., Zhao, J. X., & Wang, S. F. (2014). Numerical study of influences of primary jets on turbulent flows and spray combustion in model combustor. Journal of Aerospace Power, 29(06), 1312-1322.

[201] Torkzadeh, M. M., Bolourchifard, F., & Amani, E. (2016). An investigation of air-swirl design criteria for gas turbine combustors through a multi-objective CFD optimization. Fuel, 186, 734-749.

[202] Falcitelli, M., Pasini, S., & Tognotti, L. (2002). Modelling practical combustion systems and predicting NOx emissions with an integrated CFD based approach. Computers & chemical engineering, 26(9), 1171-1183.

[203] Singh, R. K., & Agarwal, A. K. (2021). Soot and NOx modelling for diesel engines. In Engine Modeling and Simulation (pp. 195-217). Singapore: Springer Singapore.

[204] Magnussen, B. F. (1989, October). Modeling of NOx and soot formation by the eddy dissipation concept. In International Flame Research Foundation First Topic Oriented Technical Meeting (pp. 17-19).

[205] Marosky, A., Seidel, V., Bless, S., Sattelmayer, T., & Magni, F. (2012). Impact of Cooling Air Injection on the Primary Combustion Zone of a Swirl Burner. Journal of Engineering for Gas Turbines and Power, 134(12).

[206] Bassam Mohammad, S.-M. J., M. Gurhan Andac. Influence of the Primary Jets and Fuel Injection on the Aerodynamics of a Prototype Annular Gas Turbine Combustor Sector.

[207] D. L. Baulch, D. D. Drysdall, D. G. Horne, and A. C. Lloyd. Evaluated Kinetic Data for High Temperature Reactions. 1,2,3. Butterworth. 1973.

[208] Corporan, E., Williams, V., Stouffer, S., Hendershott, T., & Monfort, J. (2023). High temperature fuel impacts on combustion characteristics of a swirl-stabilized combustor. Fuel, 335, 126993.

[209] Kumar, M., & Karmakar, S. (2023). Butyl butyrate, Jet A-1 and their blends: Combustion performance in the swirl stabilized burner at different inlet air temperature. Biomass and Bioenergy, 168, 106651.

[210] Li, D., Zhang, W., Hu, G., Jin, W., Wang, J., & Huang, Z. (2024). Investigation on unsteady formation and evolution of high-temperature zone in a staged swirl combustor. Applied Thermal Engineering, 242, 122465.

[211] Hussien, A., & Devaud, C. B. (2022). Simulations of partially premixed turbulent ethanol spray flames using doubly conditional source term estimation (DCSE). Combustion and Flame, 239, 111651.

[212] Sula, C., Grosshans, H., & Papalexandris, M. V. (2023). Numerical study of spray combustion of a biodiesel surrogate fuel using the LES-FGM approach. Combustion and Flame, 249, 112611.

[213] Kong, F., Li, T., Cheng, C., Shan, C., & Xu, B. (2022). Modeling of spray flame in gas turbine combustors with LES and FGM. Fuel, 325, 124756.

[214] Wang, K., Li, F., Zhou, T., & Wang, D. (2024). Numerical simulations on the effect of swirler installation angle on outlet temperature distribution in gas turbine combustors. Applied Thermal Engineering, 240, 122252.

[215] Chong, C. T., Chiong, M. C., Ng, J. H., Tran, M. V., Valera-Medina, A., Józsa, V., & Tian, B. (2020). Dual-fuel operation of biodiesel and natural gas in a model gas turbine combustor. Energy & fuels, 34(3), 3788-3796.

[216] Agrawal, A. K. (2022). Liquid Fuel Atomisation and Combustion. In J. O'Connor, B. Noble, & T. Lieuwen (Eds.), Renewable Fuels: Sources, Conversion, and Utilization (pp. 414–450). chapter, Cambridge: Cambridge University Press.

[217] Altaher, M. A., Li, H., & Andrews, G. E. (2012, June). Co-firing of kerosene and biodiesel with natural gas in a low NOx radial swirl combustor. In Turbo Expo: Power for Land, Sea, and Air (Vol. 44670, pp. 557-567). American Society of Mechanical Engineers.

[218] Saravanamuttoo, H. I. H., Rogers, G. F. C., Cohen, H.,, Straznicky, P. V. (2009). Gas Turbine Theory. Harlow, England; New York: Pearson Prentice Hall. ISBN: 9780132224376.

[219] Bilger, R. W. (2011). The role of combustion technology in the 21st century. In Turbulent Combustion Modeling: Advances, New Trends and Perspectives (pp. 3-18). Dordrecht: Springer Netherlands.

[220] Dalla Barba, F., Wang, J., & Picano, F. (2021). Revisiting D2-law for the evaporation of dilute droplets. Physics of Fluids, 33(5).

[221] Bouali, Z., Mura, A., & Reveillon, J. (2022). Liquid Fuel Combustion. In N. Swaminathan, X.-S. Bai, N. E. L. Haugen, C. Fureby, & G. Brethouwer (Eds.), Advanced Turbulent Combustion Physics and Applications (pp. 328–366). chapter, Cambridge: Cambridge University Press.

[222] Chiaramonti, D., Rizzo, A. M., Spadi, A., Prussi, M., Riccio, G., & Martelli, F. (2013). Exhaust emissions from liquid fuel micro gas turbine fed with diesel oil, biodiesel and vegetable oil. Applied energy, 101, 349-356.

[223] Li, J., & Li, Y. (2023). Micro gas turbine: Developments, applications, and key technologies on components. Propulsion and Power Research, 12(1), 1-43.

[224] Research Centre for High Performance Turbomachinery, URL: https://www.birmingham.ac.uk/research/activity/mechanical-engineering/turbomachinery [cited 12 March 2024].

[225] Massey, J. C. (2019). Analyses of Bluff Body and Swirl-Stabilised Flames Using Large Eddy Simulation.

[226] Kuo, K. K., & Acharya, R. (n.d.). Fundamentals of Turbulent and Multiphase Combustion. John Wiley & Sons.

[227] Turns, S. R., & Haworth, D. C. (2021). An introduction to combustion: Concepts and applications. New York, NY u.a: McGraw-Hill.

[228] Veynante, D., & Vervisch, L. (2002). Turbulent combustion modeling. Progress in energy and combustion science, 28(3), 193-266.

Appendix A

The results of URANS of different turbulence models in Chapter 4 are presented as following:

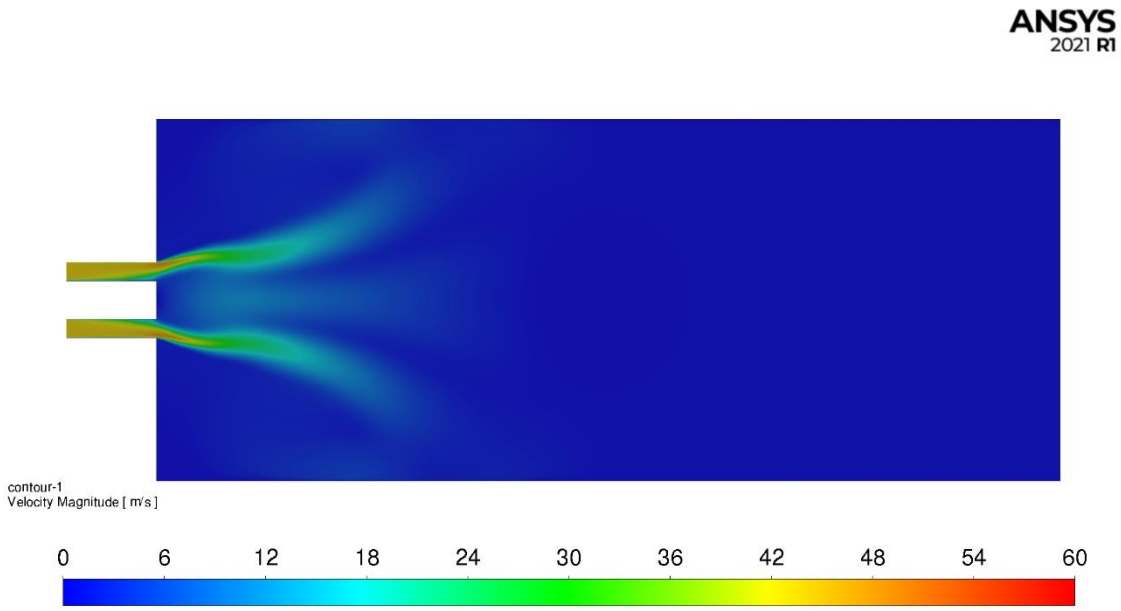

Figure A.1 Instantaneous velocity magnitude at t=0.2s (realizable k-epsilon)

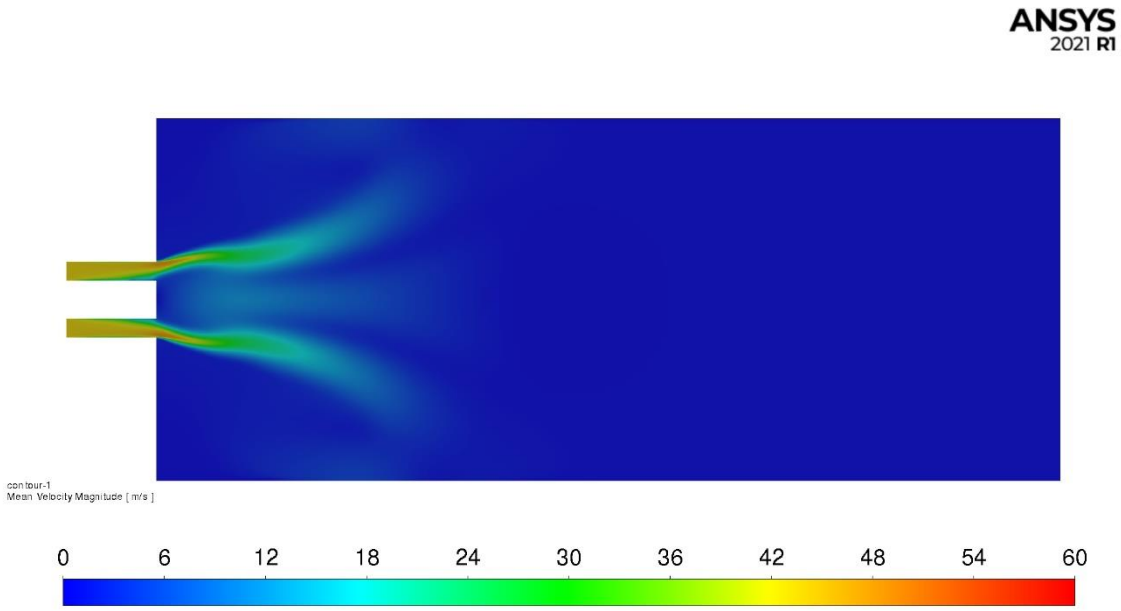

Figure A.2 Time-averaged velocity magnitude (realizable k-epsilon)

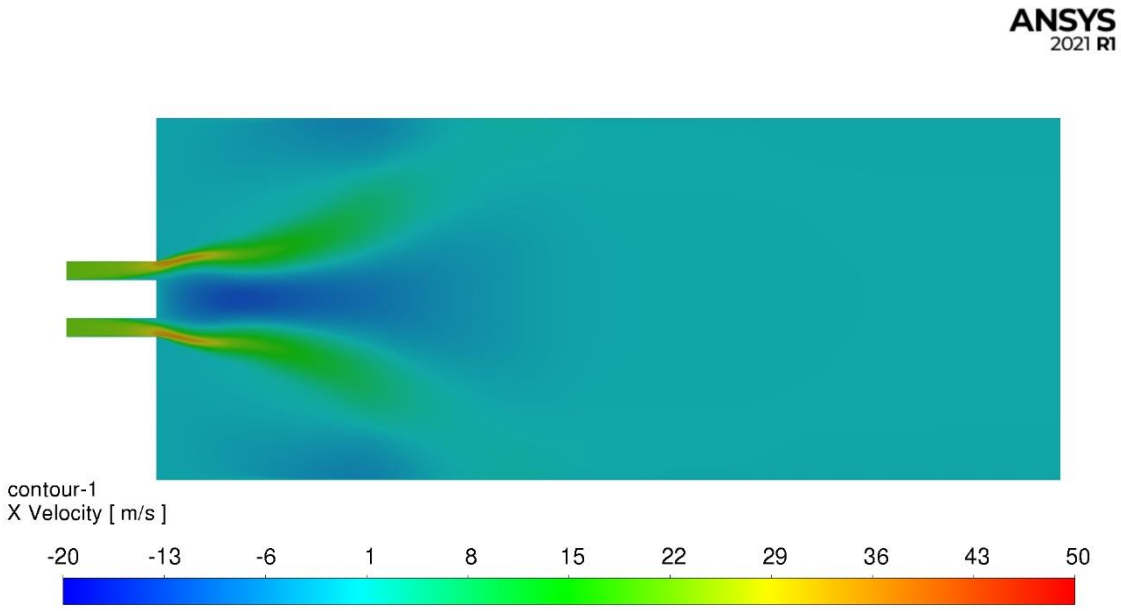

Figure A.3 Instantaneous axial velocity (realizable k-epsilon)

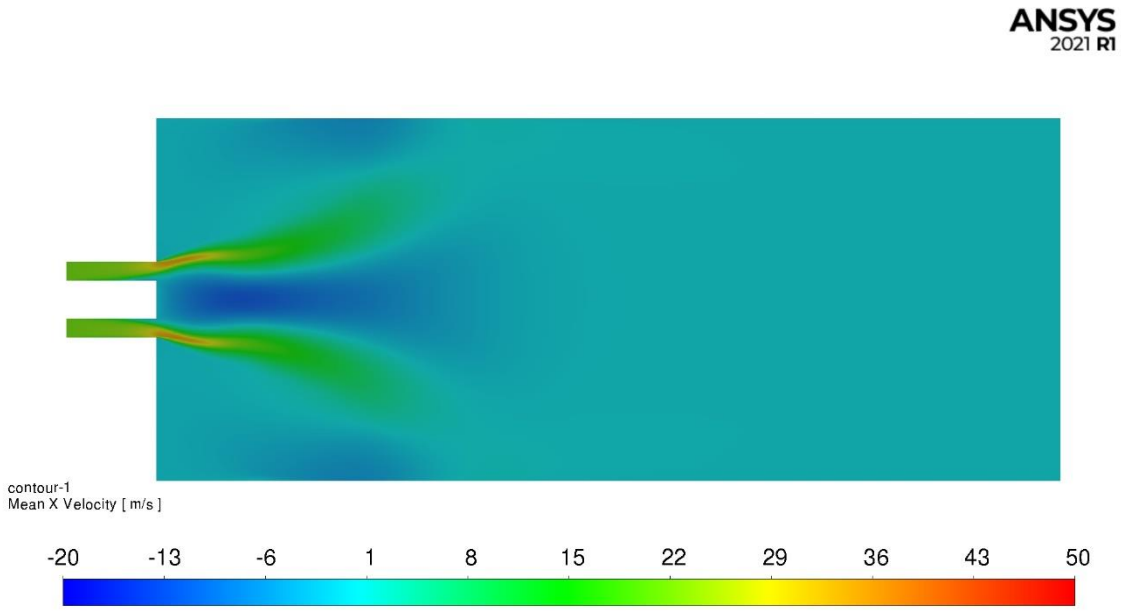

Figure A.4 Time-averaged axial velocity (realizable k-epsilon)

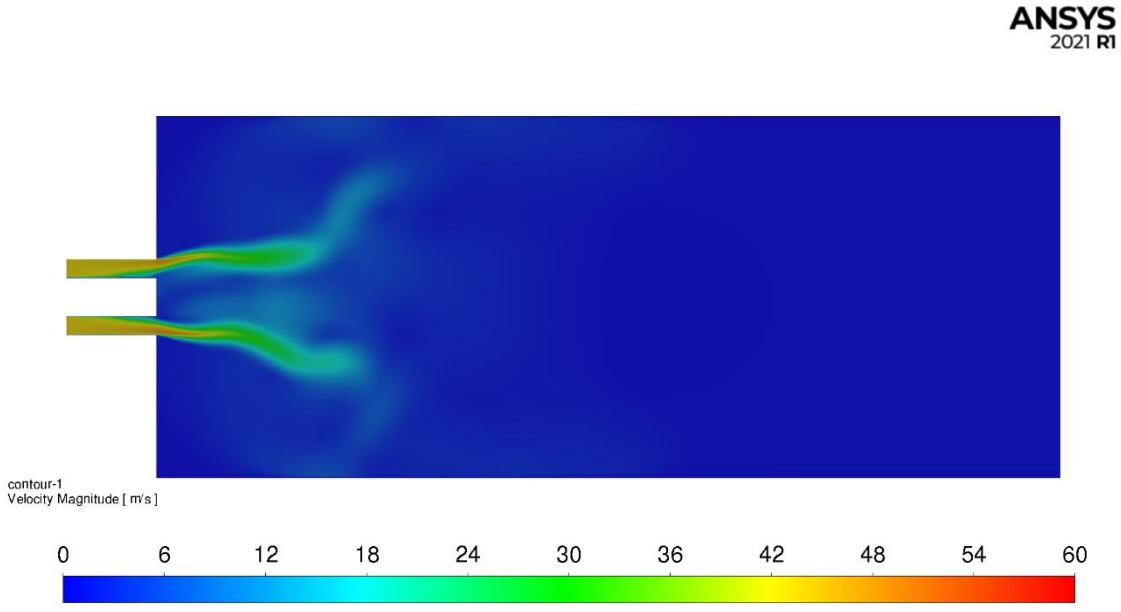

Figure A.5 Instantaneous velocity magnitude at t=0.2s (RNG k-epsilon)

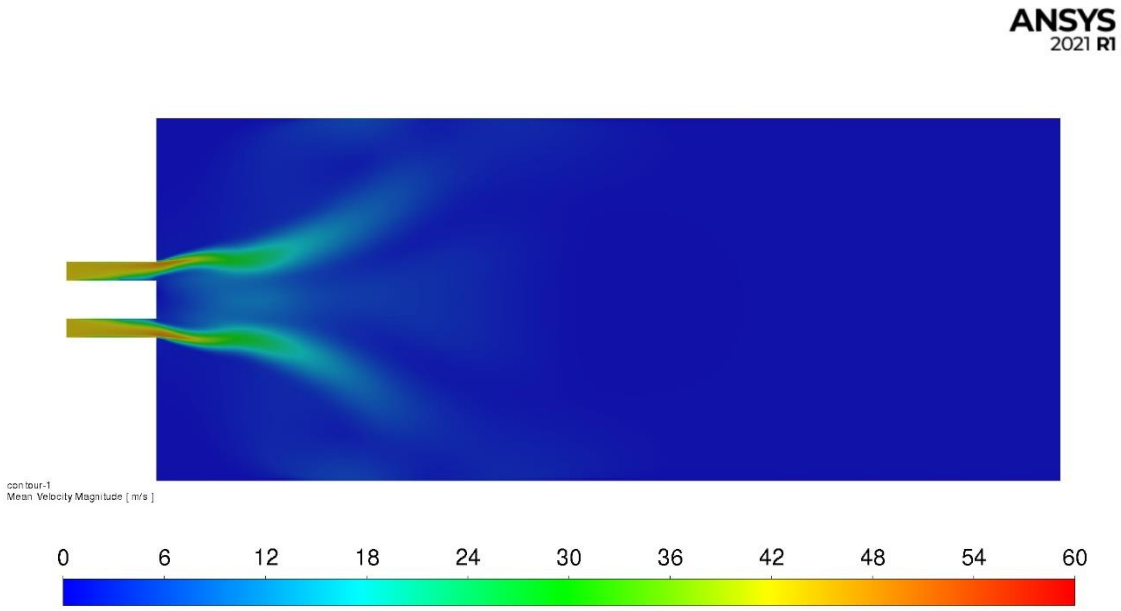

Figure A.6 Time-averaged velocity magnitude (RNG k-epsilon)

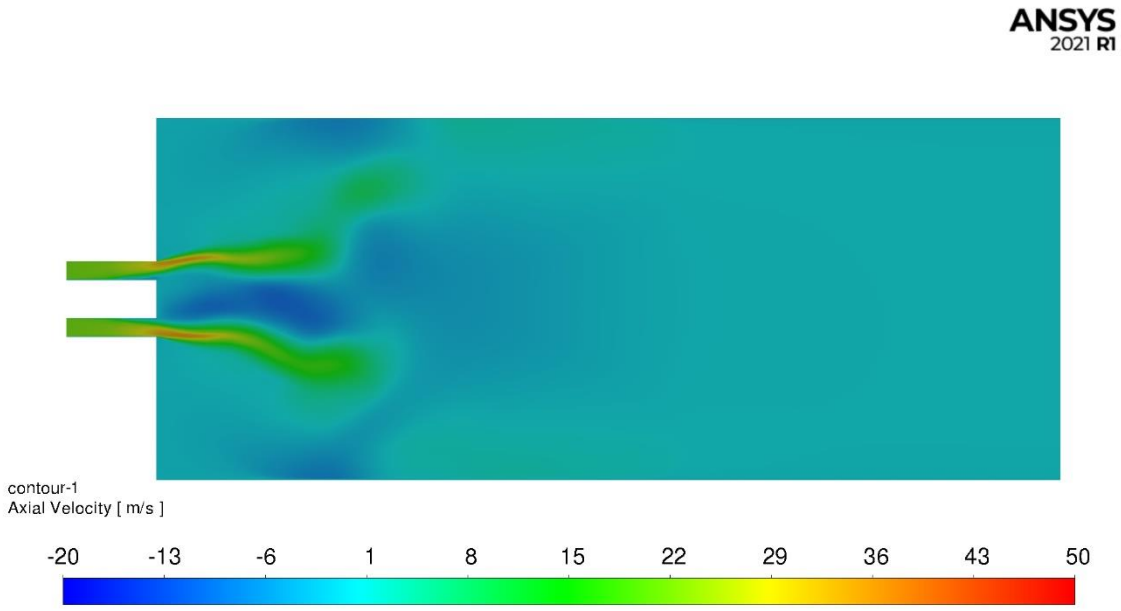

Figure A.7 Instantaneous axial velocity at t=0.2s (RNG k-epsilon)

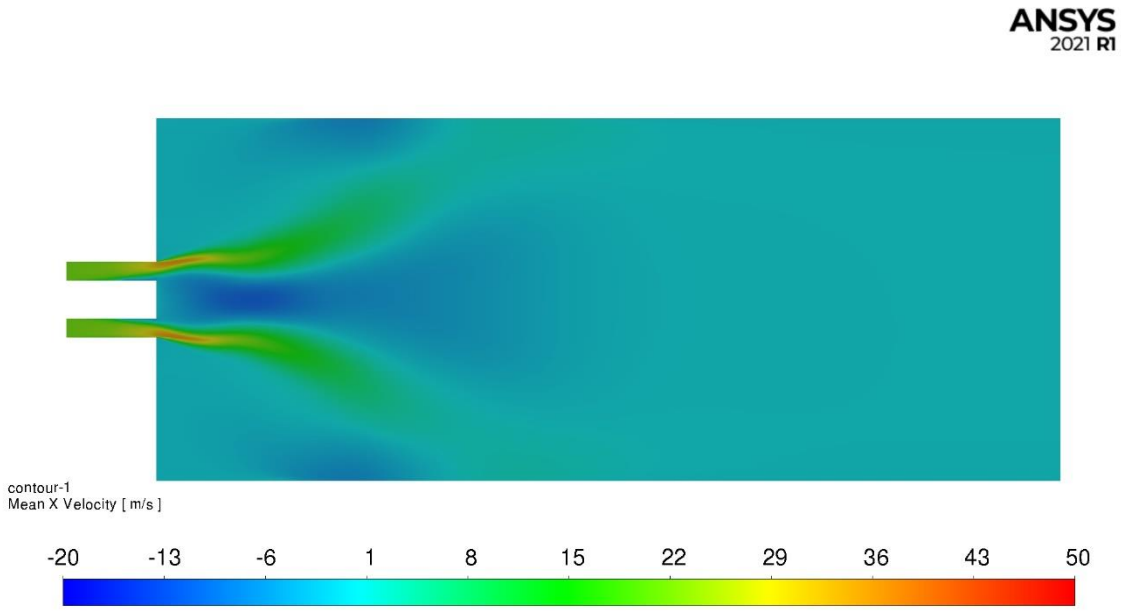

Figure A.8 Time-averaged axial velocity (RNG k-epsilon)

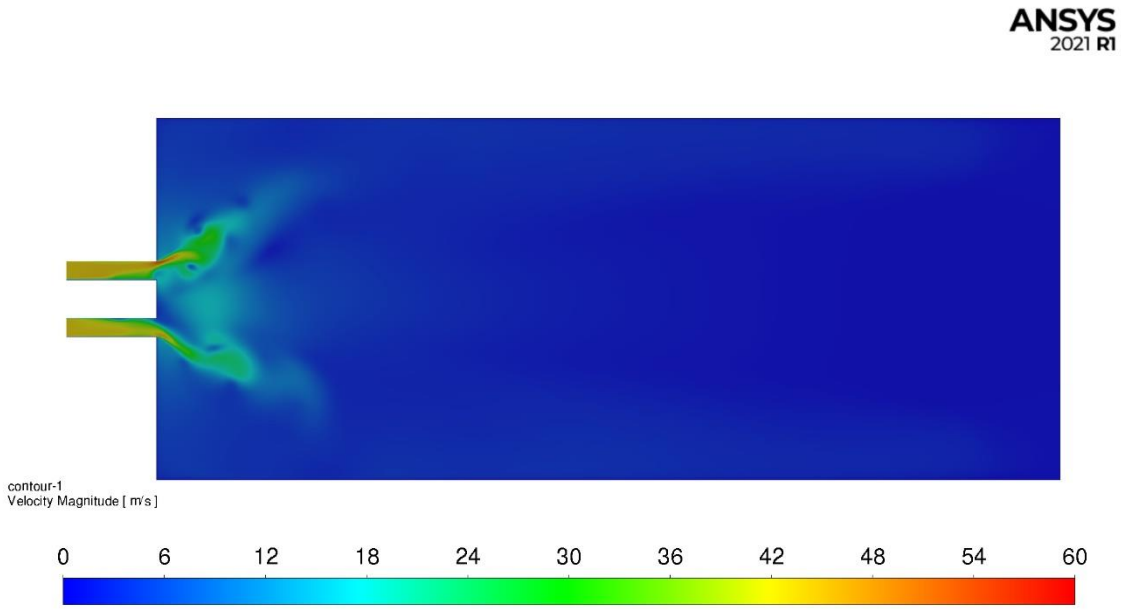

Figure A.9 Instantaneous velocity magnitude at t=0.2s (RSM-epsilon-LRR)

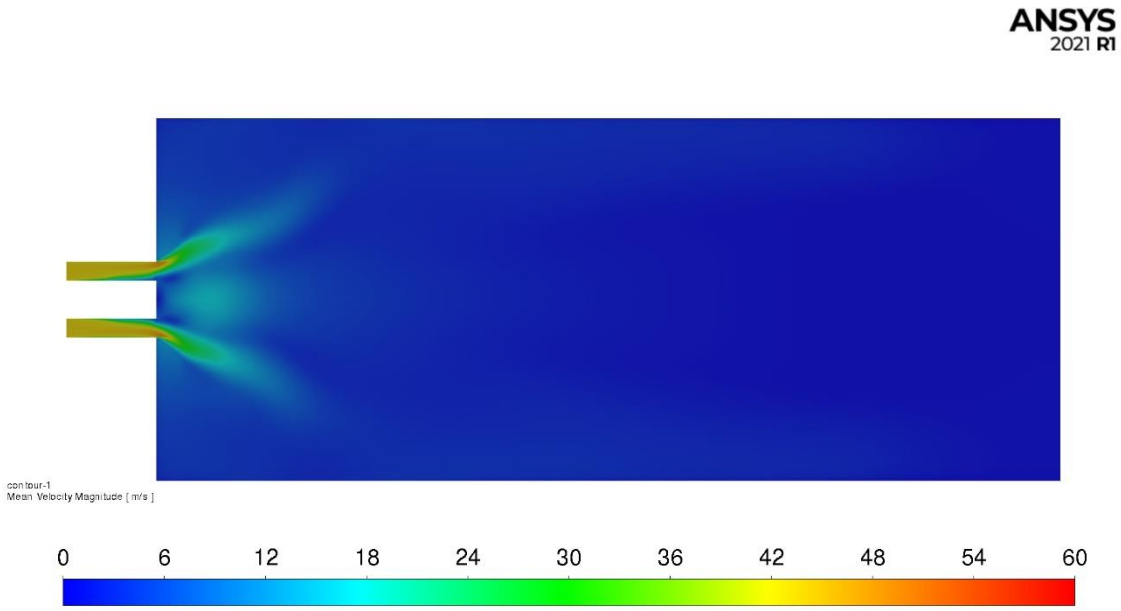

Figure A.10 Time-averaged velocity magnitude (RSM-epsilon-LRR)

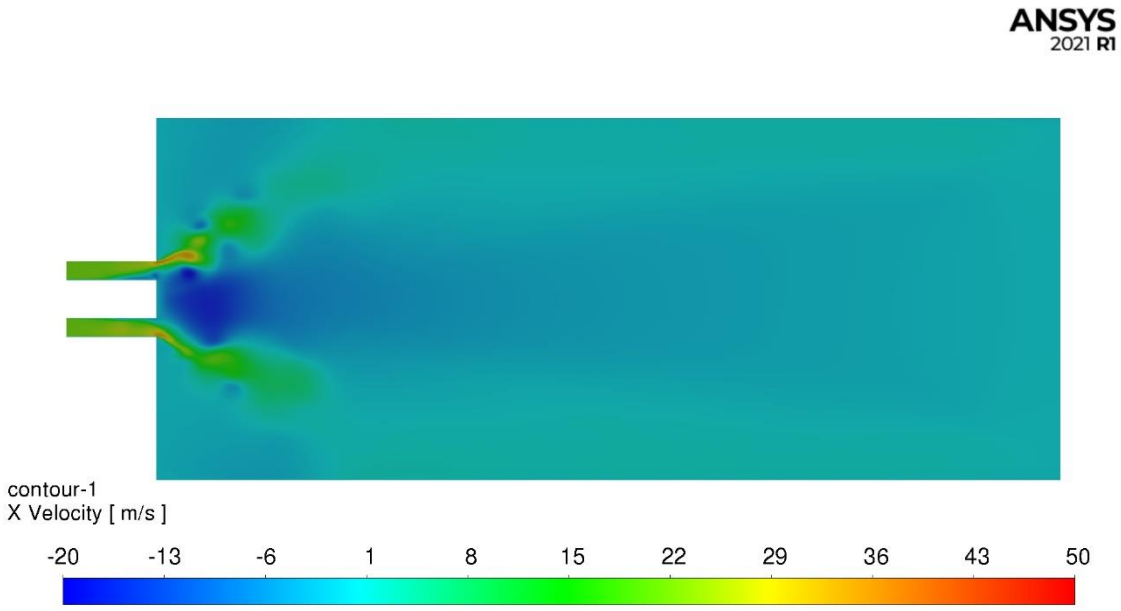

Figure A.11 Instantaneous axial velocity at t=0.2s (RSM-epsilon-LRR)

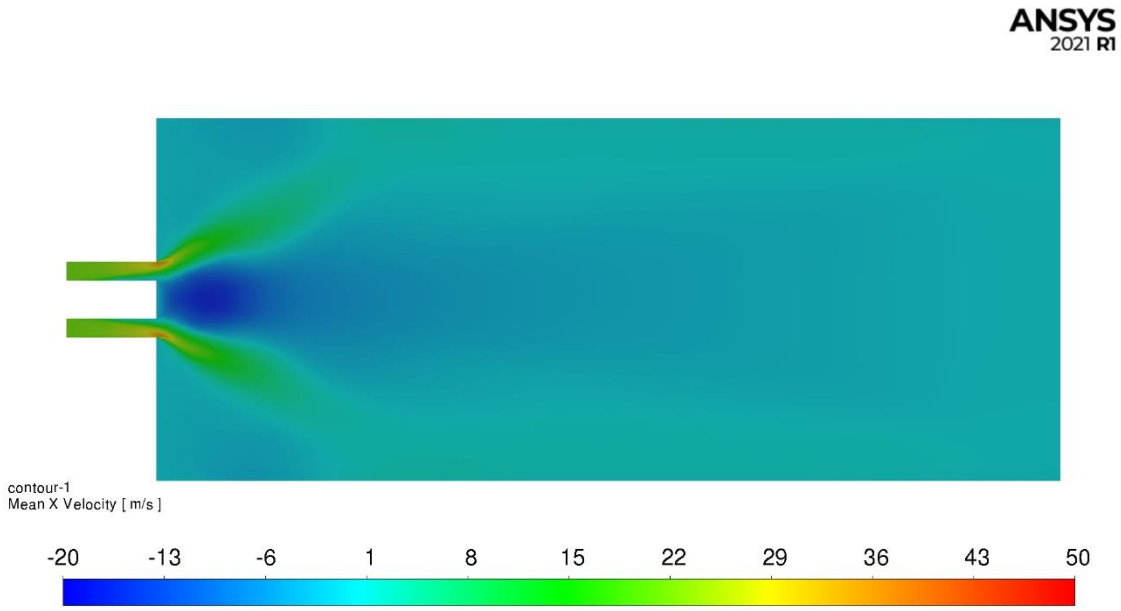

Figure A.12 Time-averaged axial velocity (RSM-epsilon-LRR)

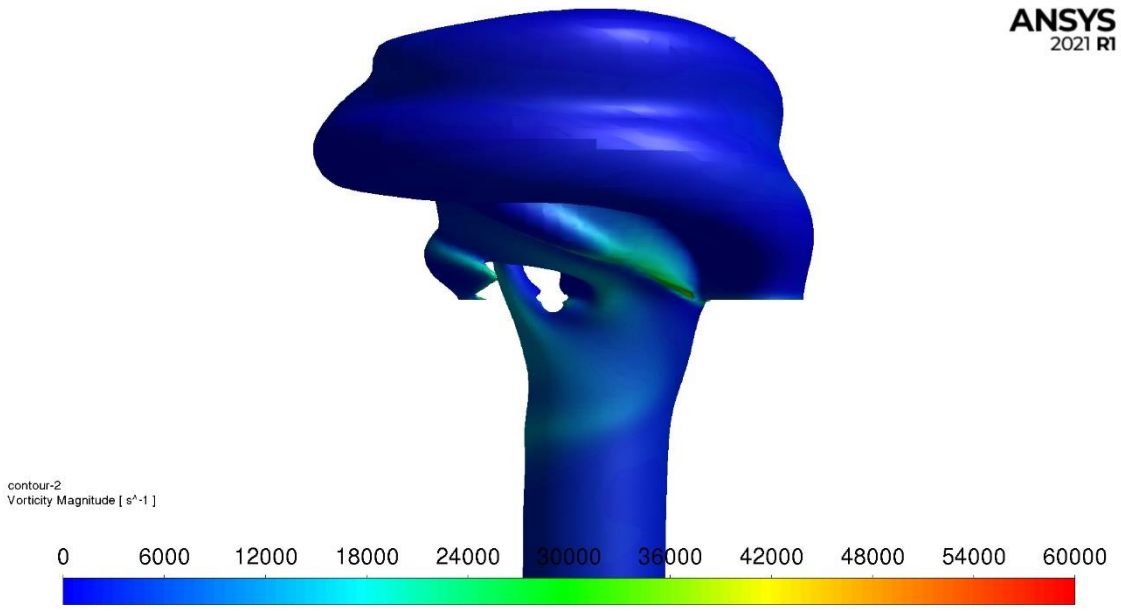

Figure A.13 PVC visualisation (RSM-epsilon-LRR)